



Thèse de doctorat de l'Université de Lille

En vue de l'obtention du Grade de Docteur en Chimie Physique et Chimie des Matériaux  
**École Doctorale des Sciences de la Matière, du Rayonnement et de  
l'Environnement (ED – SMRE)**

Soutenue publiquement par :  
**Joseph Boulos**

Le 11 Janvier 2024

---

## **Transformation de la biomasse lignocellulosique brute en glycols et dérivés aminés: conception de catalyseurs, et études de réactivité**

---

### **Direction de la thèse:**

Sébastien Royer, Professeur des Universités, Université de Lille      Directeur

Jérémy Dhainaut, Chargé de Recherche, CNRS      Co-directeur

### **Membres du Jury:**

Fabien Can	Professeur des Universités	Université de Poitiers	Rapporteur
Nathalie Tanchoux	Directrice de Recherche	Ecole Nationale Supérieure de Chimie de Montpellier	Rapporteuse
Pierrick Gaudin	Professeur des Universités	Université de Montpellier	Examineur
Laurence Pirault-Roy	Professeure des Universités	Université de Poitiers	Examineur (Présidente)
Franck Rataboul	Chargé de Recherche	Université Lyon 1	Membre invité
Léa Vilcocq	Chargée de Recherche	Université Lyon 1	Membre invitée



Ph.D. for the obtention of the degree of

Doctor of "Chimie des matériaux" delivered by  
**Lille University, Doctoral school of Sciences of matter, radiation and environment,  
Faculty of Sciences and Technologies**

Presented by  
**Joseph Boulos**

Defended on 11 January 2024

---

## **Transformation of raw lignocellulosic biomass into glycols and amine derivatives: design of catalysts, and reactivity studies**

---

### **Thesis supervision:**

Sébastien Royer, University professor, Université de Lille      Director

Jérémy Dhainaut, Researcher, CNRS      Co-director

### **Jury members:**

Fabien Can	University professor	Université de Poitiers	Reviewer
Nathalie Tanchoux	Research director	Ecole Nationale Supérieure de Chimie de Montpellier	Reviewer
Pierrick Gaudin	University professor	Université de Montpellier	Examinator
Laurence Pirault-Roy	University professor	Université de Poitiers	Examinator (President)
Franck Rataboul	Research scientist	Université Lyon 1	Invited member
Léa Vilcocq	Research scientist	Université Lyon 1	Invited member

## **Acknowledgements**

The work described in this manuscript was funded by the National Research Agency (ANR) through the CatReMo project. It was carried out at the UCCS (Unité de Catalyse et de Chimie du Solide), mixed research unit (UMR) 59655 University of Lille and CNRS, within the MATCAT research team. The ANR project was carried out in partnership with IRCELYON (Institut de Recherches sur la Catalyse et l'Environnement de Lyon) and the CP2M research laboratory (Catalyse, polymérisation, procédés et matériaux).

I would like to thank Franck Dumeignil, director of UCCS and all the staff of the institute for their welcome and for having ensured the smooth running of this thesis.

My warmest thanks go to my thesis director Sébastien Royer and my thesis co-director Jérémy Dhainaut for the trust they have placed in me. I will be eternally grateful to you for your support, advice and help provided so that I can carry out this project in the best conditions.

I stand in recognition to the project collaborators, Franck Rataboul, Noémie Perret and Firat Goc as well as the CDurable team at IRCELYON for the 7 months internship that I had the chance to do with them. It was a very constructive, rich and pleasurable experience, through it I learned a lot on catalysis and I've been able to test lots of catalysts. I would like to thank the project collaborators, Clémence Nikitine, Léa Vilcocq, Pascal Fongarland and Isaline Bonnin from CP2M for the discussions during the progress meetings, very constructive and friendly moments.

And finally, I would like to thank my family, who stood behind me to achieve this thesis, and without whom I wouldn't be able to be here today.

## List of abbreviations

AC: activated carbon

AMT: ammonium metatungstate

BG: 1,2-butanediol

CNTs: carbon nanotubes

CTAB: cetyltrimethylammonium bromide

DA: dopamine hydrochloride

DEA: diethylamine

DENP: dendrimer-encapsulated nanoparticle

DFT: discrete Fourier transform

fcc: face-centered cubic

EDX: energy dispersive X-ray spectroscopy

EELS: energy-loss X-ray spectroscopy

EG: ethylene glycol

EN: electronegativity

ERY: erythritol

ETA: ethanolamine

EtOH: ethanol

EXAFS: extended X-ray absorption fine structure

GA: glycolaldehyde

GC-MS: gas chromatography coupled with mass spectrometry

GLY: glycerol

GNSs: graphene nanosheets



HA: hydroxyacetone

HPLC: high performance liquid chromatography

ICP-OES: inductively coupled plasma emission spectroscopy

IW: incipient wetness impregnation

m: mass

MeOH: methanol

MEA: monoethylamine

MOF: metal organic framework

MWNTs: multi-walled carbon nanotubes

N-C: N-doped carbon

NRs: nanorods

NPs: nanoparticles

NMR: nuclear magnetic resonance in the liquid phase

PEG: polyethylene glycol

PG: 1,2-propylene glycol

PTA: Phosphotungstic acid

PVP: polyvinylpyrrolidone

RAC: retro-aldol reaction

Ref: reference

rpm: revolutions per minute

S<sub>BET</sub>: specific surface by Brunauer, Emmett and Teller theory

SEM: scanning electron microscopy

SOR: sorbitol

STEM: scanning transmission electron microscopy

T: temperature

t: time

TPEB: 1,2,4,5-tetrakisphenylethynylbenzene, C<sub>38</sub>H<sub>22</sub>

TEA: triethylamine

TEM: transmission electron microscopy

TOC: total organic carbon

TOE: tons of oil equivalent

TPC: temperature programmed carburation

TPR: temperature programmed reduction

V<sub>cell</sub>: cell volume

WC-NRs: Tungsten carbide nanorods

XANES: X-ray absorption near edge structure

XPS: X-ray Photoelectron Spectrometry

XRD: X-ray diffraction

ZIF: zeolitic imidazolate frameworks

# General introduction

The work carried out during this thesis is a part of a general research project, CatReMo, funded by the French National Research Agency (ANR), and carried out in partnership with IRCELYON and CP2M laboratories. It relates to the conversion of raw lignocellulose in the presence of heterogeneous catalysts. The targeted molecules are amines derived from glycols. The objective is to study their synthesis directly from lignocellulose or via an intermediate step of formation of glycols.

Glycols and amines are produced on a very large scale by petrochemical industry. The production processes involve many steps and the use of toxic products generating a large amount of waste. The robust lignocellulosic biomass is composed of three highly functionalized biopolymers. The sugars released by the hydrolysis of the latter can be selectively transformed into glycols by hydrogenolysis reactions. The literature indicates that bifunctional catalysts based on metal carbides Ni-W<sub>x</sub>C/AC are effective under hydrothermal conditions and under suitable reducing atmosphere. On the other hand, the direct amination of biomass by reductive aminolysis reactions remains a challenge for the moment.

The MATCAT team at UCCS specializes in the synthesis of hierarchical materials and supported or unsupported nanoparticles for applications in heterogeneous catalysis, in particular nitrogen doped carbons as well as metal-organic frameworks (MOFs). The C'DURABLE team at IRCELYON has been conducting research for many years on the valorization of lignocellulose and biosourced products by heterogeneous catalysis, including the use of metal carbides, for the transformation of molecules derived from biomass. In this context, we report here our contribution to the transformation of lignocellulosic biomass into glycols and amino derivatives by catalysts based on innovative supported tungsten carbides from nitrogen doped carbons and MOFs.

This work was an opportunity to deepen our knowledge on the preparation, characterization and reactivity of these types of materials. This was achieved by studying the effect of the method of preparation on the composition and characteristics of the catalyst and then by correlating these data to the transformation of cellulose. The presentation of the results obtained during this thesis is divided into 5 Chapters:

Chapter 1 presents a more in-depth study on tungsten carbides. It follows the state of the art on their valorization for the conversion of lignocellulosic biomass into glycols.

Chapter 2 presents the products, operating protocols, materials and methods used for the synthesis and characterization of catalysts, as well as for carrying out catalytic tests and reaction analyses.

Chapter 3 focuses on the preparation and characterization of carbon and nitrogen doped carbon supports from biopolymers (alginate and chitosan), as well as the preparation of bimetallic nanoparticles (NiW) on these carbons. The influence of nitrogen doping on the stability of the catalyst for the hydrogenolysis reaction of cellulose is studied.

Chapter 4 describes the preparation and characterization of bimetallic nanoparticles (NiW) on carbon derived from a nickel-based MOF (DUT-8) functionalized with tungsten. The influence of synthesis methods on the activity and stability of the catalyst for the cellulose hydrogenolysis reaction are studied.

Chapter 5 presents a more exploratory study on the transformation of acetol into amino glycols in the presence of Ru-based bimetallic nanoparticle catalysts.

Chapters 3 to 5 have been directly adapted from the relating submitted articles with extra experimental data added.

Finally, a conclusion will be proposed along with some perspectives.

# Introduction générale

Les travaux effectués lors de cette thèse s'incluent dans le projet CatReMo financé par l'ANR (ANR-19-CE43-0005), et coordonné par l'IRCELYON et réalisé en partenariat avec le laboratoire CP2M. Le projet traite de la conversion de lignocellulose brute en présence de catalyseurs hétérogènes. Les molécules ciblées sont des amines dérivées de glycols. L'objectif est d'étudier leur synthèse directement à partir de lignocellulose ou via une étape intermédiaire de formation de glycols. Les glycols et les amines sont actuellement produits à grande échelle par la pétrochimie. Les procédés de production impliquent de nombreuses étapes et l'utilisation de produits toxiques, comme l'oxyde d'éthylène, générant une grande quantité de déchets.

La biomasse lignocellulosique est composée de trois biopolymères hautement fonctionnalisés. Les sucres libérés par l'hydrolyse de ces derniers peuvent être sélectivement transformés en glycols par des réactions d'hydrogénolyse. La littérature indique que des catalyseurs bifonctionnels à base de carbures métalliques Ni-W<sub>x</sub>C/AC sont efficaces dans des conditions hydrothermales et sous atmosphère réductrice adéquate. En revanche l'amination directe de la biomasse par des réactions d'aminolyse réductrice reste pour l'instant un défi.

L'équipe MATCAT à l'UCCS est spécialisée dans la synthèse de matériaux poreux et des nanoparticules supportées pour des applications dans la catalyse hétérogène. Ils étudient également l'utilisation de charbons azotés biosourcés ainsi que les MOFs comme support de catalyseurs et adsorbants. L'équipe C'DURABLE à IRCELYON mène depuis de nombreuses années des recherches sur la valorisation de la lignocellulose et de produits biosourcés par catalyse hétérogène. Une spécificité de ce groupe est notamment l'utilisation de carbure métalliques pour la transformation des molécules issues de biomasses. Dans ce contexte, nous apportons ici notre contribution à la transformation de biomasse lignocellulosique en glycols et dérivés aminés par des catalyseurs à base de carbures de tungstène supportés sur charbons azotés ou bien préparés à partir de précurseurs MOFs.

Ces travaux ont été l'occasion d'approfondir les connaissances sur la préparation, la caractérisation et la réactivité de ces matériaux. Ceci a été réalisé par l'étude de l'effet du mode de préparation sur la composition et les caractéristiques du catalyseur puis par corrélant ces propriétés à la

transformation de la cellulose. La présentation des résultats obtenus lors de cette thèse est divisée en 5 Chapitres :

Le Chapitre 1 présente l'état de l'art sur la conversion de la biomasse lignocellulosique en glycols, détaillant de manière exhaustive les propriétés des catalyseurs à base de tungstène.

Le Chapitre 2 expose les produits, les protocoles opératoires, les matériels et les méthodes utilisés pour la synthèse et la caractérisation des catalyseurs, ainsi que pour la réalisation des essais catalytiques et les analyses réactionnelles associées.

Le Chapitre 3 se concentre sur les préparations et les caractérisations des supports charbon et charbon azoté à partir de biopolymères (alginate et chitosane), ainsi que la préparation de nanoparticules bimétalliques (NiW) sur ces charbons. L'influence du dopage en azote sur l'activité et la stabilité du catalyseur pour la réaction d'hydrogénolyse de la cellulose est étudiée.

Le Chapitre 4 décrit les préparations et les caractérisations des nanoparticules bimétalliques (NiW) sur du charbon dérivé d'un MOF à base de nickel (DUT-8) fonctionnalisé avec du tungstène. L'influence des méthodes de synthèse sur l'activité et la stabilité du catalyseur pour la réaction d'hydrogénolyse de cellulose y sont étudiées.

Le Chapitre 5 présente une étude exploratoire sur la transformation de l'acétol, intermédiaire dans la transformation de la cellulose, en glycols aminés en présence de catalyseurs à base de Ru.

## Table of Contents

<b>Chapter 1: Bibliographic study .....</b>	<b>11</b>
1.1. Biorefining .....	11
1.2. Glycols amination .....	14
1.3. Nitrogen-doped carbons .....	21
1.3.1. General introduction on nitrogen-doped carbons.....	21
1.3.2. Chitosan .....	21
1.3.3. Chemical activation and Hydrothermal process .....	22
1.3.4. Pyrolysis process.....	23
1.4. Synthesis, Phase Stability, and Characterization of Tungsten carbide catalysts.....	25
1.4.1. Structure and properties .....	26
1.4.2. Synthesis of tungsten carbide catalysts via the solid phase reaction.....	29
1.4.3. Synthesis of transition metal carbide catalysts via the liquid phase reaction.....	33
1.4.4. Synthesis of transition metal carbides via the gas phase carburization.....	39
1.4.5. Tungsten carbides as catalysts .....	42
1.5. Carbon supported tungsten carbides for Biomass Conversion .....	43
1.5.1. Catalytic conversion of (hemi)cellulose and derived sugars.....	43
1.5.2. Catalytic Conversion of cellulose from different biomass feedstocks .....	49
1.6. Summary and Outlook .....	54
1.7. References.....	55
<b>Chapter 2: Materials and methods.....</b>	<b>68</b>
2.1. Preparation of catalysts .....	68
2.1.1. Starting Materials.....	68
2.1.2. N-doped carbon-based materials.....	68
2.1.3. DUT-8(Ni) derived carbon materials .....	69
2.1.4. Synthesis of Ruthenium based materials.....	71
2.2. Physico-chemical characterization of catalysts.....	73
2.2.1. Structural Properties.....	73
2.2.2. Elemental analysis.....	76
2.2.3. Surface Properties (X-ray photoelectron spectroscopy).....	77

2.2.4. Textural analysis (N <sub>2</sub> Physisorption) .....	77
2.2.5. Morphological Properties.....	80
2.2.6. Chemical and thermal properties .....	83
2.3. Biomass transformation .....	84
2.3.1. Experimental protocols .....	84
2.3.2. Products analysis.....	86
2.3.3. Exploitation of the results .....	89
2.4. References.....	91
<b>Chapter 3 : N-doped Ni-WxC catalysts for cellulose hydrogenolysis.....</b>	<b>92</b>
3.1. Introduction.....	93
3.2 Experimental .....	96
3.3. Results and discussion .....	96
3.3.1. Characterization of materials .....	96
3.3.2. Application to the catalytic conversion of cellulose .....	106
3.3.3. Characterization of catalysts after catalysis .....	110
3.4. Conclusion .....	111
3.5. References.....	111
3.6. Supplementary information.....	114
<b>Chapter 4 : MOF-derived Ni-WxC catalysts for cellulose hydrogenolysis.....</b>	<b>129</b>
4.1. Introduction.....	130
4.2. Experimental .....	132
4.3. Results and discussion .....	132
4.3.1. Synthesis and Characterization of materials .....	132
4.3.2. Catalytic conversion of cellulose .....	145
4.4. Conclusion .....	149
4.5. References.....	150
4.6. Supplementary information.....	153
<b>Chapter 5 : Catalytic reductive amination of acetol over Ruthenium based catalysts.....</b>	<b>169</b>
5.1. Introduction.....	170
5.2. Experimental .....	173
5.3. Results and discussion .....	173



5.3.1. Initial studies with 5.3%Ru/AC catalyst .....	173
5.3.2. Variation of catalyst composition .....	176
5.3.3. Recycling studies with 4.5%Ru-4.5%Ni/AC catalyst.....	183
5.3.4. Reactivity of acetol biosourced precursors .....	185
5.4. Conclusion .....	188
5.5. References.....	190
5.6. Supplementary Information .....	194
5.6.1. Literature.....	194
5.6.2. Experimental section.....	195
5.6.3. Reaction mixture analysis after reductive amination of acetol .....	196
5.6.4. Characterisation of carbon-supported Ru and Ru-Ni catalysts .....	199
5.6.5. Reactivity study of products .....	202
5.6.6. Characterisation of 4.5%Ru-4.5%Ni/AC recovered after a catalytic reaction.....	204
5.6.7. Characterisation of 7.5%Ru-36%W <sub>x</sub> C/AC .....	207
5.6.8. Reactivity study of acetol biosourced precursors.....	211
5.6.9. References.....	212
<b>Conclusion and perspectives .....</b>	<b>213</b>

# Chapter 1: Bibliographic study

## 1.1. Biorefining

The proved reserves of oil reached more than 200 billion TOE in 2018 worldwide, according to experts from British Petroleum (who have been drawing up an inventory of the resource since 1980). These reserves could cover 50.2 years of annual consumption at the rate of 2017's consumption. This was confirmed by the Commissariat for Atomic Energy and Alternative Energies (CEA) and by the International Energy Agency (IEA). They do not consider the oil sands of Canada, nor the reserves of Venezuela, nor the reserves considered difficult to capture with current techniques. The reserves could therefore be greater than the estimates suggest<sup>1</sup>.

In recent decades, despite the dwindling amount of nonrenewable fossil resources, the growing demand for chemicals, fuels, and materials has urged researchers to use renewable alternative energy as well as sustainable chemical resources<sup>2,3</sup>. Biomass, being the most abundant neutral carbon renewable source, has thus received attention from multiple research fields<sup>4-6</sup>. The concept of a biorefinery that converts biomass into fuels and chemicals has been developing in the last two decades, and academic research on biomass also flourished during this period<sup>5,7,8</sup>.

Biomass refers to materials produced from agricultural crops and their residues, herbs and forest residues, and organic waste. The treatment of biomass dates back to thousands of years whereas it was directly burned to generate heat. It is now recognized that biomass is also a utile feedstock and can be transformed into various valuable products such as biogas, bioethanol, and biodiesel, providing the concept of biorefinery. Significant energy generation from biomass necessitates vast amounts of cultivable land and water. At present consumption rates, it is predicted that substituting 5% of gasoline and diesel fuels for Europe and the United States would claim around 20% of their cultivable land<sup>9</sup>. The fundamental economic goal is to construct a self-sustaining biorefinery, which does not require government aid or reinvestment since it has the requisite profitability. Which is often difficult when profits calculations are made. In terms of the social aspect, studies have examined two edges: the first is connected to job creation, and the second to societal well-being in terms of food security. The latter is a factor to consider especially if the biomass source is agricultural, so it will enter in competition with food production<sup>10</sup>. The set of limitations introduces significant uncertainties that impact the efficiency of a biorefinery, potentially leading

to unattainable supply chain network or inferior performance<sup>11</sup>. These limits create a complicated picture for decision-makers and biorefinery investors, necessitating the development of tools to assist in assessing these uncertainties<sup>12</sup>. Table 1 contains a complete summary of these uncertainties and their sources.

**Table 1.** Biorefinery supply chain network uncertainties<sup>10</sup>.

<b>Classification</b>	<b>Uncertainties</b>
Cost	<ul style="list-style-type: none"> <li>Cost of transporting biomass</li> <li>Operation cost for conversion processing</li> <li>Cost of transporting intermediate products</li> <li>Cost of transporting final products</li> <li>Acquisition cost for each biomass type</li> <li>Annualized capital cost of conversion processing</li> <li>Expansion plans</li> </ul>
Profits (Value)	<ul style="list-style-type: none"> <li>Value of each intermediate product at conversion processing site</li> <li>Sale price of each final product</li> </ul>
Production Process	<ul style="list-style-type: none"> <li>Yield of final product from intermediate product at conversion processing</li> <li>Yield of intermediate product from biomass at conversion processing</li> </ul>
Extern	<ul style="list-style-type: none"> <li>Demand fluctuations</li> <li>Natural or human disasters</li> <li>Weather</li> <li>Technology availability</li> <li>Change in regulations and policies</li> </ul>
Nature of biomass	<ul style="list-style-type: none"> <li>Biomass availability for each biomass type</li> <li>Biomass properties such as moisture content</li> </ul>

The catalyst is critical in biorefinery processes because it minimizes the overall complexity of the process and the struggles to shift the flow into the desired output. Catalysts of many varieties are used in biorefineries, including homogeneous, enzymatic, and heterogeneous catalysts. Here are some instances of each category, along with its benefits and drawbacks:

Homogeneous catalysts are soluble in the reaction media. Metal complexes, acids, and bases are examples of substances that enable chemical reactions in a homogenous phase. For example, palladium or ruthenium catalysts can be used in oxidation or hydrogenation reactions<sup>13</sup>. This type of catalysis achieves high catalytic activity and selectivity. In addition, well-defined structures allow for exact control of reaction conditions. However, it frequently necessitates precisely regulated reaction conditions. Separation and recycling of homogenous catalysts might be difficult.

Enzymes are naturally occurring catalysts that can speed up particular biological processes. Under moderate circumstances, they are often proteins with great selectivity and activity. Lipases, for example, are used to convert lipids into biodiesel<sup>14</sup>. They are renewable and biodegradable, as well as extremely selective and function under mild reaction conditions, eliminating the need for harsh chemicals. However, they are expensive to produce and purify, and they have low stability under specific reaction conditions.

Heterogeneous catalysts are materials that intervene in reactions of gaseous, liquid, or solid substrates by providing active sites on which the reaction can take place. They are readily separated and regenerated, and they are extremely stable under strong reaction conditions. Nonetheless, because of diffusion in porous catalysts, they have mass transfer restrictions as well as lower selectivity for some reactions. Table 2 compares heterogeneous and homogeneous catalysis in terms of catalyst properties, catalytic effectiveness, and catalyst separation<sup>15</sup>.

**Table 2.** Comparison between heterogeneous and homogeneous catalysis<sup>15</sup>.

	<b>Homogeneous</b>	<b>Heterogeneous</b>
<b>Active Centers</b>	All atoms	Only surface atoms
<b>Selectivity</b>	High	Low
<b>Mass Transfer Limitations</b>	Very rare	Can be severe
<b>Structure/Mechanism</b>	Defined	Undefined
<b>Catalyst Separation</b>	Tedious/Expensive (extraction or distillation)	Easy
<b>Applicability</b>	Limited	Wide
<b>Cost of Catalyst Losses</b>	High	Low

The increasing need for sustainable energy resources has promoted investigations into biomass conversion using a wide range of catalysts. Among them, zeolites, due to their unique properties, are widely used as heterogeneous catalysts in the field of biorefining. Their three-dimensional crystalline structure and large specific surface area make them effective catalytic materials for various reactions converting biomass into high value-added chemicals and fuels. For example, studies have shown that ZSM-5 zeolite is an effective catalyst for the cracking of cellulose into value-added chemicals. In one study, Wang *et al.* used both Mn-doped bismuth oxyiodide and ZSM-5 zeolite for cellulose hydrolysis and oxidation to glycolic acid in an O<sub>2</sub> atmosphere and at 180 °C, a yield of 82.6% was achieved<sup>16</sup>. Mixed oxides are also of great interest in biorefining. These catalysts provide a diversity of active sites for catalytic reactions. Mixed oxides exhibit excellent thermal stability, high catalytic activity and controlled selectivity, making them attractive for various catalytic reactions in biorefining. For example, copper-chromium catalysts were employed in the hydrogenolysis of glycerol at 220 °C under H<sub>2</sub> pressure of 8 MPa<sup>17</sup>. The catalyst prepared by precipitation showed a higher catalytic activity (conversion of around 80% with a selectivity of 85 % towards propylene glycol) than the impregnated catalyst (conversion of around 38% with a selectivity of 42 % towards propylene glycol). The reduced copper chromite spinel structure, that constitutes a single phase, appeared to be responsible for this high catalytic activity. Tungsten carbides are an emerging type of heterogeneous catalyst that has significant advantages in biorefining. Tungsten carbides are tough materials, resistant to corrosion and catalytic poisoning. They also possess excellent thermal stability, making them suitable for high temperature catalytic reactions involved in biorefining. For all those reasons we decided to further study them in this field, particularly in cellulose hydrogenolysis.

## 1.2. Glycols amination

The production of chemicals from renewable and non-edible lignocellulosic biomass is considered as a promising way to reduce dependence on fossil resources. Nitrogen-containing molecules are widely used for the synthesis of pharmaceuticals, polymers, surfactants, agrochemicals, and dyes. Among them, short-chain primary amines of interest include alaninol, an intermediate for the synthesis of ofloxacin (antimicrobial agent), aminopropan-2-ol (solubilizer of oil and fat), diaminopropane, (building block in the synthesis of heterocycles). Therefore, there is a great interest to form such amines from biosourced reactants. Owing to its high O/C ratio (~1/1), the production of oxygenates from biomass feedstocks is rather straightforward and has been largely

studied. However, the further production of valuable nitrogen-containing products is far less evident due to the deficit of efficient amination strategies of such oxygenates.

Noble metals, such as platinum (Pt), palladium (Pd) and rhodium (Rh), are often used as catalysts in biorefining<sup>18,19</sup>. These metals are generally supported on materials such as alumina or silica, which improves their stability and their catalytic activity. Supported noble metal catalysts are commonly used for hydrogenation, hydrogenolysis, hydrodeoxygenation and amination reactions, which are key steps in converting biomass into high value chemicals and fuels. A promising route is the catalytic reductive amination of aldehydes and ketones. Of great demand in the polymer industry, the amine products are mainly obtained from petrochemicals where alkane oxides or chlorinated alkanes are aminated<sup>5</sup>. Thus, in the same way as for glycols formation, a large energy demand is necessary and many by-products are obtained by aminating glycols obtained from lignocellulosic biomass. For this, processes from glycols by homogeneous and heterogeneous catalysis have emerged<sup>20,21</sup>. Examples of biological pathways through amino acid reduction have also been studied<sup>22</sup>. These amine derivatives are mainly used as surfactants but they are also used by the polymer, pharmaceutical and food industries. The demand is fewer than for glycols, however these are products with higher added value (for example the price of ethanolamine is almost double that of EG)<sup>23</sup>. There is relatively little literature on the formation of these amines from glycols. By heterogeneous catalysis, these products can be obtained by reductive amination of hydroxyl groups. This is done in two steps, first the hydroxyl function is dehydrogenated to form a carbonyl intermediate and then an addition of the amine is performed. After removal of a water molecule, the imine is formed. This second intermediate is hydrogenated to an amine. The by-products observed generally come from the condensation of the substrate with the product obtained. From biomass, a two-step synthesis can be carried out with the formation of glycols or intermediates, followed in a second step by the amination of these products under more specific conditions. The one-step strategy induces conditions similar to hydrogenolysis. Hydrolysis and C-C cleavage reactions of the retro-aldol type make it possible to obtain glycolaldehyde and hydroxyacetone, then these intermediates are aminated. Differently, prior amination of the sugar can lead to reductive aminolysis reactions<sup>24,25</sup>. The amination of alcohols is difficult because a preliminary dehydrogenation step is necessary in order to obtain a carbonyl function. It is therefore better to turn to the amination of carbonyl reaction intermediates (glycolaldehyde and hydroxyacetone). Among these molecules, aldehydes are the most reactive, followed by ketones.

Based on these categories of molecules, a variety of catalysts exist and different operating conditions have been established in heterogeneous catalysis (Table 3). The role of the catalysts is to facilitate the addition of amine and then to hydrogenate the imine intermediate formed. However, it is better to employ slightly less active catalysts and reaction conditions to avoid rapid hydrogenation before the formation of the imine and that are also active for the necessary dehydrogenations. For this reaction a large number of supported metals are used. The metals of choice seem to be similar to those for hydrogenation: Ru and Ni. For supports, oxides are mostly used. It should be noted that the very basic conditions of the reaction, due to the presence of amines, induce severe constraints on the material used. The temperature have a strong impact on the selectivity of the obtained products, its increase can enhance the production of aminoalcohols<sup>26</sup>. The gases used are H<sub>2</sub> or a H<sub>2</sub>/NH<sub>3</sub> mixture. Regarding aminating agents in the liquid phase, they are used in large excess because there is a competition between amination and hydrogenation. There are many aminating agents, the simplest being ammonia. Aromatic amines can also be used. To the best of our knowledge the earliest study corresponds to that of Baiker *et al.* who reacted ethylene glycol with dimethylamine in the presence of a Cu/Al<sub>2</sub>O<sub>3</sub> catalyst in a continuous reactor, yielding tertiary mono and diamines<sup>21</sup>. The selectivity depended on temperature and the aminoalcohol was favored at highest temperatures. While H<sub>2</sub> pressure had no impact, the presence of water increased the selectivity into the aminoalcohol. Liang *et al.* formed ethanolamine with aqueous NH<sub>3</sub> in the presence of Ru/ZrO<sub>2</sub> with a 95% at 85 °C, 20 bar H<sub>2</sub><sup>24</sup>. It was found that on Ru catalysts, direct hydrogenation of glycolaldehyde into EG was considerably repressed, whereas ETA was produced as the primary product with a tiny quantity of ethylenediamine. The activity of Ru catalysts was highly dependent on the supports. The results suggest that the coexistence of Ru species and ZrO<sub>2</sub> in close proximity is required for a high ETA output. The reductive amination of EtOH was studied over Ni/Al<sub>2</sub>O<sub>3</sub> catalysts<sup>29</sup>. In terms of catalyst efficiency, during long-term stability testing (*e.g.*, over 90 h), the EtOH conversion declined significantly during the first 10 hours of the reaction due to metal nitride formation, but a rather steady conversion was maintained after this time. Furthermore, the partial pressures of NH<sub>3</sub> and H<sub>2</sub> had an effect on EtOH conversion and product selectivities. An overabundance of NH<sub>3</sub> in the reactant stream boosted monoethylamine selectivity, whereas an increase in the H<sub>2</sub> partial pressure raised overall selectivities to the various ethylamine products. Furthermore, the conversion of EtOH changed with NH<sub>3</sub> and H<sub>2</sub> partial pressures. As displayed in Figure 1, EtOH reductive amination proceeds

in steps, starting with EtOH dehydrogenation to acetaldehyde. Condensation and reactivity of the carbonyl molecule with  $\text{NH}_3$  yields an imine intermediate. Because amine compounds can be created as primary, secondary, or tertiary amines, MEA can be produced by hydrogenation of the imine intermediate, whereas DEA and TEA are formed via a sequential route<sup>27</sup>.

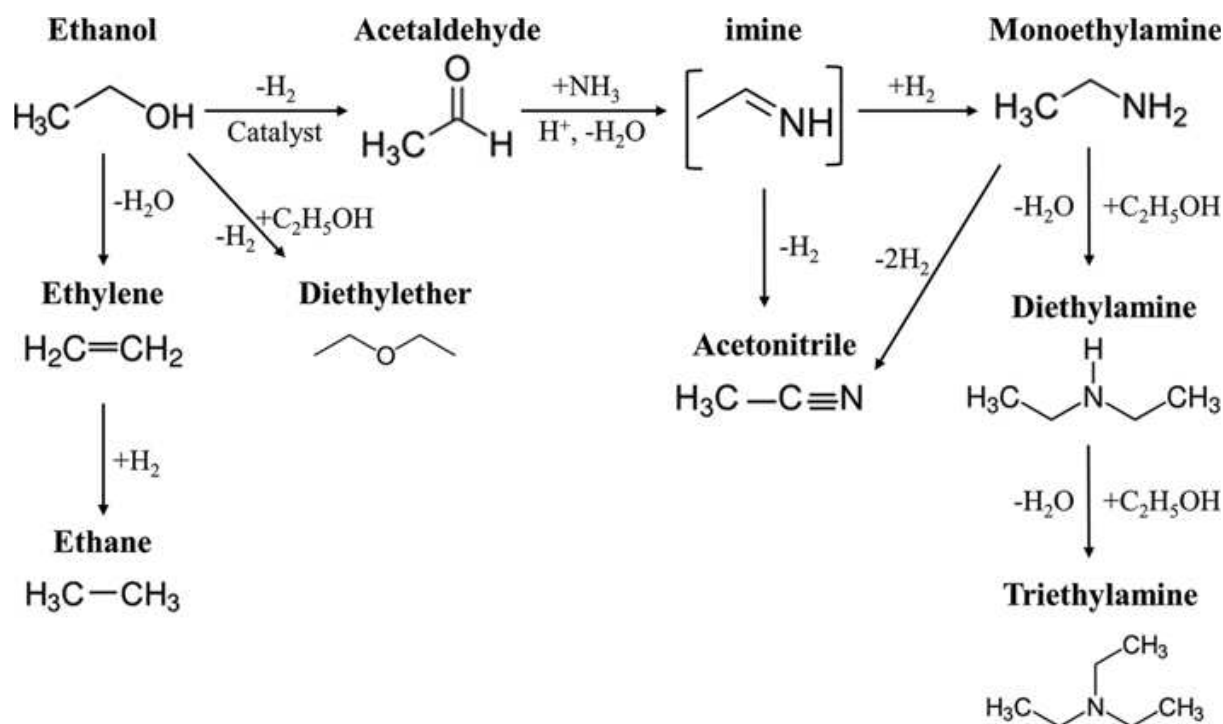


**Figure 1.** Possible reaction pathways for ethanol reductive amination<sup>27</sup>.

Yue *et al.* obtained a 39% yield of propylene glycol-derived amines, mostly alaninol, in the presence of a  $\text{Co}/\text{La}_3\text{O}_4$  catalyst ( $160\text{ }^\circ\text{C}$ , 6 h) at 40% conversion. The reaction was carried out in aqueous  $\text{NH}_3$  but without the addition of external  $\text{H}_2$  since it appeared that the hydrogen produced during the dehydrogenation of propylene glycol was enough to carry out the reduction step<sup>28</sup>. Wang *et al.* recently reported aqueous  $\text{NH}_3$  amination of glycerol with a  $\text{RuNi}/\text{MgO}$  catalyst, yielding the amino acid alanine via the intermediate production of lactic acid under basic conditions. The authors proposed a potential reaction route as described in Figure 2. Lactic acid is produced from glycerol by sequential dehydrogenation, dehydration, and rearrangement. Then through a dehydrogenation-amination-hydrogenation route, lactic acid combines with ammonia to generate alanine. The primary side reactions include hydrogenolysis of the C3 species into C1 and C2 products<sup>29</sup>.





Glycol-aldehyde	2 mmol substrate, 2 mL NH <sub>3</sub> (25 wt%), 0.1 g catalyst, 75 °C, 12 h, 30 bar H <sub>2</sub>	Ru/ZrO <sub>2</sub>	Ethanolamine	93	24
Ethanol	3 kPa substrate, 0.2 g catalyst, 190 °C, 0.9 h <sup>-1</sup> , EtOH/NH <sub>3</sub> /H <sub>2</sub> (molar ratio of 1/1/6)	Ni/Al <sub>2</sub> O <sub>3</sub>	Ethylamine	43	27
1,2-Propylene glycol	2 mL substrate, 18 mL NH <sub>3</sub> , 0.1 g catalyst, 160 °C, 6h, no H <sub>2</sub>	Co/La <sub>3</sub> O <sub>4</sub>	2-Amino-1-propanol	60	28
Glycerol	0.1 g substrate, 2 mL NH <sub>3</sub> (25 wt%), 0.2 g NaOH, 0.07 g catalyst, 220 °C, 4 h, 10 bar H <sub>2</sub>	RuNi/MgO	Alanine	43	29
Furfural	0.5 mmol substrate, 16 equiv. NH <sub>3</sub> , 5 mL MeOH, 0.02 g catalyst, 90 °C, 4 h, 40 bar H <sub>2</sub>	Ru/Nb <sub>2</sub> O <sub>5</sub>	Aminofurfural	89	30
2-Octanone	1 mmol substrate, 3 mL o-xylene, 0.02 g catalyst, 100 °C, 20 h, 2 bar H <sub>2</sub> , 4 bar NH <sub>3</sub>	Pt-MoO <sub>x</sub> /TiO <sub>2</sub>	2-Aminooctane	77	31

(\*) Mass based.

Concerning acetol there exists some more, but still few, reports, presented in Table 4. They are all about the production of primary amine derivatives utilizing heterogeneous catalysis. This transformation is extremely difficult due to the requirement to combine smooth circumstances to regulate the reaction with the relative difficulty of activating ammonia<sup>33</sup>. Also, because of the stronger reactivity of the carbonyl function, alaninol is always the primary amino product, whereas compounds like 1,2-diaminopropane and 1-aminopropane-2-ol were seldom detected or even reported. Hence, Liang *et al.* reported the reductive amination of a range of aldehydes and ketones, including acetol, yielding alaninol and propylene glycol employing Ru/ZrO<sub>2</sub>. The catalyst was made of partially reduced Ru, resulting in RuO<sub>2</sub> particles capable of promoting acid activation of carbonyl group to amine and Ru particles capable of promoting the imine intermediate hydrogenation. Trégner *et al.* proposed using NiO/Al<sub>2</sub>O<sub>3</sub> as a fixed-bed catalyst for gas phase transformation that yielded 45% alaninol and 22% propylene glycol at complete conversion from a direct reduction of acetol<sup>34</sup>. Sheng *et al.* recently published the synthesis of alaninol from acetol over 50-150 nm Co<sub>2</sub>P nanorods featuring unsaturated Co-Co active sites in aqueous NH<sub>3</sub> under

low H<sub>2</sub> pressure<sup>35</sup>. Finally, Shin *et al.* reported the production of optically active (L)-alaninol by an asymmetric amination reaction using (S)- $\alpha$ -methylbenzylamine in the presence of a Pd/SBA-15. A Pd/NaY catalyst increased conversion but decreased enantiomeric excess<sup>36</sup>.

**Table 4.** Literature data on the reductive amination of acetol with NH<sub>3</sub>.

Reaction conditions	Catalyst	Y <sub>ALA</sub> (%)	Y <sub>DAP</sub> (%)	Y <sub>A2P</sub> (%)	Ref.
2 mmol substrate, 2 mL NH <sub>3</sub> (25 wt%), 0.1 g catalyst, 65 °C, 6 h, 30 bar H <sub>2</sub>	Ru/ZrO <sub>2</sub>	26	10	-	24
8.3 g.h <sup>-1</sup> substrate, 107 g catalyst, 130 °C, 0.078 h <sup>-1</sup> , 1 bar H <sub>2</sub> , 1 bar NH <sub>3</sub>	NiO/Al <sub>2</sub> O <sub>3</sub>	45	traces	3	34
0.5 mmol substrate, 3 mL NH <sub>3</sub> (25 wt%), 0.004 g catalyst, 100 °C, 10 h, 5 bar H <sub>2</sub>	Co <sub>2</sub> P nanorods	70	-	-	35
0.01 mol substrate, 70 mL MeOH, 2.42 g (S)- $\alpha$ -methylbenzylamine, 25 °C, 12 h, 3.5 bar H <sub>2</sub>	Pd/SBA-15	80	-	-	36

The only example to date directly related to the two-steps amines' production from cellulose was given by Zhang *et al.* who obtained ethanolamine in two steps with a total yield of 10%<sup>24</sup>. The first step consists in obtaining glycolaldehyde at 21% yield with H<sub>2</sub>WO<sub>4</sub> as a homogeneous catalyst, then in aminating it during a second step with Ru/ZrO<sub>2</sub> in a reducing medium in the presence of ammonia. Sels *et al.* were able to aminate sugar monomers or dimers with dimethylamine<sup>25,37</sup>. The yields obtained reach 50% in the presence of Ru/C. However, the authors conclude that it would not be possible to use cellulose as a substrate because of the strongly basic conditions. Thus, direct glycols amination remains highly challenging.

Carbon materials are attractive as catalyst supports due to their chemical stability, low density, tunable textural characteristics, electric and thermal conductivity, low price, and availability<sup>117-119</sup>. All those properties, especially for N-doped carbons, allow to improve the dispersion and stability of the supported metallic phases. As a result, we further studied those materials.

### 1.3. Nitrogen-doped carbons

#### 1.3.1. General introduction on nitrogen-doped carbons

The discovery of fullerenes, carbon nanotubes, and graphene have even heightened interest towards advanced carbon materials. The inclusion of heteroatoms in the carbon matrix (*e.g.*, N, B, P, and S) also opened up novel opportunities for functional carbon materials<sup>120</sup>. Nitrogen functional groups, such as pyridinic, pyrrolic, graphitic (quaternary), and oxidized nitrogen species can be stabilized over carbon surface upon nitrogen incorporation<sup>121,122</sup>. The strong electron donating characteristic of nitrogen species supplies the carbon materials with metal-ligation ability, substantial basicity, and modified electronic properties<sup>123</sup>. So far, methods for nitrogen-containing carbon materials manufacturing have included (a) carbonization of nitrogen-rich synthetic materials (*e.g.*, polyamide, polypyrrole, etc.) or natural raw materials (*e.g.*, bio-sourced carbon from chitosan, gelatin, proteins, etc.); (b) post nitrogen enrichment of as-synthesized carbon materials by liquid-phase impregnation or gas phase treatments. Unfortunately, the usage of synthetic precursors and post nitrogen enrichment of the carbon materials are plagued by high production costs, low conversion efficiency, severe and energy-intensive synthetic conditions (*e.g.*, chemical vapor deposition, electric-arc discharge, and laser ablation), environmental issues (*e.g.*, waste generation and release of hazardous chemicals), and a heavy reliance on unsustainable fossil fuel resources<sup>117,124</sup>.

#### 1.3.2. Chitosan

Beyond its eco-friendly nature, the exploitation of renewable biomass-derived materials offers many advantages, including the availability and abundance of starting materials, and provides additional benefits in terms of structural and morphological diversities<sup>125</sup>. Chitosan, for instance, as an N-containing (~7 wt %), renewable, cheap, and abundant biomass resource has a vast potential for the synthesis of N-doped carbon materials. Chitosan properties relate to its several functional groups, including amino, hydroxyl, and acetamido groups, and to its sugar-based polymeric and polyelectrolytic properties<sup>126</sup>. The presence of those functional groups is the reason behind chitosan chelating and gelation properties<sup>127,128</sup>. Multiple synthetic procedures have been used for the conversion of chitosan into N-doped carbon materials. They include hydrothermal treatment, pyrolysis under an inert atmosphere, and microwave-assisted assembly. Given the chitosan skeleton thermally induced evolution during pyrolysis, the precise control of the experimental parameters is crucial. An inert gas atmosphere is usually required, and the choice of

the pyrolysis temperature range and its increasing rate are also pivotal for the nature of the target carbon materials.

### ***1.3.3. Chemical activation and Hydrothermal process***

Chitosan carbonization is a complex process, which involves a decrease in oxygen content and the structure rearrangement through successive reactions (decarboxylation, hydrolysis, dehydration, aromatization, ring opening, cyclization, and condensation)<sup>119</sup>.

The hydrothermal treatment is typically carried out in an aqueous medium at a moderate temperature (100-350 °C) and under autogenous pressure (Table 5). Carbon is formed as a result of water loss, condensation, polymerization, and aromatization processes<sup>129</sup>. Several characteristics distinguish this process, including<sup>130</sup>: (i) easily generated porosity; (ii) the possibility of combining with other components (*e.g.*, metal species) to form composites with special physicochemical and/or catalytic features; and (iii) the generation of surface-reactive functional groups<sup>131,132</sup> that facilitates post synthetic treatment. Notably, the temperature of the hydrothermal treatment has a significant impact on the characteristics of the resulting carbon compounds. Hydrothermal treatment of chitosan at 180 °C, for example, yields porous nitrogen-doped carbon with great chemical stability, good dissolution in acid solutions, and high Cr(VI) adsorption capability. However, above this temperature, a drop in the oxygen and nitrogen contents, as well as in the adsorption capacity of the resulting carbon for what, was observed<sup>133</sup>. Chemical activation may be employed to improve the texture of N-Cs. N-C activation is often achieved by one of two methods: (i) The first method involves thermal treatment of chitosan (450-700 °C), followed by mixing with an activating agent (*e.g.*, NaOH, KOH, ZnCl<sub>2</sub>, K<sub>2</sub>FeO<sub>4</sub>, KHCO<sub>3</sub>) and high temperature treatment (700-900 °C); (ii) the second method involves mixing chitosan first with the activator, accompanied by high temperature treatment (600-950 °C)<sup>134-136</sup>.

The use of additives and the activation procedure at the same time lead to ultrahigh surface area materials. According to Huang *et al.*<sup>137</sup>, the addition of acetic acid favored the formation of an optimal setting for the accessibility of the activation agents (*e.g.*, KOH), as well as the formation of a rigid semicarbonized framework, resulting in N-Cs with an ultrahigh surface area of 3532 m<sup>2</sup>.g<sup>-1</sup> and a hierarchical porous carbon structure. The resulting N-Cs material had an abundance of electrochemically active sites that aided fast ion transport, resulting in outstanding capacitive behavior. The addition of polyethylene glycol as a binding agent and the activation of KOH

resulted in N-Cs with a high surface area of  $2269 \text{ m}^2 \cdot \text{g}^{-1}$ <sup>131</sup>. The PEG content has an impact on the textural characteristics and should be tailored because a PEG excess may result in larger pores that can fall in during the heat treatment.

#### **1.3.4. Pyrolysis process**

In contrast to hydrothermal treatment which is performed at relatively moderate temperature (100-180 °C), chitosan pyrolysis is frequently carried out at high temperatures (600-1000 °C) (Table 5). To avoid oxidation of the carbon and generation of CO<sub>2</sub>, an inert atmosphere of nitrogen or argon is required. The temperature of pyrolysis has a considerable impact on the textural properties of the resultant carbon material<sup>138</sup>. This method may also result in the formation of porous graphitic carbon compounds<sup>139</sup> with enhanced conductivity. A good balance is required for reconciling the two opposing processes, since crystallization frequently occurs at the expense of the porosity<sup>140</sup>. Of note, converting amorphous carbon to crystalline graphene sheets does not result in crystal size expansion, which is commonly observed in metal oxide chemistry<sup>141</sup>.

The textural properties (*e.g.*, large surface area and hierarchical porous structure) of chitosan-derived N-Cs are among the most important properties for their usage in various applications (*e.g.*, metal-free catalysts and catalyst supports in electrocatalysis and photocatalysis). Direct heat treatment of chitosan frequently results in a small surface area. Verma *et al.*, for example, found a surface area of  $93 \text{ m}^2 \cdot \text{g}^{-1}$  when N-C is synthesized by carbonizing chitosan at 300 °C in a nitrogen environment<sup>142</sup>. The activation of the resulting carbon compounds, on the other hand, and/or the introduction of specific reagents, can aid in the formation of larger porosity in N-Cs.

The addition of additives (such as urea, acetic acid, polyethylene glycol, hexaketocyclohexane, and ionic liquids) during the hydrothermal treatment of chitosan has several benefits, including: (i) the simple creation of an open porous structure that displays larger surface area; (ii) an increase in nitrogen content and amount of surface functional groups; (iii) the avoidance of extra functionalization processes; and (iv) eventually enhanced framework graphitization. Jordan *et al.* described an activation-free method for producing porous N-Cs materials<sup>132</sup>. Their method involved crosslinking a chitosan network with urea and hexaketocyclohexane, resulting in a stiff monolithic-like polymer network (Figure 3). Mesoporous materials with a surface area of  $348 \text{ m}^2 \cdot \text{g}^{-1}$ , a pore volume of  $0.71 \text{ mL} \cdot \text{g}^{-1}$ , and a high N content of 12 wt.% were produced after hydrothermal treatment (100 °C, 12 h), CO<sub>2</sub> supercritical drying (to maintain the porous structure),

and carbonization (500 °C, 1 h). These materials displayed high carbon dioxide capture and dye removal efficiency by adsorption.

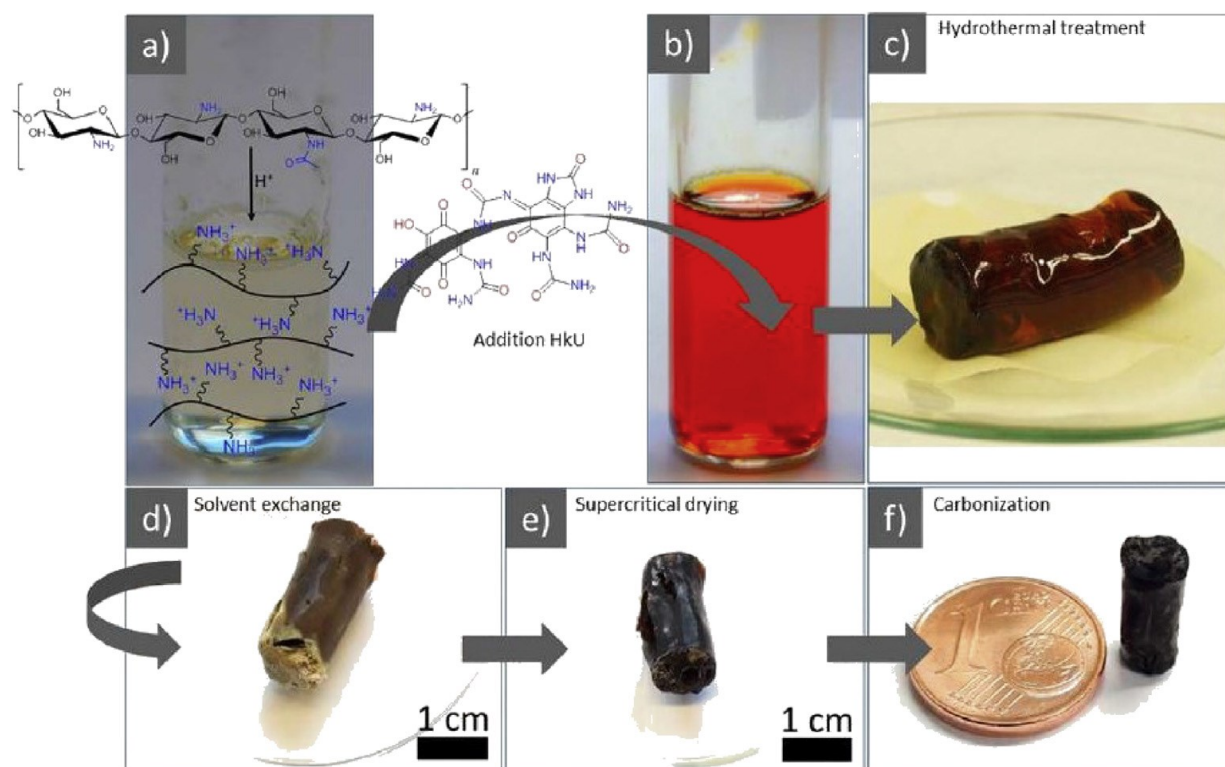


**Figure 3.** Schematic illustration of preparation of carbon monoliths. (a) Chitosan dissolved in 0.1 M acetic acid; (b) Chitosan gel after addition of the urea/hexaketocyclohexane complex precursor; (c) Gel monolith after hydrothermal treatment; (d) Monolith after solvent exchange; (e) Monolith after supercritical drying; (f) Carbon monolith after carbonization at 500 °C<sup>132</sup>.

Ren *et al.* produced carbon compounds by pyrolyzing a chitosan-urea combination. During pyrolysis, urea degraded to NH<sub>3</sub> and subsequently transported nitrogen into the carbon structure. The pyrolysis temperature was used to modify the type of nitrogen groups and the surface area. The catalytic activity of the obtained material for the oxidation of 5-hydroxymethylfurfural to 2,5-diformylfuran was impacted by the experimental synthesis conditions. The material pyrolyzed at 950 °C had the greatest activity and catalytic stability. With a surface area of 2446 m<sup>2</sup>.g<sup>-1</sup> and a nitrogen amount of 4.3 at.%, this material provided a complete 5-hydroxymethylfurfural conversion with a diformylfuran yield of 95% in 14 hours at 100 °C and 10 bar<sup>143</sup>.

**Table 5.** Synthesis of chitosan-derived N-doped carbons and properties.

Additive	Activator	Synthesis method	Synthesis conditions	S <sub>BET</sub> (m <sup>2</sup> .g <sup>-1</sup> )	D <sub>pores</sub> (nm)	N content (%)	Ref.
-	-	Hydrothermal	180 °C, 10 h	-	-	-	133
-	KOH	Pretreatment & pyrolysis	N <sub>2</sub> , 450 °C, 4 h, 900 °C, 2.5 h, 5 °C.min <sup>-1</sup>	3496	2-8	-	134
-	KOH	Pretreatment & pyrolysis	N <sub>2</sub> , 350 °C, 3 h, 5 °C.min <sup>-1</sup> , 850 °C, 2 h	2334	-	2.5	135
-	NaOH	Pyrolysis	N <sub>2</sub> , 800 °C, 1.5 h, 10 °C.min <sup>-1</sup>	318	3.2	-	136
PEG	KOH	Pyrolysis	N <sub>2</sub> , 800 °C, 2 h, 5 °C.min <sup>-1</sup>	2269	3.5	-	131
-	-	Pyrolysis	N <sub>2</sub> , 300 °C, 4 h	93	-	-	142
C <sub>6</sub> O <sub>6</sub> , urea	-	Hydrothermal & pyrolysis	100 °C, 12 h, 500 °C, 1 h, N <sub>2</sub>	348	8.2	12	132

C<sub>6</sub>O<sub>6</sub> = Hexaketocyclohexane.

Tungsten carbides are an emerging type of heterogeneous catalyst that has significant advantages in biorefining. Tungsten carbides are tough materials, resistant to corrosion and catalytic poisoning. They also possess excellent thermal stability, making them suitable for high temperature catalytic reactions involved in biorefining. For all those reasons we decided to further study them in this field.

#### 1.4. Synthesis, Phase Stability, and Characterization of Tungsten carbide catalysts

Suitable carbon precursors such as solid carbons, hydrocarbons, polymers, and carbonaceous chemicals can be used to prepare tungsten carbide catalysts<sup>38</sup>. Common synthesis routes include solid, liquid, and gas-phase reactions (carbon source in the corresponding form). More sophisticated methods that benefit from technological advances are also presented in this section. A table summarizing the contents is provided at the end of each subsection.



### 1.4.1. Structure and properties

Tungsten carbides ( $W_xC$ ), which regroup several crystallographic phases and W/C ratios, belong to the group of refractory carbides and cemented carbides. They have the advantages of high hardness, high melting point (2600-2850 °C), low coefficient of friction, high thermal stability, high Young's modulus of elasticity, and low coefficient of thermal expansion<sup>39</sup>. These properties make tungsten carbide suitable for various engineering applications such as the manufacture of cutting tools, rock drill bits, dies, tools, and general wear parts<sup>40-46</sup>. In addition to these extensive structural applications,  $W_xC$  has been used as for photothermal therapy of cancer<sup>52</sup> and WC erosion-resistant coatings for aerospace components<sup>53</sup>. The two main phases of the binary tungsten-carbon system are tungsten subcarbides ( $W_2C$ ) and tungsten monocarbides (WC), with a number of polymorphs for each as presented in Table 6. It is worth noting that the fcc WC phase, cited here as  $\gamma$ -WC, has many nomenclatures in the literature as  $\gamma$ - $WC_{1-x}$ ,  $\beta$ -WC,  $\alpha$ - $WC_{1-x}$ , or  $WC_{1-x}$ . Similarly, the  $\delta$ -WC phase is sometimes referred to as  $\alpha$ -WC. The computed cell parameters, presented in Table 6, agree with the experimental reports<sup>68,69</sup>. To avoid vagueness, we use the same nomenclature for  $W_xC$  phases.

**Table 6.** PBE-Computed Cell Parameters (a, b, and c in Å;  $V_{cell}$  in Å<sup>3</sup>) and Bulk Energies (eV/Atom) of tungsten carbide phases  $\alpha$ - $W_2C$   $\beta$ -  $W_2C$   $\delta$ -WC  $\epsilon$ -  $W_2C$   $\gamma$ -  $W_2C$   $\gamma$ -WC<sup>70</sup>

phase	$\alpha$ - $W_2C$	$\beta$ - $W_2C$	$\delta$ -WC	$\epsilon$ - $W_2C$	$\gamma$ - $W_2C$	$\gamma$ -WC
space group	P $\bar{3}m1$	Pbcn	P $\bar{6}m2$	P $\bar{3}1m$	Pnnm	Fm $\bar{3}m$
a	3.07	4.76	2.93	5.26	3.03	4.39
b	3.07	6.11	2.93	5.26	6.1	4.39
c	4.68	5.24	2.85	4.8	4.74	4.39
$V_{cell}$	37.85	150.72	20.99	113.32	75.32	83.92
$E_{W_xC_y}$	-11.70	-11.77	-11.26	-11.75	-11.76	-10.80

Figure 4 depicts the W-C system phase diagram, which was built with consideration of the presence of the  $\gamma$ -WC temperature interval, as well as experimental results and in particular the results of magnetic and structural susceptibility studies of tungsten carbides synthesized in the corresponding study<sup>71</sup>. Tungsten monocarbide WC has two polymorphs: a low-temperature hexagonal ( $\delta$ -WC) and a high-temperature, metastable cubic one ( $\gamma$ -WC). Carbon and tungsten atoms form hexagonal sublattices in the stable phase  $\delta$ -WC (space group P-6m2), where carbon

atoms occupy the centers of the metal sublattice's trigonal prismatic interstices. The latter occupies octahedral interstices in the fcc metal sublattice of the  $\gamma$ -WC phase, which has a cubic structure (space group Fm-3m). Interatomic interactions in  $\gamma$ -WC and  $\delta$ -WC are of heterogeneous nature, including ionic, covalent, and metallic bonds.

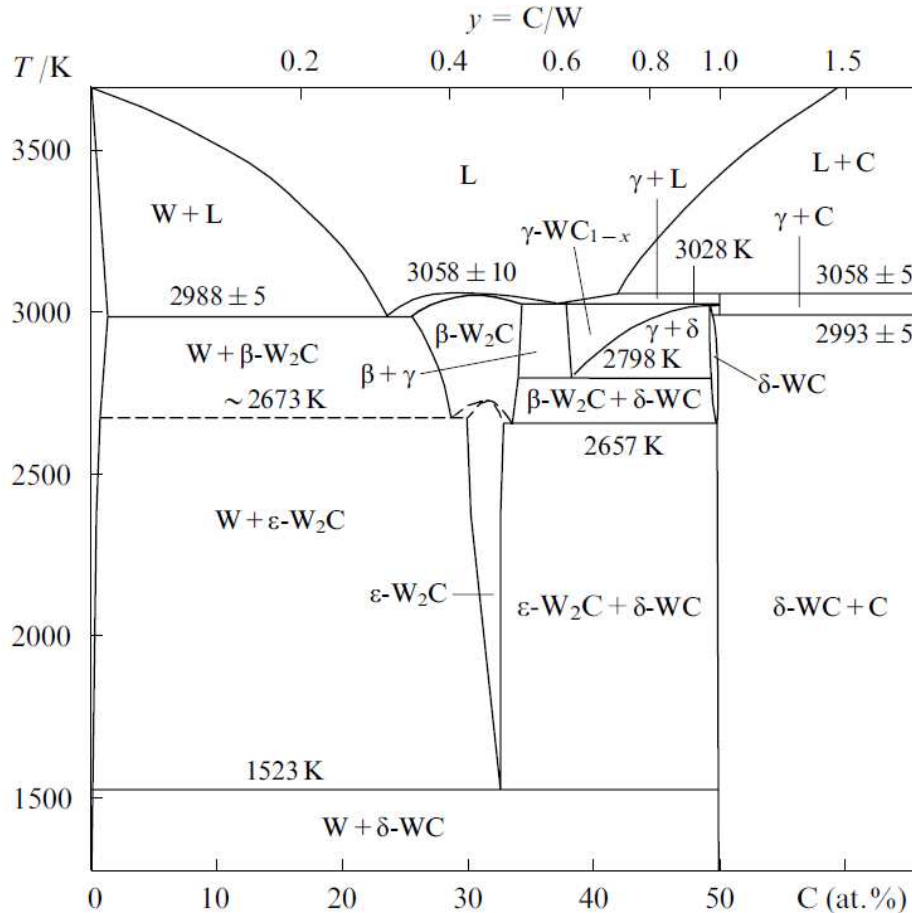


**Figure 4.** Phase diagram of the W-C system with corrected positions of phase boundaries in the region of lower tungsten carbide  $W_2C$ . Corrections were introduced according to the neutron diffraction results<sup>71</sup>.

Today, four  $W_2C$  polymorphs are known:  $\alpha$ -,  $\beta$ -,  $\gamma$ -, and  $\epsilon$ -subcarbides. They differ in the kind of carbon atom distribution across octahedral interstices of the metallic sublattice. For example, in the  $\gamma$ - $W_2C$  structure, carbon atoms fill spots randomly in the carbon sublattice (with a 50% chance). The rhombohedral  $\alpha$ - $W_2C$  structure is made up of carbon atoms layers and vacancies that alternate along the  $c$  axis. Carbon atoms and vacancies are arranged in some order over all the nonmetal sublattice planes in the  $\beta$ - $W_2C$  and  $\epsilon$ - $W_2C$  polymorphs. The structural, electrical, and other characteristics of the  $\alpha$ -,  $\beta$ -,  $\gamma$ -, and  $\epsilon$ -subcarbides of the  $W_2C$  phase were studied using *ab initio*

methods of energy band theory. The experimental findings correspond with the hypothesized structural characteristics<sup>72</sup>. The computed densities of all  $W_2C$  polymorphs revealed that the theoretical density of  $W_2C$  ( $g.cm^{-3}$ ) is 9% greater than that of the monocarbides WC and declines in the following manner:  $\beta-W_2C > \gamma-W_2C > \varepsilon-W_2C > \alpha-W_2C$ .

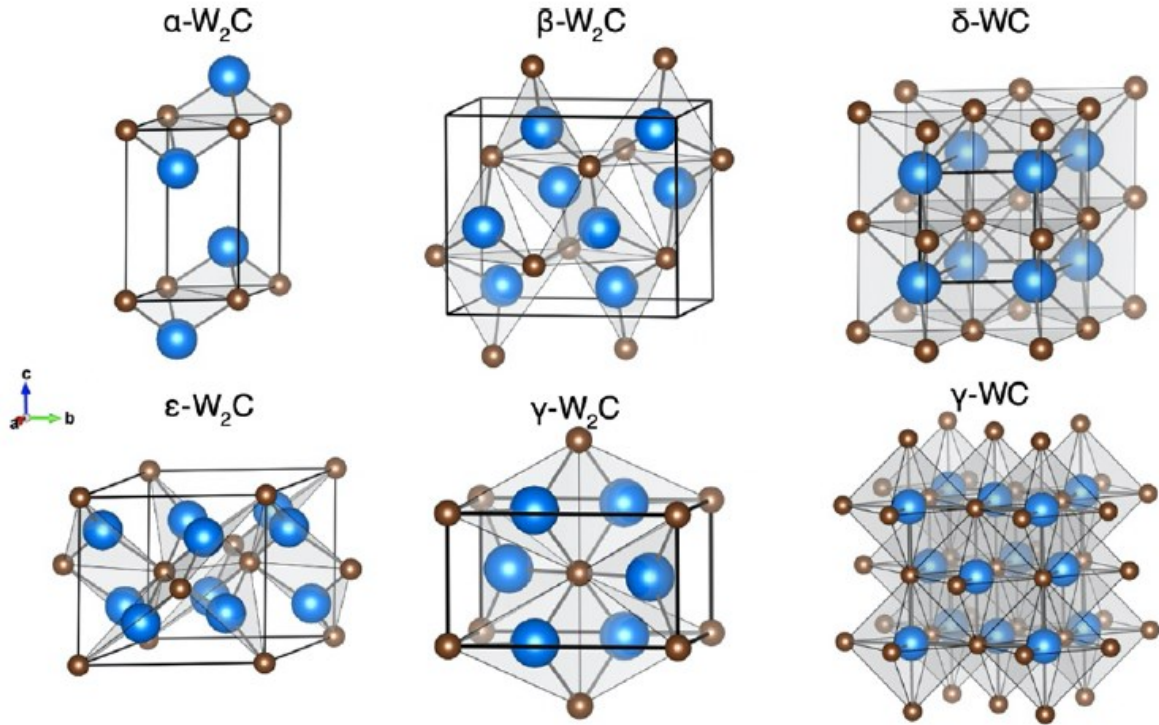


**Figure 5.** Bulk structures of tungsten carbide phases. Blue atoms are W, brown atoms are C<sup>70</sup>.

During the synthesis of tungsten carbide nanoparticles, the appearance of several phases is commonly observed but cannot be accurately characterized by classical phase diagrams. As a result, Shrestha *et al.* present a first principles-based technique for predicting the relative stabilities of several phases in tungsten carbides with varied synthesis circumstances and particle sizes<sup>70</sup>. Using Wulff structures and NN-assisted filtering of high index facets, they discovered numerous facets with considerable area fractions for phases that are overlooked in the literature. Figure 5 shows the atomic structures and unit cells of six distinct  $W_xC_y$  structures that were investigated. The Materials Project database was used to create all of the initial structures<sup>73</sup>.

Figure 6 depicts the equilibrium particle morphologies with  $\Delta\mu_C$  (the carbon chemical potential) = 0.15 eV. All facets found on the Wulff geometries (using DFT calculations)  $\gamma$ -WC,  $\delta$ -WC,  $\varepsilon$ - $W_2C$ , and  $\beta$ - $W_2C$  have been experimentally confirmed. There are few references for  $\alpha$ - $W_2C$ ;

nevertheless, all facets of the Wulff constructs have been previously published with the exception of (213). Experimentally, the calculated forms resemble that of the experimental data in the literature. For instance, the cubic form for  $\gamma$ -WC<sup>74</sup>, the prismatic shape of the  $\varepsilon$ -W<sub>2</sub>C particle<sup>75</sup>, and the approximately spherical shape of  $\delta$ -WC<sup>76</sup> have all been reported.

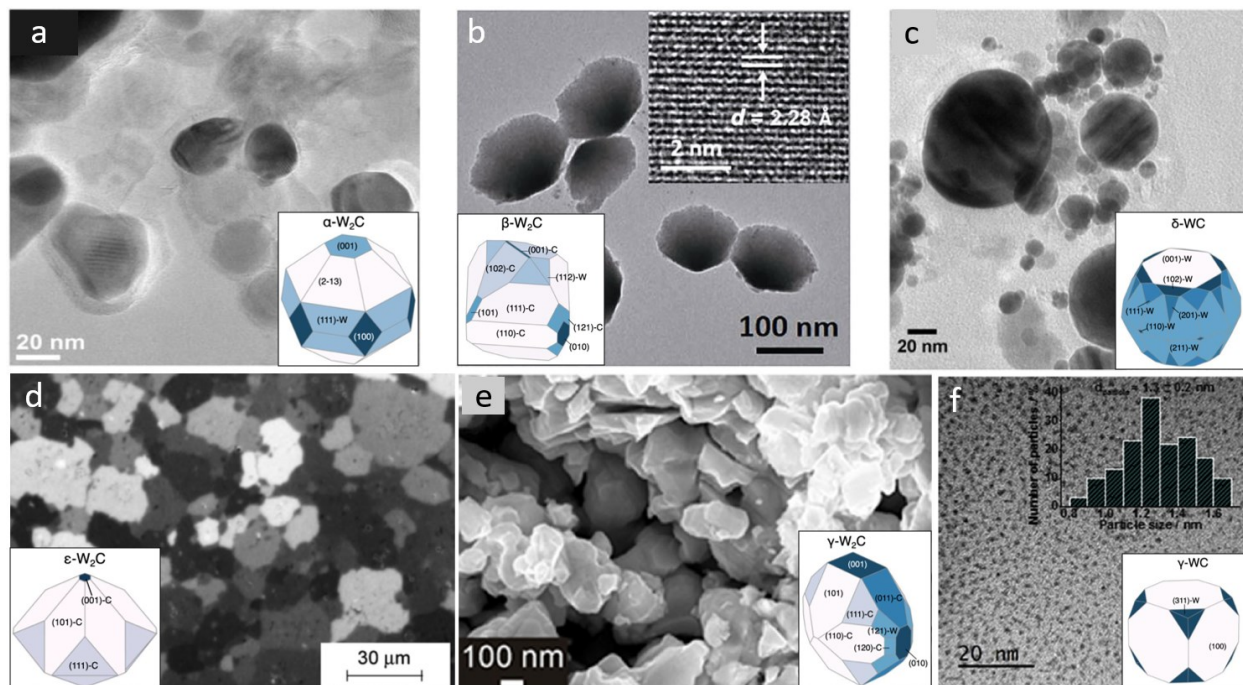


**Figure 6.** SEM and TEM images of different tungsten carbide phases; (a)  $\alpha$ -W<sub>2</sub>C<sup>77</sup>, (b)  $\beta$ -W<sub>2</sub>C<sup>52</sup>, (c)  $\delta$ -WC<sup>76</sup>, (d)  $\varepsilon$ -W<sub>2</sub>C<sup>75</sup>, (e)  $\gamma$ -W<sub>2</sub>C<sup>78</sup>, (f)  $\gamma$ -WC<sup>74</sup>. Inserts: Computed Wulff constructions of the equilibrium particle morphologies of different tungsten carbide phases at  $\Delta\mu_C = -0.15$  eV<sup>70</sup>.

#### 1.4.2. Synthesis of tungsten carbide catalysts via the solid phase reaction

In the solid-solid phase reaction, solid carbon materials are used as a carbon resource to introduce C atoms into the metallic W lattice. In this particular case, the carbon resource may come directly from a solid carbon such as AC or CNTs. In the following paragraphs, we summarize the synthesis of tungsten carbide catalysts via the solid phase reaction and their applications in various fields (see Table 7).

Originally, powder metallurgy was used to synthesize tungsten carbides<sup>57,79</sup>, in which the metal oxides were carburized in the presence of solid carbon at a temperature of up to 1800 K. Typically, catalysts prepared by this method have a very low surface area ( $< 10$  m<sup>2</sup>.g<sup>-1</sup>) and activity<sup>57</sup>. In metal matrix composites, it is usually a difficult task to achieve synergistic toughening between zero-

dimensional NPs and two-dimensional graphene, since their dimensions are far apart. Nevertheless, an *in situ* solid-state reaction method was developed to incorporate  $\gamma$ -WC NPs and GNSs into a copper matrix. Thermodynamic and crystallographic calculations demonstrated for the first time that the unusual  $\gamma$ -WC phase can arise from the solid-state reaction and remain stable at room temperature. The measured thermal conductivity was similar to that of pure Cu, which is a promising prospect for applications as advanced multifunctional materials<sup>80</sup>. Later, a carbothermal method was developed in which solid carbon reacts with vaporized metal oxides at temperatures above 1000 K to produce the metal carbide. The surface area of the resulting carbides is slightly larger (20-40 m<sup>2</sup>.g<sup>-1</sup>) than those synthesized by the powder metallurgical method<sup>57,81</sup>. DFT calculations clearly show that W<sub>2</sub>C is a potentially more active HER electrocatalyst than WC. Moreover, W<sub>2</sub>C is more active than WC in converting cellulose to glycols<sup>63</sup>. However, the preparation of nanosized W<sub>2</sub>C is challenging, as the W-C phase diagram (see Figure 4) suggests that the formation of W<sub>2</sub>C below 1250 °C is not thermodynamically favored<sup>82</sup>. In addition, the synthesis must be carried out in a low-carbon environment to circumvent the undesired WC formation. Most conventional approaches (*e.g.*, using gaseous carbon precursors) are unable to produce W<sub>2</sub>C as the main product because the ratio of carbon to tungsten precursors often gets out of control, and diffusion of carbon through the solid-gas interface into the metal lattice is usually too rapid to allow careful control of the product phase<sup>83,84</sup>. The use of a nonvolatile, crystalline, solid carbon precursor like MWNTs may provide a solution to this problem. At high temperatures, the chemical reactivity of solid carbon precursors is much lower. They would make the diffusion of carbon through the solid-state interface much slower, opening up the possibility of tailoring the product phase by choosing the right reaction conditions.

Researchers also developed other modified carbothermal methods (*e.g.*, carbothermal hydrogen reduction) to prepare highly dispersed supported tungsten carbide catalysts (< 10 nm) with the stabilization of the metastable W<sub>2</sub>C phase at lower temperatures using (1) a reducing agent such as nickel at 700 °C<sup>63</sup>, (2) the carburization of a dry hybrid of well-reacted CNT and WCl<sub>6</sub> in ethanol at 900 °C<sup>85</sup>, by coupling the use of carbon nanotubes with the use of a high vacuum environment (320 Pa, 900 °C) and giving W<sub>2</sub>C with a higher purity, due to the further reduction of the rate of carbon diffusion from MWNTs to WO<sub>x</sub> through the solid-state interface<sup>86</sup>, (3) a phosphorus-containing tungsten precursor (H<sub>3</sub>PW<sub>12</sub>O<sub>40</sub>) at 1000 °C<sup>87</sup>, or (4) reactive carbon precursors such as TPEB to form core-shell morphologies at 1300 °C<sup>78</sup>.

Fang *et al.* presented a different strategy to synthesize well-defined tungsten carbide NPs by depositing the metal precursor ( $\text{WCl}_6$ ) on carbon nanotubes (CNTs), wrapping a thin polymer layer, and performing controlled carburization. The polymer served as a carbon source to modulate the metal to carbon ratio in the carbides and to introduce amorphous carbons around the NPs to prevent their sintering. The as-prepared catalyst exhibited high stability in hydrogenolysis of aryl ether C-O bonds in guaiacol for more than 150 h. Its activity was far higher than those prepared *via* usual temperature-programmed reduction with gaseous carbon precursor and carbothermal reduction with intrinsic carbon support<sup>85</sup>. Garcia-Esparza employed tungsten hexachloride precursor ( $\text{WCl}_6$ ) for tungsten carbide synthesis<sup>88</sup>. It was found that  $\text{WCl}_6$  first reacted with ethanol to form a stable intermediate  $\text{WCl}_3(\text{OC}_2\text{H}_5)_2$ . The intermediate was then gradually converted to  $\text{W}_2\text{C}$  and WC at elevated temperatures (1073-1373 K) at the expense of mesoporous graphitic  $\text{C}_3\text{N}_4$  (synthesized by a template method using cyanamide and an aqueous colloidal silica suspension composed of silica nanoparticles). The particle size of the obtained carbide ( $\text{W}_2\text{C}$  or WC) is about 5 nm, which is much smaller than that obtained from ammonium metatungstate precursor over activated carbon supports (10-50 nm)<sup>89</sup>. The same precursor was used to synthesize  $\text{W}_2\text{C}$  nanocrystals embedded in porous graphene<sup>90</sup>.

X-ray methods have been extensively used in many studies on tungsten carbides catalysts to determine their phase compositions. For example, an examination of the physical and chemical characteristics of Ni-promoted tungsten carbides supported on activated carbon was carried out using both *in situ* and *ex situ* approaches<sup>91</sup>.



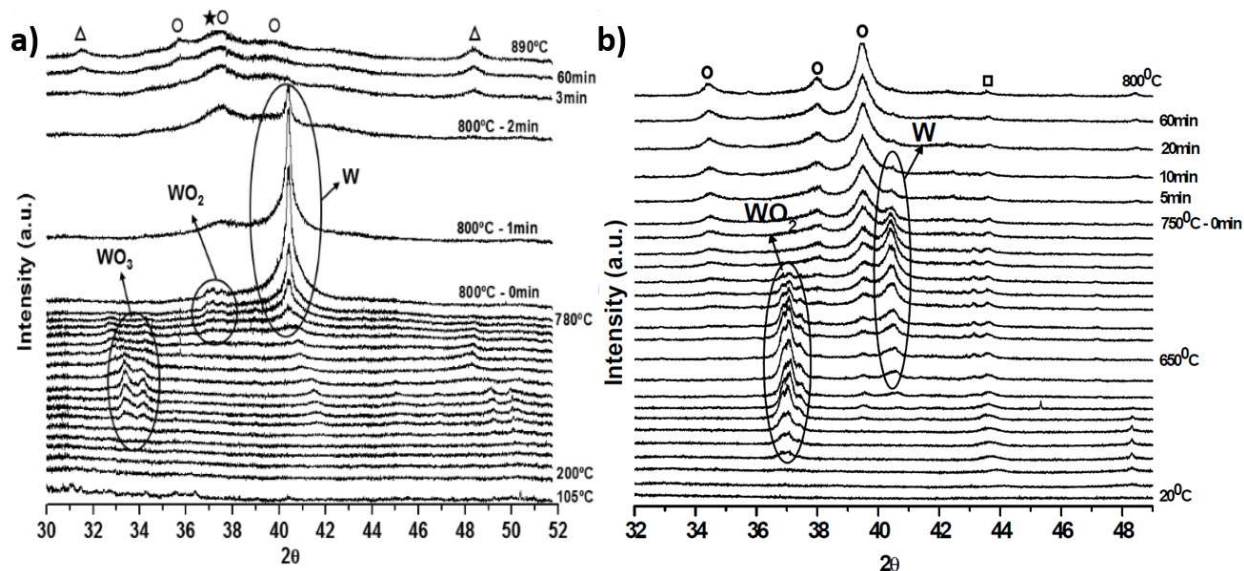


**Figure 7.** *In situ* X-ray diffraction patterns obtained during carburization of a)  $W_xC/C$  b)  $Ni-W_xC/C$  samples;  $\Delta$   $\delta$ -WC,  $\circ$   $W_2C$ ,  $\star$   $\gamma$ -WC and  $\square$   $Ni_4W$  alloy<sup>91</sup>.

As illustrated in Figure 7, during the carburization process, *in situ* XRD measurements revealed that non-promoted samples generated a combination of nanosized  $W_2C$ ,  $\gamma$ -WC and  $\delta$ -WC carbide phases. In the case of Ni-promoted catalysts, *in situ* XRD, XANES, XPS, and TEM examination demonstrated that Ni not only helps to lower the carburization temperature by 50 °C, but it also aids in the coating of polymeric carbon over the catalyst surface, reducing cellulose conversion. Another effect of the nickel promoter was to improve the stability of the pure  $W_2C$  phase. This metastable carbide phase was shown to be stable throughout the carburization temperature range and the isothermal treatment for 1 hour at 800 °C. The following reactions are expected to occur during the whole process<sup>71,92,93</sup>:

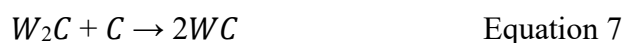
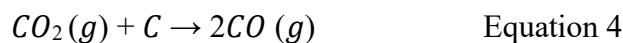
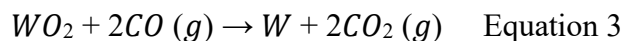
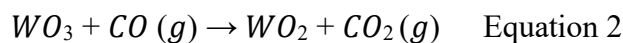
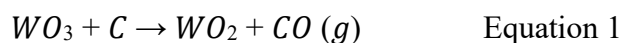


**Table 7.** Synthesis *via* solid phase reaction and main properties of tungsten carbide catalysts.

Tungsten precursor	Carbon source	Synthesis conditions	S <sub>BET</sub> (m <sup>2</sup> .g <sup>-1</sup> )	Carbide phase	NP size (nm)	Ref.
scheelite (CaWO <sub>4</sub> )	active carbon supports	Air, 700 °C, 4 h	-	δ-WC	14	79
AMT	graphene nanosheets (GNSs)	1) H <sub>2</sub> , 200 mL.min <sup>-1</sup> , 750 °C, 2 h ; 2) 50 MPa, 700-900 °C, 1 h, 10 °C.min <sup>-1</sup>	-	γ-WC	30	80
AMT	AC	H <sub>2</sub> , 900 °C, 6 h	602	δ-WC	10-50	89
AMT	mesoporous carbon	H <sub>2</sub> , 900 °C, 6 h	433	W <sub>2</sub> C	< 10	89
WCl <sub>6</sub>	CNT	Ar, 900–950 °C, 2–6 h	100.6*	W <sub>2</sub> C	10–20	85
WCl <sub>6</sub>	MWNT	Ar, 320 Pa, 900 °C, 1 h, 10 °C.min <sup>-1</sup>	-	β- W <sub>2</sub> C	2–5	86
(H <sub>3</sub> PW <sub>12</sub> O <sub>40</sub> , H <sub>2</sub> WO <sub>4</sub> )	carbon black	N <sub>2</sub> , 1000 °C, (1 h, 3 h)	-	(α-W <sub>2</sub> C, δ-WC)	1–50	87
W	TPEB prepolymer	ball milling, Ar, 1300 °C, 2 h, 2 °C.min <sup>-1</sup>	-	γ- W <sub>2</sub> C	40	78
WCl <sub>6</sub>	Graphene	Ar, 1000 °C, 1 h		W <sub>2</sub> C	10–20	90
WCl <sub>6</sub>	Graphitic C <sub>3</sub> N <sub>4</sub>	N <sub>2</sub> , (800 °C, 1100 °C)	(151, 25)	(α-W <sub>2</sub> C, δ-WC)	(2, 15)	88

\* From the support. AMT = ammonium metatungstate (NH<sub>4</sub>)<sub>6</sub>H<sub>2</sub>W<sub>12</sub>O<sub>40</sub>·xH<sub>2</sub>O.

### 1.4.3. Synthesis of transition metal carbide catalysts via the liquid phase reaction

The above solid phase method has the disadvantages of a limited choice of supports, a small metal-carbon interface, and the formation of mixed carbide phases as well as a difficulty in controlling particle sizes. Therefore, different liquid carbonaceous precursors were used to better control the structure and solid-liquid interface for the metal-carbon reaction during carbide synthesis. Specifically, suitable carbon and metal precursors are dissolved in the liquid phase, where they form polymeric networks. The resulting solid is then carburized in an inert or reducing atmosphere to form metal carbides. We divide this section according to the type of pyrolyzed hybrid; ordered



crystal structures (other than MOFs) and tungsten-containing MOF precursors, with detailed information on synthesis, properties and applications in Table 8 and Table 9 respectively.

#### 1.4.4.1. Pyrolysis of ordered crystal structures

The urea-glass and amine-oxide procedures are two common liquid-derived solid-solid processes for preparing metal carbides. Giordano *et al.* were the first to use the urea-glass process to make metal nitrides and carbides. Urea is commonly utilized as both a carbon source and a polymerizing agent for carbide production.  $WCl_4$  interacted with alcohols and urea to form a polymer-like substance, which was then reduced to nitrides or carbides by changing the metal precursor/urea molar ratio<sup>94</sup>. WC-NRs of 350-400 nm length and 94 nm diameter are manufactured by a high-temperature pseudomorphic transformation of chemically generated  $W_3O_8$  nanorods with glucose as a carbon precursor<sup>95</sup>. A different approach was used to prepare phase-pure  $W_2C$  nanorods (lengths of 2-4  $\mu m$ , diameters of 100-600 nm, and  $W_2C$  particle size of 30 nm) with varying amounts of crystal defects; the pyrolysis of metatungstate and melamine hybrid nanorods. The nanoscale alternating structure of tungsten oxide and melamine efficiently promotes tungsten oxide reduction and the creation of tungsten carbide, avoiding carbon deposition at the surface<sup>96</sup>.

$W_2C$  NPs were made via self-assembly of PTA and DA, followed by carbonization, according to Li *et al.* procedure. The resulting  $W_2C$  NPs were oval in form, measuring  $150 \pm 12$  nm in length and  $90 \pm 10$  nm in width<sup>52</sup>. To make another structure of tungsten carbide, Zhu *et al.* employed a simple salt template approach. For this synthesis, they employed 1-ethyl-3-methylimidazolium dicyanamide as the carbon source, a salt template of KCl and  $ZnCl_2$ , and tungsten chlorides ( $WCl_5$ ) as the metal precursor. The scientists got metal carbide nanoparticles (WC) with an average particle size of 3 nm after carburization and removal of the salt templates, which were rigidly implanted into the vertically aligned two-dimensional structure carbon nanosheets<sup>97</sup>. Other researchers reported that they carburized ammonium metatungstate with CTAB *in situ* under ultrahigh vacuum conditions and produced phase-pure WC films<sup>98</sup>.

Bernard d'Arbigny *et al.* reported tungsten carbide microspheres with a carbon outer shell and a compact WC core prepared by a simple hydrothermal process using glucose as a carbon precursor, with a very large surface area ( $55 m^2.g^{-1}$ ) allowing high dispersion of platinum nanoparticles ( $d = 4$  nm). Argon heat treatment following the hydrothermal process was employed to reduce tungsten oxide NPs to tungsten carbide, using the carbon from the spheres as a reducing agent. During  $H_2$

heat treatment, methanation of the spheres residual carbon induces porosity formation and causes migration of tungsten carbide nanoparticles toward the sphere centre, resulting in the formation of a porous core with a size of about 1  $\mu\text{m}$ . The shell consists of residual carbon and dispersed WC NPs<sup>99</sup>. Han *et al.* reported the fabrication of 200 nm core-shell carbon spheres with confined WC<sub>x</sub> matrix in a two-step procedure<sup>100</sup>. First, they synthesized the polydopamine-tungsten hybrids using *in situ* polymerization of dopamine and metatungstate precursors. The metallic species in the hybrid materials were localized in the polymerized matrix, that eventually led to the formation of tungsten carbide NPs (< 5 nm) after carburization. Tungsten carbide microspheres with hexagonal close-packed W<sub>2</sub>C structure were synthesized by polymer-induced carburization method<sup>101,102</sup>. Later, uniformly dispersed tungsten carbides (4-8 nm) on 2  $\mu\text{m}$  carbon spheres with phase composition control ( $\delta$ -WC or  $\epsilon$ -W<sub>2</sub>C) were successfully synthesized by controlling the carburization time using the same approach with a small decrease of the pyrolysis temperature<sup>103</sup>.  $\gamma$ -WC support was successfully formed by a polyol method, based on the thermal decomposition of W(CO)<sub>6</sub> in the presence of oleylamine in an inert atmosphere at a low temperature of 350 °C<sup>74</sup>. This synthesis is very interesting since a low temperature was employed and a rarely formed phase was obtained.

**Table 8.** Synthesis of tungsten carbides from ordered crystal structures and properties.

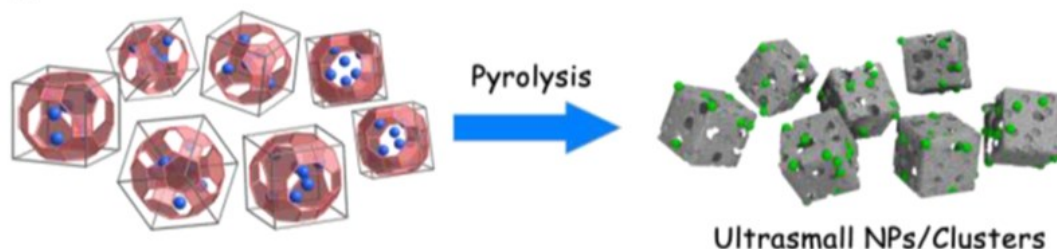
Tungsten precursor	Carbon source	Synthesis conditions	S <sub>BET</sub> (m <sup>2</sup> .g <sup>-1</sup> )	Carbide phases	NP size (nm)	Ref.
WCl <sub>4</sub>	urea	N <sub>2</sub> , 800 °C, 3 h	84	δ-WC	3-6	94
AMT	dopamine	N <sub>2</sub> , 900 °C, 2-16 h	80.4	δ-WC	< 5	100
W <sub>3</sub> O <sub>8</sub>	glucose	25% H <sub>2</sub> -75% Ar, 900 °C, 3 h	401	δ-WC	-	95
nanorods						
AMT	melamine	Ar, 750 °C, 1 h, 2 °C.min <sup>-1</sup>	18.5	W <sub>2</sub> C	30	96
WCl <sub>5</sub>	EMIM-DCA	Ar, 900 °C, 3 h	-	δ-WC	3	97
H <sub>3</sub> PW <sub>12</sub> O <sub>40</sub>	DA/PVP	5% H <sub>2</sub> -95% Ar: 1) 400 °C, 2 h, 2) 800 °C, 3 h	-	β-W <sub>2</sub> C	90-150	52
AMT	resorcinol/HCHO	900 °C, 1) Ar, 1 h 2) H <sub>2</sub> , 2 h	176	W <sub>2</sub> C	12	101
AMT	resorcinol/HCHO	Ar, 900 °C	176	W <sub>2</sub> C	7	102
AMT	resorcinol/HCHO	H <sub>2</sub> , 850 °C, 1 h	113	ε-W <sub>2</sub> C	4-8	103
		H <sub>2</sub> , 850 °C, 6 h	52	δ-WC		
AMT	glucose	Ar, 900 °C, 2 h H <sub>2</sub> , 900 °C, 4 °C.min <sup>-1</sup>	64	WC	11	99
WO <sub>x</sub> /CNT	resorcinol/HCHO	Ar, 850 °C, 1.5 h	100.6*	W <sub>2</sub> C	-	85
		Ar, 850 °C, 4 h	100.4	γ-WC	7	
		Ar, 850 °C, 6 h	100.6*	δ-WC	-	
W(CO) <sub>6</sub>	oleylamine	N <sub>2</sub> , 350 °C, 1 h, 20 °C.min <sup>-1</sup>	-	γ-WC	2	74
AMT	CTAB	high vacuum, 1000 °C, 1 h, 1 °C.min <sup>-1</sup>	-	δ-WC	100	98

\* From the support. CTAB = cetyltrimethylammonium bromide ; HCHO = formaldehyde ; EMIM-DCA = 1-Ethyl-3-methylimidazolium dicyanamide ; AMT = ammonium metatungstate (NH<sub>4</sub>)<sub>6</sub>H<sub>2</sub>W<sub>12</sub>O<sub>40</sub>·xH<sub>2</sub>O.

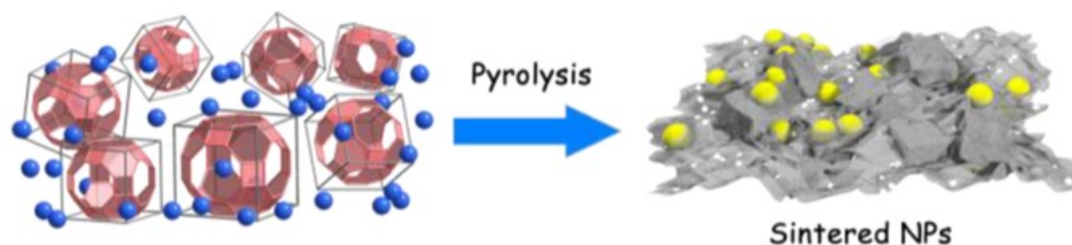
#### 1.4.4.2. Pyrolysis of tungsten-containing porous hybrid materials

Pyrolysis of porous hybrid materials such as metal-organic frameworks (MOFs), initially explored to stabilize transition metal and metal oxide discrete NPs on a highly porous carbon support<sup>104,105</sup>, has also been used to synthesize nanoparticles of calibrated size following a cage-confinement strategy, as first demonstrated by Xu *et al.* who prepared ultrasmall tungsten carbide NPs<sup>106</sup>. As shown in Figure 8.a, the authors utilized a zeolitic-based MOF structure, ZIF, as a nanoreactor to entrap  $W(CO)_6$ . During carburization, the carbon nanopolyhedron was maintained, the zinc was evaporated, and the carbides were formed in the carbon cages. The latter appear as polyhedral porous particles adopting the crystal morphology of ZIF.

##### a) Cage-confinement



##### Non-confinement



##### b)

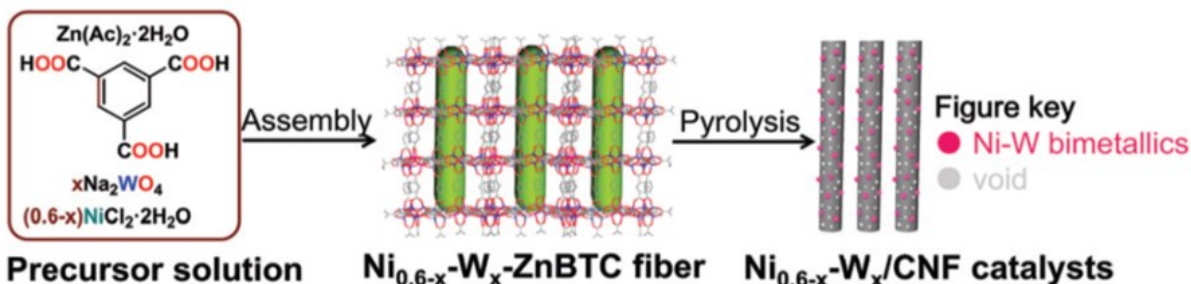


**Figure 8.** (a) Comparison of the non-confinement, cage and 2D confinement pyrolysis methods for tungsten carbides synthesis<sup>106</sup> (b) Synthesis of nickel–tungsten bimetallics/carbon nanofiber catalysts<sup>107</sup>.

This strategy was applied to a variety of MOFs to form uniformly distributed bimetallic nickel-tungsten carbide particles on hierarchical porous carbon nanofibers (Figure 8.b)<sup>107</sup>. Other examples exist on the synthesis of tungsten carbide single atom catalysts with high surface areas and phase control (ZIF-8<sup>108</sup>, UiO-66-NH<sub>2</sub><sup>109</sup>, IRMOF-3<sup>110</sup>). It is noteworthy that the metal center of the MOF may be used as such to form bimetallic particles (nickel) or may be eliminated by evaporation above 900 °C (zinc or zirconium). Moreover, the shape of the MOF (prismatic fibers<sup>107</sup>, polyhedral<sup>109</sup>, rhombododecahedral<sup>108</sup>) is inherited by the final carbon-based catalysts, while the dimensions shrink and the surface becomes rough.

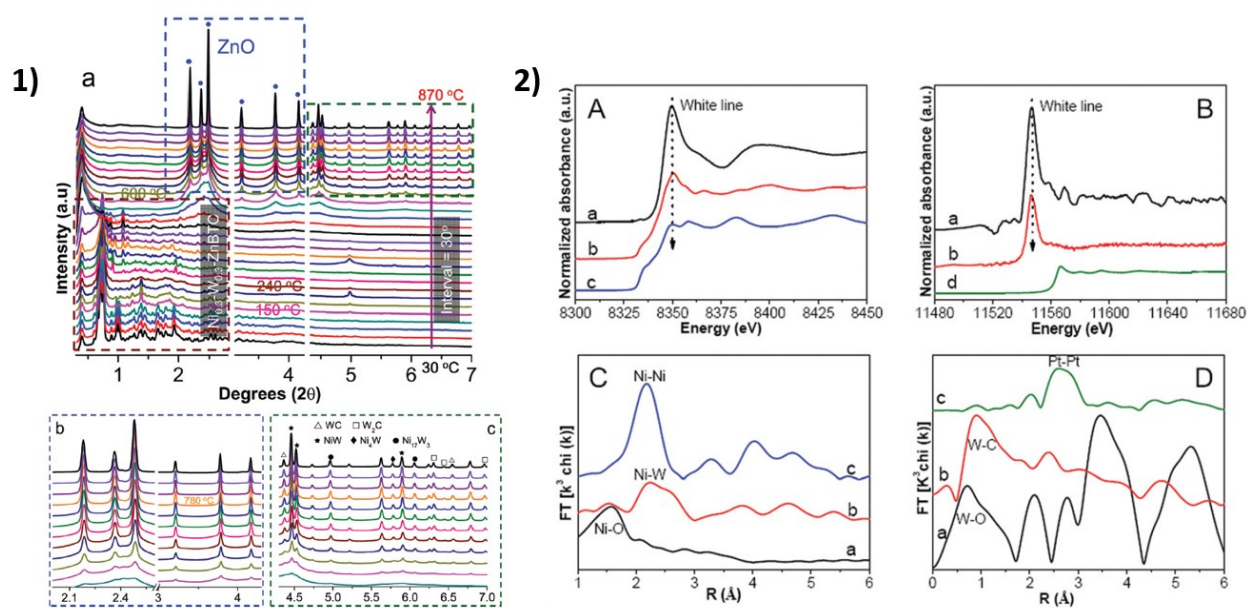


**Figure 9.** (1) *In situ* synchrotron high-energy X-ray diffraction patterns recorded by pyrolysis of Ni<sub>0.3</sub>-W<sub>0.3</sub>-ZnBTC. (2) (A) Ni K-edge XANES, (B) W L<sub>2</sub>-edge XANES, (C) Ni K-edge EXAFS, (D) W L<sub>2</sub>-edge EXAFS for (a) Ni<sub>0.3</sub>-W<sub>0.3</sub>-ZnBTC, (b) Ni<sub>0.3</sub>-W<sub>0.3</sub>/CNF, (c) Ni foil and (d) Pt foil<sup>107</sup>.

To investigate the pyrolysis of a nickel-tungsten MOF hybrid (Ni<sub>0.3</sub>-W<sub>0.3</sub>-ZnBTC), *in situ* high-energy X-ray diffraction patterns were collected in an Ar environment at temperatures ranging from ambient temperature to 870 °C (Figure 9.1.a)<sup>107</sup>. The increasing intensity of the characteristic peaks (2θ from 2° to 5°) below 780 °C shows ZnO was created from the metallic cluster of the MOF, followed by its reduction from 780 °C into metallic Zn and further volatilization (Figure 9.1.b). After pyrolysis at 950 °C for 2 hours, no ZnO can be identified. XAFS was measured via both Ni K-edge and W L<sub>2</sub>-edge scans to further validate the production of Ni-W alloys and

tungsten carbides. As shown in Figure 9.2.A and B, the catalyst (Ni<sub>0.3</sub>-W<sub>0.3</sub>/CNF) has a lower white line intensity than the precursor (Ni<sub>0.3</sub>-W<sub>0.3</sub>-ZnBTC), showing that the Ni<sup>2+</sup> and WO<sub>4</sub><sup>2-</sup> species have been largely reduced. Because the edge location of these reduced species shifted positively compared to Ni and Pt foils, those species contain some positive charges. The occurrence of large peaks in the radial distribution curves of the catalyst (Figure 9.2.C and D), attributed to the Ni-W and W-C pairs, confirms the synthesis of alloyed Ni-W and tungsten carbide NPs (WC and W<sub>2</sub>C).

**Table 9.** Synthesis of MOF-derived tungsten carbide catalysts and properties.

<b>Tungsten precursor</b>	<b>Carbon source</b>	<b>Synthesis conditions</b>	<b>S<sub>BET</sub> (m<sup>2</sup>.g<sup>-1</sup>)</b>	<b>d<sub>pores</sub> (nm)</b>	<b>Carbide phases</b>	<b>NP size (nm)</b>	<b>Ref.</b>
W(O-Et) <sub>5</sub>	IRMOF-3	Ar, 1000 °C, 6 h, 10 °C.min <sup>-1</sup>	890	3	γ-WC	2.8-5	110
W(CO) <sub>6</sub>	ZIF	N <sub>2</sub> , 980 °C, 5 h	800	10-20	δ-WC	2	106
WCl <sub>6</sub>	ZIF-8	Ar, 1000 °C, 2 h	807	1.5-4	γ-WC	0.12	108
Na <sub>2</sub> WO <sub>4</sub> , 2H <sub>2</sub> O	Zn-BTC fibers	Ar, 950 °C, 2 h, 5 °C.min <sup>-1</sup>	848	0.6-3.8	WC, W <sub>2</sub> C	68	107
WCl <sub>5</sub>	UiO-66-NH <sub>2</sub>	Ar, 950 °C, 3 h, 5 °C.min <sup>-1</sup>	536	3.5	WC	0.1	109

#### ***1.4.4. Synthesis of transition metal carbides via the gas phase carburization***

The solid-gas phase reaction process has been the predominant method for preparing carbide catalysts up to now. Generally, the metal precursor is loaded on a support by impregnation before carburization in flowing CO or hydrocarbon gases (C<sub>1</sub> to C<sub>4</sub> and aromatic compounds), with or without added hydrogen. Table 10 summarizes the different synthesis and properties for this synthesis route. In the 1980s, Boudart's group first outlined this method for carbide synthesis and named it the temperature-programmed reduction method. They carburized WO<sub>2</sub> in 20% CH<sub>4</sub>/H<sub>2</sub>, with CH<sub>4</sub> serving as the carbon source. The size of as-obtained carbide particles was found to be

dependent on the shapes of the metal and carbon precursors<sup>57</sup>. Moreover, the same group studied the influence of synthesis parameters on the final carbide. Three types of tungsten carbides could be obtained by adjusting the carburizing temperature and atmosphere<sup>111</sup>. Since then, the temperature-programmed reduction process has been widely used to prepare high surface area supported tungsten carbide catalysts, including but not limited to carbon supports.

Ma *et al.* prepared tungsten carbide microspheres by spray-drying, using AMT as a precursor, carbon monoxide and carbon dioxide as a mixture of reducing and carrier gases. SEM results show that hollow microspheres are formed as a result of the spray drying process, while a mesoporous network is formed by the gas-solid reaction during the subsequent heat treatment. In accordance with the results of the carbothermal reduction process, the sample undertakes a phase transition during the heat treatment step as a function of the final temperature, the duration of the dwelling step, and the heating rate<sup>112</sup>. Other methods proved to allow controlling the NPs size and phases of tungsten carbides. In particular, Hunt *et al.* employed a three-steps process to prepare uniformly distributed tungsten carbide catalysts. They first prepared tungsten oxide encapsulated in silica by a reverse microemulsion method, the latter was then carburized under CH<sub>4</sub>/H<sub>2</sub> atmosphere. After dissolving the silica, the tungsten carbide NPs were redispersed on other supports. This process is a versatile technique for the synthesis of carbides in the range of 1-4 nm with tunable size, crystal phase, and composition<sup>84</sup>. It is noteworthy that the  $\delta$ -WC phase reported in these two studies was obtained as a unique phase for very small particle sizes, although DFT predicted that both  $\gamma$ -WC and  $\delta$ -WC are stable phases in this range<sup>70</sup>.

In another approach, mesoporous W<sub>2</sub>C were synthesized by replication, using ordered mesoporous KIT-6 as a hard silica template<sup>113</sup>. KIT-6 was mixed with phosphotungstic acid and dried before heat treatment under CH<sub>4</sub> at 650 °C for 5h. After dissolution of the silica matrix with HF, mesoporous W<sub>2</sub>C with a surface area of 73 m<sup>2</sup>.g<sup>-1</sup> was obtained. A nickel-tungsten (Ni-W) carbide catalyst deposited on an Al-SBA-15 support was developed by Al Alwan *et al.* A DENP (encapsulation of W NPs within an amine dendrimer matrix, followed by chemical reduction of the NPs) process was used to minimize alloy formation and increase metal dispersion on the support<sup>114</sup>. In addition, other studies were conducted to obtain metal carbides with larger surface area by applying the solid-gas phase reaction method on supports with large surface area such as activated carbon (AC)<sup>115</sup>, carbon nanotubes (CNTs)<sup>85</sup>, and alumina ( $\gamma$ -Al<sub>2</sub>O<sub>3</sub>)<sup>116</sup>.

**Table 10.** Synthesis of tungsten carbides via the gas phase reaction and properties.

Tungsten precursor	Catalyst support	Synthesis conditions	S <sub>BET</sub> (m <sup>2</sup> .g <sup>-1</sup> )	Carbide phases	NP size (nm)	Ref.
AMT	Al-SBA-15	20% CH <sub>4</sub> -80% H <sub>2</sub> , 30 mL.min <sup>-1</sup> , 1) 250 °C, 10 °C.min <sup>-1</sup> 2) 730 °C, 2 °C.min <sup>-1</sup>	376	WC	-	114
WO <sub>x</sub> /CNT	CNT	15% CH <sub>4</sub> -85% H <sub>2</sub> , 15 ml.min <sup>-1</sup> , 850 °C, 2h	100.6*	W <sub>2</sub> C	20–40	85
AMT	γ-Al <sub>2</sub> O <sub>3</sub>	20% CH <sub>4</sub> -80% H <sub>2</sub> , 650 °C, 2h, 8 °C.min <sup>-1</sup>	158	W <sub>2</sub> C	-	116
H <sub>3</sub> PW <sub>12</sub> O <sub>40</sub>	KIT-6	CH <sub>4</sub> , 30 ml.min <sup>-1</sup> , 650 °C, 5h	73	α-W <sub>2</sub> C	3–4	113
AMT	AC	1) N <sub>2</sub> , 650 °C, 3.5 °C.min <sup>-1</sup> 2) 20% CH <sub>4</sub> -80% H <sub>2</sub> , 650-950 °C, 2 h, 1.7 °C.min <sup>-1</sup>	358	WC	-	115
AMT	-	9% CO <sub>2</sub> -91% CO, 1) 400 °C, 1 h 2) 400-650 °C, 10-12 h	-	δ-WC	4	112
WO <sub>3</sub>	-	10% CH <sub>4</sub> -90% H <sub>2</sub> , 627 °C	71	α-W <sub>2</sub> C	4	111
WO <sub>3</sub>	-	20% CH <sub>4</sub> -80% H <sub>2</sub> , 877 °C	39	δ-WC	-	111
WO <sub>3</sub>	-	1) NH <sub>3</sub> , 777 °C 2) 20% CH <sub>4</sub> -80% H <sub>2</sub> , 777 °C	64	γ-WC	-	111
W[O-iPr] <sub>6</sub>	SiO <sub>2</sub> -carbon black	18% CH <sub>4</sub> -82% H <sub>2</sub> , 775 °C	-	W <sub>2</sub> C	-	84
W[O-iPr] <sub>6</sub>	SiO <sub>2</sub> -carbon black	21% CH <sub>4</sub> -79% H <sub>2</sub> , 835 °C	90	δ-WC**	3–6	84
W[O-iPr] <sub>6</sub>	SiO <sub>2</sub> -carbon black	21% CH <sub>4</sub> -79% H <sub>2</sub> , 835 °C	-	γ-WC	1–3	84

\* From the support, \*\*was obtained when lowering the methanol/heptane ratio used for precipitation prior to carburization. AMT = ammonium metatungstate (NH<sub>4</sub>)<sub>6</sub>H<sub>2</sub>W<sub>12</sub>O<sub>40</sub>·xH<sub>2</sub>O ; W[O-iPr]<sub>6</sub> = tungsten(VI) isopropoxide.



#### 1.4.5. Tungsten carbides as catalysts

Tungsten carbide was synthesized first by H. Moissan in 1893. Industrial production of hard metals based on WC began 20-25 years after the discovery of tungsten carbide. WC in electrocatalysis has been largely studied since the 1970s for various processes such as oxygen reduction reaction<sup>47</sup>, methanol oxidation<sup>48</sup>, hydrogen evolution reaction<sup>49</sup>, electrooxidation of ethanol<sup>50</sup>, and anodic oxidation of hydrogen in fuel cells<sup>51</sup>. Then, Levy and Boudart<sup>54</sup> reported that tungsten carbides exhibited Pt-like catalytic activity in various catalytic reactions, like the catalytic isomerization of 2,2-dimethylpropane to 2-methylbutane. This catalytic behavior, which is typical of platinum, was not exhibited by sole metallic tungsten. The subsequent investigation showed that Pt-like properties are due to the change of electron distribution in tungsten by the addition of carbon atoms<sup>55</sup>. Thus, tungsten carbides are potential substitutes for platinum-based catalysts due to their high catalytic activity, selectivity, low cost, and good thermal stability under severe conditions<sup>56</sup>.

Afterward, Oyama *et al.*<sup>57</sup> showed that tungsten carbides were active in a number of reactions such as cyclohexene hydrogenation and ammonia synthesis. Iglesia *et al.*<sup>58</sup> further showed that tungsten carbides could replace Pt in hydroisomerization reactions, at the same reaction conditions (341 °C and 0.95 bar H<sub>2</sub>) but they also underlined that the performance of the carbides was highly dependent on their pretreatment and especially on the presence of surface oxygen-containing species, *e.g.*, oxides and/or oxycarbides. Turnover rates of n-alkanes isomerization on Pt/SiO<sub>2</sub> (0.075 s<sup>-1</sup>) are lower than those of WC (0.28 s<sup>-1</sup>) and W<sub>2</sub>C (0.11 s<sup>-1</sup>) systems. Isomerization selectivities are also lower on Pt/SiO<sub>2</sub> due to secondary (1,5) and (1,6) ring closure reactions (forming methylcyclopentane and benzene products, respectively). At the reaction temperatures, ring closure reactions do not occur on tungsten carbides. The ratio of the isomerization rate to the hydrogenolysis rate is similar on Pt/SiO<sub>2</sub> (7.2) and on W<sub>2</sub>C (6.7) system.

The  $\delta$ -WC phase has been used in polymer electrolyte membrane fuel cells<sup>59</sup>, chlorofluorocarbon hydrodechlorination, and hydrogenolysis of ethane and neopentane<sup>60,61</sup>. For catalyzing alkane hydrogenolysis processes, the  $\beta$ -W<sub>2</sub>C phase has been used. Only recently, tungsten carbides have been shown to be active in the conversion of bio-based materials<sup>62-65</sup>, sometimes even outperforming noble metals. Hence, Gosselink *et al.*<sup>66,67</sup> have shown that when tungsten carbides are used for the hydrodeoxygenation of oleic acid, high yields of valuable unsaturated compounds (olefins) can be obtained, even in the presence of H<sub>2</sub> under high pressure. On the other hand, only

saturated products (paraffins) were formed when noble metals were used as catalysts for this reaction. The applications of tungsten carbides in biomass transformation involve the upgrading of raw lignocellulosic biomass and its separated components; hemicellulose, cellulose, and lignin. In addition, WC-based catalysts could also be used to efficiently reform biomass-derived oxygenated hydrocarbons and upgrade biomass-derived platform chemicals or other biomass resources. In the following part we will discuss in more details biomass conversion over tungsten carbides.

## **1.5. Carbon supported tungsten carbides for Biomass Conversion**

Over the past decade, many catalytic systems based on tungsten carbide catalysts have been developed<sup>144</sup>. These materials' distinct catalytic capabilities are closely connected to their phase and surface structures as seen in Section 1.5. This section aims to provide a comprehensive inquiry of catalytic systems using tungsten carbide or related catalysts for biomass conversion<sup>70</sup>.

### ***1.5.1. Catalytic conversion of (hemi)cellulose and derived sugars***

Tungsten carbide catalysts were initially used to substitute noble metal catalysts in cellulose hydrolytic hydrogenation. Unexpectedly, EG was produced at a yield of 27 wt.% using a W<sub>2</sub>C/AC catalyst, and the yield was upgraded up to 61 wt.% on Ni-W<sub>2</sub>C/AC<sup>63</sup>. Optimizing the catalyst preparation, by using mesostructured carbons, allowed improving the yield of EG up to 72–76 wt.%<sup>89</sup>. Fabiovicová *et al.* investigated the hydrogenolysis of cellulose at 488 K under 65 bars H<sub>2</sub>, without catalyst as well as over six different catalytic formulations containing nickel and/or tungsten on activated carbon (AC) to understand the role of individual active substances (AC, Ni/AC, W/AC, a physical mixture of Ni/AC + W/AC, and two different Ni/W/AC catalysts). When the Ni/W/AC catalyst was prepared using a two-step incipient wetness impregnation (IWI) approach, and using a cellulose/catalyst ratio of 10, an EG yield of 43.7 wt.% was obtained (total polyol yield = 62.1 wt.%). For comparison, the co-impregnated Ni/W/AC catalyst and the Ni/AC + W/AC mixture gave EG yields of 6 wt.% and 4 wt.%, respectively. This result has been attributed to the presence of metallic tungsten in the Ni/W/AC catalyst prepared using IWI following its reduction under H<sub>2</sub> up to 1128 K. Finally, by changing the nature of the AC (Figure 10), high space-time yields of up to 2.5 g polyols (g<sub>catalyst</sub>.h)<sup>-1</sup> could be obtained while retaining a high polyol yield (56 wt.%). After two runs, there was a minor deactivation, followed by a significant fall in polyol output in the next two runs. Deactivation is primarily caused by leaching and structural

modifications on the catalyst surface (formation of  $\text{NiWO}_4$ )<sup>145</sup>. The differences in activity/space-time yield in Figure 10 were mainly attributed to the influence of production technologies of activated carbons on their surface properties: Elorit and MRX are activated under steam, while SX Plus, SX Ultra and Norit Rox are activated under steam and acid washed.

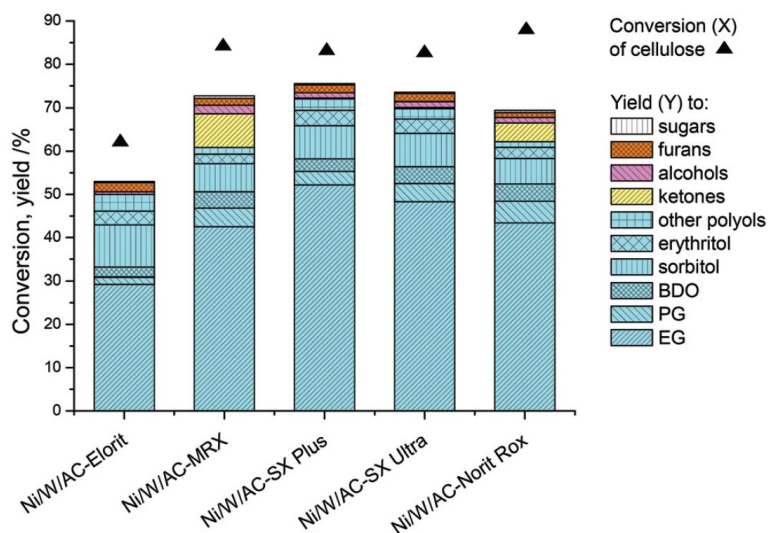


**Figure 10.** Conversion of cellulose and related yields using Ni/W catalysts supported on different activated carbons. Reaction conditions: 488 K, 65 bars  $\text{H}_2$  (at 488 K), 5 g cellulose, 0.5 g catalyst, 100 mL deionized water, 1000 rpm, 3 hours<sup>145</sup>.

Beside carbides, tungsten phosphide, and metallic tungsten- and tungsten oxide-based bifunctional catalysts were all effective for EG synthesis. Very uniquely, besides promoting catalytic RAC reaction, tungsten carbide, phosphide and nitride also provide hydrogenation active sites for GA conversion into EG owing to their Pt-like catalytic behaviors. Inversely, over bifunctional catalysts (like  $\text{H}_2\text{WO}_4 + \text{Ru}/\text{AC}$ ), RAC and hydrogenation reactions are independently fulfilled by  $\text{H}_x\text{WO}_3$  and metallic Ru, respectively. Zheng *et al.* looked into the evolution of cellulose conversion and selectivity as a function of W:Ni ratio using Ni-W catalysts supported on an ordered mesoporous silica (SBA-15). At a W:Ni ratio of 1:1, the yield of EG was 36.8 mol.% but the yields of erythritol and hexitol were also high as they reached 17.2 mol.% and 40.4 mol.%, respectively. When the W:Ni ratio was increased to 3:1, the EG yield was enhanced to a maximum of 76.1 mol.% while decreasing the other polyols overall yield (14 mol.%). Similarly, Zhao *et al.* explored the effect of W:Ru ratio in the catalytic conversion of glucose into EG and found that the EG yield follows a volcano-shaped curve with the increase in the amount of Ru/AC introduced<sup>146</sup>.

Of note, sugar (glucose, fructose, galactose, etc.) degradation mechanisms on tungstenic catalysts have been scarcely studied at the molecular-level. Tai *et al.* identified the tungsten bronze ( $H_xWO_3$ ; a non-stoichiometric tungsten oxide synthesized by hydrogen reduction) as the active species for sugar RAC under homogeneous conditions<sup>147</sup>. Liu *et al.* tried different reactants to probe the C–C bond breakage mechanism at the  $\beta$  position from the carbonyl group in the sugar molecule<sup>148</sup>. They noticed that, unlike the base-catalyzed RAC reaction that requires the reactant to have a  $\beta$ -hydroxyl carbonyl structure, the W-catalyzed C–C bond cleavage needs the reactant to have an  $\alpha$ -hydroxyl carbonyl structure. They supposed that this process may be related to the sugar epimerization in which the C–C bond is reordered. Although this speculation is yet to be verified experimentally or by theoretical calculations, very concurrently, sugar epimerization reactions, especially those involving C1 and C2 positions switch, are catalytically promoted over W, Mo, Sn, and La(III) species. Those species have been found to be active in the C–C bond cracking of glucose into GA under suitable conditions<sup>146,149</sup>. Rodella *et al.*, by studying Ni-promoted tungsten carbide catalyst for cellulose hydrogenolysis, proved that Ni facilitates the deposition of carbon on the catalyst surface. Although the deposited polymeric carbon was partly eliminated during the catalytic reaction, it still had a negative impact on the catalytic activity even if the deposited carbon was evidenced to ameliorate the stability of the  $W_2C$  phase. The existence of Ni and  $SO_3H$  groups throughout carburization had a direct impact on the final product distribution.  $SO_3H$  groups not only accelerate cellulose hydrolysis but also stabilize the Ni promoter and resulted in smaller, more dispersed  $W_2C$  phase and enhanced Ni/ $W_2C$ /C interaction. This leads to a great selectivity towards ethylene glycol, 26%<sup>91</sup>. Furthermore, Xiao *et al.* developed a series of Ni-W/ $SiO_2$  catalysts that were adorned with  $C_xN_y$  species using C- and N-additives and used in the conversion of cellulose to polyols (Figure 11). These catalysts, which went through a self-assembling and complexing process, displayed unusual heterojunctions with strong contacts primarily between the Ni phase and the  $C_xN_y$  layers. Catalytic studies demonstrated that the heterojunctions and outer  $C_xN_y$  layers significantly increased ethylene glycol (EG) production and boosted recycling stability by thriving in Lewis pairs density from the Ni-N-N structure and encapsulating metallic nanoclusters. Thus, 48 wt.% of EG was obtained after 2 h under 240 °C in water and 5 MPa  $H_2$ <sup>150</sup>.

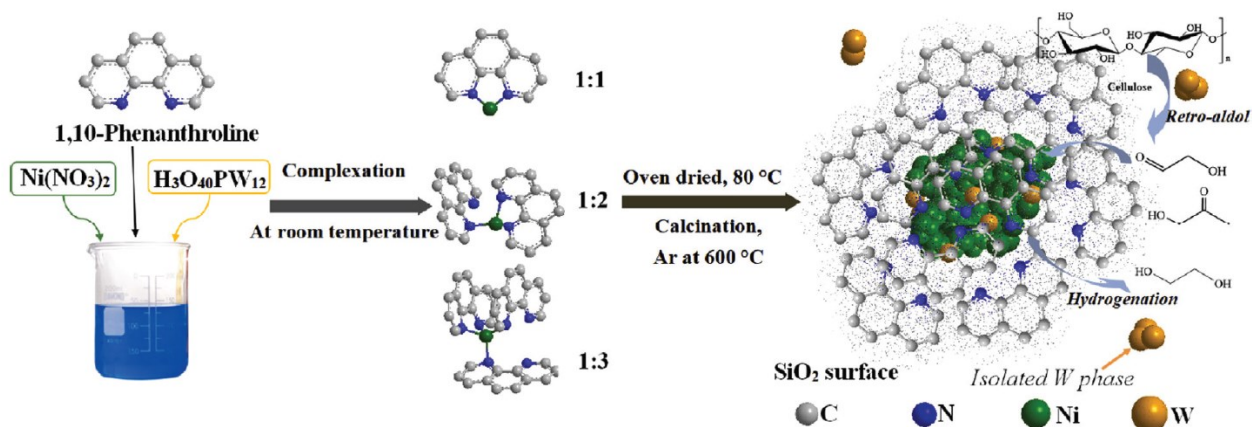


**Figure 11.** Illustration of the synthesis procedure for Ni-W/SiO<sub>2</sub>@C<sub>x</sub>N<sub>y</sub> catalyst<sup>150</sup>.

In repeated studies, Ru/W/AC converted 100 mol.% of microcrystalline cellulose to polyols with an optimal yield of 84 mol.% and an ethylene glycol productivity of 3.7 g (g<sub>catalyst</sub>·h)<sup>-1</sup>. The effect of mixing the catalyst with cellulose, *e.g.* cellulose mechanocatalytic activation, was investigated too. Full cellulose conversion was obtained after three hours of reaction time with just four minutes of ball-milling preprocessing. The increased solid-solid contact between nanosized cellulose and the catalyst after milling has the potential to increase the total polyol yield to 84 mol.% (Figure 12)<sup>151</sup>.

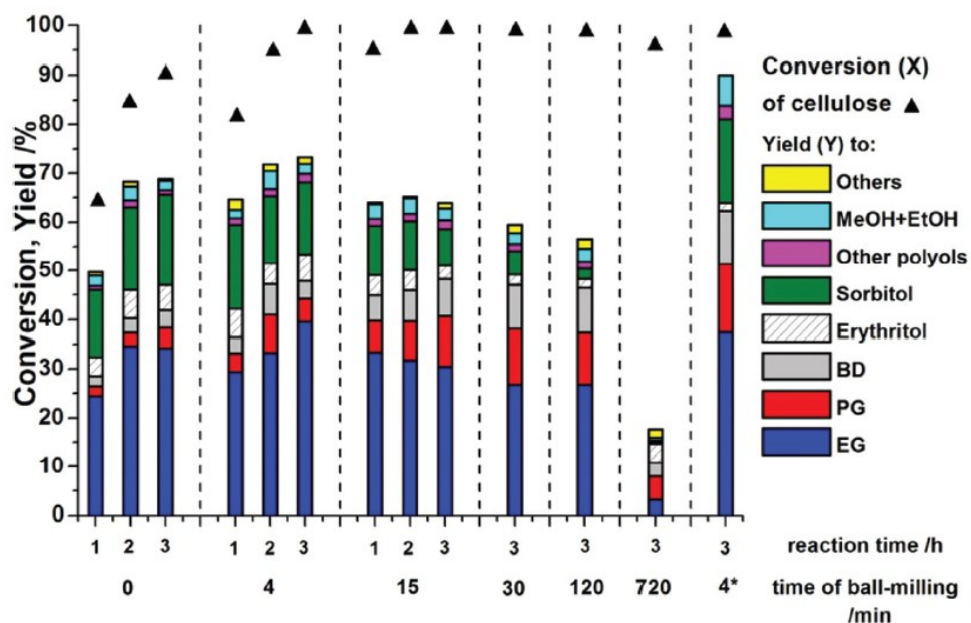


**Figure 12.** Conversion and product yields for Ru/W/AC with non-pretreated cellulose (0 min) and ball-milled cellulose (4, 15, 30, 120, and 720 min). Reaction conditions: 0.5 g of catalyst, 5 g of cellulose, 100 mL of water, reaction temperature of 493 K, 65 bars of hydrogen pressure (measured at the reaction temperature), 1000 rpm. \* = mix-milling the catalyst and cellulose<sup>151</sup>.

Pd promoting influence on the tungsten carbide resulted in excellent physical and chemical characteristics for the carbide phase. Pd-W interaction improves the catalyst capacity to execute multi-step reactions, resulting in better conversion and selectivity toward ethylene glycol<sup>152</sup>. Table 11 summarizes main previous studies using W supported catalysts for the formation of EG and PG:

**Table 11.** Production of EG and PG from cellulose under hydrothermal conditions.

Reaction conditions	Catalyst	Y <sub>EG</sub> (wt%)	Y <sub>PG</sub> (wt%)	Diols conversion loss (mol.%) at 3 <sup>rd</sup> cycle	Ref.
0.5 g cellulose, 50 mL H <sub>2</sub> O, 0.15 g catalyst, 245 °C, 0.5h, H <sub>2</sub> 60 bar	W <sub>2</sub> C/AC	27.4	5.5	7.6	63
0.5 g cellulose, 50 mL H <sub>2</sub> O, 0.15 g catalyst, 245 °C, 0.5h, H <sub>2</sub> 60 bar	Ni-W <sub>2</sub> C/AC	49.8	4.3	4.7	63
1 g cellulose, 100 mL H <sub>2</sub> O, 0.3 g catalyst, 245 °C, 0.5h, H <sub>2</sub> 60 bar	Ni-WC <sub>x</sub> /MC	72.9	5.1	1.6	89
5 g cellulose, 100 mL H <sub>2</sub> O, 1 g catalyst, 225 °C, 3h, H <sub>2</sub> 65 bar	Ni/W/AX-SX Ultra	47	7.5	52	145
0.5 g cellulose, 50 mL H <sub>2</sub> O, 0.2 g catalyst, 240 °C, 2h, H <sub>2</sub> 50 bar	Ni-W/SiO <sub>2</sub> @C <sub>x</sub> N <sub>y</sub>	50	5	6.5	150
1 g cellulose, 150 mL H <sub>2</sub> O, 0.3 g catalyst, 220 °C, 1.5h, H <sub>2</sub> 43 bar	Ni-W <sub>x</sub> C/C-SO <sub>3</sub> H	26 (*)	-	-	91
1 g microcrystalline cellulose, 150 mL H <sub>2</sub> O, 0.3 g catalyst, 220 °C, 2h, H <sub>2</sub> 58 bar	Pd-W <sub>2</sub> C/C	78 (*)	6 (*)	47 (*)	152
5 g microcrystalline cellulose, 100 mL H <sub>2</sub> O, 0.5 g catalyst, 220 °C, 3h, H <sub>2</sub> 65 bar	Ru/W/AC	36.7 (*)	3.4 (*)	2.5 (*)	151

(\*) Molar based.

### 1.5.2. Catalytic Conversion of cellulose from different biomass feedstocks

Both cellulose (C6 sugars) and hemicellulose (C5/C6 sugars) components can yield glycols. Regarding the direct lignocellulose (LC) valorization, lignocellulose deconstruction should occur prior to catalytic transformation. Table 12 summarizes studies on lignocellulose conversion into glycols. Surprisingly, the reaction conditions are similar to those for cellulose transformation, which may be severe enough to deconstruct LC. Zhang *et al.* used a Ni-W<sub>2</sub>C/activated carbon catalyst previously applied for cellulose conversion, to convert raw birch wood. The reaction medium was water and no acid or base were required (they are generally regarded as a crucial ingredient for the degradation of lignin). Also, the biomass was used without any previous pretreatment, rendering this simple process as environmentally friendly as possible. EG and PG were acquired at 51 and 14 mol.% yields. Especially, 1,2-PG yield from birch wood is about twice that obtained from cellulose. Since 19.3 wt.% of birch wood consisted of hemicellulose, it was hypothesized that this would be accountable for the higher 1,2-PG yield. Besides diols, a 36.9 mol.% monophenols yield (based on lignin) was obtained. Other biomass sources (ash tree, poplar, pine) gave comparable yields. Noble metals (Ru, Pd, Pt, Ir) based catalysts were also employed but with lower efficiency than Ni which remains the most efficient catalyst promoter to date for tungsten carbide phase. Moreover, the catalyst could be reused for at least three times (Figure 13) without any important activity loss (only -10 mol.% EG after 4 runs). The leaching of W and Ni components and the oxidation of W<sub>2</sub>C may be responsible for this activity loss<sup>153</sup>.

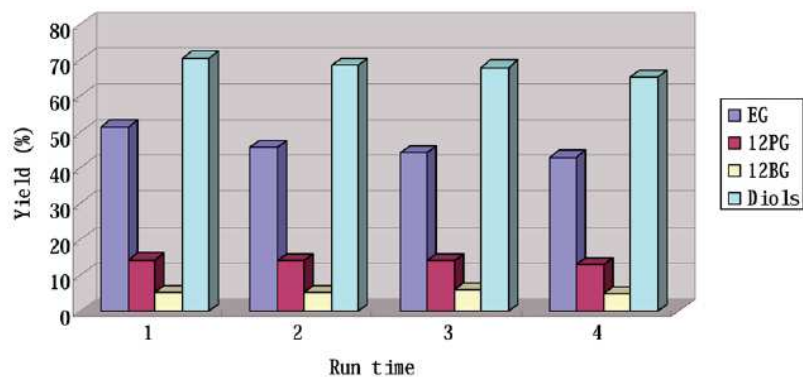


**Figure 13.** Ni-W<sub>2</sub>C/AC catalyst recycling results for birch wood hydrocracking reaction<sup>153</sup>.

Pan *et al.* reported the conversion of alkali-pretreated corn stalk over Ni-W mesoporous silica catalysts yielding EG as the main product. A strong electronic interaction between tungsten and nickel, as shown by XPS, enhanced the C-C bond cleavage and the hydrogenation ability. The



overall diols yield was 37 wt.% by raw corn stalk conversion, which was notably lower than that of diols produced from pretreated corn stalk (71 wt.%). The catalyst stability was also studied. The overall diols yield decreased from 68 wt.% to 54 wt.% from the first to the third run for pre-treated matter. This is caused by the disappearance of  $\text{Ni}_{17}\text{W}_3$  and crystalline W and the appearance of crystalline  $\text{NiWO}_4$  as shown in XRD measurement<sup>154</sup>. More recently, Wang and co. reported the use of Ru/C catalysts for the production of sugar alcohols from corn stalk. Nevertheless, they showed that the presence of  $\text{RuO}_2$  species on the surface was responsible for the cleavage of lignin-carbohydrates linkages, promoting the retro-adol reaction and leading to glycols<sup>155</sup>.

The conversion of corn stalk was also reported over nickel-promoted tungsten carbide trying 9 different pretreatment methods.<sup>156</sup> It has been found that raw corn stalks biomass pretreated with 1,4-butanediol,  $\text{H}_2\text{O}_2$ , NaOH, and  $\text{NH}_3$  produced much higher diols yields (the overall yields of EG and 1,2-PG varied from 35% to 48%, in contrast to the 3.3% overall yield of EG and 1,2-PG for the raw corn stalk) compared to the same biomass pretreated with supercritical  $\text{CO}_2$ , hot water, hot limewater, and ethanol solution which only slightly improved the diols yield (the overall yields of EG and 1,2-PG varied from 5% to 12%, in contrast to the 3.3% overall yield of EG and 1,2-PG for the raw corn stalk.). Seeing the low cost, environmental benignity, and high efficiency, both ammonia or/and diluted  $\text{H}_2\text{O}_2$  pretreatment may be further considered in the next step of diols production from corn stalk conversion<sup>156</sup>.

Pang *et al.* also reported miscanthus conversion with a catalytic system of Ru/C and  $\text{H}_2\text{WO}_4$  giving EG yield (52%) similar to that obtained from cellulose (58%), by promoting the carbohydrate fraction accessibility to the catalytic sites applying 3 to 6 h of ball milling at a speed of 450 rpm (both ball milling time and speed were optimized). The mild ball milling pretreatment reduced the small aldoses self-polymerization, and their reaction with the lignin fractions, and consequently enhanced the EG yield (from 23% to 52%)<sup>157</sup>.

Miscanthus resource was also used for EG production via one-pot catalytic conversion over a binary catalyst composed of Raney Ni and commercial tungstic acid. The miscanthus (1 wt.% concentration in water) was converted into EG with a 35.5 mol.% yield. As the strong adsorption of organic compounds on the Raney Ni was the essential reason for the EG yield decrease during cycling reaction studies, especially during the fourth cycle, the used Raney Ni was rinsed with ethanol after magnetic separation and was reused with the tungstic acid which was recycled by

filtration. As shown in Figure 14, the recycled binary catalyst gave an EG yield of 30.1 mol.% in the second and third runs with Ethanol-NaOH pretreated miscanthus as the feedstock. The small decrease of EG yield in the fourth run was due to the accumulated leaching of the tungstic acid. The EG yield was restored to 39.5 mol.% in the fifth run after adding 0.05 g of tungstic acid<sup>158</sup>.

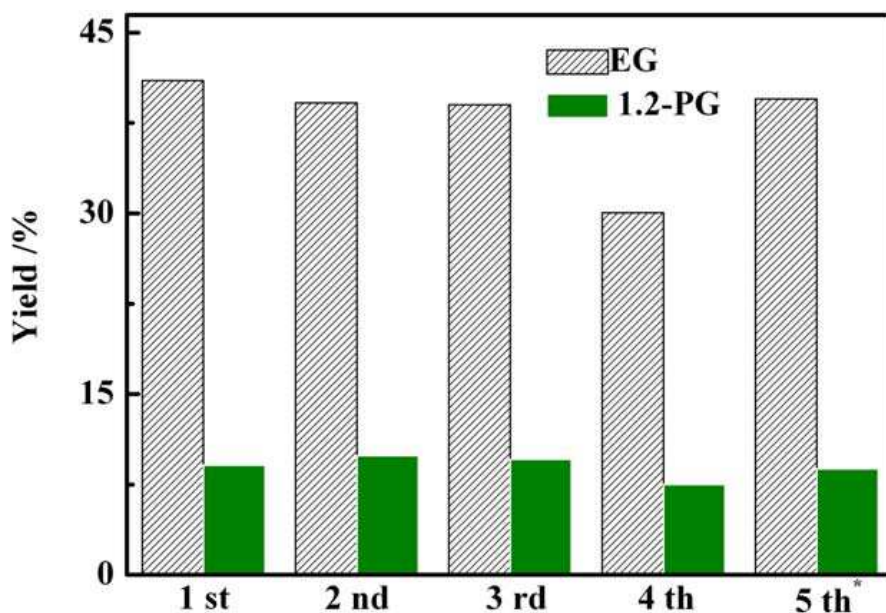


**Figure 14.** The binary catalysts reusability in miscanthus conversion (Ethanol-NaOH-Miscanthus: 2.78 g, tungstic acid: 0.33 g, Raney Ni: 0.33 g; H<sub>2</sub>O: 25 mL, 6 MPa H<sub>2</sub>, 518 K, 2 h). \* = 0.05 g tungstic acid was supplemented for the fifth reaction<sup>158</sup>.

Fabircovicova *et al.* proposed a two-step polyols production from renewable lignocellulose-based feedstock. The first step is the organosolv (with ethanol/water mixtures) fractionation while the second step is the hydrogenolysis on Ru-W/activated carbon catalyst. The influence of several pretreatment parameters was investigated (*e.g.*, ethanol/water ratio, reaction time, and reaction temperature) on the composition of the Barley straw pulp and the hydrogenolysis products distribution. The optimal organosolv reaction conditions (50:50 wt.% ethanol/water solution, 150 min cooking time, 170 °C) were transferred with success for the bamboo foliage and hemp shives delignification. After the pretreatment, the polyols yield was notably enhanced.

The catalyst with a 2 wt.% ruthenium loading and a 40 wt.% tungsten (relative to WO<sub>3</sub>) loading was determined to be the optimal catalyst for the production of diols, especially ethylene glycol (35%). To improve the atom efficiency of the process, the organosolv liquor could be distilled for

ethanol recycling, while the recovery of the solid lignin is possible by centrifugation. The residual mixture of hemicellulose building blocks (*e.g.*, arabinose, xylose) and water and degradation products (*e.g.*, furfural) could be also utilized in the downstream upgrading (*e.g.*, hemicellulose chemistry; through fermentation)<sup>159</sup>. Deactivation of catalysts including acid leaching and active sites aggregation following this biomass transformation is still one of the core issues. To address these problems some recent works suggested to use N-doped catalysts. For instance, Xiao *et al.* monitored the catalytic conversion of bamboo pulp to low carbon polyols using Nickel Tungsten catalysts, revealing that the graphitic carbon nitride (g-C<sub>3</sub>N<sub>4</sub>) phase present on the support showed a high chemical stability under hydrothermal conditions. The binding configuration of N elements in a given carbon matrix were pyrrolic, pyridinic and graphitic N. The nitrogen doped carbon supports demonstrated much better catalytic efficiency than the carbon supports, with an EG yield of 55.8 wt.% versus 36.9 wt.% for the carbon supports catalysts. The catalyst supported on N-rich support showed relatively good stability under reaction conditions (Figure 15), with only -12 wt.% of polyols decrease after 5 recycle use times. It was deduced that the Ni-W and C<sub>3</sub>N<sub>4</sub> phases were the main contributors to this great catalyst stability<sup>160</sup>.

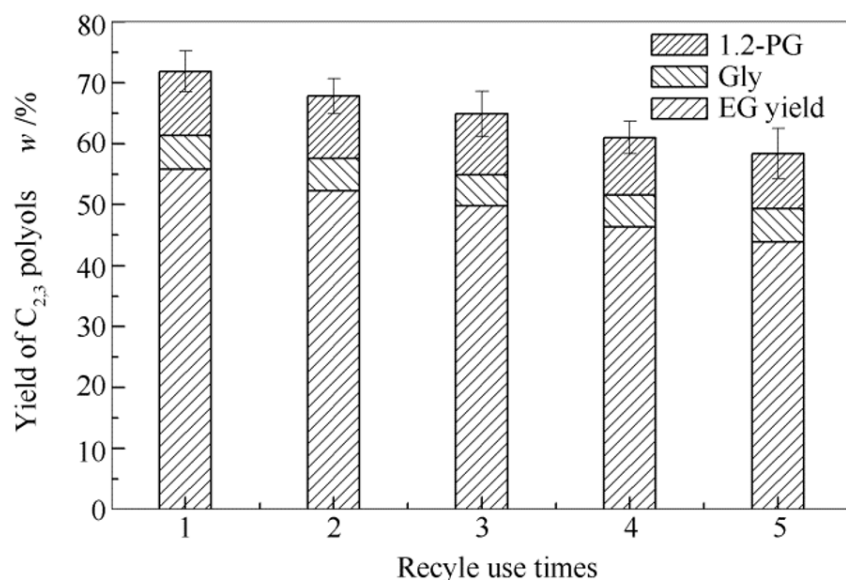


**Figure 15.** Recycling experiments of the conversion of bamboo pulp into diols over Ni-W/NC catalyst; 5 MPa H<sub>2</sub>, 240°C for 1.5 h<sup>160</sup>.

**Table 12.** EG and PG production from cellulose or lignocellulose under hydrothermal conditions.

LC pretreatment	Reaction conditions	Catalyst	Y <sub>EG</sub> (mol.%)	Y <sub>PG</sub> (mol.%)	Diols conversion loss (mol.%) at 3 <sup>rd</sup> cycle	Ref.
Zirconia ball milling	1 g miscanthus, 100 mL H <sub>2</sub> O, 0.25 g 5-Ru/C, 0.1 g H <sub>2</sub> WO <sub>4</sub> , 245 °C, H <sub>2</sub> 50 bar	Ru/C + H <sub>2</sub> WO <sub>4</sub>	52	8.6	-	157
H <sub>2</sub> O <sub>2</sub> +NH <sub>3</sub> treatment (cellulose fraction: from 38% to 72.4%)	0.5 g corn stalk, 50 mL H <sub>2</sub> O, 0.15 g catalyst, 245 °C, H <sub>2</sub> 60 bar	Ni- W <sub>2</sub> C/AC	31	16.0	-	156
-	1 g birch, 100 mL H <sub>2</sub> O, 0.4 g catalyst, 235 °C, H <sub>2</sub> 60 bar	Ni- W <sub>2</sub> C/AC	51	14.2	3	153
1) chopping-milling: powders <80 mesh	0.5 g corn stalk, 50 mL H <sub>2</sub> O, 0.25 g catalyst, 250 °C, 2h, H <sub>2</sub> 60 bar	Ni- W/MCM- 41	54 (*)	14 (*)	14 (*)	154
2) NaOH treatment (cellulose fraction: from 41% to 59%)	0.5 g bamboo pulp, 50 mL H <sub>2</sub> O, 0.2 g catalyst, 240 °C, 1.5h, H <sub>2</sub> 50 bar	Ni-W/NC	55 (*)	10 (*)	5 (*)	160
-	2.78 g miscanthus, 25 mL H <sub>2</sub> O, 0.33 g Raney Ni, 0.33 g H <sub>2</sub> WO <sub>4</sub> , 245 °C, 2 h, H <sub>2</sub> 60 bar	Raney Ni + H <sub>2</sub> WO <sub>4</sub>	39	7.5	3	158
Drying-milling: powders <60 mesh	5 g barley straw, 100 mL H <sub>2</sub> O, 0.5 g catalyst, 220 °C, 3 h, H <sub>2</sub> 65 bar	Ru-W/AC	35	10.0	-	159
Organosolv fractionation (cellulose fraction: from 41% to 58%)						

(\*) Mass based.

## 1.6. Summary and Outlook

Lignocellulosic biomass, a renewable carbon source, is a promising alternative to fossil resources. Glycols, important chemical products, are currently produced from natural gas by energy-intensive processes, generating a lot of toxic wastes. According to the literature, different methods of transforming lignocellulosic biomass into glycols exist, and in particular its conversion by heterogeneous catalysis.

Transition metal carbides are known for their high stability in catalysis, particularly for reactions involving hydrogen, their performances can approach that of noble metals. Several methods for preparing these materials are available. In the case of  $W_xC$ , two different stoichiometries with several crystal structures are obtained. Those are tungsten monocarbide WC and tungsten hemi-carbide  $W_2C$ . The  $\delta$ -WC phase has been used in polymer hydrogenolysis of ethane and neopentane<sup>57</sup>, electrolyte membrane fuel cells<sup>161</sup>, and chlorofluorocarbon hydrodechlorination<sup>162</sup>. For catalyzing alkane hydrogenolysis processes, the  $\beta$ - $W_2C$  phase has been used<sup>58</sup>. Their distinct catalytic capabilities are intricately tied to the structure of their phase and surface characteristics.

For the transformation of lignocellulose into glycols by catalysts based on tungsten carbides like Ni- $W_xC/AC$ , the literature lacks stability enhancement studies hence it does not explicitly show the relationship between the structure, composition of these carbides and their catalytic efficiency. During this thesis work, we studied the influence of the preparation mode of these materials on their catalytic activity and stability. We also sought to correlate the nature of the sites to the hydrogenolysis activity.

In a first experimental chapter, a series of transition metals (nickel-tungsten) based catalysts supported on porous carbons, either standard (C) or N-doped (NC), has been prepared. The synthesis process involves the hydrothermal treatment of biopolymers, followed by pyrolysis under an inert atmosphere, and further metals deposition by wet impregnation. While no significant advantage of using N-carbon can be evidenced for the activity, the presence of N-containing surface functions seems beneficial to the stability in reaction: the EG yield remained about the same during 3 cycles (~50%).

In the second experimental chapter, the potential of using a nickel-based MOF (DUT-8) supporting tungsten precursor, to prepare Ni- $W_xC/NC$  catalysts via an encapsulation strategy followed by pyrolysis is evaluated. Pure phase WC (via liquid-mediated synthesis) or  $W_2C$  (via vapor-mediated

synthesis) were obtained through this novel synthesis route. Notably, similar EG and PG yields with lower  $n_W/n_{Ni}$  ratio were obtained as compared to the literature and the results of the previous chapter.

Finally, in a third chapter, the possibility to produce amino derivatives of glycols is explored. In order to do so, the formation of primary amino-derivatives and propylene glycol, from the reductive amination of acetol by  $NH_3$ , has been studied. The effect of reaction conditions (time, pressure, temperature) were investigated when reaction is conducted in the presence of a Ru/AC catalyst. A bimetallic synergy possibility was further explored by trying transition (Ni, Co, Cu, W) and noble metals (Pt, Rh) associated with Ru. Only the NiRu/AC catalyst showed an amelioration in activity.

## 1.7. References

- (1) *L'avenir du pétrole, entre impératif économique et urgence écologique*. vie-publique.fr. <http://www.vie-publique.fr/eclairage/271741-lavenir-du-petrole-entre-imperatif-economique-et-urgence-ecologique> (accessed 2023-07-16).
- (2) Tuck, C. O.; Pérez, E.; Horváth, I. T.; Sheldon, R. A.; Poliakoff, M. Valorization of Biomass: Deriving More Value from Waste. *Science* **2012**, *337* (6095), 695–699. <https://doi.org/10.1126/science.1218930>.
- (3) Biddy, M. J.; Scarlata, C.; Kinchin, C. *Chemicals from Biomass: A Market Assessment of Bioproducts with Near-Term Potential*; NREL/TP-5100-65509; National Renewable Energy Lab. (NREL), Golden, CO (United States), 2016. <https://doi.org/10.2172/1244312>.
- (4) Zhu, Y.; Romain, C.; Williams, C. K. Sustainable Polymers from Renewable Resources. *Nature* **2016**, *540* (7633), 354–362. <https://doi.org/10.1038/nature21001>.
- (5) Esposito, D.; Antonietti, M. Redefining Biorefinery: The Search for Unconventional Building Blocks for Materials. *Chem. Soc. Rev.* **2015**, *44* (16), 5821–5835. <https://doi.org/10.1039/C4CS00368C>.
- (6) Huber, G. W.; Iborra, S.; Corma, A. Synthesis of Transportation Fuels from Biomass: Chemistry, Catalysts, and Engineering. *Chem. Rev.* **2006**, *106* (9), 4044–4098. <https://doi.org/10.1021/cr068360d>.
- (7) Aresta, M.; Dibenedetto, A.; Dumeignil, F. *Biorefinery: From Biomass to Chemicals and Fuels*; Walter de Gruyter, 2012.
- (8) Clark, J. H.; Budarin, V.; Deswarte, F. E. I.; Hardy, J. J. E.; Kerton, F. M.; Hunt, A. J.; Luque, R.; Macquarrie, D. J.; Milkowski, K.; Rodriguez, A.; Samuel, O.; Tavener, S. J.; White, R. J.; Wilson, A. J. Green Chemistry and the Biorefinery: A Partnership for a Sustainable Future. *Green Chem.* **2006**, *8* (10), 853–860. <https://doi.org/10.1039/B604483M>.
- (9) Armaroli, N.; Balzani, V. The Future of Energy Supply: Challenges and Opportunities. *Angew. Chem. Int. Ed.* **2007**, *46* (1–2), 52–66. <https://doi.org/10.1002/anie.200602373>.
- (10) Espinoza Pérez, A. T.; Camargo, M.; Narváez Rincón, P. C.; Alfaro Marchant, M. Key Challenges and Requirements for Sustainable and Industrialized Biorefinery Supply Chain

- Design and Management: A Bibliographic Analysis. *Renew. Sustain. Energy Rev.* **2017**, *69*, 350–359. <https://doi.org/10.1016/j.rser.2016.11.084>.
- (11) Gebreslassie, B. H.; Yao, Y.; You, F. Design under Uncertainty of Hydrocarbon Biorefinery Supply Chains: Multiobjective Stochastic Programming Models, Decomposition Algorithm, and a Comparison between CVaR and Downside Risk. *AIChE J.* **2012**, *58* (7), 2155–2179. <https://doi.org/10.1002/aic.13844>.
  - (12) Kim, J.; Realff, M. J.; Lee, J. H. Optimal Design and Global Sensitivity Analysis of Biomass Supply Chain Networks for Biofuels under Uncertainty. *Comput. Chem. Eng.* **2011**, *35* (9), 1738–1751. <https://doi.org/10.1016/j.compchemeng.2011.02.008>.
  - (13) Deuss, P. J.; Barta, K.; De Vries, J. G. Homogeneous Catalysis for the Conversion of Biomass and Biomass-Derived Platform Chemicals. *Catal Sci Technol* **2014**, *4* (5), 1174–1196. <https://doi.org/10.1039/C3CY01058A>.
  - (14) Karmee, S. K.; Linardi, D.; Lee, J.; Lin, C. S. K. Conversion of Lipid from Food Waste to Biodiesel. *Waste Manag.* **2015**, *41*, 169–173. <https://doi.org/10.1016/j.wasman.2015.03.025>.
  - (15) Fadhel, A. Z.; Pollet, P.; Liotta, C. L.; Eckert, C. A. Combining the Benefits of Homogeneous and Heterogeneous Catalysis with Tunable Solvents and Nearcritical Water. *Molecules* **2010**, *15* (11), 8400–8424. <https://doi.org/10.3390/molecules15118400>.
  - (16) Wang, F.; Dong, W.; Qu, D.; Huang, Y.; Chen, Y. Synergistic Catalytic Conversion of Cellulose into Glycolic Acid over Mn-Doped Bismuth Oxyiodide Catalyst Combined with H-ZSM-5. *Ind. Eng. Chem. Res.* **2022**, *61* (31), 11382–11389. <https://doi.org/10.1021/acs.iecr.1c04008>.
  - (17) Kim, N. D.; Oh, S.; Joo, J. B.; Jung, K. S.; Yi, J. Effect of Preparation Method on Structure and Catalytic Activity of Cr-Promoted Cu Catalyst in Glycerol Hydrogenolysis. *Korean J. Chem. Eng.* **2010**, *27* (2), 431–434. <https://doi.org/10.1007/s11814-010-0070-5>.
  - (18) Albilali, R.; Douthwaite, M.; He, Q.; H. Taylor, S. The Selective Hydrogenation of Furfural over Supported Palladium Nanoparticle Catalysts Prepared by Sol-Immobilisation: Effect of Catalyst Support and Reaction Conditions. *Catal. Sci. Technol.* **2018**, *8* (1), 252–267. <https://doi.org/10.1039/C7CY02110K>.
  - (19) Szczyglewska, P.; Feliczak-Guzik, A.; Nowak, I. A Support Effect on the Hydrodeoxygenation Reaction of Anisole by Ruthenium Catalysts. *Microporous Mesoporous Mater.* **2020**, *293*, 109771. <https://doi.org/10.1016/j.micromeso.2019.109771>.
  - (20) 3t Marsella1987.Pdf.
  - (21) Runeberg, J.; Baiker, A.; Kijenski, J. Copper Catalyzed Amination of Ethylene Glycol. *Appl. Catal.* **1985**, *17* (2), 309–319. [https://doi.org/10.1016/S0166-9834\(00\)83211-X](https://doi.org/10.1016/S0166-9834(00)83211-X).
  - (22) Jere, F. T.; Jackson, J. E.; Miller, D. J. Kinetics of the Aqueous-Phase Hydrogenation of L-Alanine to L-Alaninol. *Ind. Eng. Chem. Res.* **2004**, *43* (13), 3297–3303. <https://doi.org/10.1021/ie034046n>.
  - (23) Chen, X.; Liu, Y.; Wang, J. Lignocellulosic Biomass Upgrading into Valuable Nitrogen-Containing Compounds by Heterogeneous Catalysts. *Ind. Eng. Chem. Res.* **2020**, *59* (39), 17008–17025. <https://doi.org/10.1021/acs.iecr.0c01815>.
  - (24) Liang, G.; Wang, A.; Li, L.; Xu, G.; Yan, N.; Zhang, T. Production of Primary Amines by Reductive Amination of Biomass-Derived Aldehydes/Ketones. *Angew. Chem. Int. Ed.* **2017**, *56* (11), 3050–3054. <https://doi.org/10.1002/anie.201610964>.
  - (25) Pelckmans, M.; Mihaylov, T.; Faveere, W.; Poissonnier, J.; Van Waes, F.; Moonen, K.; Marin, G. B.; Thybaut, J. W.; Pierloot, K.; Sels, B. F. Catalytic Reductive Aminolysis of

- Reducing Sugars: Elucidation of Reaction Mechanism. *ACS Catal.* **2018**, *8* (5), 4201–4212. <https://doi.org/10.1021/acscatal.8b00619>.
- (26) Takanashi, T.; Nakagawa, Y.; Tomishige, K. Amination of Alcohols with Ammonia in Water over Rh–In Catalyst. *Chem. Lett.* **2014**, *43* (6), 822–824. <https://doi.org/10.1246/cl.140051>.
- (27) Park, J.-H.; Hong, E.; An, S. H.; Lim, D.-H.; Shin, C.-H. Reductive Amination of Ethanol to Ethylamines over Ni/Al<sub>2</sub>O<sub>3</sub> Catalysts. *Korean J. Chem. Eng.* **2017**, *34* (10), 2610–2618. <https://doi.org/10.1007/s11814-017-0164-4>.
- (28) Yue, C.-J.; Di, K.; Gu, L.-P.; Zhang, Z.-W.; Ding, L.-L. Selective Amination of 1,2-Propanediol over Co/La<sub>3</sub>O<sub>4</sub> Catalyst Prepared by Liquid-Phase Reduction. *Mol. Catal.* **2019**, *477*, 110539. <https://doi.org/10.1016/j.mcat.2019.110539>.
- (29) Wang, Y.; Furukawa, S.; Song, S.; He, Q.; Asakura, H.; Yan, N. Catalytic Production of Alanine from Waste Glycerol. *Angew. Chem. Int. Ed.* **2020**, *59* (6), 2289–2293. <https://doi.org/10.1002/anie.201912580>.
- (30) Komanoya, T.; Kinemura, T.; Kita, Y.; Kamata, K.; Hara, M. Electronic Effect of Ruthenium Nanoparticles on Efficient Reductive Amination of Carbonyl Compounds. *J. Am. Chem. Soc.* **2017**, *139* (33), 11493–11499. <https://doi.org/10.1021/jacs.7b04481>.
- (31) Nakamura, Y.; Kon, K.; Touchy, A. S.; Shimizu, K.; Ueda, W. Selective Synthesis of Primary Amines by Reductive Amination of Ketones with Ammonia over Supported Pt Catalysts. *ChemCatChem* **2015**, *7* (6), 921–924. <https://doi.org/10.1002/cctc.201402996>.
- (32) Faveere, W.; Mihaylov, T.; Pelckmans, M.; Moonen, K.; Gillis-D’Hamers, F.; Bosschaerts, R.; Pierloot, K.; Sels, B. F. Glycolaldehyde as a Bio-Based C<sub>2</sub> Platform Chemical: Catalytic Reductive Amination of Vicinal Hydroxyl Aldehydes. *ACS Catal.* **2020**, *10* (1), 391–404. <https://doi.org/10.1021/acscatal.9b02437>.
- (33) Verma, R.; Jing, Y.; Liu, H.; Aggarwal, V.; Kumar Goswami, H.; Bala, E.; Ke, Z.; Kumar Verma, P. Employing Ammonia for Diverse Amination Reactions: Recent Developments of Abundantly Available and Challenging Nitrogen Sources. *Eur. J. Org. Chem.* **2022**, *2022* (25). <https://doi.org/10.1002/ejoc.202200298>.
- (34) Trégner, T.; Trejbal, J.; Ruhswurmová, N.; Zapletal, M. Reductive Amination of 1-Hydroxy-2-Propanone Over Nickel and Copper Catalysts. *Chem. Biochem. Eng. Q.* **2017**, *31* (4), 455–470. <https://doi.org/10.15255/CABEQ.2017.1077>.
- (35) Sheng, M.; Fujita, S.; Yamaguchi, S.; Yamasaki, J.; Nakajima, K.; Yamazoe, S.; Mizugaki, T.; Mitsudome, T. Single-Crystal Cobalt Phosphide Nanorods as a High-Performance Catalyst for Reductive Amination of Carbonyl Compounds. *JACS Au* **2021**, *1* (4), 501–507. <https://doi.org/10.1021/jacsau.1c00125>.
- (36) Shin, C.-K.; Kim, S.-H.; Chang, K.-H.; Lee, H.-C.; Kim, G.-J. New Synthesis of Optically Active (L)-Alaninol over Palladium Supported Catalysts. In *Studies in Surface Science and Catalysis*; Elsevier, 2006; Vol. 159, pp 313–316. [https://doi.org/10.1016/S0167-2991\(06\)81596-X](https://doi.org/10.1016/S0167-2991(06)81596-X).
- (37) Pelckmans, M.; Vermandel, W.; Van Waes, F.; Moonen, K.; Sels, B. F. Low-Temperature Reductive Aminolysis of Carbohydrates to Diamines and Aminoalcohols by Heterogeneous Catalysis. *Angew. Chem. Int. Ed.* **2017**, *56* (46), 14540–14544. <https://doi.org/10.1002/anie.201708216>.
- (38) Pang, J.; Sun, J.; Zheng, M.; Li, H.; Wang, Y.; Zhang, T. Transition Metal Carbide Catalysts for Biomass Conversion: A Review. *Appl. Catal. B Environ.* **2019**, *254*, 510–522. <https://doi.org/10.1016/j.apcatb.2019.05.034>.



- (39) Kosolapova, T. Y. *Carbides: Properties, Production, and Applications*; Springer Science & Business Media, 1971.
- (40) Mukhopadhyay, A.; Basu, B. Consolidation–Microstructure–Property Relationships in Bulk Nanoceramics and Ceramic Nanocomposites: A Review. *Int. Mater. Rev.* **2007**, *52* (5), 257–288. <https://doi.org/10.1179/174328007X160281>.
- (41) Schubert, W. D.; Bock, A.; Lux, B. General Aspects and Limits of Conventional Ultrafine WC Powder Manufacture and Hard Metal Production. *Int. J. Refract. Met. Hard Mater.* **1995**, *13* (5), 281–296. [https://doi.org/10.1016/0263-4368\(95\)92674-9](https://doi.org/10.1016/0263-4368(95)92674-9).
- (42) Jia, K.; Fischer, T. E.; Gallois, B. Microstructure, Hardness and Toughness of Nanostructured and Conventional WC-Co Composites. *Nanostructured Mater.* **1998**, *10* (5), 875–891. [https://doi.org/10.1016/S0965-9773\(98\)00123-8](https://doi.org/10.1016/S0965-9773(98)00123-8).
- (43) Einarsrud, M.-A.; Hagen, E.; Pettersen, G.; Grande, T. Pressureless Sintering of Titanium Diboride with Nickel, Nickel Boride, and Iron Additives. *J. Am. Ceram. Soc.* **1997**, *80* (12), 3013–3020. <https://doi.org/10.1111/j.1151-2916.1997.tb03227.x>.
- (44) Basu, B.; Raju, G. B.; Suri, A. K. Processing and Properties of Monolithic TiB<sub>2</sub> Based Materials. *Int. Mater. Rev.* **2006**, *51* (6), 352–374. <https://doi.org/10.1179/174328006X102529>.
- (45) Bounhoure, V.; Lay, S.; Loubradou, M.; Missiaen, J.-M. Special WC/Co Orientation Relationships at Basal Facets of WC Grains in WC–Co Alloys. *J. Mater. Sci.* **2008**, *43* (3), 892–899. <https://doi.org/10.1007/s10853-007-2181-x>.
- (46) Sternitzke, M. Structural Ceramic Nanocomposites. *J. Eur. Ceram. Soc.* **1997**, *17* (9), 1061–1082. [https://doi.org/10.1016/S0955-2219\(96\)00222-1](https://doi.org/10.1016/S0955-2219(96)00222-1).
- (47) Zhu, H.; Sun, Z.; Chen, M.; Cao, H.; Li, K.; Cai, Y.; Wang, F. Highly Porous Composite Based on Tungsten Carbide and N-Doped Carbon Aerogels for Electrocatalyzing Oxygen Reduction Reaction in Acidic and Alkaline Media. *Electrochimica Acta* **2017**, *236*, 154–160. <https://doi.org/10.1016/j.electacta.2017.02.156>.
- (48) Shi, M.; Zhang, W.; Li, Y.; Chu, Y.; Ma, C. Tungsten Carbide-Reduced Graphene Oxide Intercalation Compound as Co-Catalyst for Methanol Oxidation. *Chin. J. Catal.* **2016**, *37* (11), 1851–1859. [https://doi.org/10.1016/S1872-2067\(16\)62535-4](https://doi.org/10.1016/S1872-2067(16)62535-4).
- (49) Bukola, S.; Merzougui, B.; Akinpelu, A.; Zeama, M. Cobalt and Nitrogen Co-Doped Tungsten Carbide Catalyst for Oxygen Reduction and Hydrogen Evolution Reactions. *Electrochimica Acta* **2016**, *190*, 1113–1123. <https://doi.org/10.1016/j.electacta.2015.12.074>.
- (50) Singla, G.; Singh, K.; Pandey, O. P. Catalytic Activity of Tungsten Carbide-Carbon (WC@C) Core-Shell Structured for Ethanol Electro-Oxidation. *Mater. Chem. Phys.* **2017**, *186*, 19–28. <https://doi.org/10.1016/j.matchemphys.2016.07.022>.
- (51) George, M.; Baker, B. S. *New Materials for Fluoro Sulfonic Acid Electrolyte Fuel Cells. Interim Report No. 2, 7 March--7 November 1975*; AD-A-022466; ERC-0123-S1; Energy Research Corp., Danbury, CT (USA), 1975. <https://www.osti.gov/biblio/7224947> (accessed 2022-03-16).
- (52) Li, S.-H.; Yang, W.; Liu, Y.; Song, X.-R.; Liu, R.; Chen, G.; Lu, C.-H.; Yang, H.-H. Engineering of Tungsten Carbide Nanoparticles for Imaging-Guided Single 1,064 Nm Laser-Activated Dual-Type Photodynamic and Photothermal Therapy of Cancer. *Nano Res.* **2018**, *11* (9), 4859–4873. <https://doi.org/10.1007/s12274-018-2075-z>.

- (53) Garg, D.; Dyer, P. N. Tungsten Carbide Erosion Resistant Coating for Aerospace Components. *MRS Online Proc. Libr. OPL* **1989**, *168*. <https://doi.org/10.1557/PROC-168-213>.
- (54) Levy, R. B.; Boudart, M. Platinum-Like Behavior of Tungsten Carbide in Surface Catalysis. *Science* **1973**, *181* (4099), 547–549. <https://doi.org/10.1126/science.181.4099.547>.
- (55) Ma, Y.; Guan, G.; Hao, X.; Cao, J.; Abudula, A. Molybdenum Carbide as Alternative Catalyst for Hydrogen Production – A Review. *Renew. Sustain. Energy Rev.* **2017**, *75*, 1101–1129. <https://doi.org/10.1016/j.rser.2016.11.092>.
- (56) Wu, M.; Lin, X.; Hagfeldt, A.; Ma, T. Low-Cost Molybdenum Carbide and Tungsten Carbide Counter Electrodes for Dye-Sensitized Solar Cells. *Angew. Chem.* **2011**, *123* (15), 3582–3586. <https://doi.org/10.1002/ange.201006635>.
- (57) Oyama, S. T. Preparation and Catalytic Properties of Transition Metal Carbides and Nitrides. *Catal. Today* **1992**, *15* (2), 179–200. [https://doi.org/10.1016/0920-5861\(92\)80175-M](https://doi.org/10.1016/0920-5861(92)80175-M).
- (58) Ribeiro, F. H.; Boudart, M.; Betta, R. A. D. Catalytic Reactions of N-Alkanes on/3-W2C and WC: The Effect of Surface Oxygen on Reaction Pathways.
- (59) Wu, M.; Lin, X.; Hagfeldt, A.; Ma, T. Low-Cost Molybdenum Carbide and Tungsten Carbide Counter Electrodes for Dye-Sensitized Solar Cells. *Angew. Chem. Int. Ed.* **2011**, *50* (15), 3520–3524. <https://doi.org/10.1002/anie.201006635>.
- (60) Oyama, S. T. Preparation and Catalytic Properties of Transition Metal Carbides and Nitrides. *Catal. Today* **1992**, *15* (2), 179–200. [https://doi.org/10.1016/0920-5861\(92\)80175-M](https://doi.org/10.1016/0920-5861(92)80175-M).
- (61) Delannoy, L.; Giraudon, J.-M.; Granger, P.; Leclercq, L.; Leclercq, G. Group VI Transition Metal Carbides as Alternatives in the Hydrodechlorination of Chlorofluorocarbons. *Catal. Today* **2000**, *59* (3), 231–240. [https://doi.org/10.1016/S0920-5861\(00\)00289-3](https://doi.org/10.1016/S0920-5861(00)00289-3).
- (62) Hwu, H. H.; Chen, J. G. Surface Chemistry of Transition Metal Carbides. *Chem. Rev.* **2005**, *105* (1), 185–212. <https://doi.org/10.1021/cr0204606>.
- (63) Ji, N.; Zhang, T.; Zheng, M.; Wang, A.; Wang, H.; Wang, X.; Chen, J. G. Direct Catalytic Conversion of Cellulose into Ethylene Glycol Using Nickel-Promoted Tungsten Carbide Catalysts. *Angew. Chem. Int. Ed.* **2008**, *47* (44), 8510–8513. <https://doi.org/10.1002/anie.200803233>.
- (64) Furimsky, E. Hydroprocessing Challenges in Biofuels Production. *Catal. Today* **2013**, *217*, 13–56. <https://doi.org/10.1016/j.cattod.2012.11.008>.
- (65) Stellwagen, D. R.; Bitter, J. H. Structure–Performance Relations of Molybdenum- and Tungsten Carbide Catalysts for Deoxygenation. *Green Chem.* **2014**, *17* (1), 582–593. <https://doi.org/10.1039/C4GC01831A>.
- (66) Hollak, S. A. W.; Gosselink, R. W.; van Es, D. S.; Bitter, J. H. Comparison of Tungsten and Molybdenum Carbide Catalysts for the Hydrodeoxygenation of Oleic Acid. *ACS Catal.* **2013**, *3* (12), 2837–2844. <https://doi.org/10.1021/cs400744y>.
- (67) Gosselink, R. W.; Hollak, S. A. W.; Chang, S.-W.; van Haveren, J.; de Jong, K. P.; Bitter, J. H.; van Es, D. S. Reaction Pathways for the Deoxygenation of Vegetable Oils and Related Model Compounds. *ChemSusChem* **2013**, *6* (9), 1576–1594. <https://doi.org/10.1002/cssc.201300370>.

- (68) Kurlov, A. S.; Gusev, A. I. Phase Equilibria in the W–C System and Tungsten Carbides. *Russ. Chem. Rev.* **2006**, *75* (7), 617–636. <https://doi.org/10.1070/RC2006v075n07ABEH003606>.
- (69) Li, Y.; Gao, Y.; Xiao, B.; Min, T.; Fan, Z.; Ma, S.; Xu, L. Theoretical Study on the Stability, Elasticity, Hardness and Electronic Structures of W–C Binary Compounds. *J. Alloys Compd.* **2010**, *502* (1), 28–37. <https://doi.org/10.1016/j.jallcom.2010.04.184>.
- (70) Shrestha, A.; Gao, X.; Hicks, J. C.; Paolucci, C. Nanoparticle Size Effects on Phase Stability for Molybdenum and Tungsten Carbides. **20**.
- (71) Sakaki, M.; Bafghi, M. Sh.; Vahdati Khaki, J.; Zhang, Q.; Saito, F. Conversion of W<sub>2</sub>C to WC Phase during Mechano-Chemical Synthesis of Nano-Size WC–Al<sub>2</sub>O<sub>3</sub> Powder Using WO<sub>3</sub>–2Al–(1+x)C Mixtures. *Int. J. Refract. Met. Hard Mater.* **2013**, *36*, 116–121. <https://doi.org/10.1016/j.ijrmhm.2012.08.002>.
- (72) Suetin, D.; Shein, I.; Ivanovskii, A. Structural, Electronic Properties and Stability of Tungsten Mono- and Semi-Carbides: A First Principles Investigation. *J. Phys. Chem. Solids* **2009**, *70*, 64–71. <https://doi.org/10.1016/j.jpcs.2008.09.004>.
- (73) Jain, A.; Ong, S. P.; Hautier, G.; Chen, W.; Richards, W. D.; Dacek, S.; Cholia, S.; Gunter, D.; Skinner, D.; Ceder, G.; Persson, K. A. Commentary: The Materials Project: A Materials Genome Approach to Accelerating Materials Innovation. *APL Mater.* **2013**, *1* (1), 011002. <https://doi.org/10.1063/1.4812323>.
- (74) Bott-Neto, J. L.; Beck, W.; Varanda, L. C.; Ticianelli, E. A. Electrocatalytic Activity of Platinum Nanoparticles Supported on Different Phases of Tungsten Carbides for the Oxygen Reduction Reaction. *Int. J. Hydrog. Energy* **2017**, *42* (32), 20677–20688. <https://doi.org/10.1016/j.ijhydene.2017.07.065>.
- (75) Kurlov, A. S.; Gusev, A. I. Neutron and X-Ray Diffraction Study and Symmetry Analysis of Phase Transformations in Lower Tungsten Carbide W<sub>2</sub>C. *Phys. Rev. B* **2007**, *76* (17), 174115. <https://doi.org/10.1103/PhysRevB.76.174115>.
- (76) Aravinth, S.; Sankar, B.; Kamaraj, M.; Chakravarthy, S. R.; Sarathi, R. Synthesis and Characterization of Hexagonal Nano Tungsten Carbide Powder Using Multi Walled Carbon Nanotubes. *Int. J. Refract. Met. Hard Mater.* **2012**, *33*, 53–57. <https://doi.org/10.1016/j.ijrmhm.2012.02.010>.
- (77) Fan, X.; Zhou, H.; Guo, X. WC Nanocrystals Grown on Vertically Aligned Carbon Nanotubes: An Efficient and Stable Electrocatalyst for Hydrogen Evolution Reaction. *ACS Nano* **2015**, *9* (5), 5125–5134. <https://doi.org/10.1021/acsnano.5b00425>.
- (78) Kolel-Veetil, M. K.; Goswami, R.; Fears, K. P.; Qadri, S. B.; Lambrakos, S. G.; Laskoski, M.; Keller, T. M.; Saab, A. P. Formation and Stability of Metastable Tungsten Carbide Nanoparticles. *J. Mater. Eng. Perform.* **2015**, *24* (5), 2060–2066. <https://doi.org/10.1007/s11665-015-1476-3>.
- (79) Singh, H.; Pandey, O. P. A Novel Approach for Direct Synthesis of Nanocrystalline Tungsten Carbide from Milled Scheelite Ore. *Metall. Mater. Trans. B* **2013**, *44* (6), 1428–1434. <https://doi.org/10.1007/s11663-013-9945-2>.
- (80) Xu, Z.; Zhang, X.; Zhao, N.; He, C. Synergistic Strengthening Effect of In-Situ Synthesized WC<sub>1-x</sub> Nanoparticles and Graphene Nanosheets in Copper Matrix Composites. *Compos. Part Appl. Sci. Manuf.* **2020**, *133*, 105891. <https://doi.org/10.1016/j.compositesa.2020.105891>.
- (81) Pang, J.; Li, J. Low Thermal Expansion Porous SiC–WC Composite Ceramics. *Ceram. Int.* **2009**, *35* (8), 3517–3520. <https://doi.org/10.1016/j.ceramint.2009.05.008>.

- (82) Kurlov, A. S.; Gusev, A. I. Tungsten Carbides and W-C Phase Diagram. *Inorg. Mater.* **2006**, *42* (2), 121–127. <https://doi.org/10.1134/S0020168506020051>.
- (83) Chen, W.-F.; Muckerman, J. T.; Fujita, E. Recent Developments in Transition Metal Carbides and Nitrides as Hydrogen Evolution Electrocatalysts. *Chem. Commun.* **2013**, *49* (79), 8896–8909. <https://doi.org/10.1039/C3CC44076A>.
- (84) Hunt, S. T.; Nimmanwudipong, T.; Román-Leshkov, Y. Engineering Non-Sintered, Metal-Terminated Tungsten Carbide Nanoparticles for Catalysis. *Angew. Chem. Int. Ed.* **2014**, *53* (20), 5131–5136. <https://doi.org/10.1002/anie.201400294>.
- (85) Fang, H.; Chen, W.; Wu, L.; Zhao, P.; Roldan, A.; Yuan, Y. Stable and Antisintering Tungsten Carbides with Controllable Active Phase for Selective Cleavage of Aryl Ether C–O Bonds. *ACS Appl. Mater. Interfaces* **2021**, *13* (7), 8274–8284. <https://doi.org/10.1021/acsami.0c19599>.
- (86) Gong, Q.; Wang, Y.; Hu, Q.; Zhou, J.; Feng, R.; Duchesne, P. N.; Zhang, P.; Chen, F.; Han, N.; Li, Y.; Jin, C.; Li, Y.; Lee, S.-T. Ultrasmall and Phase-Pure W<sub>2</sub>C Nanoparticles for Efficient Electrocatalytic and Photoelectrochemical Hydrogen Evolution. *Nat. Commun.* **2016**, *7* (1), 13216. <https://doi.org/10.1038/ncomms13216>.
- (87) Ishii, T.; Yamada, K.; Osuga, N.; Imashiro, Y.; Ozaki, J. Single-Step Synthesis of W<sub>2</sub>C Nanoparticle-Dispersed Carbon Electrocatalysts for Hydrogen Evolution Reactions Utilizing Phosphate Groups on Carbon Edge Sites. *ACS Omega* **2016**, *1* (4), 689–695. <https://doi.org/10.1021/acsomega.6b00179>.
- (88) Garcia-Esparza, A. T.; Cha, D.; Ou, Y.; Kubota, J.; Domen, K.; Takanabe, K. Tungsten Carbide Nanoparticles as Efficient Cocatalysts for Photocatalytic Overall Water Splitting. *ChemSusChem* **2013**, *6* (1), 168–181. <https://doi.org/10.1002/cssc.201200780>.
- (89) Zhang, Y.; Wang, A.; Zhang, T. A New 3D Mesoporous Carbon Replicated from Commercial Silica as a Catalyst Support for Direct Conversion of Cellulose into Ethylene Glycol. *Chem Commun* **2010**, *46* (6), 862–864. <https://doi.org/10.1039/B919182H>.
- (90) Huang, L.; Zhu, D.; Chen, Y. W<sub>2</sub>C/Porous Graphene Nanocomposite as an Efficient Non-Noble Metal Catalyst for Hydrogen and Oxygen Recombination in Nickel–Iron Battery. *Ionics* **2019**, *25* (8), 3749–3759. <https://doi.org/10.1007/s11581-019-02907-8>.
- (91) Rodella, C. B.; Barrett, D. H.; Moya, S. F.; Figueroa, S. J. A.; Pimenta, M. T. B.; Curvelo, A. A. S.; Silva, V. T. da. Physical and Chemical Studies of Tungsten Carbide Catalysts: Effects of Ni Promotion and Sulphonated Carbon. *RSC Adv.* **2015**, *5* (30), 23874–23885. <https://doi.org/10.1039/C5RA03252K>.
- (92) Hoier, P. Effect of Carbon Sources and Carbonaceous Atmospheres on the Effective Synthesis of Nanostructured Tungsten Carbide Powders, 2014.
- (93) Islam, M.; Martinez-Duarte, R. A Sustainable Approach for Tungsten Carbide Synthesis Using Renewable Biopolymers. *Ceram. Int.* **2017**, *43* (13), 10546–10553. <https://doi.org/10.1016/j.ceramint.2017.05.118>.
- (94) Giordano, C.; Erpen, C.; Yao, W.; Antonietti, M. Synthesis of Mo and W Carbide and Nitride Nanoparticles via a Simple “Urea Glass” Route. *Nano Lett.* **2008**, *8* (12), 4659–4663. <https://doi.org/10.1021/nl8018593>.
- (95) Vijayakumar, P.; Senthil Pandian, M.; Lim, S. P.; Pandikumar, A.; Huang, N. M.; Mukhopadhyay, S.; Ramasamy, P. Facile Synthesis of Tungsten Carbide Nanorods and Its Application as Counter Electrode in Dye Sensitized Solar Cells. *Mater. Sci. Semicond. Process.* **2015**, *39*, 292–299. <https://doi.org/10.1016/j.mssp.2015.05.023>.

- (96) Li, Y.; Zhang, R.; Du, L.; Zhang, Q.; Wang, W. Catalytic Mechanism of C–F Bond Cleavage: Insights from QM/MM Analysis of Fluoroacetate Dehalogenase. *Catal. Sci. Technol.* **2016**, *6* (1), 73–80. <https://doi.org/10.1039/C5CY00777A>.
- (97) Zhu, J.; Sakaushi, K.; Clavel, G.; Shalom, M.; Antonietti, M.; Fellingner, T.-P. A General Salt-Templating Method To Fabricate Vertically Aligned Graphitic Carbon Nanosheets and Their Metal Carbide Hybrids for Superior Lithium Ion Batteries and Water Splitting. *J. Am. Chem. Soc.* **2015**, *137* (16), 5480–5485. <https://doi.org/10.1021/jacs.5b01072>.
- (98) Ren, H.; Chen, Y.; Huang, Y.; Deng, W.; Vlachos, D. G.; Chen, J. G. Tungsten Carbides as Selective Deoxygenation Catalysts: Experimental and Computational Studies of Converting C3 Oxygenates to Propene. *Green Chem* **2014**, *16* (2), 761–769. <https://doi.org/10.1039/C3GC41256C>.
- (99) d'Arbigny, J. B.; Taillades, G.; Marrony, M.; Jones, D. J.; Rozière, J. Hollow Microspheres with a Tungsten Carbide Kernel for PEMFC Application. *Chem. Commun.* **2011**, *47* (28), 7950. <https://doi.org/10.1039/c1cc11422k>.
- (100) Han, L.; Xu, M.; Han, Y.; Yu, Y.; Dong, S. Core-Shell-Structured Tungsten Carbide Encapsulated within Nitrogen-Doped Carbon Spheres for Enhanced Hydrogen Evolution. *ChemSusChem* **2016**, *9* (19), 2784–2787. <https://doi.org/10.1002/cssc.201601039>.
- (101) Ganesan, R.; Lee, J. S. Tungsten Carbide Microspheres as a Noble-Metal-Economic Electrocatalyst for Methanol Oxidation. *Angew. Chem. Int. Ed.* **2005**, *44* (40), 6557–6560. <https://doi.org/10.1002/anie.200501272>.
- (102) Ham, D.; Ganesan, R.; Lee, J. Tungsten Carbide Microsphere as an Electrode for Cathodic Hydrogen Evolution from Water. *Int. J. Hydrog. Energy* **2008**, *33* (23), 6865–6872. <https://doi.org/10.1016/j.ijhydene.2008.05.045>.
- (103) Fang, H.; Du, J.; Tian, C.; Zheng, J.; Duan, X.; Ye, L.; Yuan, Y. Regioselective Hydrogenolysis of Aryl Ether C–O Bonds by Tungsten Carbides with Controlled Phase Compositions. *Chem. Commun.* **2017**, *53* (74), 10295–10298. <https://doi.org/10.1039/C7CC05487D>.
- (104) McNamara, N. D.; Kim, J.; Hicks, J. C. Controlling the Pyrolysis Conditions of Microporous/Mesoporous MIL-125 To Synthesize Porous, Carbon-Supported Ti Catalysts with Targeted Ti Phases for the Oxidation of Dibenzothiophene. *Energy Fuels* **2016**, *30* (1), 594–602. <https://doi.org/10.1021/acs.energyfuels.5b01946>.
- (105) Kim, J.; McNamara, N. D.; Her, T. H.; Hicks, J. C. Carbothermal Reduction of Ti-Modified IRMOF-3: An Adaptable Synthetic Method to Support Catalytic Nanoparticles on Carbon. *ACS Appl. Mater. Interfaces* **2013**, *5* (21), 11479–11487. <https://doi.org/10.1021/am404089v>.
- (106) Xu, Y.-T.; Xiao, X.; Ye, Z.-M.; Zhao, S.; Shen, R.; He, C.-T.; Zhang, J.-P.; Li, Y.; Chen, X.-M. Cage-Confinement Pyrolysis Route to Ultrasmall Tungsten Carbide Nanoparticles for Efficient Electrocatalytic Hydrogen Evolution. *J. Am. Chem. Soc.* **2017**, *139* (15), 5285–5288. <https://doi.org/10.1021/jacs.7b00165>.
- (107) Yang, Y.; Zhang, W.; Yang, F.; Brown, D. E.; Ren, Y.; Lee, S.; Zeng, D.; Gao, Q.; Zhang, X. Versatile Nickel–Tungsten Bimetallics/Carbon Nanofiber Catalysts for Direct Conversion of Cellulose to Ethylene Glycol. *Green Chem.* **2016**, *18* (14), 3949–3955. <https://doi.org/10.1039/C6GC00703A>.
- (108) Jiang, B.; Sun, H.; Yuan, T.; He, W.; Zheng, C.; Zhang, H.-J.; Yang, J.; Zheng, S. Framework-Derived Tungsten Single-Atom Catalyst for Oxygen Reduction Reaction. *Energy Fuels* **2021**, *35* (9), 8173–8180. <https://doi.org/10.1021/acs.energyfuels.1c00758>.

- (109) Chen, W.; Pei, J.; He, C.-T.; Wan, J.; Ren, H.; Wang, Y.; Dong, J.; Wu, K.; Cheong, W.-C.; Mao, J.; Zheng, X.; Yan, W.; Zhuang, Z.; Chen, C.; Peng, Q.; Wang, D.; Li, Y. Single Tungsten Atoms Supported on MOF-Derived N-Doped Carbon for Robust Electrochemical Hydrogen Evolution. *Adv. Mater.* **2018**, *30* (30), 1800396. <https://doi.org/10.1002/adma.201800396>.
- (110) Kim, J.; Neumann, G. T.; McNamara, N. D.; Hicks, J. C. Exceptional Control of Carbon-Supported Transition Metal Nanoparticles Using Metal-Organic Frameworks. *J. Mater. Chem. A* **2014**, *2* (34), 14014. <https://doi.org/10.1039/C4TA03050H>.
- (111) Claridge, J. B.; York, A. P. E.; Brungs, A. J.; Green, M. L. H. Study of the Temperature-Programmed Reaction Synthesis of Early Transition Metal Carbide and Nitride Catalyst Materials from Oxide Precursors. *Chem. Mater.* **2000**, *12* (1), 132–142. <https://doi.org/10.1021/cm9911060>.
- (112) Ma, C.; Brandon, N.; Li, G. Preparation and Formation Mechanism of Hollow Microspherical Tungsten Carbide with Mesoporosity. *J. Phys. Chem. C* **2007**, *111* (26), 9504–9508. <https://doi.org/10.1021/jp072378q>.
- (113) Lu, Q.; Chen, C.-J.; Luc, W.; Chen, J. G.; Bhan, A.; Jiao, F. Ordered Mesoporous Metal Carbides with Enhanced Anisole Hydrodeoxygenation Selectivity. *ACS Catal.* **2016**, *6* (6), 3506–3514. <https://doi.org/10.1021/acscatal.6b00303>.
- (114) Al Alwan, B.; Sari, E.; Salley, S. O.; Ng, K. Y. S. Effect of Metal Ratio and Preparation Method on Nickel–Tungsten Carbide Catalyst for Hydrocracking of Distillers Dried Grains with Solubles Corn Oil. *Ind. Eng. Chem. Res.* **2014**, *53* (17), 6923–6933. <https://doi.org/10.1021/ie500241b>.
- (115) Li, S. Highly Stable Activity of Cobalt Based Catalysts with Tungsten Carbide-Activated Carbon Support for Dry Reforming of Methane: Role of Tungsten Carbide. **2022**, 11.
- (116) Venkatesan, K.; He, S.; Seshan, K.; Selvam, P.; Vinu, R. Selective Production of Aromatic Hydrocarbons from Lignocellulosic Biomass via Catalytic Fast-Hydrolysis Using W<sub>2</sub>C/γ-Al<sub>2</sub>O<sub>3</sub>. *Catal. Commun.* **2018**, *110*, 68–73. <https://doi.org/10.1016/j.catcom.2018.03.011>.
- (117) Deng, J.; Li, M.; Wang, Y. Biomass-Derived Carbon: Synthesis and Applications in Energy Storage and Conversion. *Green Chem.* **2016**, *18* (18), 4824–4854. <https://doi.org/10.1039/C6GC01172A>.
- (118) Gao, Z.; Zhang, Y.; Song, N.; Li, X. Biomass-Derived Renewable Carbon Materials for Electrochemical Energy Storage. *Mater. Res. Lett.* **2017**, *5* (2), 69–88. <https://doi.org/10.1080/21663831.2016.1250834>.
- (119) Hu, B.; Wang, K.; Wu, L.; Yu, S.-H.; Antonietti, M.; Titirici, M.-M. Engineering Carbon Materials from the Hydrothermal Carbonization Process of Biomass. *Adv. Mater.* **2010**, *22* (7), 813–828. <https://doi.org/10.1002/adma.200902812>.
- (120) Inagaki, M.; Toyoda, M.; Soneda, Y.; Morishita, T. Nitrogen-Doped Carbon Materials. *Carbon* **2018**, *132*, 104–140. <https://doi.org/10.1016/j.carbon.2018.02.024>.
- (121) Antolini, E. Nitrogen-Doped Carbons by Sustainable N- and C-Containing Natural Resources as Nonprecious Catalysts and Catalyst Supports for Low Temperature Fuel Cells. *Renew. Sustain. Energy Rev.* **2016**, *58*, 34–51. <https://doi.org/10.1016/j.rser.2015.12.330>.
- (122) Zhang, Y.; Jiang, W.-J.; Zhang, X.; Guo, L.; Hu, J.-S.; Wei, Z.; Wan, L.-J. Engineering Self-Assembled N-Doped Graphene–Carbon Nanotube Composites towards Efficient

- Oxygen Reduction Electrocatalysts. *Phys Chem Chem Phys* **2014**, *16* (27), 13605–13609. <https://doi.org/10.1039/C4CP00757C>.
- (123) Zhou, Y.; Neyerlin, K.; Olson, T. S.; Pylypenko, S.; Bult, J.; Dinh, H. N.; Gennett, T.; Shao, Z.; O’Hayre, R. Enhancement of Pt and Pt-Alloy Fuel Cell Catalyst Activity and Durability via Nitrogen-Modified Carbon Supports. *Energy Environ. Sci.* **2010**, *3* (10), 1437. <https://doi.org/10.1039/c003710a>.
- (124) Ilnicka, A.; Lukaszewicz, J. Marine and Freshwater Feedstocks as a Precursor for Nitrogen-Containing Carbons: A Review. *Mar. Drugs* **2018**, *16* (5), 142. <https://doi.org/10.3390/md16050142>.
- (125) Yaman, S. Pyrolysis of Biomass to Produce Fuels and Chemical Feedstocks. *Energy Convers. Manag.* **2004**, *45* (5), 651–671. [https://doi.org/10.1016/S0196-8904\(03\)00177-8](https://doi.org/10.1016/S0196-8904(03)00177-8).
- (126) Jayakumar, R.; Menon, D.; Manzoor, K.; Nair, S. V.; Tamura, H. Biomedical Applications of Chitin and Chitosan Based Nanomaterials—A Short Review. *Carbohydr. Polym.* **2010**, *82* (2), 227–232. <https://doi.org/10.1016/j.carbpol.2010.04.074>.
- (127) El Kadib, A.; Bousmina, M. Chitosan Bio-Based Organic–Inorganic Hybrid Aerogel Microspheres. *Chem. – Eur. J.* **2012**, *18* (27), 8264–8277. <https://doi.org/10.1002/chem.201104006>.
- (128) El Kadib, A. Green and Functional Aerogels by Macromolecular and Textural Engineering of Chitosan Microspheres. *Chem. Rec.* **2020**, *20* (8), 753–772. <https://doi.org/10.1002/tcr.201900089>.
- (129) Sevilla, M.; Fuertes, A. B. Chemical and Structural Properties of Carbonaceous Products Obtained by Hydrothermal Carbonization of Saccharides. *Chem. - Eur. J.* **2009**, *15* (16), 4195–4203. <https://doi.org/10.1002/chem.200802097>.
- (130) Wang, Q.; Li, H.; Chen, L.; Huang, X. Monodispersed Hard Carbon Spherules with Uniform Nanopores. *Carbon* **2001**, *39* (14), 2211–2214. [https://doi.org/10.1016/S0008-6223\(01\)00040-9](https://doi.org/10.1016/S0008-6223(01)00040-9).
- (131) Ba, Y.; Pan, W.; Pi, S.; Zhao, Y.; Mi, L. Nitrogen-Doped Hierarchical Porous Carbon Derived from a Chitosan/Polyethylene Glycol Blend for High Performance Supercapacitors. *RSC Adv.* **2018**, *8* (13), 7072–7079. <https://doi.org/10.1039/C8RA00016F>.
- (132) Jordan, T.; Yu, Z.-L.; Yu, S.-H.; Antonietti, M.; Fechler, N. Porous Nitrogen-Doped Carbon Monoliths Derived from Biopolymer-Structured Liquid Precursors. *Microporous Mesoporous Mater.* **2018**, *255*, 53–60. <https://doi.org/10.1016/j.micromeso.2017.07.032>.
- (133) Shen, F.; Su, J.; Zhang, X.; Zhang, K.; Qi, X. Chitosan-Derived Carbonaceous Material for Highly Efficient Adsorption of Chromium (VI) from Aqueous Solution. *Int. J. Biol. Macromol.* **2016**, *91*, 443–449. <https://doi.org/10.1016/j.ijbiomac.2016.05.103>.
- (134) Jin, Q.; Li, Y.; Yang, D.; Cui, J. Chitosan-Derived Three-Dimensional Porous Carbon for Fast Removal of Methylene Blue from Wastewater. *RSC Adv.* **2018**, *8* (3), 1255–1264. <https://doi.org/10.1039/C7RA11770A>.
- (135) Liu, Y.; Xu, W.; Wang, G.; Qin, X. Material Basis Research for Huangqi Jianzhong Tang against Chronic Atrophic Gastritis Rats through Integration of Urinary Metabonomics and SystemsDock. *J. Ethnopharmacol.* **2018**, *223*, 1–9. <https://doi.org/10.1016/j.jep.2018.05.015>.
- (136) Marrakchi, F.; Ahmed, M. J.; Khanday, W. A.; Asif, M.; Hameed, B. H. Mesoporous-Activated Carbon Prepared from Chitosan Flakes via Single-Step Sodium Hydroxide

- Activation for the Adsorption of Methylene Blue. *Int. J. Biol. Macromol.* **2017**, *98*, 233–239. <https://doi.org/10.1016/j.ijbiomac.2017.01.119>.
- (137) Zuo, X.; Chang, K.; Zhao, J.; Xie, Z.; Tang, H.; Li, B.; Chang, Z. Bubble-Template-Assisted Synthesis of Hollow Fullerene-like MoS<sub>2</sub> Nanocages as a Lithium Ion Battery Anode Material. *J. Mater. Chem. A* **2016**, *4* (1), 51–58. <https://doi.org/10.1039/C5TA06869J>.
- (138) Hao, P.; Zhao, Z.; Leng, Y.; Tian, J.; Sang, Y.; Boughton, R. I.; Wong, C. P.; Liu, H.; Yang, B. Graphene-Based Nitrogen Self-Doped Hierarchical Porous Carbon Aerogels Derived from Chitosan for High Performance Supercapacitors. *Nano Energy* **2015**, *15*, 9–23. <https://doi.org/10.1016/j.nanoen.2015.02.035>.
- (139) Xu, X.; Liu, J.; Zhang, Q.; Wang, H. A Facile Approach to Suppress the Sulfation in Lead Acid Batteries Using N-Doped Carbon Derived from Chitosan. *Mater. Lett.* **2019**, *247*, 29–31. <https://doi.org/10.1016/j.matlet.2019.03.055>.
- (140) Brahmi, Y.; Katir, N.; Ianchuk, M.; Collière, V.; Essassi, E. M.; Ouali, A.; Caminade, A.-M.; Bousmina, M.; Majoral, J. P.; El Kadib, A. Low Temperature Synthesis of Ordered Mesoporous Stable Anatase Nanocrystals: The Phosphorus Dendrimer Approach. *Nanoscale* **2013**, *5* (7), 2850. <https://doi.org/10.1039/c3nr00058c>.
- (141) Brahmi, Y.; Katir, N.; Agullo, J. A. M.; Primo, A.; Bousmina, M.; Pierre Majoral, J.; Garcia, H.; El Kadib, A. Organophosphonate Bridged Anatase Mesocrystals: Low Temperature Crystallization, Thermal Growth and Hydrogen Photo-Evolution. *Dalton Trans.* **2015**, *44* (35), 15544–15556. <https://doi.org/10.1039/C5DT02367J>.
- (142) Verma, S.; Nadagouda, M. N.; Varma, R. S. Porous Nitrogen-Enriched Carbonaceous Material from Marine Waste: Chitosan-Derived Carbon Nitride Catalyst for Aerial Oxidation of 5-Hydroxymethylfurfural (HMF) to 2,5-Furandicarboxylic Acid. *Sci. Rep.* **2017**, *7* (1), 13596. <https://doi.org/10.1038/s41598-017-14016-5>.
- (143) Behling, R.; Valange, S.; Chatel, G. Heterogeneous Catalytic Oxidation for Lignin Valorization into Valuable Chemicals: What Results? What Limitations? What Trends? *Green Chem.* **2016**, *18* (7), 1839–1854. <https://doi.org/10.1039/C5GC03061G>.
- (144) Sun, Z.; Zhang, Z.-H.; Yuan, T.-Q.; Ren, X.; Rong, Z. Raney Ni as a Versatile Catalyst for Biomass Conversion. *ACS Catal.* **2021**, *11* (16), 10508–10536. <https://doi.org/10.1021/acscatal.1c02433>.
- (145) Fabičovicová, K.; Malter, O.; Lucas, M.; Claus, P. Hydrogenolysis of Cellulose to Valuable Chemicals over Activated Carbon Supported Mono- and Bimetallic Nickel/Tungsten Catalysts. *Green Chem* **2014**, *16* (7), 3580–3588. <https://doi.org/10.1039/C4GC00664J>.
- (146) Zheng, M.; Pang, J.; Sun, R.; Wang, A.; Zhang, T. Selectivity Control for Cellulose to Diols: Dancing on Eggs. *ACS Catal.* **2017**, *7* (3), 1939–1954. <https://doi.org/10.1021/acscatal.6b03469>.
- (147) Tai, Z.; Zhang, J.; Wang, A.; Zheng, M.; Zhang, T. Temperature-Controlled Phase-Transfer Catalysis for Ethylene Glycol Production from Cellulose. *Chem. Commun.* **2012**, *48* (56), 7052. <https://doi.org/10.1039/c2cc32305b>.
- (148) Liu, Y.; Luo, C.; Liu, H. Tungsten Trioxide Promoted Selective Conversion of Cellulose into Propylene Glycol and Ethylene Glycol on a Ruthenium Catalyst. *Angew. Chem. Int. Ed.* **2012**, *51* (13), 3249–3253. <https://doi.org/10.1002/anie.201200351>.



- (149) Sun, R.; Wang, T.; Zheng, M.; Deng, W.; Pang, J.; Wang, A.; Wang, X.; Zhang, T. Versatile Nickel–Lanthanum(III) Catalyst for Direct Conversion of Cellulose to Glycols. *ACS Catal.* **2015**, *5* (2), 874–883. <https://doi.org/10.1021/cs501372m>.
- (150) Xiao, Z.; Wang, X.; Yang, Q.; Xing, C.; Ge, Q.; Gai, X.; Mao, J.; Ji, J. Fabrication of Immobilized Nickel Nanoclusters Decorated by C N Species for Cellulose Conversion to C<sub>2,3</sub> Oxygenated Compounds: Rational Design via Typical C- and N-Sources. *J. Energy Chem.* **2020**, *50*, 25–36. <https://doi.org/10.1016/j.jechem.2020.02.054>.
- (151) Fabičovicová, K.; Lucas, M.; Claus, P. From Microcrystalline Cellulose to Hard- and Softwood-Based Feedstocks: Their Hydrogenolysis to Polyols over a Highly Efficient Ruthenium–Tungsten Catalyst. *Green Chem.* **2015**, *17* (5), 3075–3083. <https://doi.org/10.1039/C5GC00421G>.
- (152) Leal, G. F.; Moya, S. F.; Meira, D. M.; Barrett, D. H.; Teixeira-Neto, E.; Curvelo, A. A. S.; Teixeira Da Silva, V.; Rodella, C. B. Promotion Effects of Pd on Tungsten Carbide Catalysts: Physicochemical Properties and Cellulose Conversion Performance. *RSC Adv.* **2016**, *6* (90), 87756–87766. <https://doi.org/10.1039/C6RA15819F>.
- (153) Li, C.; Zheng, M.; Wang, A.; Zhang, T. One-Pot Catalytic Hydrocracking of Raw Woody Biomass into Chemicals over Supported Carbide Catalysts: Simultaneous Conversion of Cellulose, Hemicellulose and Lignin. *Energy Env. Sci* **2012**, *5* (4), 6383–6390. <https://doi.org/10.1039/C1EE02684D>.
- (154) Pan, G.-Y.; Ma, Y.-L.; Ma, X.-X.; Sun, Y.-G.; Lv, J.-M.; Zhang, J.-L. Catalytic Hydrogenation of Corn Stalk into Polyol over Ni–W/MCM-41 Catalyst. *Chem. Eng. J.* **2016**, *299*, 386–392. <https://doi.org/10.1016/j.cej.2016.04.074>.
- (155) Li, X.; Guo, T.; Xia, Q.; Liu, X.; Wang, Y. One-Pot Catalytic Transformation of Lignocellulosic Biomass into Alkylcyclohexanes and Polyols. *ACS Sustain. Chem. Eng.* **2018**, *6* (3), 4390–4399. <https://doi.org/10.1021/acssuschemeng.8b00012>.
- (156) Pang, J.; Zheng, M.; Wang, A.; Zhang, T. Catalytic Hydrogenation of Corn Stalk to Ethylene Glycol and 1,2-Propylene Glycol. *Ind. Eng. Chem. Res.* **2011**, *50* (11), 6601–6608. <https://doi.org/10.1021/ie102505y>.
- (157) Pang, J.; Zheng, M.; Li, X.; Sebastian, J.; Jiang, Y.; Zhao, Y.; Wang, A.; Zhang, T. Unlock the Compact Structure of Lignocellulosic Biomass by Mild Ball Milling for Ethylene Glycol Production. *ACS Sustain. Chem. Eng.* **2019**, *7* (1), 679–687. <https://doi.org/10.1021/acssuschemeng.8b04262>.
- (158) Pang, J.; Zheng, M.; Wang, A.; Sun, R.; Wang, H.; Jiang, Y.; Zhang, T. Catalytic Conversion of Concentrated Miscanthus in Water for Ethylene Glycol Production. *AIChE J.* **2014**, *60* (6), 2254–2262. <https://doi.org/10.1002/aic.14406>.
- (159) Fabičovicová, K.; Lucas, M.; Claus, P. From Barley Straw to Valuable Polyols: A Sustainable Process Using Ethanol/Water Mixtures and Hydrogenolysis over Ruthenium–Tungsten Catalyst. *ChemSusChem* **2016**, *9* (19), 2804–2815. <https://doi.org/10.1002/cssc.201600695>.
- (160) Xiao, Z.; Zhang, Q.; Wang, X.; Ge, Q.; Gai, X.; Mao, J.; Ji, J. Organic Nitrogen Promotes Stability of Metallic Catalysts in Conversion of Bamboo Pulp to Low Carbon Polyols. *J. Fuel Chem. Technol.* **2019**, *47* (6), 675–687. [https://doi.org/10.1016/S1872-5813\(19\)30029-5](https://doi.org/10.1016/S1872-5813(19)30029-5).
- (161) Wu, M.; Lin, X.; Hagfeldt, A.; Ma, T. Low-Cost Molybdenum Carbide and Tungsten Carbide Counter Electrodes for Dye-Sensitized Solar Cells. *Angew. Chem. Int. Ed.* **2011**, *50* (15), 3520–3524. <https://doi.org/10.1002/anie.201006635>.

- (162) Delannoy, L.; Giraudon, J.-M.; Granger, P.; Leclercq, L.; Leclercq, G. Group VI Transition Metal Carbides as Alternatives in the Hydrodechlorination of Chlorofluorocarbons. *Catal. Today* **2000**, *59* (3–4), 231–240.  
[https://doi.org/10.1016/S0920-5861\(00\)00289-3](https://doi.org/10.1016/S0920-5861(00)00289-3).

# Chapter 2: Materials and methods

## 2.1. Preparation of catalysts

### 2.1.1. Starting Materials

All chemicals needed for the preparation of the catalysts mentioned in the manuscript were used without further purification: alginic acid sodium salt (sodium alginate, Sigma Aldrich), chitosan (degree of deacetylation  $\geq 95\%$ , high molecular weight, Sigma Aldrich), ammonium (meta) tungstate hydrate  $((\text{NH}_4)_6\text{H}_2\text{W}_{12}\text{O}_{40}\cdot x\text{H}_2\text{O}$ , Alfa Aesar), Nickel (II) nitrate hexahydrate  $(\text{Ni}(\text{NO}_3)_2\cdot 6\text{H}_2\text{O}$  99%, Alfa Aesar), acetic acid (99-100%, VWR chemicals), melamine (99%, Sigma Aldrich), sodium tungstate dihydrate  $(\text{Na}_2\text{WO}_4\cdot 2\text{H}_2\text{O}$   $\geq 99\%$ , Alfa Aesar), tungsten hexacarbonyl  $(\text{W}(\text{CO})_6$  99%, Alfa Aesar), 2,6-naphthalene dicarboxylic acid ( $\text{H}_2\text{NDC}$ ,  $\text{C}_{10}\text{H}_6(\text{CO}_2\text{H})_2$  99%, Alfa Aesar), 1,4-diazabicyclo[2.2.2]octane (dabco,  $\text{N}_2(\text{C}_2\text{H}_4)_3$   $\geq 99\%$ , Alfa Aesar), N,N-dimethylformamide (DMF,  $(\text{CH}_3)_2\text{NCOH}$  99.8%, Alfa Aesar), L3S activated carbon (Acticarbone/Chemviron), Ruthenium(III) nitrosyl nitrate  $(\text{Ru}(\text{NO})(\text{NO}_3)_3$  31%, Alfa Aesar); ammonia aqueous solution ( $\text{NH}_3$  28-30 wt%, Sigma Aldrich), acetol ( $\text{C}_3\text{H}_6\text{O}_2$  90%, Sigma Aldrich), alaninol ( $\text{C}_3\text{H}_9\text{NO}$  96%, Sigma Aldrich), amino-2-propanol ( $\text{C}_3\text{H}_9\text{NO}$  93%, Sigma Aldrich), 1,2-diaminopropane ( $\text{C}_3\text{H}_{10}\text{N}_2$  99%, Sigma Aldrich), ethylene glycol ( $\text{C}_2\text{H}_6\text{O}_2$ , 99.8%, Sigma Aldrich), 1,2-propylene glycol ( $\text{C}_3\text{H}_8\text{O}_2$  99.5%, Sigma Aldrich), glucose ( $\text{C}_6\text{H}_{12}\text{O}_6$  96%, Sigma Aldrich), fructose ( $\text{C}_6\text{H}_{12}\text{O}_6$  99%, Sigma Aldrich) and Sigmacell cellulose  $((\text{C}_6\text{H}_{12}\text{O}_5)_n$ , Sigma Aldrich).

### 2.1.2. N-doped carbon-based materials

#### 2.1.2.1. Hydrothermal synthesis of carbon materials

Carbon-based materials were synthesized following a hydrothermal conversion (HTC) approach<sup>1</sup>. For nitrogen-doped carbons, 0.4 g of chitosan was dissolved in 64 mL of a 1 wt.% acetic acid solution and stirred overnight. The obtained viscous solution was transferred to a 170 mL PTFE-lined autoclave which was placed for 24 h in an oven at 180 °C. The obtained solid products were collected by filtration and washed until the solution was clear, prior to be dried overnight at 80 °C. Finally, pyrolysis was conducted in a horizontal furnace heated to a temperature of 700 °C ( $5\text{ }^\circ\text{C}\cdot\text{min}^{-1}$ ) for 1 h under a nitrogen flow of  $100\text{ mL}\cdot\text{min}^{-1}$ . The total process yield reached about 15 wt.% and the sample was labelled [NC].

Nitrogen-enriched carbons, labelled [M+NC], were produced by the addition of 0.08 g of melamine to the initial solution. Finally, pure carbons, labelled [C], were produced similarly by replacing chitosan with 2.1 g of sodium alginate. For catalytic tests, the hydrothermal synthesis process was scaled-up using an 8 L autoclave, all quantities were multiplied by a factor of 47. No noticeable effect on the carbonaceous mass yield was detected for the process scale-up.

### 2.1.2.2. Wet impregnation and metal activation procedures

A solution of 7 g.L<sup>-1</sup> of ammonium (meta) tungstate hydrate was prepared by dissolving 1.22 g of precursor in 174 mL of water under sonication (1 h, 45 °C). In a 250 mL flask were added 2 g of carbon support ([NC], or [M+NC], or [C]), 0.32 g of nickel (II) nitrate, and the W solution previously prepared<sup>2</sup>. The solution was stirred at room temperature for 2 hours and then evaporated at 60 °C under 72 mbar residual pressure. The solid was then dried in an oven at 80 °C overnight. The material was activated under a flow of N<sub>2</sub> or H<sub>2</sub> of 100 mL.min<sup>-1</sup> (10 °C.min<sup>-1</sup> from RT to 450 °C, then 1 °C.min<sup>-1</sup> from 450 °C to 700 °C) with a final dwell time of 1 h at 700 °C. The sample was finally passivated under a flow of 1% O<sub>2</sub> / N<sub>2</sub> (100 mL.min<sup>-1</sup>) at ambient temperature for 6 h. The targeted metal loadings were 5 wt% of nickel and 30 wt% of tungsten. The following nomenclature was adopted in the manuscript (Chapter 3): NiW-[name of the support]-treatment atmosphere. "-AR" was added at the end to indicate post-reaction samples.

**Table 1.** Main characteristics of the sample prepared for cellulose conversion into glycols

Carbon sample name	NiW sample name	Precursors	Carbon sample main characteristics
[C]	NiW-[C]	Alginate	Pure carbon
[NC]	NiW-[NC]	Chitosan	Carbon with 5% N
[M+NC]	NiW-[M+NC]	Chitosan, Melamine	Carbon enriched in carbon, up to 7% N

### **2.1.3. DUT-8(Ni) derived carbon materials**

#### 2.1.3.1. DUT-8(Ni) synthesis

The synthesis of DUT-8(Ni) was adapted from the literature<sup>3</sup>. The chemicals were dissolved as follows: Ni(NO<sub>3</sub>)<sub>2</sub>·6H<sub>2</sub>O (4.428 g) in 160 mL DMF, H<sub>2</sub>NDC (3.136 g) and dabco (3.584 g) in 160

mL DMF. Subsequently, the ligand solution was transferred into the metal solution, and the resultant mixture was stirred at 350 rpm for one hour before being transferred into a polytetrafluoroethylene-lined (PTFE) closed flask (500 mL) and heated at 140 °C for 24 h. After cooling down to room temperature, the sample was washed three times with DMF with centrifugation at the end of each cycle. The resulting solid was dried overnight at 80 °C (nickel theoretical loading = 17.8 wt%).

#### 2.1.3.2. Tungsten deposition on DUT-8(Ni)

Two synthesis routes were followed; a liquid-mediated synthesis and a chemical vapor deposition route.  $x$  ( $n_W/n_{Ni}$ ) was calculated on the basis of the W precursor masses introduced in the DUT-8(Ni) hybrid material synthesis, except for  $W(CO)_6$  in the chemical vapor deposition route where the  $W(CO)_6$  consumed mass was used for the calculation.

##### 2.1.3.2.1. Liquid-mediated incorporation

Two tungsten precursors have been considered,  $Na_2WO_4 \cdot H_2O$ , and  $W(CO)_6$ . The  $n_W/n_{Ni}$  ratio was set to be 0.3. The corresponding amount of precursor was added to the ligand solution and the mixture was stirred at 350 rpm for one hour before being transferred into a PTFE-lined autoclave (500 mL) and heated at 140 °C for 24 h. After cooling down to room temperature, the sample was washed three times with DMF with centrifugation at the end of each cycle. The resulting solid was dried overnight at 80 °C. The following nomenclature was adopted for the resulting materials: DUT-8(Ni)-WNaO-l, and DUT-8(Ni)-WCO-l was prepared using  $W(CO)_6$ .

##### 2.1.3.2.2. Chemical vapor deposition route

Here  $W(CO)_6$  was used as precursor. The  $n_W/n_{Ni}$  ratio was set to be 0.21. DUT-8(Ni) (1.125 g) was placed in a 5 mL glass vial. This vial was introduced in a glass bottle containing the corresponding amount of  $W(CO)_6$ . The bottle was sealed and then heated at 85 °C for 24 hours. The following nomenclature was adopted for the resulting material: DUT-8(Ni)-WCO-v.

##### 2.1.3.3. DUT-8(Ni) derived materials pyrolysis

The obtained materials were activated, in an oven schematized in Figure 1, under a flow of  $N_2$  or  $H_2$  of  $100 \text{ mL} \cdot \text{min}^{-1}$  applying a temperature increase rate of  $10 \text{ }^\circ\text{C} \cdot \text{min}^{-1}$  (from RT to 450 °C), then  $1 \text{ }^\circ\text{C} \cdot \text{min}^{-1}$  (from 450 °C to 700 °C) with a final dwelling time of 1 h at 700 °C. The samples were finally passivated under a flow of 1%  $O_2 / N_2$  of  $60 \text{ mL} \cdot \text{min}^{-1}$  at ambient temperature for 6 h. Table

2 summarizes the samples prepared for the study. The following nomenclature was adopted in the manuscript (Chapter 4):

- For the liquid-mediated route materials: NiWNaO-I-H<sub>2</sub>; NiWNaO-I-N<sub>2</sub>; NiWCO-I-H<sub>2</sub> and NiWCO-I-N<sub>2</sub> depending on the activation atmosphere.
- For the chemical vapor deposition route materials: NiWCO-v-H<sub>2</sub>; NiWCO-v-N<sub>2</sub> depending on the activation atmosphere.
- When "-AR" was added to the sample name, it refers to post-reaction samples.

**Table 2.** Main characteristics of the prepared samples.

Sample name (W@DUT-8 materials)	Sample name (pyrolyzed materials)	Tungsten precursor	Pyrolysis atmosphere
DUT-8(Ni)	-	-	-
DUT-8(Ni)-WNaO-I	NiWNaO-I-N <sub>2</sub>	Na <sub>2</sub> WO <sub>4</sub> ·2H <sub>2</sub> O	N <sub>2</sub>
	NiWNaO-I-H <sub>2</sub>	Na <sub>2</sub> WO <sub>4</sub> ·2H <sub>2</sub> O	H <sub>2</sub>
DUT-8(Ni)-WCO-I	NiWCO-I-N <sub>2</sub>	W(CO) <sub>6</sub>	N <sub>2</sub>
	NiWCO-I-H <sub>2</sub>	W(CO) <sub>6</sub>	H <sub>2</sub>
DUT-8(Ni)-WCO-v	NiWCO-v-N <sub>2</sub>	W(CO) <sub>6</sub>	N <sub>2</sub>
	NiWCO-v-H <sub>2</sub>	W(CO) <sub>6</sub>	H <sub>2</sub>

#### 2.1.4. Synthesis of Ruthenium based materials

The nomenclature in Table 3 was adopted in the manuscript (Chapter 5).

##### 2.1.4.1. Synthesis of x%Ru-y%Ni/AC

Under N<sub>2</sub> atmosphere, 2 g of AC were introduced in a 80 mL water solution of Ru(NO)(NO<sub>3</sub>)<sub>3</sub> and Ni(NO<sub>3</sub>)<sub>2</sub>·6H<sub>2</sub>O in a round-bottom flask. The mixture was stirred at room temperature for 4 h. After water evaporation (60 °C, 200 mbar), the solid was dried at 80 °C overnight. The dry solid (2.3 g) was introduced in a quartz tubular reactor (Figure 1) for reduction under H<sub>2</sub> flow (100 mL.min<sup>-1</sup>, 2 °C.min<sup>-1</sup>, 450 °C, 2 h). After cooling, the reactor was purged under Ar flow and the solid was passivated under O<sub>2</sub> (1 vol.%) in N<sub>2</sub> flow for 6 h. Table 3 indicated the amount of

precursor used to obtain the selected compositions, and the experimental compositions as measured by ICP. Catalyst labelling refers to the label used in the main text.

#### 2.1.4.2. Synthesis of 7.5%Ru-36%W<sub>2</sub>C/AC

A 70 mL aqueous solution of 0.66 g (NH<sub>4</sub>)<sub>10</sub>H<sub>2</sub>(W<sub>2</sub>O<sub>7</sub>)<sub>6</sub> was prepared under ultrasound at 45 °C for 1 h. The solution was introduced in a round-bottom flask containing 0.25 g Ru(NO)(NO<sub>3</sub>)<sub>3</sub> and 1 g of AC. The mixture was stirred at room temperature for 4 h. After water evaporation (60 °C, 200 mbar), the solid was dried at 80 °C overnight under N<sub>2</sub> atmosphere. The dry solid (3 g) was introduced into a quartz tubular reactor (Figure 1) for temperature-programmed carburization under H<sub>2</sub> flow (100 mL.min<sup>-1</sup>, 25-450 °C at 10 °C.min<sup>-1</sup>, 450-700 °C at 1 °C.min<sup>-1</sup>, 1 h). After cooling, the reactor was purged under Ar, and the solid surface was passivated under O<sub>2</sub> (1 vol.%) in N<sub>2</sub> flow for 6 h.

**Table 3.** Composition Activated Carbon (AC) supported Ru-based catalysts studied in this work.

Target composition (wt.% of metal)	Mass of Ru(NO)(NO <sub>3</sub> ) <sub>3</sub> (g) <sup>(a)</sup>	Mass of Ni(NO <sub>3</sub> ) <sub>2</sub> ·6H <sub>2</sub> O (g) <sup>(a)</sup>	Experimental Composition (wt.% of metal) <sup>(b)</sup>	Catalyst labelling
5%Ni	-	0.52	Ni: 5.6	5.5%Ni/AC
1%Ru	0.063	-	Ru: 1.2	1%Ru/AC
5%Ru	0.33	-	Ru: 5.3	5.3%Ru/AC
5%Ru-2.5%Ni	0.34	0.27	Ru: 4.5; Ni: 2.4	4.5%Ru-2.5%Ni/AC
5%Ru-5%Ni	0.35	0.55	Ru: 4.6; Ni: 4.4	4.5%Ru-4.5%Ni/AC
5%Ru-7.5%Ni	0.36	0.85	Ru: 5.3; Ni: 7.9	5.3%Ru-8%Ni/AC
1%Ru-5%Ni	0.067	0.53	Ru: 1.2; Ni: 5.1	1%Ru-5%Ni/AC
5%Ru-30%W <sub>2</sub> C	0.48	1.25 of (NH <sub>4</sub> ) <sub>10</sub> H <sub>2</sub> (W <sub>2</sub> O <sub>7</sub> ) <sub>6</sub>	Ru: 7.5; W: 36	7.5%Ru-36%W <sub>2</sub> C/AC

<sup>(a)</sup> For 2 g of AC. <sup>(b)</sup> determined by ICP-EOS, average of 2 sample analyses.

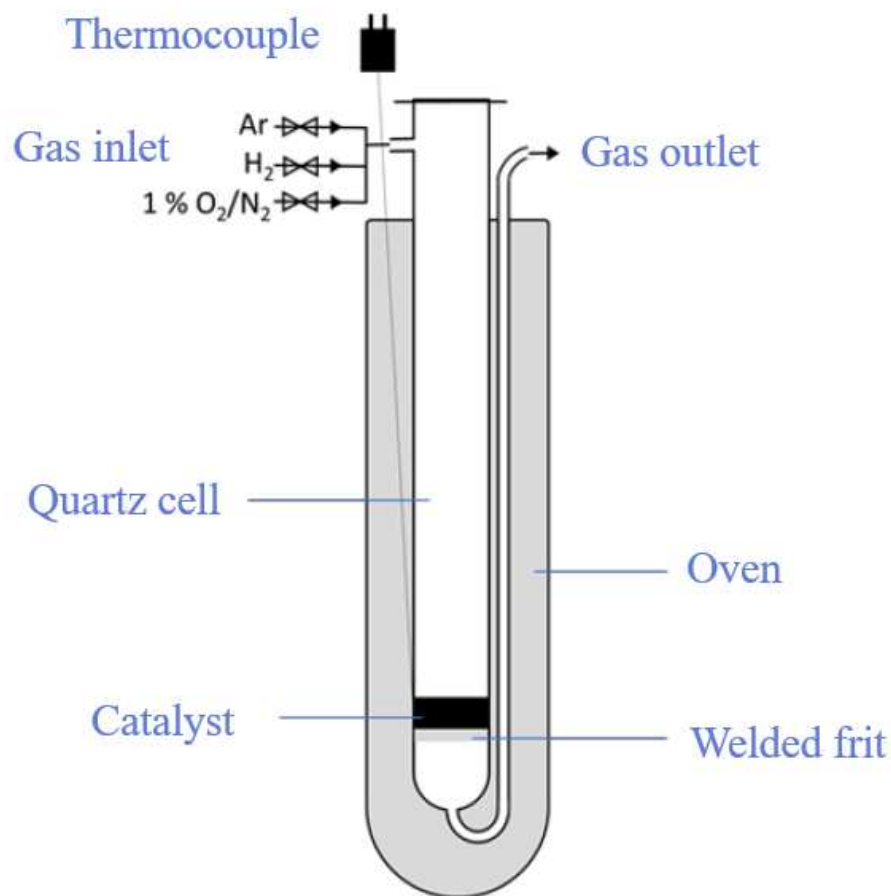


**Figure 1.** Experimental setup used for the reduction/carburation of catalysts.

## 2.2. Physico-chemical characterization of catalysts

### 2.2.1. Structural Properties

#### 2.2.1.1. X-Ray diffraction experiments

XRD reveals the crystalline structure of the material. Thus, several information can be obtained such as the identification and quantification of the main phases, the calculation of the average size of crystallites and lattice parameters. Within the X-ray source, the cathode, consisting of a filament, is heated to produce electrons which are accelerated by the application of a voltage and used to bombard the anode, a copper tube. When the electrons have sufficient energy to free the inner shell electrons of Cu, they produce characteristic Cu X-Rays, Cu K $\alpha$  lines, having an energy (E) of  $\sim 8.04$  keV and a wavelength ( $\lambda$ ) of  $1.54 \text{ \AA}$ . These X-rays are collimated and directed towards the sample.



X-Ray diffraction is based on the elastic scattering of X-Rays by atoms that compose a matter periodic lattice structure (Figure 2). Thus, constructive interference takes place once the scattered X-Ray photons become “in phase” which enables their detection afterwards<sup>4</sup>. By measuring the angle ( $\theta$ ) and the intensity of each diffracted beam it is possible to identify the crystallographic planes, according to Bragg's law:

$$n * \lambda = 2 * d * \sin\theta$$

$n$ : the diffraction order of the lines

$\lambda$ : the wavelength of the X – ray (Å)

$d$ : the interreticular distance (the space between 2 crystallographic planes in Å)

$\theta$ : the diffraction angle (rad)

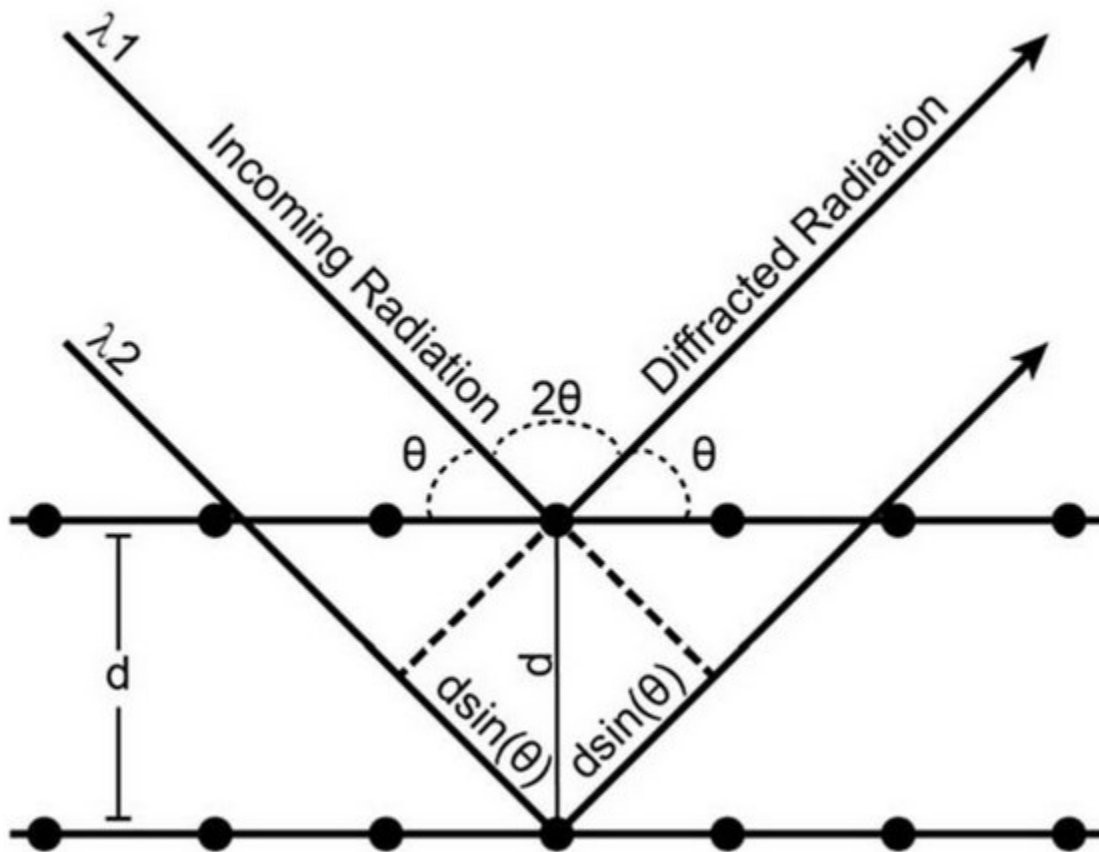


**Figure 2.** Schematic representation of X-Ray photons diffracted from a crystalline matter<sup>4</sup>.

The analyses were performed using a Bruker D8-Advance apparatus equipped with a LynxEye detector using Cu K $\alpha$  ( $\lambda = 1,54184 \text{ \AA}$ ) source with a Ni filter which eliminates the K $\beta$  line of the anticathode. The diffractograms were obtained with a step of  $0.02^\circ \cdot s^{-1}$  over a  $2\theta$  measurement range between  $4^\circ$  and  $80^\circ$ . The phases were identified using PDF-4+ databases from ICSD (Inorganic Crystal Structure Database) and ICDD (International Centre for Diffraction Data). These data were processed using the DIFFRAC EVA software. The average crystallite sizes were calculated using the Debye-Scherrer equation:

$$d = \frac{k * \lambda}{\beta * \cos\theta}$$

*d*: the average crystallite size ( $\text{\AA}$ )

*k*: Scherrer constant (0.89 for spherical crystals)

$\beta$ : the width at half signal height of the signal

It is possible to calculate the composition of alloys thanks to the lattice parameters using Vegard's law. Juškėnas *et al.* have proposed a simplification of the law for the NiW system<sup>5</sup>, which makes it possible to estimate the composition of the alloy according to the formula:

$$XW = -7.5208 + 2.13429 * a$$

*a* : the lattice parameter of the alloy ( $\text{\AA}$ )

*XW* : atomic fraction of W in the alloy

#### 2.2.1.2. Attenuated Total Reflectance-Infrared Spectroscopy (ATR-IR)

Infrared spectroscopy is the common vibrational spectroscopy. Vibrations in molecules are usually triggered by infrared light absorption and allow to characterize structural features of a specimen through its distinctive vibrations. There are different modes for performing infrared spectroscopy such as transmission, diffuse reflectance (DRIFTS), and attenuated total reflectance (ATR). The selection of operating mode is influenced by the nature of the item under investigation. Among the aforementioned methods of infrared spectroscopy, ATR is now one of the most commonly utilized techniques. It refers to the interaction of the examined material with an evanescent wave. The latter is caused by the reflection of IR light inside a crystal with a high refractive index and a high resilience (often diamond or germanium). This evanescent wave

emerges from the crystal, normally it has a penetrating depth of about 2  $\mu\text{m}$ , allowing contact with the sample and so activating its distinctive vibrational modes.

IR spectra were acquired in ATR mode utilizing a Nicolet iS50 FT-IR spectrometer from Thermo-Fisher that included a diamond crystal, an iS50 ATR sampling station, as well as a DTGS (deuterated triglycine sulfate) detector. Typically, a small quantity of sample was placed on the sampling station, and 50 scans were recorded with a resolution of  $2\text{ cm}^{-1}$  over a scanning range of  $2200\text{ cm}^{-1}$  to  $525\text{ cm}^{-1}$ .

### **2.2.2. Elemental analysis**

#### 2.2.2.1. Carbon Hydrogen Nitrogen and Sulfur analysis (CHNS)

CHNS elemental analysis quantifies the carbon present in the sample. The principle is based on the combustion of the sample (approximately 1 mg) at temperatures above  $1000\text{ }^\circ\text{C}$ . These formed gases are separated using a gas phase chromatography column and then the quantity of carbon dioxide produced was measured by a thermal conductivity detector. Elemental tests (C, H, and N) were conducted by a VarioMICRO Elementar Analysen systeme GmbH.

#### 2.2.2.2. Inductively Coupled Plasma Emission Spectroscopy

ICP-OES is used to determine the metal content of catalysts (wt.%). The dosage was carried out in an Agilent 5800. The samples (between 10 and 50 mg) were mineralized with  $\text{HNO}_3$ -HF mixture, followed by final dissolution in concentrated  $\text{H}_2\text{SO}_4$  at  $100\text{ }^\circ\text{C}$  overnight. Then the solution was vaporized and ionized by injecting it into an argon plasma where extreme temperatures were reached. The principle is based on the emission of photons from the electrons of the excited atoms when they return to the ground state. Each element has a characteristic energy and an intensity proportional to the number of photons emitted which is detected by optical emission spectrometer. The uncertainty of the quantities of metals measured is 0.1%.

The post-reaction solutions were analyzed by ICP-OES, to determine the solubilized metal concentrations and deduce the leaching extent of the catalysts during reaction. Metal leaching from catalysts was determined by equation (3):

$$\text{Leaching (\%)} = \frac{m_{\text{metal}}^{\text{Out}}}{m_{\text{metal}}^{\text{In}}} * 100 \quad (3);$$

$m_{\text{metal}}^{\text{Out}}$  : the mass of the metal found in the post – reaction solution ;

$m_{metal}^{In}$  : the mass of the metal in the catalyst after its synthesis

### **2.2.3. Surface Properties (X-ray photoelectron spectroscopy)**

Surface analysis was performed by XPS. It makes it possible to determine and quantify the species present on the surface (< 10 nm depth) as well as their degrees of oxidation. The principle is based on the measurement of the kinetic energy of the electrons escaping under the irradiation of the catalyst by an X-ray beam. By plotting the number of photoelectrons emitted against the binding energy an XPS spectrum is obtained. The kinetic energy of the electron depends on the energy of the photon and the binding energy of the electron according to the following formula:

$$KE = h\nu - BE$$

*KE*: the kinetic energy (eV)

*hν*: the energy of the photon (eV)

*BE*: the binding energy (eV)

Data were obtained on a KRATOS Axis Ultra spectrometer operating under ultrahigh vacuum conditions, employing a twin Al X-ray source (1486.6 eV) at a 40 eV pass energy. The sample in the form of a pellet, was fixed on a Cu holder. The binding energy values (B.E.) were estimated after positioning the C 1s peak of the contaminant carbon at 284.6 eV. The Casa XPS software was employed for data analysis.

### **2.2.4. Textural analysis (N<sub>2</sub> Physisorption)**

The specific surface area of the material, the pore volume and the mesoporous surface are determined by nitrogen physisorption. The adsorption-desorption isotherms are obtained at the N<sub>2</sub> liquefaction temperature (-196 °C). The International Union of Pure and Applied Chemistry (IUPAC) updated recently its recommendations for physical adsorption characterization, including isotherm classification<sup>6</sup>. Figure 3 shows the IUPAC isotherm classifications, which give preliminary guidance on how to interpret adsorption isotherms for structural characterization. In summary: Microporous materials generate Type I isotherms; nonporous or macroporous adsorbents result in Type II isotherms; Type III and Type V isotherms represent cases where there is no recognizable multilayer formation, indicating relatively limited interactions between the adsorbent and the adsorbate; mesoporous materials lead to Type IV isotherms; and Type VI isotherms indicate a layer by layer adsorption on a nonporous surface<sup>7</sup>. The hysteresis of the Type IV(a) isotherm correlates with the textural features of the materials. IUPAC has also categorized the various forms of hysteresis loops.

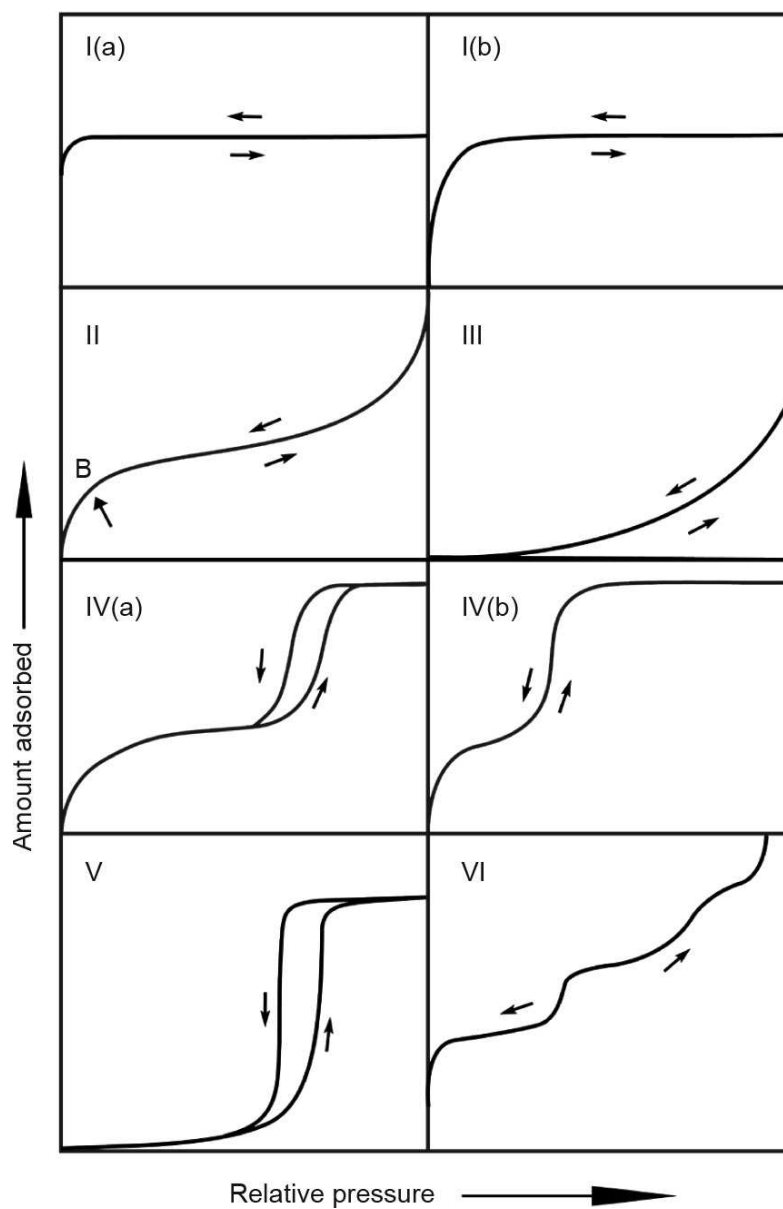


**Figure 3.** Classification of physisorption isotherms; B represents monolayer formation<sup>6,7</sup>.

Figure 4 shows a few instances<sup>8</sup>. The typical example of capillary condensation is shown in Figure 4.a, where metastable adsorption of the fluid occurs during the adsorption, whereas evaporation proceeds via equilibrium from open pores. This hysteresis is common for ordered mesoporous materials with homogeneous cylindrical pore networks or in ordered 3D pore networks. In materials with complex pore networks, like inkbottle-shaped pore systems, pore evaporation is delayed; the larger pore body remains filled till a lower pressure is attained, at which point the neck evaporates, resulting in Types H2(a) and H2(b) hysteresis (Figure 4). When the pore cavity

size distribution is wider than the neck size distribution, type H2(a) hysteresis (Figure 4.b) emerges, resulting in a sharp desorption step in the isotherm. In the reverse case, type H2(b) hysteresis (Figure 4.c) takes place: a limited distribution of pore bodies with a large neck size range.

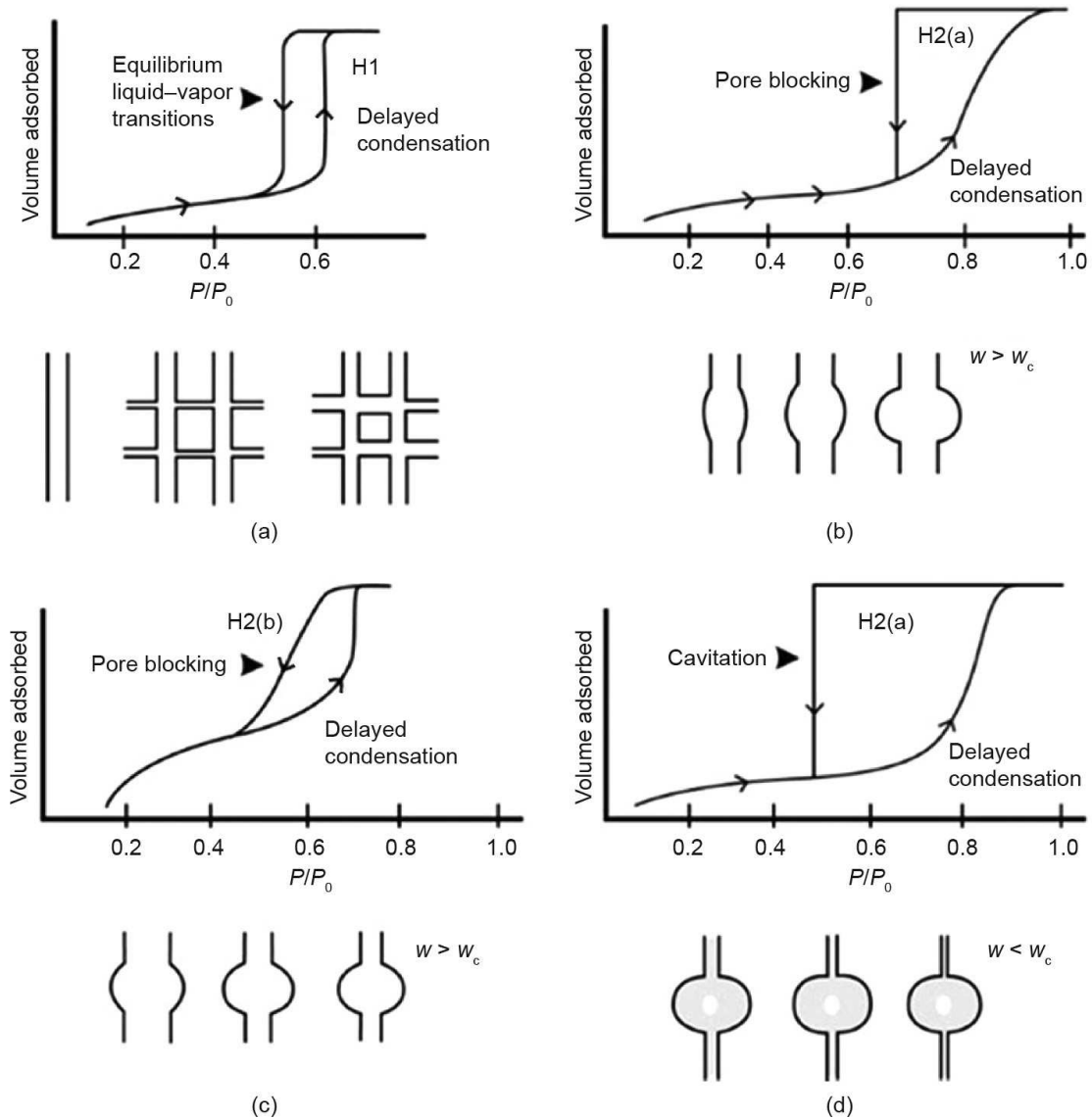


**Figure 4.** The different hysteresis loop shapes and how they are correlated to both pore network and adsorption mechanism<sup>8</sup>. (a) Type H1 hysteresis; (b) Type H2(a) hysteresis showing desorption pore blocking effects; (c) Type H2(b) hysteresis also showing desorption pore blocking effects; (d) Type H2(a) hysteresis indicating cavitation in the desorption branch. The pore illustrations represent an example of the connectivity that would lead to each isotherm above it.  $W$ : neck width;  $W_c$ : critical neck width<sup>7</sup>.

Figure 4.d depicts a scenario of cavitation-induced desorption. It has been demonstrated that if the pore neck circumference is less than a specific critical size at a certain temperature and adsorption, desorption happens by cavitation, that is spontaneous seeding of a bubble in the pore, causing the pore core to empty while the pore neck stays full. The critical neck size for argon (87 K) and nitrogen (77 K) adsorption is 5-6 nm [13-15]. To discriminate among equilibrium evaporation/desorption, pore blockage, and cavitation, a thorough comprehension of the observed hysteresis loop is required. In the event of pore blockage or cavitation, attention must be given to select the proper branch of the isotherm (adsorption) for calculating the pore size distribution, as well as a technique that takes into consideration the correct adsorption mechanism<sup>7</sup>.

The measurement for the first adsorbed N<sub>2</sub> layer makes it possible to determine the surface area of the solid from the obtained isotherms at  $p/p_0$  between 0.05 to 0.25, according to the Brunauer, Emmett and Teller (BET) equation:

$$\frac{P}{V * (P_0 - P)} = \frac{1}{V_m * C} + \frac{C - 1}{V_m * C} * \frac{P}{P_0}$$

*P: the partial pressure*

*V: the volume adsorbed at P*

*P<sub>0</sub>: the saturation pressure at the experimental temperature*

*V<sub>m</sub>: the volume adsorbed at the cover of the monolayer*

*C: the constant*

The Barrett, Joyner and Halenda (BJH) method and the t-plot method are used to determine the distribution of mesopores and the volume of micropores, respectively. The total pore volume is evaluated on the plateau of the adsorption branch at  $P/P_0 = 0.98$ .

Before analysis, the solids (0.05 g) were initially heated under vacuum in a Micromeritics Smart VacPrep apparatus ( $1.10^{-6}$  bar,  $5 \text{ }^\circ\text{C}\cdot\text{min}^{-1}$ ,  $250 \text{ }^\circ\text{C}$ , 6 h). Analyses were performed on a Micromeritics ASAP 2020 apparatus.

### **2.2.5. Morphological Properties**

The size and shape of solid particles are examined via electron microscopy techniques. Interaction of the matter with high-energy electrons (primary electron beam) having wavelengths in the range of interatomic distances or even smaller causes a variety of phenomena (Figure 5). Thus-produced electrons are used to further derive valuable information on the chemical composition or internal

structure of a sample under study therefore greatly expanding the application of electron microscopy.

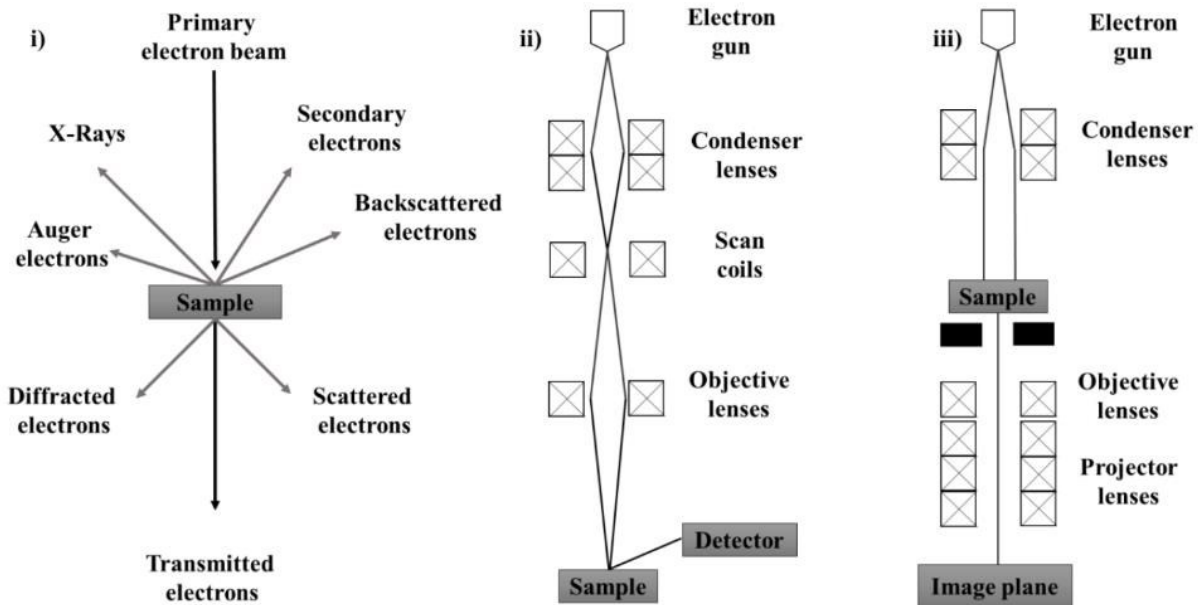


**Figure 5.** Schematic representation of the detectable signals upon the interaction between the primary electron beam and the sample (i) as well as the simplified configurations of SEM (ii) and TEM (iii)<sup>9</sup>.

As depicted in Figure 5.i, the electron-sample interaction causes the emission of the following species:

- secondary electrons (SE) which are emitted by the sample due to inelastic scattering of the primary electron beam and originate from the surface region, thus providing information on its topology;
- backscattered electrons (BSE) which are the result of collisions of the primary electrons with the atoms constituting the sample. They originate from a deeper part than SE and are sensible to the atomic mass. Therefore, heavier atoms appear brighter in a resulting image due to a higher yield of BSE;
- X-rays which are generated in the same way as in XRD experiments *e.g.* due to ejection of an electron from an inner atomic shell, leaving the atom in an ionized state, followed by the filling of the vacancy by an electron from an outer shell. This process generates X-ray photons characteristic to a certain element, which are further used for its identification;



- Auger electrons which are produced following the interaction of X-rays, generated as described above, with electrons from other shells. They are typically used in Auger Electron Spectroscopy (AES);
- diffracted electrons which can be used to further derive crystallographic information *e.g.* orientation of diffracting planes and interplanar distance (d);
- transmitted electrons which are a fraction of electrons passing through the sample without energy loss. Transmission strongly depends on the energy carried by the primary electrons as well as the thickness of the sample. Higher electron energies and thinner samples favor transmission.

#### 2.2.5.1. Scanning Electron Microscopy analysis (SEM)

SEM commonly employs low-energy electrons with energies ranging from 15-20 keV that are focused on the material by a series of lenses. Secondary electrons, X-rays, backscattered electrons, and a small portion of diffracted electrons are generated, and used to obtain information on particles size and shape (SE), surface topology, elemental analysis and mapping (X-Rays), contrast topographic imaging (BSE), and atomic planes orientation (diffraction) at a typical resolution of 25-30 nm. In this work, SEM images were registered using a JEOL JSM 7800F microscope with an electron beam energy of 5-10 keV. Prior to examination, the samples were coated with a thin coating of Cr (150 Å). When SEM was used in conjunction with EDS (Energy Dispersive X-Ray Spectroscopy) for the elemental analysis, the samples were coated with a thin carbon layer (200 Å) and examined with an electron beam of 15 keV energy.

#### 2.2.5.2. High Resolution Transmission Electron Microscopy analysis (HRTEM)

HRTEM provides information at the atomic scale on the structure, size and dispersion of particles as well as the crystallographic structure of catalysts. The principle is based on the irradiation of the sample by an electron beam. Electromagnetic lenses are used to focus the electrons onto the very finely deposited material. The detection of the transmitted electrons following their diffraction makes it possible to form contrasting images. Additional information on chemical composition and dispersion can be obtained by energy dispersive X-ray (EDX) and energy loss (EELS) spectroscopy.

Micrographs of HRTEM were taken using TITAN Themis 300 S/TEM equipped with high brightness Schottkey field emission gun, a probe aberration corrector that allows energy and resolution of about 150 meV and 70 pm respectively, and a monochromator. The microscope is equipped with several annular dark field detectors as well as a super-X detector system with 4

windowless silicon drift detectors for the electron dispersive X-ray spectroscopy (EDS). The experiments have been performed at 300 kV with semi-convergence angle of about 20 mrad, a probe size of the order of 500 pm and a probe current between 60 and 100 pA. For the high angle annular dark field (HAADF) imaging, collection angles have been between 50 and 200 mrad. EDS mapping was obtained in spectrum imaging mode with a dwell time per pixel of about 15  $\mu\text{s}$  and continuous scanning frames until total acquisition time of 15 to 20 minutes.

## **2.2.6. Chemical and thermal properties**

### 2.2.6.1. Thermogravimetric analysis

TGA is a thermogravimetric analysis technique in which the mass of a sample is continually measured as the temperature rises. When combined with DTA (Differential Thermal Analysis) or DSC (Differential Scanning Calorimetry), it enables the detection of processes occurring at various temperatures, such as combustion, desorption, phase change, and others. TGA is particularly useful for determining the thermal stability of materials by measuring, for example, the organic content in them and the temperature at which decomposition begins. TGA was performed using a thermal analyzer equipment Q600 from TA equipment. Samples (~5 mg) were placed in a ceramic pan, and pyrolyzed under a flow of  $\text{N}_2$  at 80  $\text{mL}\cdot\text{min}^{-1}$  following a temperature increase rate of 10  $^\circ\text{C}\cdot\text{min}^{-1}$  (from RT to 450  $^\circ\text{C}$ ), then 1  $^\circ\text{C}\cdot\text{min}^{-1}$  (from 450  $^\circ\text{C}$  to 700  $^\circ\text{C}$ ) with a final dwelling time of 1 h at 700  $^\circ\text{C}$ .

### 2.2.6.2. Hydrogen-Temperature programmed reduction ( $\text{H}_2$ -TPR)

Temperature programmed reduction is an approach for monitoring the behavior of a solid sample in a reducing environment. This method is commonly employed in heterogeneous catalysis; it involves heating the oxide material under a reducing hydrogen gas flow. The amount of hydrogen consumed is monitored as a function of temperature. It allows to evaluate the species reducibility (the number of reducible species within the material and the temperature at which the reduction phenomena occur).  $\text{H}_2$ -TPR analysis was run on a Micromeritics AutoChem II 2920 chemisorption analyzer, equipped with a TCD. Before the test, a catalyst mass of about 50 mg was inserted in a quartz reactor and degassed under an inert gas. A flow of 5 vol.%  $\text{H}_2/\text{Ar}$  was stabilized with a total flow rate of 50  $\text{mL}\cdot\text{min}^{-1}$ , and the catalyst was heated with a ramp of 10  $^\circ\text{C}\cdot\text{min}^{-1}$ , from 50  $^\circ\text{C}$  to 700  $^\circ\text{C}$ .

### 2.2.6.3. CO chemisorption

Many catalysts have active metals located on the surface of the support. The dispersion and state of the active metal are heavily influenced by the catalyst synthesis method. Because these metals often reside as clusters on the support surface, only a percentage of the total deposited metal is really exposed to the incoming reactant substrates for the reaction.

The sample should be subjected to a gas that can chemisorb on the accessible metals. The number of surface metal atoms associated with each gas molecule adsorption is calculated at monolayer coverage. If the stoichiometry of the chemisorption process is known, an accurate estimation of metal dispersion is possible. To measure the quantity of gas molecules adsorbed on the catalyst surface, the pulse technique is commonly employed.

The adsorbate gas for a specific catalyst is selected to minimize adsorption on the support and to have irreversible chemisorption on the metal. The most widely used adsorbate gases are H<sub>2</sub> and CO. CO adsorption is far more complicated than H<sub>2</sub>. CO may chemisorb in many forms on metals such as Fe, Ni, Ru, Pt, and Pd. Temperature, metal dispersion, metal loading, and pretreatment all affect chemisorption stoichiometry. The dispersion (D) of a metal is defined as:

$$D = \frac{N_S}{N_T}$$

*N<sub>S</sub>: total number of exposed surface atoms*

*N<sub>T</sub>: total number of metal atoms present in the material*

The analysis was conducted on a Micromeritics 3 Flex instrument. The samples were reduced in H<sub>2</sub> (30 mL.min<sup>-1</sup>) at 300 °C for 1 h, then flushed with Ar and cooled to 35 °C before CO pulses. The particle sizes were estimated from irreversibly adsorbed CO.

## **2.3. Biomass transformation**

### **2.3.1. Experimental protocols**

#### 2.3.1.1. Hydrogenolysis

The hydrogenolysis reactions were carried out in a closed 100 mL Hastelloy Parr reactor (Figure 6). The system was equipped with gas inlet and outlet valves, a calibrated pressure gauge from 0 to 200 bar, a suitable bursting disc, a mechanical stirrer, a thermocouple and a heating device.

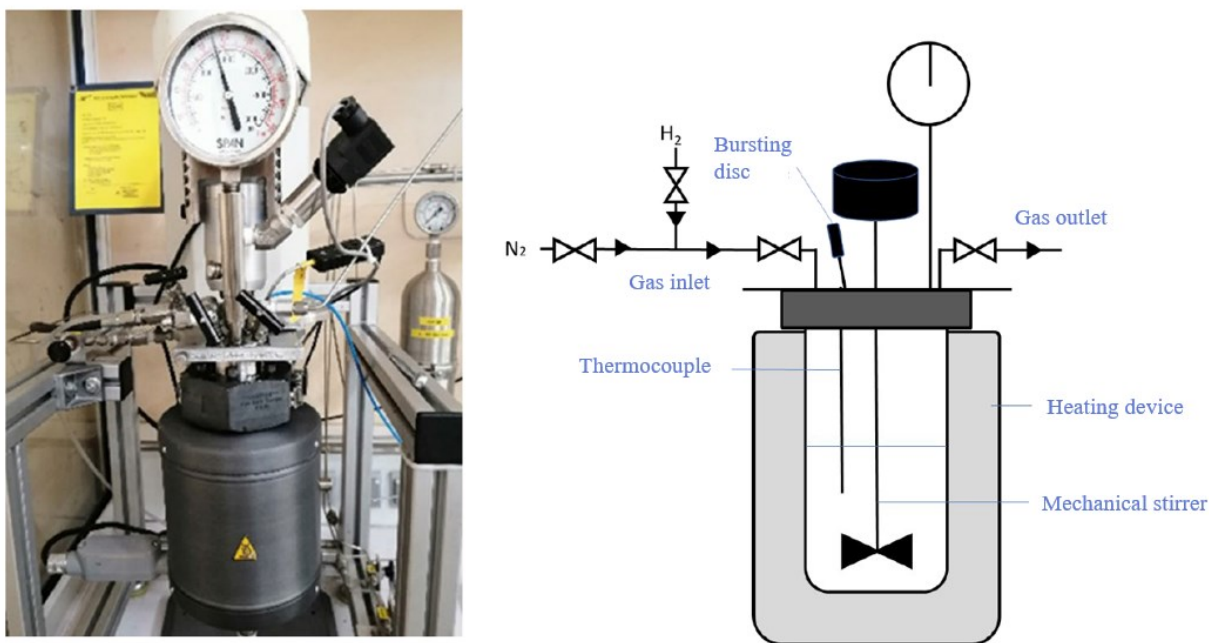


**Figure 6.** Photo and diagram of the closed reactor used for hydrogenolysis reactions

Prior to reaction, the cellulose was dried in oven under a nitrogen flow at 80 °C for 4 h. A suspension of 0.5 g of substrate and 0.15 g of catalyst in 50 mL of deionized water was prepared in the autoclave. Afterwards, the autoclave was purged 3 times with 30 bars of Ar then 1 time with 60 bars of H<sub>2</sub>. Subsequently, 60 bars H<sub>2</sub> were introduced, the autoclave was heated to 245 °C (rise in temperature of 15 min) and stirred at 1000 rpm. When 245°C was reached, corresponding to  $t = 0$  (at  $t = 0$ , the pressure was approximately 90 bars), this temperature was maintained for 1 hour. At the end of this time the heating was stopped and the oven was lowered. The reactor was left to cool under air with stirring maintained for 15 min, then the stirring was stopped and the autoclave was immersed in a cold water bath (about 1 hour).

Thus, at the end of each reaction, the aqueous phases were recovered and filtered under vacuum (with a 50 µm PVDF filter). The solid recovered was dried and the filtrate was analyzed by total organic carbon (TOC) then by high performance liquid phase chromatography (HPLC).

The catalyst recycling tests were carried out by recovering the aqueous solution at the end of each reaction cycle. The catalyst was thus left in the autoclave and cellulose and water were added along with the catalyst residue recovered by vacuum filtration for the next test.

### 2.3.1.2. Amination

Experiments were performed in a 300 mL PARR Hastelloy reactor equipped with a mechanical stirrer and counter-blades on the sides to increase the gas-liquid contact. In a typical experiment, 10 g of hydroxyacetone (acetol) and 1 g of catalyst were introduced in 100 mL of the NH<sub>3</sub> aqueous solution. The system was purged with argon then the reactor was stirred (1000 rpm), pressurized with H<sub>2</sub> and heated to the desired temperature. After a certain time, the gas phase was evacuated, the liquid phase was collected and filtered under vacuum with a 50 µm PVDF filter. The solid recovered was dried and the filtrate was analysed by total organic carbon (TOC) then by nuclear magnetic resonance spectroscopy (NMR).

### **2.3.2. Products analysis**

#### 2.3.2.1. Total organic carbon (TOC)

The carbon balance in solution was determined by measuring the amount of carbon present in the reaction solutions via a TOC method. The principle is based on the oxidation of all the organic compounds present in the solution and then the measurement of the quantity of carbon dioxide produced. The device used was a Shimadzu TOC-VCSH assembled with an ASI-V autosampler. The method used was NPOC (non-purgeable organic carbon). The carbon balance was determined by the ratio between the amount organic carbon present in the liquid phase at the end of the reaction and the amount of organic carbon introduced.

In this method, the sample was first acidified with hydrochloric acid under air flow to remove the inorganic carbon present. Then the solution was injected into a catalytic reactor at 720 °C, under air, with a Pt/Al<sub>2</sub>O<sub>3</sub> catalyst to oxidize the organic compounds into CO<sub>2</sub> which was quantified by infrared spectroscopy. Before each series of analysis, the calibration of the device was checked with a nicotinic acid solution of known concentration (the measured uncertainty was less than 5%) and between each sample a purge was carried out with a water solution. The samples were diluted approximately 10 times to reach values below the detection limit which is 500 ppm. Three measurements of the sample were taken and averaged.

#### 2.3.2.2. High performance liquid chromatography

The yields of the products obtained by the hydrogenolysis reactions were determined by HPLC analysis. The manipulations were repeated several times and reproducible yields of ± 5% were obtained. This method allows the separation of the species present in solution. The samples were

injected by a mobile phase then sent to a column (stationary phase). Depending on the affinity of the different molecules present in the mixture with this column, they will be separated and detected by differential measurement of the refractive index.

The system was composed of several devices and features:

- a Shimadzu LC-20AD pump (emitting a flow rate of 0.5 mL.min<sup>-1</sup> of an aqueous solution of sulfuric acid (0.05 M), the autogenous pressure of the system was approximately 60 bars
- a Shimadzu SIL-20A HT autosampler (10 µL injection)
- a Phenomenex Degassex DG-4400 degasser
- a Shimadzu CTO-10AS VP column oven (heated to 40°C)
- an ICSep ICE-CORAGEL-107H column of 300 x 7.8 mm (composed of PSDVB-SO<sub>3</sub>H, it is based on the principle of ion exclusion to separate sugars, alcohols and acids)
- a Shimadzu RID-10A refractive index detector.

This method makes it possible to effectively separate all the molecules but not the epimers. Identification of the retention time of all the products likely to be formed was carried out with commercial standards. Then to be able to quantify the identified products, an external calibration was carried out, according to the equation:

$$A = K * C$$

*A: the surface of the compound peak*

*K: correlation coefficient of A and C*

*C: the concentration of the compound*

For this, 4 to 5 solutions of identified products formed, at different concentrations were analyzed. An example of a chromatogram of a mixture of reaction products obtained from cellulose under standard conditions is shown in Figure 7, along with the calibration line for one of the products, ethylene glycol.

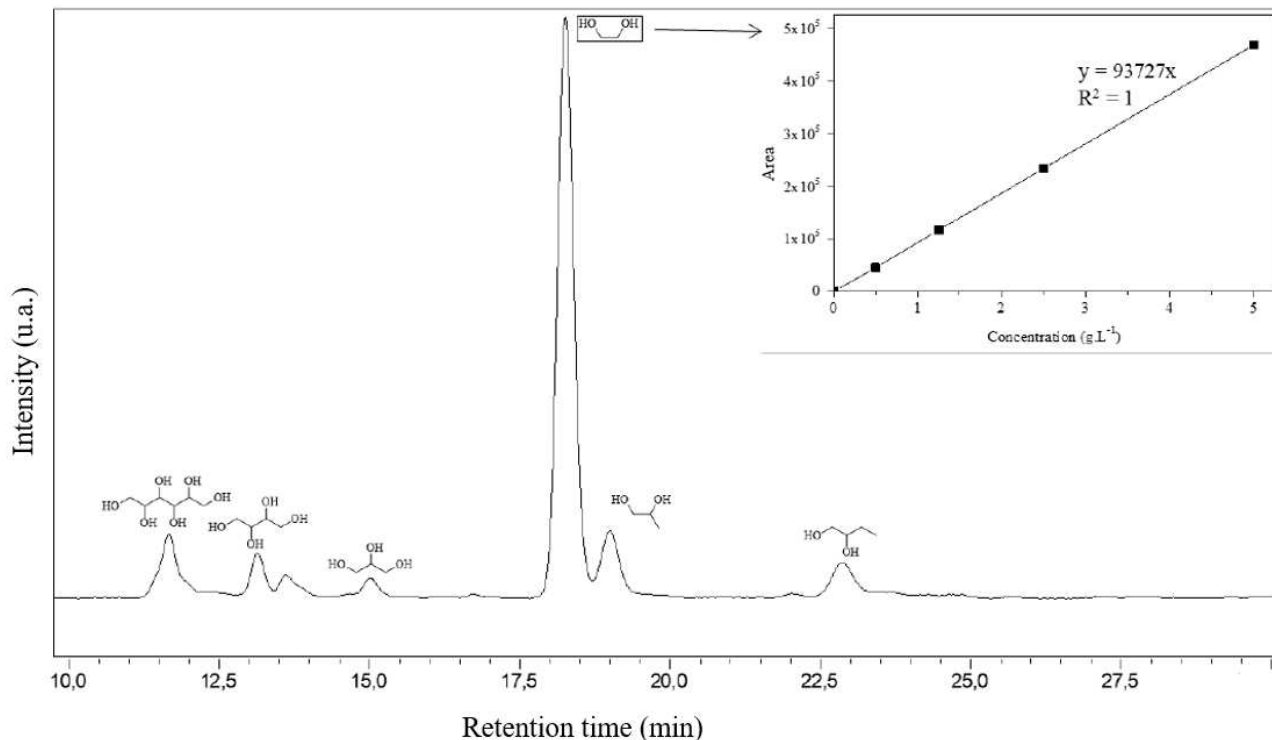


**Figure 7.** Example of HPLC chromatogram with detected molecules. Insert: ethylene glycol calibration line.

### 2.3.2.3. Liquid phase nuclear magnetic resonance

The molar yields of the products obtained during amination reaction were determined by <sup>13</sup>C liquid phase NMR. NMR makes it possible to study the nuclei having a magnetic moment because the principle is based on the polarization of the nuclei and then the observation of its relaxation.

The measurements were performed on a BRUKER AVANCE HD Spectrometer equipped with an ASCEND 400 magnet and a 5 mm BBFO probe. The pulse sequence used was zgig (inverse trigger decoupling) and 6144 scans were recorded.

The solutions were analyzed in DMSO-d<sub>6</sub> and dioxane was used as internal standard. All the products present in the post-reaction solution were calibrated. An example spectrum is shown in Figure 8 along with the calibration curve of 2-aminopropan-1-ol (alaninol).

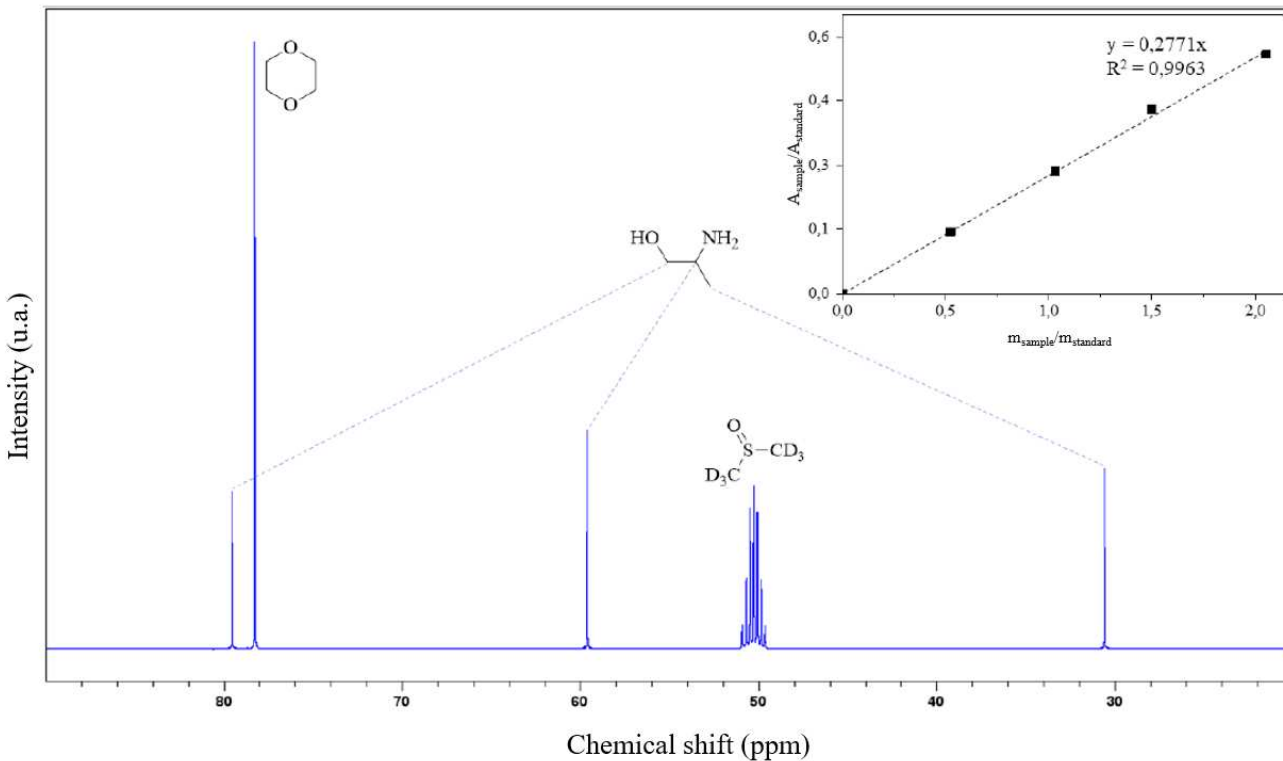


**Figure 8.**  $^{13}\text{C}$  NMR spectrum of alaninol in  $\text{dms0-d}_6$ , in the presence of dioxane standard. Insert: calibration curve of alaninol.

### 2.3.3. Exploitation of the results

The mass balance corresponds was calculated by the values obtained by TOC, according to this equation:

$$\text{Cellulose liquefaction (\%)} = \frac{C^{\text{Out}}}{C^{\text{In}}} * 100;$$

$C^{\text{Out}}$  : the C concentration measured in the post – reaction solution by TOC;

$C^{\text{In}}$  : the C concentration in the pre – reaction solution from C content in cellulose

The molar carbon yield of each product was determined by the HPLC values by:

$$\text{Products' yields (\%)} = \frac{n_p^{\text{Out}} * n_c^{\text{Out}}}{n_s^{\text{In}} * n_c^{\text{In}}} * 100 ;$$

$n_p^{\text{Out}}$  : The polyol's number of moles in the product

$n_c^{\text{Out}}$  : the number of carbon atoms in the produced polyol



$n_S^{In}$  : the number of moles of cellulose =  $m_{cellulose}/162$

$n_C^{In}$  : the number of carbon atoms in cellulose monomer  $C_6H_{10}O_5$

The molar yield of the amine products is determined by the values obtained by  $^{13}C$  NMR:

$$\text{Products' yields (\%)} = \frac{n_A^{Out} * n_C^{Out}}{n_H^{In} * n_C^{In}} * 100 ;$$

$n_A^{Out}$  : The amine's number of moles in the product

$n_C^{Out}$  : the number of carbon atoms in the produced amine

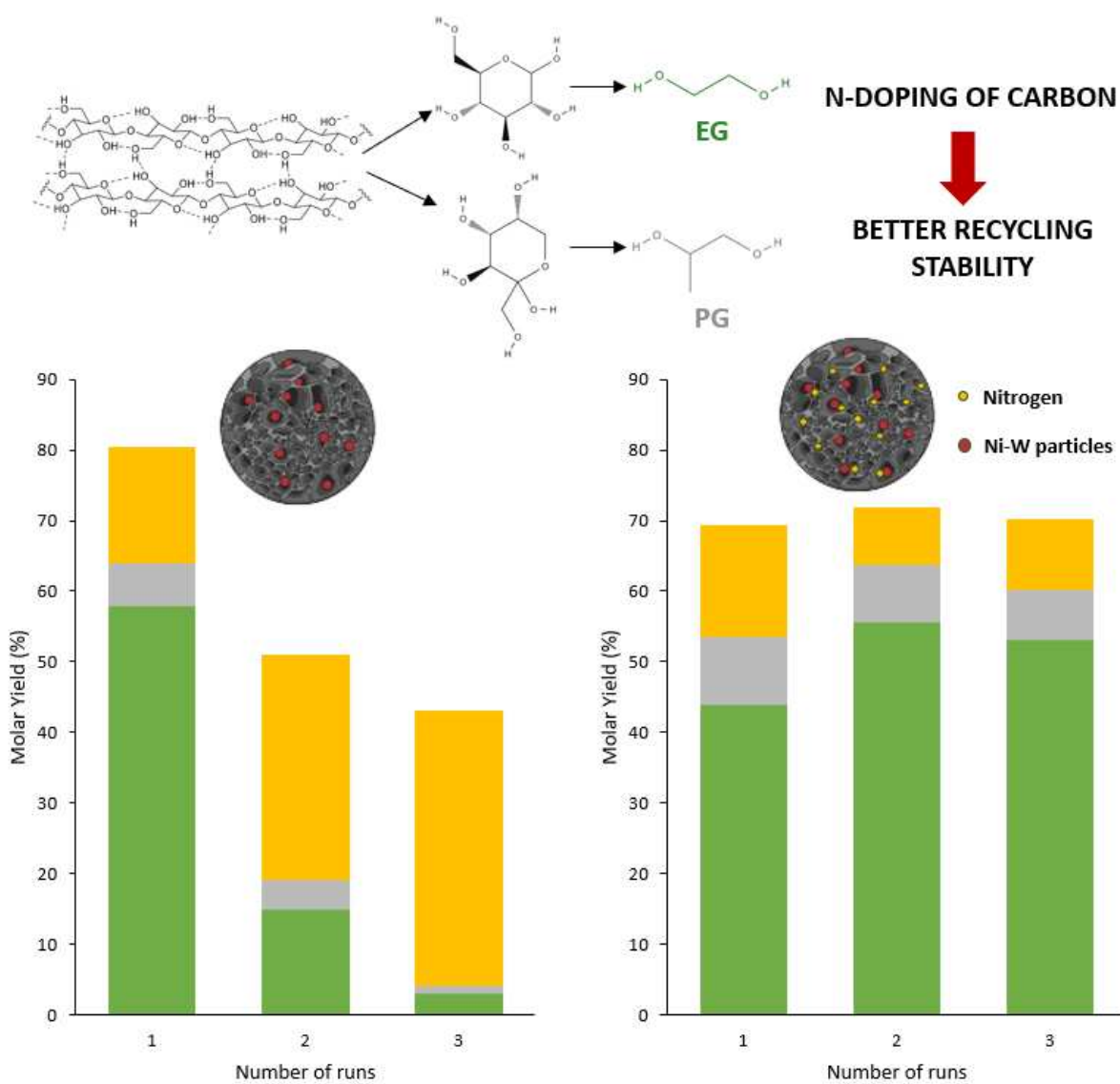
$n_H^{In}$  : the number of moles of acetol

$n_C^{In}$  : the number of carbon atoms in acetol molecule

## 2.4. References

- (1) Xing, Z.; Ju, Z.; Zhao, Y.; Wan, J.; Zhu, Y.; Qiang, Y.; Qian, Y. One-Pot Hydrothermal Synthesis of Nitrogen-Doped Graphene as High-Performance Anode Materials for Lithium Ion Batteries. *Sci. Rep.* **2016**, *6* (1), 26146. <https://doi.org/10.1038/srep26146>.
- (2) Ji, N.; Zhang, T.; Zheng, M.; Wang, A.; Wang, H.; Wang, X.; Chen, J. G. Direct Catalytic Conversion of Cellulose into Ethylene Glycol Using Nickel-Promoted Tungsten Carbide Catalysts. *Angew. Chem. Int. Ed.* **2008**, *47* (44), 8510–8513. <https://doi.org/10.1002/anie.200803233>.
- (3) Kavooosi, N.; Bon, V.; Senkovska, I.; Krause, S.; Atzori, C.; Bonino, F.; Pallmann, J.; Paasch, S.; Brunner, E.; Kaskel, S. Tailoring Adsorption Induced Phase Transitions in the Pillared-Layer Type Metal–Organic Framework DUT-8(Ni). *Dalton Trans.* **2017**, *46* (14), 4685–4695. <https://doi.org/10.1039/C7DT00015D>.
- (4) Stan, C.; Beavers, C.; Kunz, M.; Tamura, N. X-Ray Diffraction under Extreme Conditions at the Advanced Light Source. *Quantum Beam Sci.* **2018**, *2*. <https://doi.org/10.3390/qubs2010004>.
- (5) Juškėnas, R.; Valsiūnas, I.; Pakštas, V.; Giraitis, R. On the State of W in Electrodeposited Ni–W Alloys. *Electrochimica Acta* **2009**, *54* (9), 2616–2620. <https://doi.org/10.1016/j.electacta.2008.10.060>.
- (6) Thommes, M.; Kaneko, K.; Neimark, A. V.; Olivier, J. P.; Rodriguez-Reinoso, F.; Rouquerol, J.; Sing, K. S. W. Physisorption of Gases, with Special Reference to the Evaluation of Surface Area and Pore Size Distribution (IUPAC Technical Report). *Pure Appl. Chem.* **2015**, *87* (9–10), 1051–1069. <https://doi.org/10.1515/pac-2014-1117>.
- (7) Cychosz, K. A.; Thommes, M. Progress in the Physisorption Characterization of Nanoporous Gas Storage Materials. *Engineering* **2018**, *4* (4), 559–566. <https://doi.org/10.1016/j.eng.2018.06.001>.
- (8) Cychosz, K. A.; Guillet-Nicolas, R.; García-Martínez, J.; Thommes, M. Recent Advances in the Textural Characterization of Hierarchically Structured Nanoporous Materials. *Chem. Soc. Rev.* **2017**, *46* (2), 389–414. <https://doi.org/10.1039/C6CS00391E>.
- (9) Andoni, A. (Adelaida). A Flat Model Approach to Ziegler-Natta Olefin Polymerization Catalysts. **2009**. <https://doi.org/10.6100/IR638773>.

# Chapter 3 : N-doped Ni-W<sub>x</sub>C catalysts for cellulose hydrogenolysis



This Chapter has been submitted to ACS Nanomaterials in 2023.

### 3.1. Introduction

Currently, energy and chemical industries depend on non-renewable – fossil - resources which have limited reserves. Therefore, it is now urgent for industries to develop the utilization of renewable resources like biomass<sup>1</sup> to produce chemicals and fuels. Owing to its renewability and abundance, lignocellulose has been considered as a promising resource<sup>2,3</sup>. Cellulose, hemicelluloses, and lignin constitute the 3 main components of lignocellulose and they have been revealed to have huge potential. Lignin can be used to produce phenolic compounds and derived fuels, while hemicellulose has been explored to synthesize C5 chemicals<sup>4-6</sup>. Concerning cellulose, its reactivity has been much more exploited and there have been various studies on its conversion to produce valuable chemicals, the most important being glucose, polyols, carboxylic acids, 5-hydroxymethyl furfural, and, ethanol<sup>7</sup>.

Valorization of cellulose requires depolymerization through hydrolysis, a reaction typically conducted using concentrated liquid Brønsted acids. However, liquid acids are very corrosive and their uses induce additional steps of product separation and purification, generating considerable wastes and consuming energy. Alternatively, the use of solid acids (heterogeneous catalysts) can not only overcome these drawbacks but also give access to peculiar chemicals thanks to the specific reaction conditions they can afford. These chemicals include low carbon polyols (C2, C3) like ethylene glycol (EG), propylene glycol (PG), and glycerol (GLY), which are prevailing intermediates in the manufacture of polymers, pharmaceuticals, additives, cosmetics, etc.

While glycerol can be obtained from vegetable oils, to date EG and PG are still manufactured from natural gas. However, they can theoretically be obtained from carbohydrates, and particularly cellulose. Some studies reported the production of these polyols using heterogeneous catalysis conducted under hydrogen pressure and high temperature. Reported catalysts are materials based on supported noble metals (Ru, Pt, Pd.) or transition metals (Ni, W, Cu)<sup>8</sup>.

Among them, catalysts containing nickel and tungsten under various states (carbides  $W_xC^9$ , oxides NiO and  $WO_x^{10}$ , and alloys  $Ni_xW_y^{11,12}$ ) have been reported to be active and selective towards C2 and C3 polyols production, especially EG. The accepted reaction mechanism implies, after an acid catalyzed depolymerization of cellulose, the selective cleavage of C-C bonds from glucosides intermediates through the so-called retro-aldol condensation, promoted by

the tungsten sites into carbonyl-containing products. Next, nickel sites catalyze the hydrogenation of produced unsaturated intermediates, leading to polyols production<sup>9</sup>. Table S1 summarizes main previous studies using Ni- and W supported catalysts for the formation of EG and PG. Using activated carbon-supported tungsten carbide (W<sub>2</sub>C/AC) catalysts, Zhang *et al.* obtained an EG yield of 27 % starting from cellulose<sup>2</sup>. Besides being a cheap non-noble metal derived phase, a noteworthy advantage of tungsten carbide over other tungsten species (oxides and metal) is the preferential formation of EG among other polyols due to its Pt-like catalytic behavior. When changing the support by a mesoporous carbon (obtained by replication from a commercial silica) and further nickel-doping, the EG yield was enhanced up to 72-76 %<sup>13</sup>. The improvement was attributed to the high dispersion of tungsten carbide and nickel, and the more efficient diffusion of reactants and products inside the support porosity. Fabičovicová *et al.* compared the hydrogenolysis of cellulose without a catalyst, and in the presence of 6 different catalytic systems composed of nickel and/or of tungsten on activated carbon (AC) in order to distinguish the role of each active component<sup>14</sup>. The two-steps incipient wetness impregnation prepared catalyst, Ni/W/AC, yielded 43.7 % of EG. Drastically lower EG yields were obtained with the Ni/AC+W/AC physical mixture and the Ni-W/AC catalyst prepared by co-impregnation. By varying the carbon support type, high space-time yields of about 2.5 g<sub>polyols</sub> (g<sub>catalyst</sub>.h)<sup>-1</sup> were achieved. They also reported that structural changes (formation of NiWO<sub>4</sub>), and leaching was responsible for catalyst deactivation over 3 runs. Yang *et al.* prepared Ni-W/C nanofiber catalysts, *in situ* fabricated through the pyrolysis of Ni, W-containing metal-organic framework fibers. The metal particles have uniform size distribution centered at 68 nm, evenly dispersed on the hierarchical porous carbon nanofibers. A large productivity varying from 15.3 to 70.8 mol<sub>EG</sub>.h<sup>-1</sup>.g<sub>W</sub><sup>-1</sup> was reported, which is 2 orders of magnitude higher than with previously reported Ni-W-based catalysts<sup>11</sup>. Using β-zeolite supported Ni-W catalyst (Ni-W/β) doped by ZnO, Gu *et al.* obtained high yields of EG (34.3 %) and PG (35.8 %), the latter being assigned to the promotion of glucose isomerization to fructose by ZnO surface sites<sup>15</sup>.

Organic functional groups (-SO<sub>3</sub>H, -COOH, -OH, -[C]-N, -NH<sub>2</sub>, etc.) complexation role on cellulose hydrogenolysis has been investigated by a very limited number of studies<sup>16-18</sup>. For instance, Rodella *et al.* proved that SO<sub>3</sub>H groups not only increase the hydrolysis rate of cellulose but also stabilize the Ni promoter which then led to a smaller, better dispersed W<sub>x</sub>C

phase and thus higher selectivity towards EG as compared to the non-functionalized Ni-W<sub>x</sub>C/C catalyst<sup>16</sup>.

Very few studies have been interested in the modification of the support surface composition, in order to improve the active metal phase dispersion and/or catalyst stability. For instance, Xiao *et al.* have shown that the stability of the catalyst upon recycling was promoted by the presence of nitrogen. The retaining of the catalyst activity was attributed to the presence of C<sub>3</sub>N<sub>4</sub> phase and of the Ni-W alloys. Such catalyst configuration enhanced EG production, owing to the presence of Ni-N-N Lewis pairs<sup>17</sup>. Recently, we confirmed the potential of Ni-W<sub>x</sub>C/AC catalysts for the hydrogenolysis of cellulose into EG and PG<sup>19</sup>. However, properties improvement is still awaited and the quest for supports that stabilize more efficiently the active sites operating under severe hydrothermal conditions is needed. As previously mentioned, the N-presence on the surface of carbons can affect activity and stability of Ni-W based catalysts. Methods for N-doped carbons manufacturing include (a) carbonization of nitrogen-rich materials (*e.g.*, polyamide, polypyrrole, chitosan, gelatin, proteins, etc.) and (b) nitrogen post- enrichment of carbon materials by liquid-phase impregnation or gas phase treatments. Beyond its eco-friendly nature, the exploitation of renewable biomass-derived materials offers many advantages, including the availability and abundance of the starting materials, and provides additional benefits in terms of structural and morphological diversities. Chitosan, for instance, as an N-containing (~7 wt.%) natural polymer produced from deacetylation of chitin, the second most abundant polysaccharide in nature, has a vast potential for the preparation of N-doped carbon materials. Multiple synthetic procedures, alone or combined, have been used to convert chitosan into N-doped carbon materials<sup>20</sup>. They include hydrothermal treatment, pyrolysis under an inert atmosphere<sup>21,22</sup>, and microwave-assisted treatment<sup>20</sup>. Given the chitosan skeleton thermally induced evolution during pyrolysis, the precise control of the experimental parameters is crucial. An inert gas atmosphere is usually required, and the choice of the pyrolysis temperature range and its increasing rate is also pivotal for the nature of the obtained carbon material. As a matter of fact, chitosan carbonization is a complex process, which involves a decrease in oxygen content and the structure rearrangement through sequential reactions including decarboxylation, hydrolysis, dehydration, aromatization, ring opening, cyclization, and condensation<sup>20</sup>.

For the present study, we studied the properties of N-containing carbon supported Ni-W catalysts for cellulose hydrogenolysis into polyols. A series N-doped porous carbons was prepared by hydrothermal treatment and pyrolysis starting from chitosan as C- and N-donor precursor to assess the effect N-surface presence and concentration on catalyst properties. Emphasis was given on the investigation of the active phase dispersion, catalytic efficiency, and leaching resistance in reaction.

## 3.2 Experimental

In this chapter, the following characterization techniques were used: XRD, N<sub>2</sub> physisorption, XPS, TEM, H<sub>2</sub>-TPR, TGA, ICP-OES and XPS. For more information regarding the characterization techniques and synthesis routes, please refer to Chapter 2 for all details.

## 3.3. Results and discussion

### 3.3.1. Characterization of materials

Table 1 reports the elemental composition of the carbon supports prepared by hydrothermal synthesis (HTC) for this study. Conversion of sodium alginate precursor leads to a carbon material with 85.9% of quantified carbon. The presence of some nitrogen, 1.0%, may come from the N<sub>2</sub> atmosphere used for the pyrolysis treatment at 700 °C but the content remains low compared to the content measured for the two other samples. Indeed, concerning the N-carbons, both those prepared from chitosan [NC], and chitosane+melamine [M+NC], contain a nitrogen amount of 5.4% and 7.5% respectively. The content measured after pyrolysis is lower than the nitrogen content in the precursor solution. The presence of N is clearly affected by the pyrolysis (despite being performed under N<sub>2</sub>). This is particularly observed for [M+NC], for which the N content is 2.2 times lower than the N content in the precursor. This implies that the condensation between chitosan and melamine was not fully efficient during the hydrothermal treatment and that an important part of melamine was not incorporated in the final solid and decomposed during thermal treatment. Analysis of the pyrolyzed hydrochar [NC], prepared by employing solely chitosan both as a carbon and nitrogen precursor, gives a C/N ratio agreeing well with the previously reported studies on chitosan-derived carbons<sup>24,25</sup>.

**Table 1.** Elemental analysis of precursors and HTC-derived carbons.

<b>Material</b>	<b>C (wt%)</b>	<b>H (wt%)</b>	<b>N (wt%)</b>	<b>C/N</b>
-----------------	--------------------	--------------------	--------------------	------------

Sodium alginate (theoretical C <sub>6</sub> H <sub>10</sub> O <sub>6</sub> Na)	35.8	5.0	-	-
[C] (experimental)	85.9 ± 0.1	1.3 ± 0.0	1.0 ± 0.1	85.9
Chitosan (theoretical C <sub>6</sub> NO <sub>4</sub> H <sub>10</sub> )	45	6.25	8.75	5.1
[NC] (experimental)	82.7 ± 0.2	1.9 ± 0.4	5.4 ± 0.3	15.3
Melamine (theoretical C <sub>3</sub> N <sub>6</sub> H <sub>6</sub> )	28.6	4.7	66.7	0.4
[M+NC] (theoretical C <sub>3.5</sub> O <sub>3.3</sub> N <sub>1.8</sub> H <sub>9.3</sub> considering 0.4 g of chitosan and 0.08 g of melamine)	43	6.1	16.4	2.6
[M+NC] (experimental)	80.1 ± 0.3	1.5 ± 0.0	7.5 ± 0.4	10.7

The textural properties of the three carbon materials were determined from N<sub>2</sub> adsorption-desorption isotherms. Results are presented in Figure 1 and Table 2. Isotherm for [C] sample is of type I, implying an almost pure microporous material. The N-doped and N-enriched samples [NC] and [M+NC] present type IV isotherms with H3-hysteresis loops at P/P<sub>0</sub> range 0.30-0.99. The isotherm shape suggests the presence of both micropores and mesopores with a wedge-shaped pores arrangement. The mesopores were distributed around 4-5 nm and 20-50 nm and associated with the internal pores and external interstitial of HTC materials, respectively. Mesopore presence is of huge interest in catalysis due to the facilitated diffusion of substrates to the active sites (and evacuation of products)<sup>26</sup>. Furthermore, the hysteresis does not close under P/P<sub>0</sub> = 0.3, signaling that irreversible chemical adsorption might be occurring on [NC] and [M+NC]<sup>23</sup>. All HTC-derived carbon materials exhibited relatively large surface areas in the range of 273-328 m<sup>2</sup>.g<sup>-1</sup>, making them interesting supports for metal deposition.



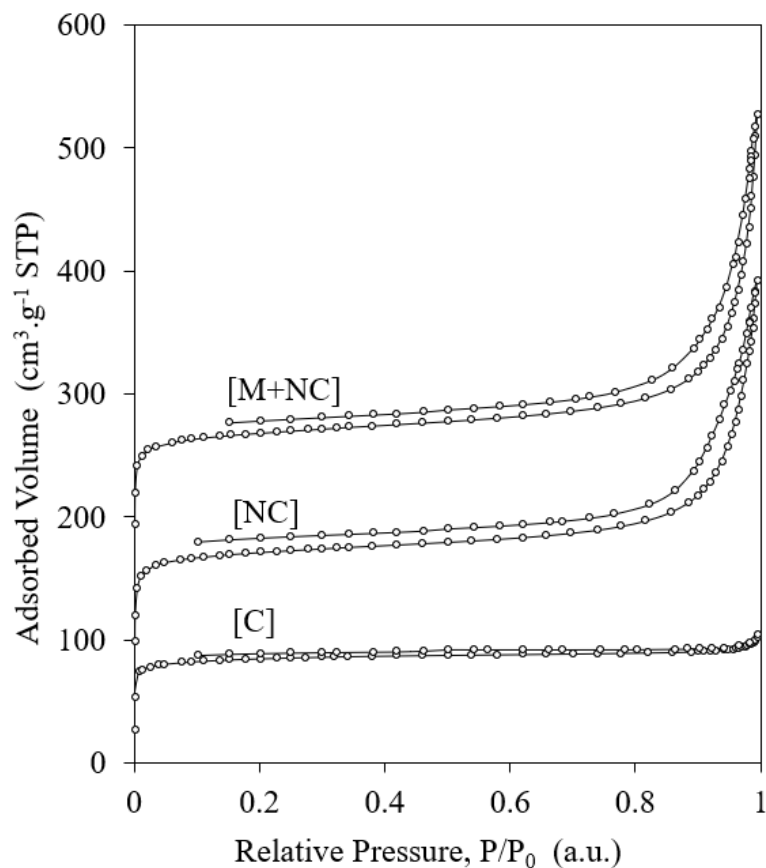


**Figure 1.** N<sub>2</sub> sorption isotherms of HTC-derived carbon samples ([NC] and [M+NC] isotherms were shifted upwards by 75 cm<sup>3</sup>.g<sup>-1</sup> and 175 cm<sup>3</sup>.g<sup>-1</sup> respectively).

**Table 2.** Textural properties of HTC-derived carbon samples and carbon-supported NiW materials.

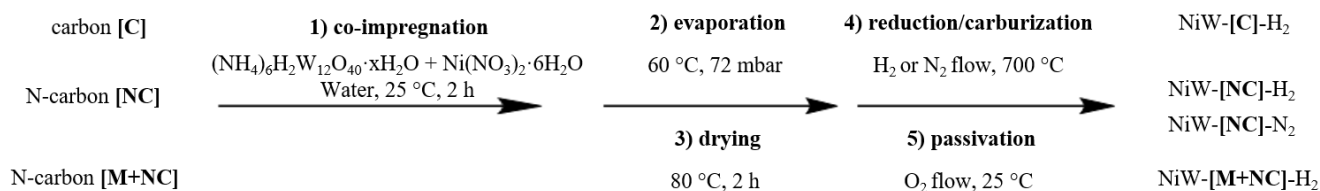
Material	S <sub>BET</sub> <sup>(a)</sup> (m <sup>2</sup> .g <sup>-1</sup> )	S <sub>μ</sub> <sup>(b)</sup> (m <sup>2</sup> .g <sup>-1</sup> )	V <sub>p</sub> <sup>(c)</sup> (cm <sup>3</sup> .g <sup>-1</sup> )	V <sub>μ</sub> <sup>(d)</sup> (cm <sup>3</sup> .g <sup>-1</sup> )	d <sub>pore</sub> <sup>(e)</sup> (nm)
[C]	273	209	0.16	0.10	3.6
[NC]	287	244	0.32	0.10	3.8-28.0
[M+NC]	328	282	0.35	0.11	3.9-32.0
NiW-[C]-H <sub>2</sub>	254	187	0.30	0.08	3.8-10.6

NiW-[NC]-N <sub>2</sub>	284	195	0.25	0.09	3.2-16.5
NiW-[NC]-H <sub>2</sub>	173	140	0.21	0.06	3.8-22.0
NiW-[M+NC]-H <sub>2</sub>	41	26	0.07	0.01	3.2-16.6

<sup>(a)</sup> BET surface area; <sup>(b)</sup> micropore surface area; <sup>(c)</sup> total pore volume; <sup>(d)</sup> micropore volume; <sup>(e)</sup> BJH pore diameter calculated on desorption branch.

Concerning the thermal stability of the hydrochars, the thermogravimetric curves (Figure S1) indicates a three-stages weight loss. The first stage, occurring at low temperatures (< 150 °C), is assigned to the release of adsorbed H<sub>2</sub>O (4 to 8 wt%). One can note that twice amount of water was desorbed from the N-modified carbons, due to higher hydrophilicity of these N-hydrochars, compared to the carbon usually considered as hydrophobic. The exothermic decomposition of hydrochars occurs in the temperature range of 200-400 °C, with weight loss close to 35-40% obtained whatever the sample. Finally, at high temperatures (> 500 °C) final decomposition occurs, by chain scission and ring-opening reactions and abstraction of side groups. The carbonaceous residues for [C], [NC], and [M+NC], after a dwell time of 1 h at 700 °C, are 48%, 51% and 45% respectively.

N-hydrochars seems more stable at high temperature, since the decomposition curves show a plateau reached in less than 1 h of dwell time, probably due to the inhibition of ring scission/opening reactions by the presence of nitrogen<sup>27</sup>. Before that, [NC] and [C] behave quite similarly while [M+NC] is notably less stable at lower temperature. This confirms that part of the melanine was not sufficiently incorporated in the carbonaceous structure during the hydrothermal synthesis and was lost at early stage (step 2, Figure S1) during thermal stabilization.



**Scheme 2.** Schematic representation of the metallic catalysts synthesis protocol.

For catalysis purpose, materials containing metal Ni and W carbide sites ( $W_xC$ ) were prepared by co-impregnation of the two metal precursors on the various carbon supports, followed by reduction and carburization occurring simultaneously under  $N_2$  or  $H_2$  atmosphere. Synthetic methodology is summarized in Scheme 2. Table 3 presents the Ni and W contents in the final (NiW) materials. Ni and W targeted loadings were chosen based on our previous study on the hydrogenolysis of cellulose<sup>19</sup>: 5 wt.% Ni and 30 wt.%W, corresponding to a W/Ni ratio of 6. Elemental analysis (Table 3) confirmed a W/Ni ratio close to 6 for all catalysts. However, the expected metal loading (5 wt.% Ni and 30 wt.%W) is only obtained for the sole sample activated under  $N_2$ , while samples activated under  $H_2$  show significantly higher metal loadings. Indeed, NiW-[NC]- $H_2$  shows 52.3 wt.% W and 8.6 wt.% Ni, while the same sample activated under  $N_2$  (NiW-[NC]- $H_2$ ) exhibits 30.4 wt.% W and 5.2 wt.% Ni close to the theoretical values (Table 3). This detrimental effect of  $H_2$  treatment on the carbon supports when Ni is present is associated to the carbon consumption by reaction with  $H_2$  to produce methane, over metallic Ni particles. N-doped carbon supports contain more metals compared to the non-modified carbon, suggesting a higher reactivity of the carbon support, with eventually the additional reaction of N atoms (to produce  $NH_3$ ) at temperature above 400 °C. In conclusion it appears somewhat difficult to control the W and Ni content on such materials when the W carburization is realised in the presence of Ni. In order to control the final metals loading, the catalyst can be synthesised by successive impregnation. Process consists in first impregnating the W precursor and perform its carburization, and in a second time in impregnating the Ni precursor and perform its reduction at a intermediate temperature (<450 °C). Such process prevents the decomposition of the carbonaceous support.<sup>14,19</sup> Nevertheless, we showed in a previous study that such catalysts prepared by successive impregnation were shown to be less efficient and stable for cellulose hydrogenolysis than catalysts prepared in a single step<sup>19</sup>. As compared to Table 1 the N content values are greatly reduced after metals' loading and  $H_2/N_2$  reduction (Table 3). Nevertheless, an increasing tendency of this content is still detected; NiW-[C]- $H_2$  (0.1%), NiW-[M+NC]- $H_2$  (0.2%), NiW-[NC]- $H_2$  (0.9%), and NiW-[NC]- $N_2$  (2.7%). The presence of N is clearly affected by the reduction gas choice,  $H_2$  is much more detrimental than  $N_2$ . This is particularly observed for the two [NC] (5.4%, Table 1) derived catalysts, where the N content of NiW-[NC]- $H_2$  (0.9%) is 3 times lower than that of NiW-[NC]- $N_2$  (2.7%).

**Table 3.** Metal loading of the carbon-supported NiW materials <sup>(a)</sup>.

<b>Material</b>	<b>C (wt%)</b>	<b>H (wt%)</b>	<b>N (wt%)</b>	<b>C/N (wt%)</b>	<b>W (wt%)</b>	<b>Ni (wt%)</b>	<b>W/Ni (wt%)</b>
NiW-[C]-H <sub>2</sub>	35.9 ± 0.8	0.3 ± 0.1	0.1 ± 0.0	359	45.8	7.7	5.9
NiW-[NC]-N <sub>2</sub>	46.0 ± 0.2	1.1 ± 0.0	2.7 ± 0.0	17.0	30.4	5.2	5.8
NiW-[NC]-H <sub>2</sub>	27.9 ± 4.1	0.6 ± 0.0	0.9 ± 0.2	31.0	52.3	8.6	6.1
NiW-[M+NC]-H <sub>2</sub>	5.5 ± 0.1	0.1 ± 0.0	0.2 ± 0.0	27.5	72.3	12.0	6.0

<sup>(a)</sup> The target metal loadings were 30 wt% of W and 5 wt% of Ni.

N<sub>2</sub> isotherms of the NiW-carbon materials, after activation, are given in Figure S2 and the textural properties are listed in Table 2.

The alginate-derived catalyst, NiW-[C]-H<sub>2</sub>, showed textural properties that are close to the values obtained for the sole support. A slight decrease in the BET surface area (from 273 to 254 m<sup>2</sup>.g<sup>-1</sup>), due to W and Ni loadings, is observed. The isotherm shape changed, shifting from type I to type IV, showing that despite a minor modification of the surface area, the support suffered from significant restructuring. This porosity restructuring is clearly observed with the presence of N<sub>2</sub> uptake at P/P<sub>0</sub> above 0.7 (Figure S2), which can be attributed to the additional presence of mesopores for the Ni-W containing catalyst. Different behaviors are observed for the N-doped samples. When the sample is activated under N<sub>2</sub> (NiW-[NC]-N<sub>2</sub>), consequent porosity is retained, with minor modification of surface area and pore volume. However, when activated under H<sub>2</sub>, significant modifications of textural properties occur. Surface area decreases from 287 to 173 m<sup>2</sup>.g<sup>-1</sup> for NiW-[NC]-H<sub>2</sub>, a decrease even more marked for NiW-[M+NC]-H<sub>2</sub> (328 vs. 41 m<sup>2</sup>.g<sup>-1</sup>), due to the fact that [M+NC] is richer in N as compared to [NC] (Table 1), thus [M+NC] is more reactive with the metals. To conclude, N<sub>2</sub> activation treatment has limited impact on textural parameter while H<sub>2</sub> treatment induces a significant modification of N-containing supports that seem far less stable than the N-free carbon support.

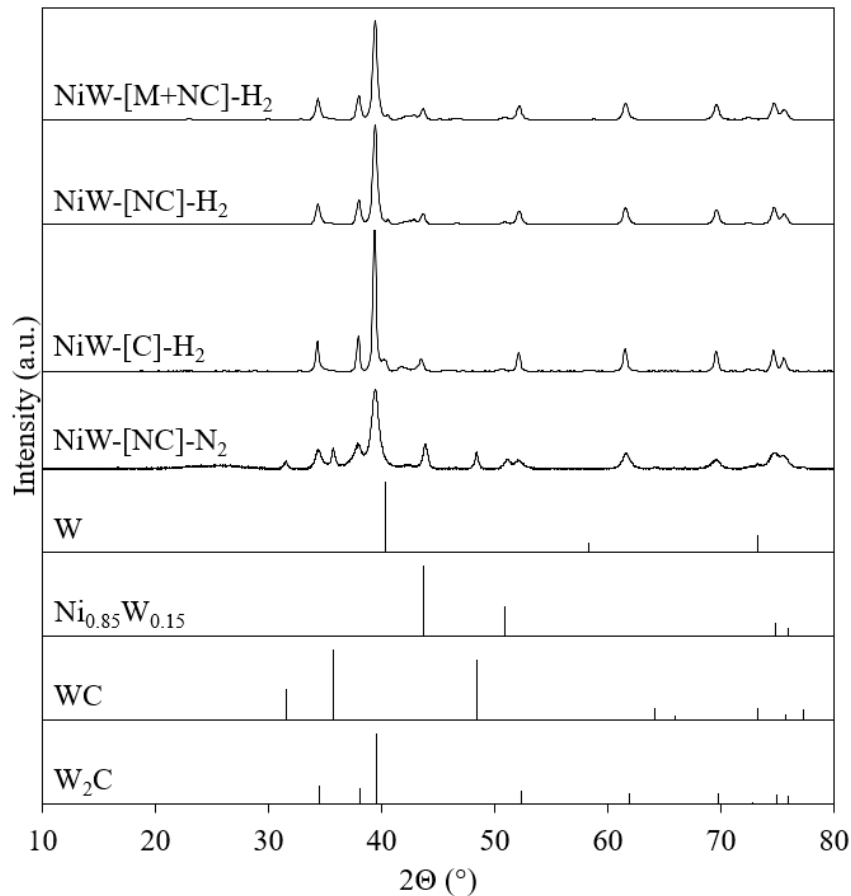


**Figure 2.** XRD patterns of the carbon-supported NiW materials.

XRD performed on material after activation are presented in Figure 2. The diffractogram obtained for NiW-[NC]-N<sub>2</sub> shows the presence of WC (JCPDS: 65-4539), W<sub>2</sub>C (JCPDS: 35-0776), and Ni<sub>0.85</sub>W<sub>0.15</sub> (JCPDS: 65-4828) phases. When activation was conducted under hydrogen (NiW-X-H<sub>2</sub>; X = [C], [NC], [M+NC]), pure W<sub>2</sub>C was formed along with the Ni<sub>0.85</sub>W<sub>0.15</sub> alloy, corresponding stoichiometrically speaking to Ni<sub>17</sub>W<sub>3</sub>, as reported by several authors for NiW supported on commercial activated carbon<sup>2,19</sup>. It is noteworthy to mention that no Ni<sub>6</sub>W<sub>6</sub>C has been detected in contrast with our previous study on activated carbon support<sup>19</sup>. A small peak identified as metallic W (JCPDS: 04-0806) was also detected for the H<sub>2</sub>-reduced samples. Therefore, different activation atmospheres lead to the formation of different metal phases, while N-doping in the support does not seem to have a crystallization directing effect since the same phases were formed in very close proportions regardless the nitrogen content in the support (Table 4): 82-87% W<sub>2</sub>C / 13-21% Ni<sub>0.85</sub>W<sub>0.15</sub>. The average crystallite diameters for detected phases were calculated using the Scherrer equation (Table 4). All materials activated

under H<sub>2</sub> present similar W<sub>2</sub>C and Ni<sub>0.85</sub>W<sub>0.15</sub> sizes, in both cases around 20 nm. When N<sub>2</sub> activation is performed, W<sub>2</sub>C crystallite retains slightly smaller sizes (15 nm) but the WC crystallites seems to stabilize at slightly larger size (30 nm). The nickel phase is not significantly affected by the gas treatment nature.

**Table 4.** Identified species from XRD analysis, with average particle size<sup>(a)</sup> and proportion for tungsten phase species<sup>(b)</sup>

NiW-[C]-H <sub>2</sub>	NiW-[NC]-N <sub>2</sub>	NiW-[NC]-H <sub>2</sub>	NiW-[M+NC]-H <sub>2</sub>
W <sub>2</sub> C (22 nm ; 87 %)	W <sub>2</sub> C (15 nm ; 95 %)	W <sub>2</sub> C (20 nm ; 79 %)	W <sub>2</sub> C (19 nm ; 82 %)
	WC (30 nm ; 1 %)		
Ni <sub>0.85</sub> W <sub>0.15</sub> (20 nm ; 13 %)	Ni <sub>0.85</sub> W <sub>0.15</sub> (19 nm ; 4 %)	Ni <sub>0.85</sub> W <sub>0.15</sub> (22 nm ; 21 %)	Ni <sub>0.85</sub> W <sub>0.15</sub> (22 nm ; 18 %)

<sup>(a)</sup> Determined using the Scherrer equation; <sup>(b)</sup> obtained by semi-quantitative analysis

XPS measurements were performed in order to identify electronic environment of metallic (W, Ni) species. The XPS spectra of passivated NiW-[C]-H<sub>2</sub>, NiW-[NC]-H<sub>2</sub>, NiW-[M+NC]-H<sub>2</sub>, and NiW-[NC]-N<sub>2</sub> (core level signals for W 4f, Ni 2p, N 1s) are presented in Figures 3 and S3.

Concentrations of Ni and W (Table 5) as well as the percentages of the oxidation states of the different elements (Table S2) are also provided. For example, NiW-[NC]-N<sub>2</sub> and NiW-[NC]-H<sub>2</sub> present Ni surface concentrations of 0.5 and 1.2 wt% and W surface concentrations of 8.8 and 9.1 wt% (Table 5). These values are significantly lower than bulk values of 5.2 and 8.6 wt% (Ni) and 30.4 and 52.3 wt% (W) for NiW-[NC]-N<sub>2</sub> and NiW-[NC]-H<sub>2</sub> respectively (Table 3). This is coherent with the limited dispersion observed for the Ni and W phases, in favor of a diminution of the element concentration as measured by XPS. Analysis of the W 4f core level spectra allow to identify 3 different tungsten species over all materials: W<sub>x</sub>C (4f<sub>7/2</sub>: 31.46 eV and 4f<sub>5/2</sub>: 33.64 eV), W<sup>6+</sup> (4f<sub>7/2</sub>: 35.6 eV, 4f<sub>5/2</sub>: 37.78 eV) and W\* (4f<sub>7/2</sub>: 35.2 eV, 4f<sub>5/2</sub>: 37.38 eV). The oxidized tungsten intermediate is commonly denoted W\*, and according to the literature its oxidation state is between 4+ and 5+<sup>16</sup>. For all the materials tungsten is highly oxidized on the surface (> 75 % of WO<sub>x</sub>), which is coherent with the formation of a passivation layer. However, with the increase of N-content, the proportion of residual W<sub>x</sub>C (W<sub>2</sub>C cannot be differentiated from WC by XPS)

increases, from 9 % for NiW-[C]-H<sub>2</sub> to 25 % for NiW-[M+NC]-H<sub>2</sub>. Residual W<sub>x</sub>C content seems to be higher on catalysts activated under H<sub>2</sub>, (9 wt% for NiW-[NC]-N<sub>2</sub> vs 17 wt% NiW-[NC]-H<sub>2</sub>) and on catalyst supported over N containing supports (9 wt% for NiW-[C]-H<sub>2</sub> vs 25 wt% NiW-[M+NC]-H<sub>2</sub>). Analyzing Ni 2p spectra show that Ni is present as metallic nickel Ni<sup>0</sup> (2p<sub>3/2</sub>: 852.6 eV and plasmon loss peaks : 856.3 eV and 858.7 eV) and oxidized Ni<sup>2+</sup> (2p<sub>3/2</sub>: 854.9 eV and satellites : 855.7 eV, 857.7 eV, 860.5 eV, 861.5 eV, and 866.5 eV)<sup>28</sup>. However, due to the passivation step, Ni is mostly present as oxidized species on the surface.

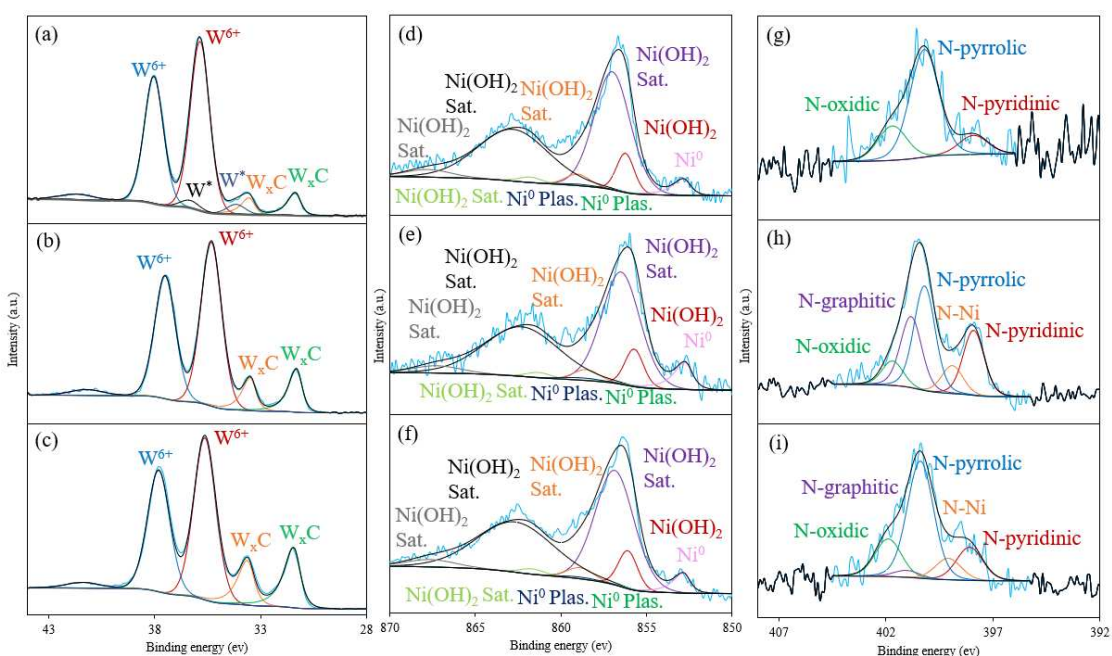


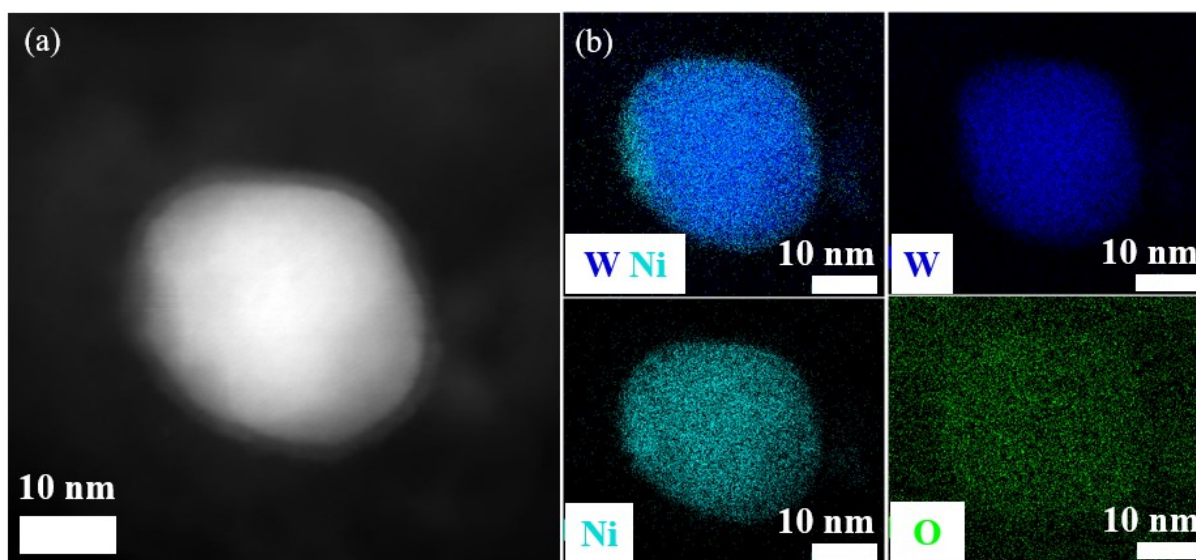
**Figure 3.** XPS results of : W 4f in (a) NiW-[C]-H<sub>2</sub>, (b) NiW-[NC]-H<sub>2</sub>, (c) NiW-[M+NC]-H<sub>2</sub> ; Ni 2p in (d) NiW-[C]-H<sub>2</sub>, (e) NiW-[NC]-H<sub>2</sub>, (f) NiW-[M+NC]-H<sub>2</sub> ; N 1s in (g) NiW-[C]-H<sub>2</sub>, (h) NiW-[NC]-H<sub>2</sub>, (i) NiW-[M+NC]-H<sub>2</sub>.

Analyzing the N 1s spectra confirms the presence of nitrogen in the NiW-[C]-H<sub>2</sub> sample (Figure 3(g)). All spectra display N-oxidic, N-pyrrolic and N-pyridinic species in addition to N-graphitic for catalysts synthesized over [NC] and [M+NC]. N-doped catalysts feature an extra peak at 398.91 eV, assigned to the interaction of Ni atoms with pyridinic N<sup>20</sup>. Pyrrolic and pyridinic N are excellent metal anchoring sites owing to their lone-pair electrons<sup>29–33</sup>.

**Table 5.** Ni and W surface concentration as measured by XPS.

Material	W (wt%)	Ni (wt%)	W/Ni
NiW-[C]-H <sub>2</sub>	12.1	1.4	8.64
NiW-[NC]-N <sub>2</sub>	8.8	0.5	17.6
NiW-[NC]-H <sub>2</sub>	9.1	1.2	7.58
NiW-[M+NC]-H <sub>2</sub>	29.4	3.3	8.91

Samples, after activation and passivation, were analyzed by HR-TEM (Figures 4 and S4-S7). Whatever the sample, TEM images show the presence of both small nanoparticles of average size < 3 nm and much bigger particles of 20-60 nm. The presence of two particle distributions could be associated to their chemical nature and their growth in different locations: *e.g.*, in micropores-mesopores or macropores, as well as outside the porous framework or even near the pore entrances<sup>34</sup>. The elemental analysis confirmed the homogeneous dispersion of nickel and tungsten at the aggregate size level. However, over large particles, an external enrichment of nickel is observed at the particle surface, leading to the formation of particles with W-rich core and Ni-rich shell (Figure 4). In addition, and whatever the activation nature or the catalyst surface, some almost pure Ni and almost pure W particles are observed (Figure S7b).

**Figure 4.** (a) HAADF-STEM and (b) TEM-EDS elemental mapping images of the material; NiW-[M+NC]-H<sub>2</sub>.



H<sub>2</sub>-TPR analysis that can give information about the reducibility of the catalyst, the metal dispersion, support-metal, and metal–metal interactions<sup>16</sup> are presented in Figure S8a-b. Figure S8b shows the H<sub>2</sub>-TPR profile of NiW-[NC]-N<sub>2</sub>. However, the catalyst seems not stable and significant signal is observed during the reduction experiment due to the reduction and methanation of the support. More conventional reduction profiles are recorded for H<sub>2</sub> activated catalysts (Figure S8a). In the following discussion, only these last samples will be considered, assuming that signal is only associated to the reduction of either Ni or W oxidized species. The low-temperature reduction peaks, can be ascribed to the reduction of Ni<sup>2+</sup>, formed after the passivation step<sup>35,36</sup>. Large Ni(OH)<sub>2</sub> particles will first reduce, followed by the reduction of smaller particles. Finally, hardly reducible Ni<sup>2+</sup> (in strong interaction with the support) are expected to reduce. Later the reduction of tungsten and tungsten oxycarbides and formation of nickel-tungsten alloy Ni<sub>0.85</sub>W<sub>0.15</sub>, as identified by XRD<sup>14,37</sup>, take place.

### ***3.3.2. Application to the catalytic conversion of cellulose***

The one-pot conversion of cellulose or woody biomass is a complex process. The literature indicates that materials with supported Ni and W sites can hydrogenolyse cellulose into light polyols like glycols. Here the tungsten and nickel species contribute respectively to the formation of unsaturated intermediates via the retro-aldol condensation, and hydrogenation reactions of these intermediates<sup>14</sup>. Particularly, some of us explored and reported<sup>19</sup> the exact nature of the metal species when the support is an active carbon with the conclusion that concerning the W<sub>x</sub>C species, no real influence of WC nor W<sub>2</sub>C was evidenced, in contrast to the NiW alloys that may present a significant effect on the efficiency of the transformation.

The goal here is to assess the influence of N-doping on carbon supports for this transformation that occurs in the conditions of the reaction at 245 °C under 60 bars of H<sub>2</sub>. In each experiment, cellulose was completely liquefied, based on the TOC measurements, ie all carbon present in the cellulose was present in the liquid phase, excluding the formation of carbon-base gaseous and of solid products. The catalytic results are presented in Figure 5 and Table S3. The first thing to note is that the catalyst NiW-[C]-H<sub>2</sub> gave a result close to that obtained with its equivalent prepared on activated carbon NiW/AC, as reported before<sup>19</sup> with a cumulated yield of 60% into glycols. (see Table S3 for side-products quantification). It is not surprising to obtain comparable

results since similar Ni and W species are present on the alginate-derived carbon (this study) and the NiW-commercial carbon catalyst (our previous study).

Concerning the catalysts with N-doped carbon supports, NiW-[NC]-H<sub>2</sub> and NiW-[M+NC]-H<sub>2</sub>, there is no significant influence with global glycols yields falling in the range of 56 to 63 %. For all H<sub>2</sub>-reduced catalysts, the PG yield is almost constant (5-8 mol.%), and the amount of side-products varied only slightly (Table S3). Thus, at this stage, the presence of nitrogen in the support does not promote the formation of glycols as long as the Ni and W surface species are the same. One can nevertheless note that the best yields were obtained with the catalyst having the highest content of Ni and W (see Table 3) despite having the lowest surface area and pore volume (see Table 2), indicating that even for the transformation of polysaccharides, textural aspects are not necessary the main influencing factors. In fact, among the 4 catalytic materials, only the catalyst activated under N<sub>2</sub>, NiW-[NC]-N<sub>2</sub>, was aside giving a low glycol yield of 28 %. This catalyst presents, according to the XPS quantification (see Table 5), the highest m<sub>W</sub>/m<sub>Ni</sub> ratio of 17.6, relatively high compared to the H<sub>2</sub> reduced samples that have values between 7.58 and 8.91. Therefore, NiW-[NC]-N<sub>2</sub> can lack nickel on its surface relatively to the H<sub>2</sub> reduced samples, resulting in lower activity.

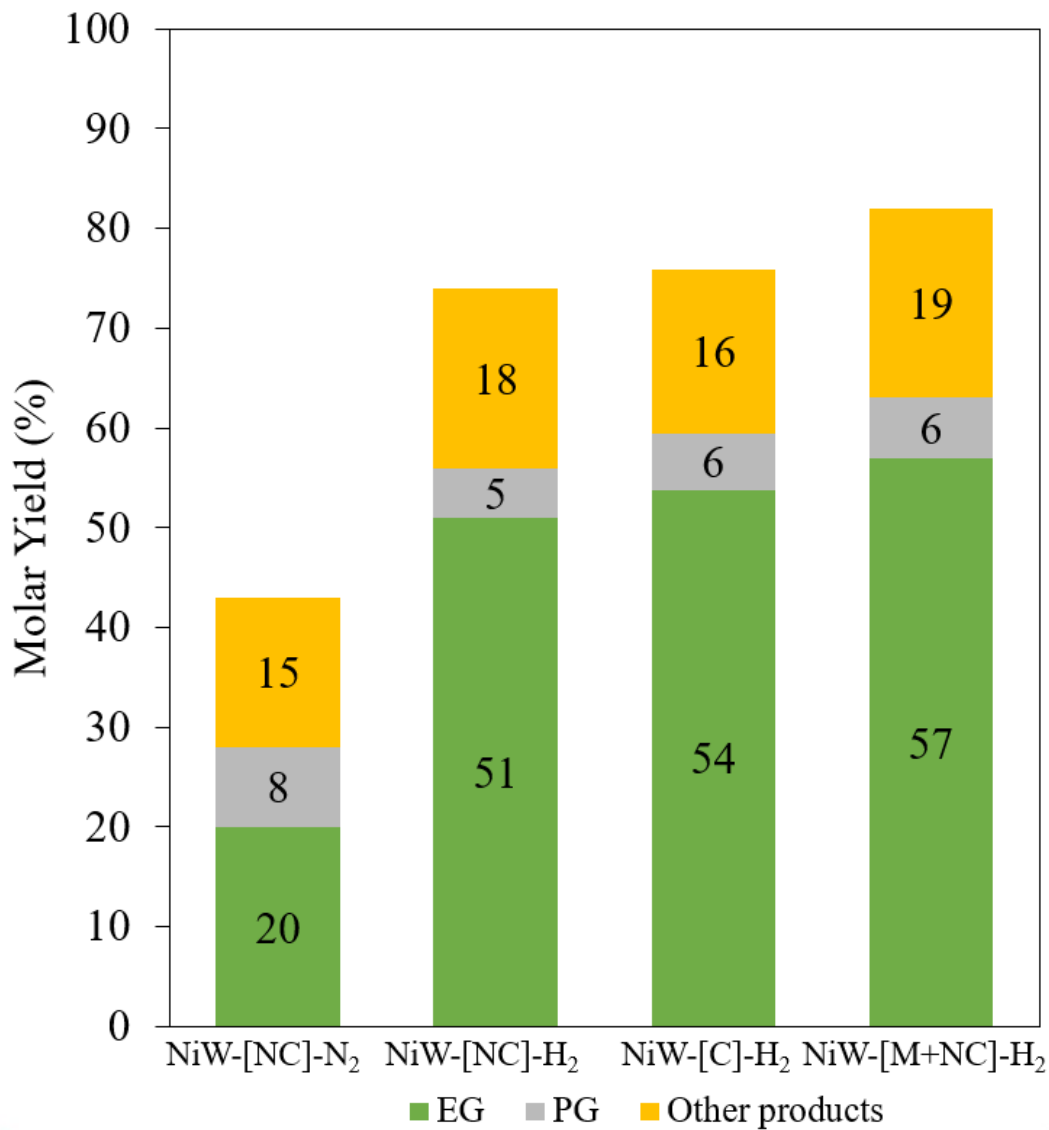


**Figure 5.** Product yields over various catalysts having different N percentages and activated in different environments. Reaction conditions: 0.50 g cellulose, 0.15 g catalyst, 50 mL water, 60 bar H<sub>2</sub>, 1000 rpm, 245 °C, and 1 hour.

Afterward, the stability of NiW-[C]-H<sub>2</sub> and NiW-[M+NC]-H<sub>2</sub> catalysts was compared to see the influence of the amount of nitrogen within the carbon support (Figure 6). The same reaction conditions were applied for each run without any reactivation treatment in between. With NiW-[C]-H<sub>2</sub> an impressive decrease in glycol yield was observed, only partly compensated by the presence of reaction intermediates. On the other hand, the yields of glycols remained relatively stable from the first to the third run for NiW-[M+NC]-H<sub>2</sub>, and therefore here the presence of additional nitrogen within the support, even in a low amount, may contribute to the observed stability.

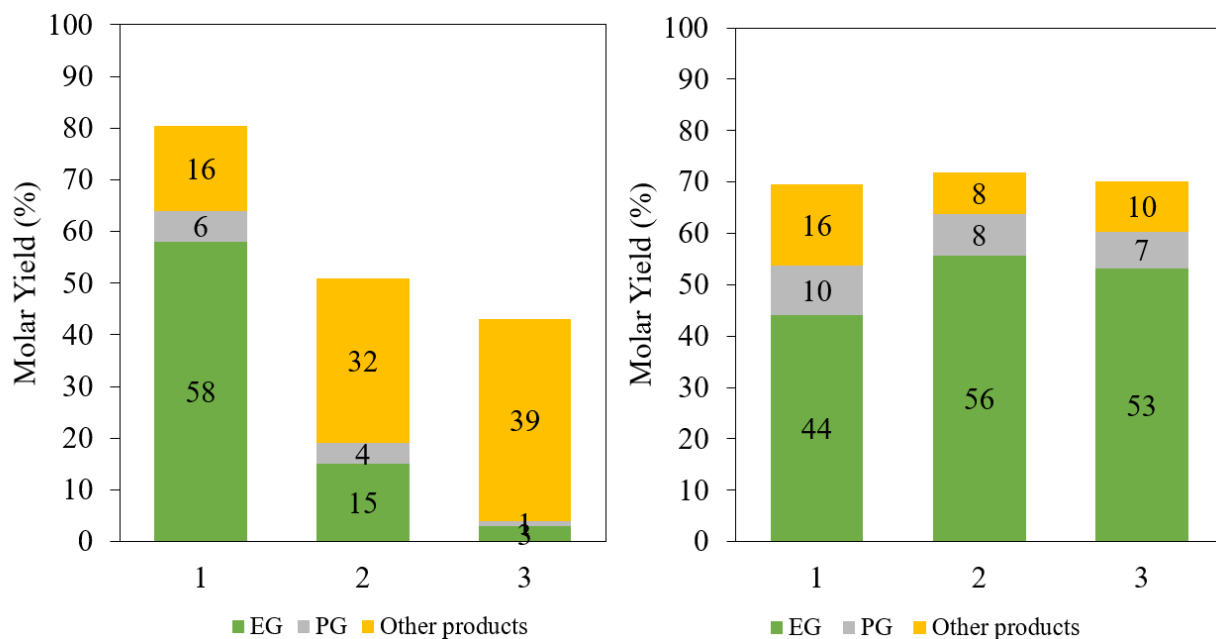


**Figure 6.** Recycling experiments on the conversion of cellulose into polyols over the 2 catalysts: (a) NiW-[C]-H<sub>2</sub> and (b) NiW-[M+NC]-H<sub>2</sub>. Reaction conditions: 0.50 g cellulose, 0.15 g catalyst, 50 mL water, 60 bar H<sub>2</sub>, 1000 rpm, 245 °C, and 1 hour.

The reaction solutions after the first run were recovered and examined by ICP-OES (Table 6). NiW-[M+NC]-H<sub>2</sub> catalyst had a small amount of Ni leached, representing 1.9 % of the initial mass of Ni present in the catalyst. In contrast, 4.4 % of the initial nickel is leached from NiW-[C]-H<sub>2</sub>. The difference is also noticeable with W leaching, which remained lower with NiW-[M+NC]-H<sub>2</sub> (2.7 wt.% vs. 5.8 wt.%). The presence of nitrogen within the support seems to be efficient to stabilize Ni and W species. The N-containing carbon layer promoted the resistance ability against acid-etching (from water autoprotonation) of nickel and tungsten sites, limiting catalyst deactivation.

**Table 6.** Concentration of Ni and W with the corresponding leaching proportion.

Material	Concentration <sup>(a)</sup> (mg.L <sup>-1</sup> )		Leaching (%)	
	Ni	W	Ni	W
NiW-[C]-H <sub>2</sub>	10.2	80	4.4	5.8
NiW-[M+NC]-H <sub>2</sub>	6.9	57.4	1.9	2.7

<sup>(a)</sup> Obtained by ICP-EOS on the liquid reaction medium.

### 3.3.3. Characterization of catalysts after catalysis

The three samples, activated under H<sub>2</sub>, were characterized after one reaction cycle. The surface areas of the samples decreased significantly after reaction (Table S4). After reaction, the surface area of NiW-[C]-H<sub>2</sub> decreased from 254 m<sup>2</sup>.g<sup>-1</sup> to 111 m<sup>2</sup>.g<sup>-1</sup>. For NiW-[M+NC]-H<sub>2</sub>, it decreased from 41 m<sup>2</sup>.g<sup>-1</sup> to 10 m<sup>2</sup>.g<sup>-1</sup> (Tables 2 and S4). No significant sintering of the W<sub>2</sub>C (d ~20 nm as determined by XRD) phase was detected after the reaction, for all the hydrogen-reduced samples (Figure S9). After reaction, W<sub>2</sub>C size for NiW-[C]-H<sub>2</sub>, NiW-[NC]-H<sub>2</sub> and NiW-[M+NC]-H<sub>2</sub> remained the same (Tables 4 and S5). From XRD, some restructuring of the alloy phase (Ni<sub>0.85</sub>W<sub>0.15</sub>; d ~20 nm; Table 4) seems to occur since the reflections disappeared after reaction and a pure nickel phase appeared (for the N-doped catalysts, Figure S9). It is noteworthy that the virtue of N-doping on the anchoring, in particular for the nickel species, is well enforced by the fact that there were no nickel phases detected for the NiW-[C]-H<sub>2</sub>-AR catalyst. Meaning that a great Ni percentage was leached for this catalyst unlike NiW-[NC]-H<sub>2</sub> and NiW-[M+NC]-H<sub>2</sub> this was also deduced from the liquid ICP results in Table 6.

According to the XPS spectra, all tungsten species identified prior to the reaction remain after the reaction. Metallic Ni concentration is significantly reduced after reaction, a disappearance that could also be attributed to the oxidation of the metallic Ni particles during the reaction: Ni<sup>0</sup> percentage decreases from 8 % to 1 % for NiW-[NC]-H<sub>2</sub> and from 5 % to 2 % for NiW-[M+NC]-H<sub>2</sub> after the reaction (Tables S2 and S7). The same nitrogen species are detected over catalysts after the reaction than before reaction, although the intensities of the N-Ni peak and the graphitic N peak were modified to some extent: N-Ni percentage increases from 0 % to 5 % for NiW-[C]-H<sub>2</sub>, it decreases from 10 % to 7 % for NiW-[NC]-H<sub>2</sub> and from 3 % to 1 % for NiW-[M+NC]-H<sub>2</sub> after the reaction (Tables S2 and S7). The graphitic N percentage decreases from 24 % to 16 % for NiW-[NC]-H<sub>2</sub> and from 18 % to 0 % for NiW-[M+NC]-H<sub>2</sub> after the reaction (Tables S2 and S7). Finally, no significant sintering can be identified by comparing the TEM images obtained before and after reaction (Figures S11-S13), which confirms the XRD results that did not allow to identify any crystal growth (Figure S9, Table S5). All these results are in favor of a deactivation mechanism occurring mostly due to active species dissolution over carbon support. When N atoms incorporate the carbon surface, better catalytic stability is observed, due to a lower dissolution rate of either Ni or W active species.

### 3.4. Conclusion

We synthesized nickel and tungsten-based catalysts supported on porous carbons, both standard and N-doped. The synthesis process includes a hydrothermal treatment starting from biosourced polymers precursors, followed by pyrolysis under an inert or reducing atmosphere. Metals incorporation was performed by wet impregnation. For example, a porous N-doped carbon of surface area  $>280 \text{ m}^2 \cdot \text{g}^{-1}$  was obtained from the hydrothermal-pyrolysis treatment of chitosan. The variation of the activation atmosphere, from nitrogen to hydrogen, of the catalyst yielded different phases of tungsten carbides: tungsten semi-carbide ( $\text{W}_2\text{C}$ ) and tungsten mono-carbide ( $\text{WC}$ ), with an influence on the catalytic activity. Indeed, when this catalyst was activated under  $\text{N}_2$  ( $\text{NiW}[\text{NC}]\text{-N}_2$ ), it transformed cellulose into, 20% of ethylene glycol and 8% in propylene glycol at  $245 \text{ }^\circ\text{C}$  in a reaction time of 1 hour ; when the catalyst was activated under  $\text{H}_2$  ( $\text{NiW}[\text{NC}]\text{-H}_2$ ), glycol yields increased up to 51% for EG and 5% in PG . As another trend, while the N-doping of carbon supports demonstrated a limited effect on the catalytic activity compared to usual carbon supports, a great influence on the catalytic stability was observed during recycling tests. The improvement of stability was associated with lower nickel and tungsten leaching during catalytic reactions, due to the active elements immobilized over N-containing species of supports. The use of N-containing carbon support is therefore a reliable strategy to manufacture resistant metallic catalysts for cellulose conversion under severe hydrothermal reaction conditions.

### 3.5. References

- (1) Kumar, A. K.; Sharma, S. Recent Updates on Different Methods of Pretreatment of Lignocellulosic Feedstocks: A Review. *Bioresour. Bioprocess.* **2017**, *4* (1), 7. <https://doi.org/10.1186/s40643-017-0137-9>.
- (2) Ji, N.; Zhang, T.; Zheng, M.; Wang, A.; Wang, H.; Wang, X.; Chen, J. G. Direct Catalytic Conversion of Cellulose into Ethylene Glycol Using Nickel-Promoted Tungsten Carbide Catalysts. *Angew. Chem. Int. Ed.* **2008**, *47* (44), 8510–8513. <https://doi.org/10.1002/anie.200803233>.
- (3) Wang, A.; Zhang, T. One-Pot Conversion of Cellulose to Ethylene Glycol with Multifunctional Tungsten-Based Catalysts. *Acc. Chem. Res.* **2013**, *46* (7), 1377–1386. <https://doi.org/10.1021/ar3002156>.
- (4) Kim, K. H.; Dutta, T.; Sun, J.; Simmons, B.; Singh, S. Biomass Pretreatment Using Deep Eutectic Solvents from Lignin Derived Phenols. *Green Chem.* **2018**, *20* (4), 809–815. <https://doi.org/10.1039/C7GC03029K>.
- (5) Luo, H.; Abu-Omar, M. M. Lignin Extraction and Catalytic Upgrading from Genetically Modified Poplar. *Green Chem.* **2018**, *20* (3), 745–753. <https://doi.org/10.1039/C7GC03417B>.

- (6) Dietrich, K.; Hernandez-Mejia, C.; Verschuren, P.; Rothenberg, G.; Shiju, N. R. One-Pot Selective Conversion of Hemicellulose to Xylitol. *Org. Process Res. Dev.* **2017**, *21* (2), 165–170. <https://doi.org/10.1021/acs.oprd.6b00169>.
- (7) Xu, G.; Wang, A.; Pang, J.; Zhao, X.; Xu, J.; Lei, N.; Wang, J.; Zheng, M.; Yin, J.; Zhang, T. Chemocatalytic Conversion of Cellulosic Biomass to Methyl Glycolate, Ethylene Glycol, and Ethanol. *ChemSusChem* **2017**, *10* (7), 1390–1394. <https://doi.org/10.1002/cssc.201601714>.
- (8) Zheng, M.; Pang, J.; Sun, R.; Wang, A.; Zhang, T. Selectivity Control for Cellulose to Diols: Dancing on Eggs. *ACS Catal.* **2017**, *7* (3), 1939–1954. <https://doi.org/10.1021/acscatal.6b03469>.
- (9) Ooms, R.; Dusselier, M.; Geboers, J. A.; Op de Beeck, B.; Verhaeven, R.; Gobechiya, E.; Martens, J. A.; Redl, A.; Sels, B. F. Conversion of Sugars to Ethylene Glycol with Nickel Tungsten Carbide in a Fed-Batch Reactor: High Productivity and Reaction Network Elucidation. *Green Chem* **2014**, *16* (2), 695–707. <https://doi.org/10.1039/C3GC41431K>.
- (10) Li, N.; Zheng, Y.; Wei, L.; Teng, H.; Zhou, J. Metal Nanoparticles Supported on WO<sub>3</sub> Nanosheets for Highly Selective Hydrogenolysis of Cellulose to Ethylene Glycol. *Green Chem.* **2017**, *19* (3), 682–691. <https://doi.org/10.1039/C6GC01327A>.
- (11) Yang, Y.; Zhang, W.; Yang, F.; Brown, D. E.; Ren, Y.; Lee, S.; Zeng, D.; Gao, Q.; Zhang, X. Versatile Nickel–Tungsten Bimetallics/Carbon Nanofiber Catalysts for Direct Conversion of Cellulose to Ethylene Glycol. *Green Chem.* **2016**, *18* (14), 3949–3955. <https://doi.org/10.1039/C6GC00703A>.
- (12) Xiao, Z.; Zhang, Q.; Chen, T.; Wang, X.; Fan, Y.; Ge, Q.; Zhai, R.; Sun, R.; Ji, J.; Mao, J. Heterobimetallic Catalysis for Lignocellulose to Ethylene Glycol on Nickel-Tungsten Catalysts: Influenced by Hydroxy Groups. *Fuel* **2018**, *230*, 332–343. <https://doi.org/10.1016/j.fuel.2018.04.115>.
- (13) Zhang, Y.; Wang, A.; Zhang, T. A New 3D Mesoporous Carbon Replicated from Commercial Silica as a Catalyst Support for Direct Conversion of Cellulose into Ethylene Glycol. *Chem Commun* **2010**, *46* (6), 862–864. <https://doi.org/10.1039/B919182H>.
- (14) Fabičovicová, K.; Malter, O.; Lucas, M.; Claus, P. Hydrogenolysis of Cellulose to Valuable Chemicals over Activated Carbon Supported Mono- and Bimetallic Nickel/Tungsten Catalysts. *Green Chem* **2014**, *16* (7), 3580–3588. <https://doi.org/10.1039/C4GC00664J>.
- (15) Gu, M.; Shen, Z.; Yang, L.; Dong, W.; Kong, L.; Zhang, W.; Peng, B.-Y.; Zhang, Y. Reaction Route Selection for Cellulose Hydrogenolysis into C<sub>2</sub>/C<sub>3</sub> Glycols by ZnO-Modified Ni-W/ $\beta$ -Zeolite Catalysts. *Sci. Rep.* **2019**, *9* (1), 11938. <https://doi.org/10.1038/s41598-019-48103-6>.
- (16) Rodella, C. B.; Barrett, D. H.; Moya, S. F.; Figueroa, S. J. A.; Pimenta, M. T. B.; Curvelo, A. A. S.; Silva, V. T. da. Physical and Chemical Studies of Tungsten Carbide Catalysts: Effects of Ni Promotion and Sulphonated Carbon. *RSC Adv.* **2015**, *5* (30), 23874–23885. <https://doi.org/10.1039/C5RA03252K>.
- (17) Xiao, Z.; Wang, X.; Yang, Q.; Xing, C.; Ge, Q.; Gai, X.; Mao, J.; Ji, J. Fabrication of Immobilized Nickel Nanoclusters Decorated by C N Species for Cellulose Conversion to C<sub>2,3</sub> Oxygenated Compounds: Rational Design via Typical C- and N-Sources. *J. Energy Chem.* **2020**, *50*, 25–36. <https://doi.org/10.1016/j.jechem.2020.02.054>.
- (18) Xiao, Z.; Zhang, Q.; Wang, X.; Ge, Q.; Gai, X.; Mao, J.; Ji, J. Organic Nitrogen Promotes Stability of Metallic Catalysts in Conversion of Bamboo Pulp to Low Carbon Polyols. *J.*

- Fuel Chem. Technol.* **2019**, *47* (6), 675–687. [https://doi.org/10.1016/S1872-5813\(19\)30029-5](https://doi.org/10.1016/S1872-5813(19)30029-5).
- (19) Goc, F.; Epicier, T.; Perret, N.; Rataboul, F. Preparation of Carbon-Supported Tungsten Carbides: Comparative Determination of Surface Composition and Influence on Cellulose Transformation into Glycols. *ChemCatChem* **2023**, e202201496. <https://doi.org/10.1002/cctc.202201496>.
- (20) Hammi, N.; Chen, S.; Dumeignil, F.; Royer, S.; El Kadib, A. Chitosan as a Sustainable Precursor for Nitrogen-Containing Carbon Nanomaterials: Synthesis and Uses. *Mater. Today Sustain.* **2020**, *10*. <https://doi.org/10.1016/j.mtsust.2020.100053>.
- (21) Hammi, N.; Chen, S.; Michon, C.; Royer, S.; El Kadib, A. Cu Nanoparticles Embedded on Reticular Chitosan-Derived N-Doped Carbon: Application to the Catalytic Hydrogenation of Alkenes, Alkynes and N-Heteroarenes. *Mol. Catal.* **2022**, *519*, 112104. <https://doi.org/10.1016/j.mcat.2021.112104>.
- (22) Hammi, N.; Marcotte, N.; Marinova, M.; Draoui, K.; Royer, S.; El Kadib, A. Nanostructured Metal Oxide@Carbon Dots Through Sequential Chitosan Templating and Carbonisation Route. *Carbohydr. Polym. Technol. Appl.* **2021**, *2*, 100043. <https://doi.org/10.1016/j.carpta.2021.100043>.
- (23) Xing, Z.; Ju, Z.; Zhao, Y.; Wan, J.; Zhu, Y.; Qiang, Y.; Qian, Y. One-Pot Hydrothermal Synthesis of Nitrogen-Doped Graphene as High-Performance Anode Materials for Lithium Ion Batteries. *Sci. Rep.* **2016**, *6* (1), 26146. <https://doi.org/10.1038/srep26146>.
- (24) Li, M.; Han, X.; Chang, X.; Yin, W.; Ma, J. Nitrogen/Sulfur-Codoped Carbon Materials from Chitosan for Supercapacitors. *J. Electron. Mater.* **2016**, *45* (8), 4331–4337. <https://doi.org/10.1007/s11664-016-4644-9>.
- (25) Jordan, T.; Yu, Z.-L.; Yu, S.-H.; Antonietti, M.; Fechler, N. Porous Nitrogen-Doped Carbon Monoliths Derived from Biopolymer-Structured Liquid Precursors. *Microporous Mesoporous Mater.* **2018**, *255*, 53–60. <https://doi.org/10.1016/j.micromeso.2017.07.032>.
- (26) Zhang, J.-F.; Zhong, R.; Zhou, Q.; Hong, X.; Huang, S.; Cui, H.-Z.; Hou, X.-F. Recyclable Silica-Supported Iridium Catalysts for Selective Reductive Transformation of Quinolines with Formic Acid in Water. *ChemCatChem* **2017**, *9* (13), 2496–2505. <https://doi.org/10.1002/cctc.201700128>.
- (27) Ziegler-Borowska, M.; Chełminiak, D.; Kaczmarek, H. Thermal Stability of Magnetic Nanoparticles Coated by Blends of Modified Chitosan and Poly(Quaternary Ammonium) Salt. *J. Therm. Anal. Calorim.* **2015**, *119* (1), 499–506. <https://doi.org/10.1007/s10973-014-4122-7>.
- (28) Biesinger, M. C.; Payne, B. P.; Lau, L. W. M.; Gerson, A.; Smart, R. St. C. X-Ray Photoelectron Spectroscopic Chemical State Quantification of Mixed Nickel Metal, Oxide and Hydroxide Systems. *Surf. Interface Anal.* **2009**, *41* (4), 324–332. <https://doi.org/10.1002/sia.3026>.
- (29) Liu, R.; Wu, D.; Feng, X.; Müllen, K. Nitrogen-Doped Ordered Mesoporous Graphitic Arrays with High Electrocatalytic Activity for Oxygen Reduction. *Angew. Chem. Int. Ed.* **2010**, *49* (14), 2565–2569. <https://doi.org/10.1002/anie.200907289>.
- (30) Zhao, X.; Yang, H.; Jing, P.; Shi, W.; Yang, G.; Cheng, P. A Metal-Organic Framework Approach toward Highly Nitrogen-Doped Graphitic Carbon as a Metal-Free Photocatalyst for Hydrogen Evolution. *Small* **2017**, *13* (9), 1603279. <https://doi.org/10.1002/sml.201603279>.



- (31) Bulushev, D. A.; Chuvilin, A. L.; Sobolev, V. I.; Stolyarova, S. G.; Shubin, Y. V.; Asanov, I. P.; Ishchenko, A. V.; Magnani, G.; Riccò, M.; Okotrub, A. V.; Bulusheva, L. G. Copper on Carbon Materials: Stabilization by Nitrogen Doping. *J. Mater. Chem. A* **2017**, *5* (21), 10574–10583. <https://doi.org/10.1039/C7TA02282D>.
- (32) Roldán, L.; Truong-Phuoc, L.; Ansón-Casaos, A.; Pham-Huu, C.; García-Bordejé, E. Mesoporous Carbon Doped with N,S Heteroatoms Prepared by One-Pot Auto-Assembly of Molecular Precursor for Electrocatalytic Hydrogen Peroxide Synthesis. *Catal. Today* **2018**, *301*, 2–10. <https://doi.org/10.1016/j.cattod.2016.12.020>.
- (33) Tian, H.; Zhang, C.; Su, P.; Shen, Z.; Liu, H.; Wang, G.; Liu, S.; Liu, J. Metal-Organic-Framework-Derived Formation of Co–N-Doped Carbon Materials for Efficient Oxygen Reduction Reaction. *J. Energy Chem.* **2020**, *40*, 137–143. <https://doi.org/10.1016/j.jechem.2019.03.004>.
- (34) Li, C.; Xie, J.; Zhang, J.; Dai, B. Nitrogen-Modified Activated Carbon Supported Cu(II)Cu(I)/NAC Catalysts for Gas–Solid Acetylene Dimerization. *Catal. Lett.* **2021**, *151* (10), 2990–2995. <https://doi.org/10.1007/s10562-021-03548-1>.
- (35) Ungureanu, A.; Dragoi, B.; Chiriac, A.; Ciotonea, C.; Royer, S.; Duprez, D.; Mamede, A. S.; Dumitriu, E. Composition-Dependent Morphostructural Properties of Ni–Cu Oxide Nanoparticles Confined within the Channels of Ordered Mesoporous SBA-15 Silica. *ACS Appl. Mater. Interfaces* **2013**, *5* (8), 3010–3025. <https://doi.org/10.1021/am302733m>.
- (36) Chen, S.; Ciotonea, C.; Ungureanu, A.; Dumitriu, E.; Catrinescu, C.; Wojcieszak, R.; Dumeignil, F.; Royer, S. Preparation of Nickel (Oxide) Nanoparticles Confined in the Secondary Pore Network of Mesoporous Scaffolds Using Melt Infiltration. *Catal. Today* **2019**, *334*, 48–58. <https://doi.org/10.1016/j.cattod.2019.01.064>.
- (37) Zhang, H.; Chen, G.; Bai, L.; Chang, N.; Wang, Y. Selective Hydrogenation of Aromatics in Coal-Derived Liquids over Novel NiW and NiMo Carbide Catalysts. *Fuel* **2019**, *244*, 359–365. <https://doi.org/10.1016/j.fuel.2019.02.015>.

### 3.6. Supplementary information

**Table S1.** Some representative results for the production of EG and PG from cellulose and lignocellulose under hydrothermal conditions with heterogeneous catalysts.

Reactant Conditions	Catalyst	Y <sub>EG</sub> (%)	Y <sub>PG</sub> (%)	Overall conversion loss after 3 cycles (%)	Ref
0.5 g cellulose, 245 °C, H <sub>2</sub> 60 bar, 0.5 h	Ni-W <sub>2</sub> C/AC	49.8	4.3	7.1	1
1 g cellulose, 245 °C, H <sub>2</sub> 60 bar, 0.5 h	Ni-WC <sub>x</sub> /MC	72.9	5.1	3	2

0.5 g cellulose, 245 °C, H <sub>2</sub> 60 bar, 0.5 h	Ni <sub>0.3</sub> -W <sub>0.3</sub> /CNF	34.1 <sup>(a)</sup>	5.3 <sup>(a)</sup>	13.2 <sup>(a)</sup>	3
0.5 g cellulose, 245 °C, H <sub>2</sub> 60 bar, 0.5 h	Ni-W/ $\beta$ + ZnO	34.3	35.8	5	4
1 g cellulose, 220 °C, H <sub>2</sub> 43 bar, 1 h	Ni-W <sub>x</sub> C/C-SO <sub>3</sub> H	26 <sup>(a)</sup>	-	-	5
0.5 g cellulose, 240 °C, H <sub>2</sub> 50 bar, 2 h	Ni-W/SiO <sub>2</sub> @C <sub>x</sub> N <sub>y</sub>	50	5	4	6
0.5 g bamboo pulp, 240 °C, H <sub>2</sub> 50 bar, 1.5 h	Ni-W/C@C <sub>3</sub> N <sub>4</sub>	55 <sup>(b)</sup>	10 <sup>(b)</sup>	5 <sup>(b)</sup>	7

---

<sup>(a)</sup> Molar based; <sup>(b)</sup> Feedstock based.

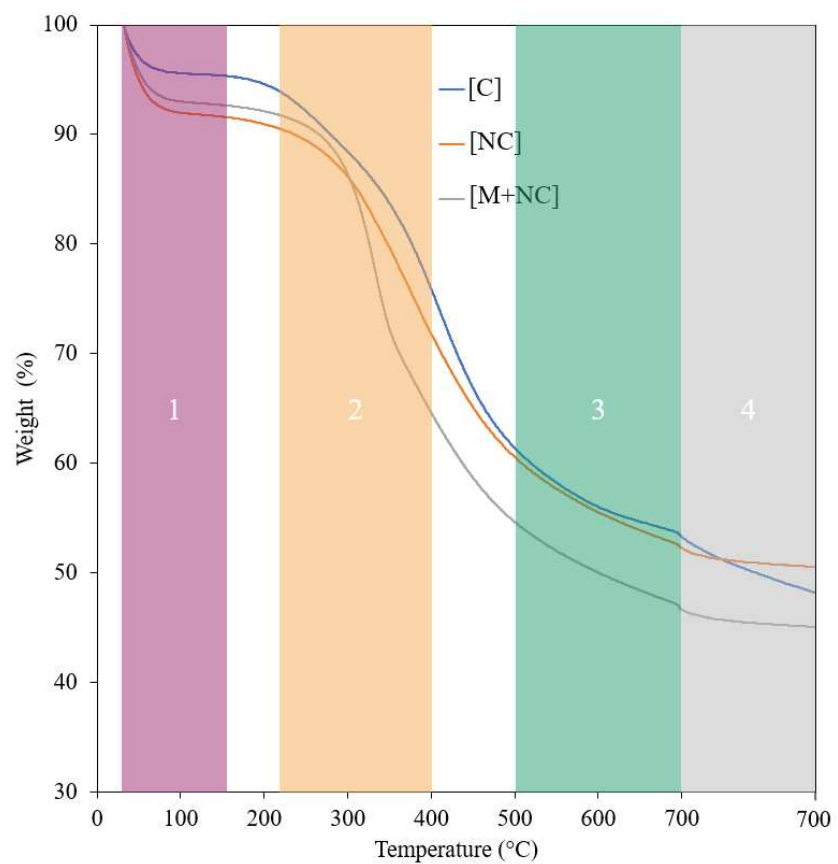


**Figure S1.** Thermogravimetric curves (TG) under nitrogen atmosphere of HTC-derived carbons.

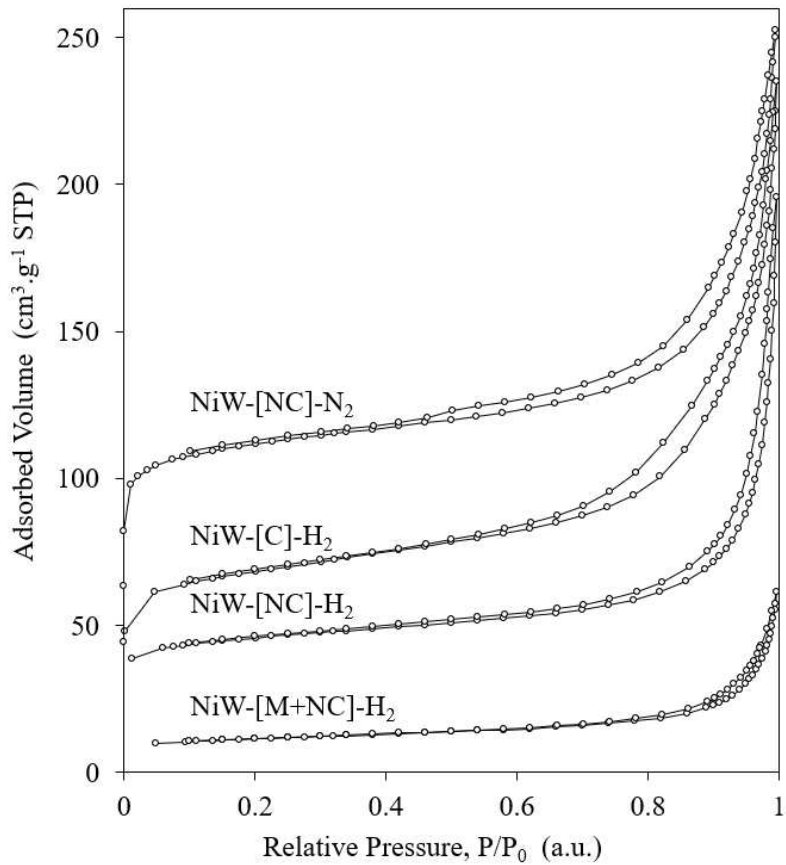


**Figure S2.** N<sub>2</sub> adsorption-desorption isotherms obtained for the NiW-X-Y<sub>2</sub> materials. (X = [C], [NC], [M+NC]; Y = H, N; the isotherm of NiW-[NC]-N<sub>2</sub> was shifted upwards by 25 cm<sup>3</sup>.g<sup>-1</sup>).

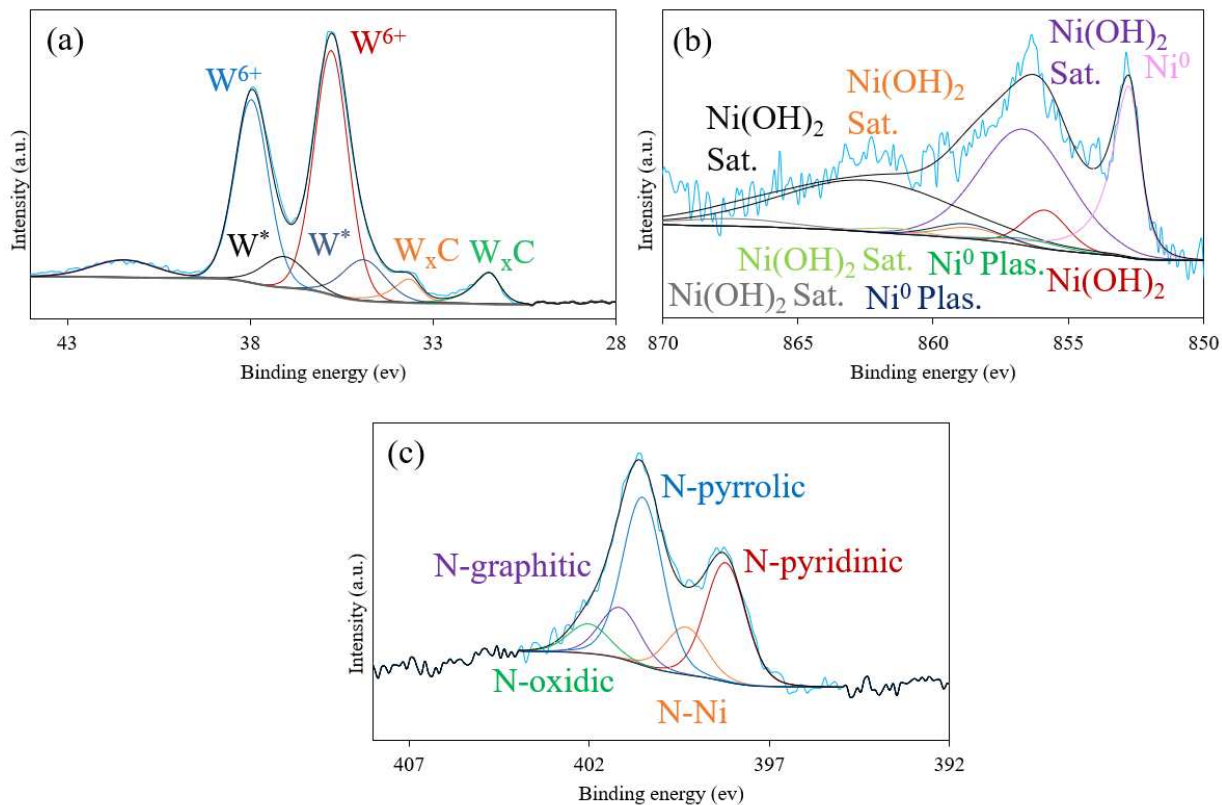


**Figure S3.** (a) W 4f, (b) Ni 1s, (c) N 1s core level spectra recorded for NiW-[NC]-N<sub>2</sub>.

**Table S2.** Surface proportion of the different Ni, W, N species in the activated catalysts obtained by XPS.

Material	Ni		W		N	
	ox. state	%	ox. st.	%	ox. state	%
NiW-[NC]-N <sub>2</sub>	Ni <sup>2+</sup>	76	W <sup>6+</sup>	75	N-pyrid.	29
	Ni <sup>0</sup>	24	W*	16	N-Ni	11
			W <sub>x</sub> C	9	N-pyrro.	41
					N-graph.	12
				N-ox.	7	
NiW-[C]-H <sub>2</sub>	Ni <sup>2+</sup>	95	W <sup>6+</sup>	86	N-pyrid.	12
	Ni <sup>0</sup>	5	W*	5	N-pyrro..	67
			W <sub>x</sub> C	9	N-ox.	21
NiW-[NC]-H <sub>2</sub>	Ni <sup>2+</sup>	92	W <sup>6+</sup>	83	N-pyrid.	22
	Ni <sup>0</sup>	8	W <sub>x</sub> C	17	N-Ni	10

						N-pyrro.	36
						N-graph.	24
						N-ox.	8
	Ni <sup>2+</sup>	95	W <sup>6+</sup>	75		N-pyrid.	15
	Ni <sup>0</sup>	5	W <sub>x</sub> C	25		N-Ni	3
NiW-[M+NC]-H <sub>2</sub>						N-pyrro.	10
						N-graph.	18
						N-ox.	54

(\*) oxidation state.

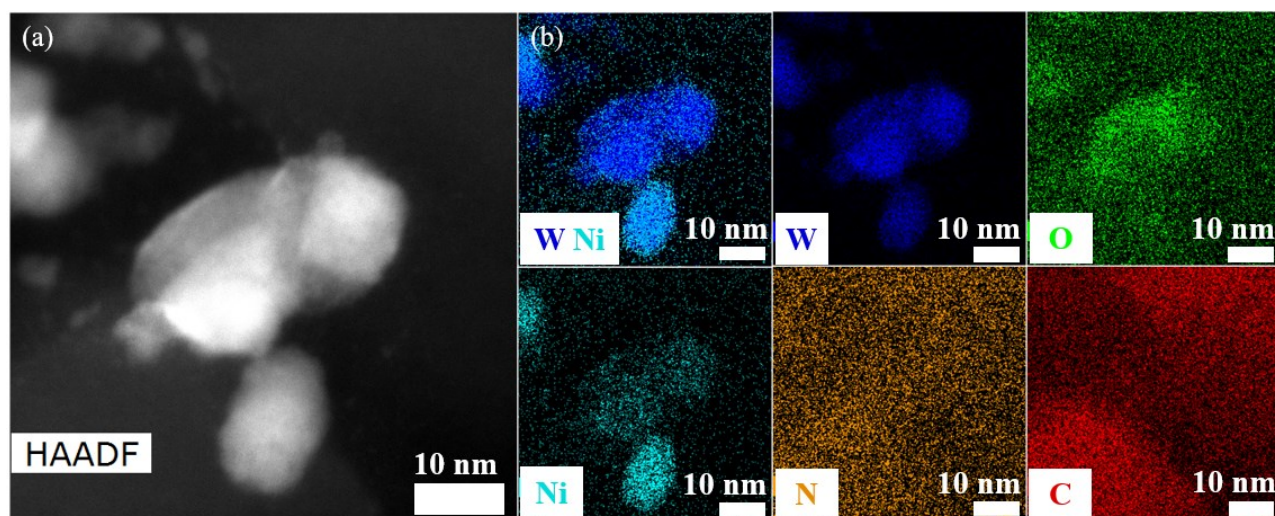


**Figure S4.** (a) HAADF-STEM; (b) TEM-EDS elemental mapping images obtained for NiW-[NC]-N<sub>2</sub>.

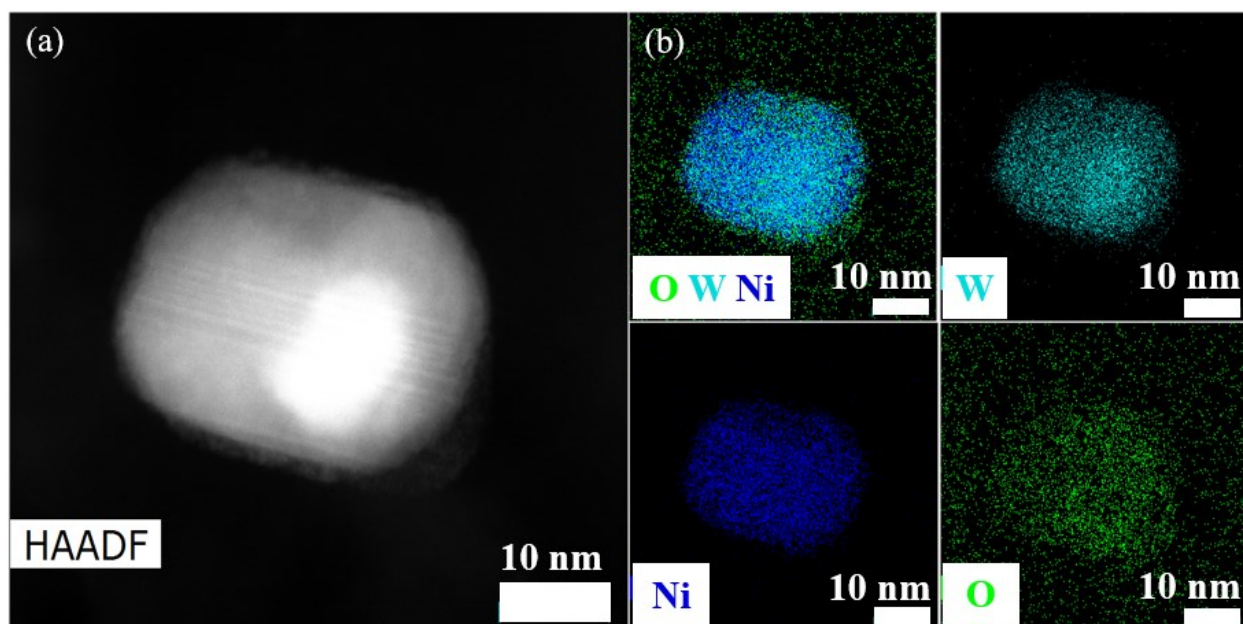


**Figure S5.** (a) HAADF-STEM; (b) TEM-EDS elemental mapping images obtained for NiW-[C]-H<sub>2</sub>.

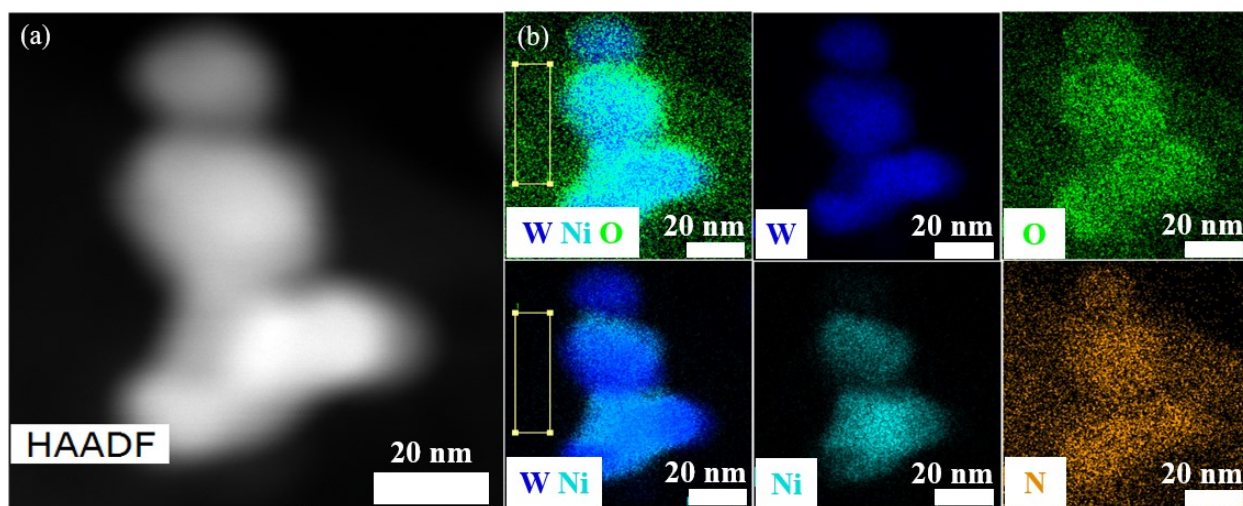


**Figure S6.** (a) HAADF-STEM; (b) TEM-EDS elemental mapping images obtained for NiW-[NC]-H<sub>2</sub>.



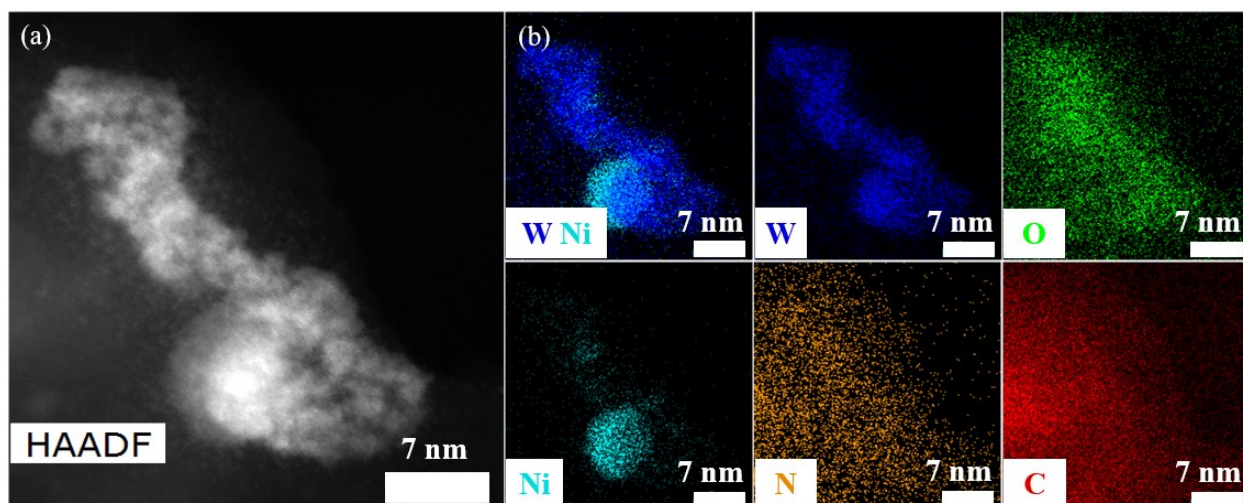


**Figure S7a.** (a) HAADF-STEM; (b) TEM-EDS elemental mapping images obtained for NiW-[M+NC]-H<sub>2</sub>.

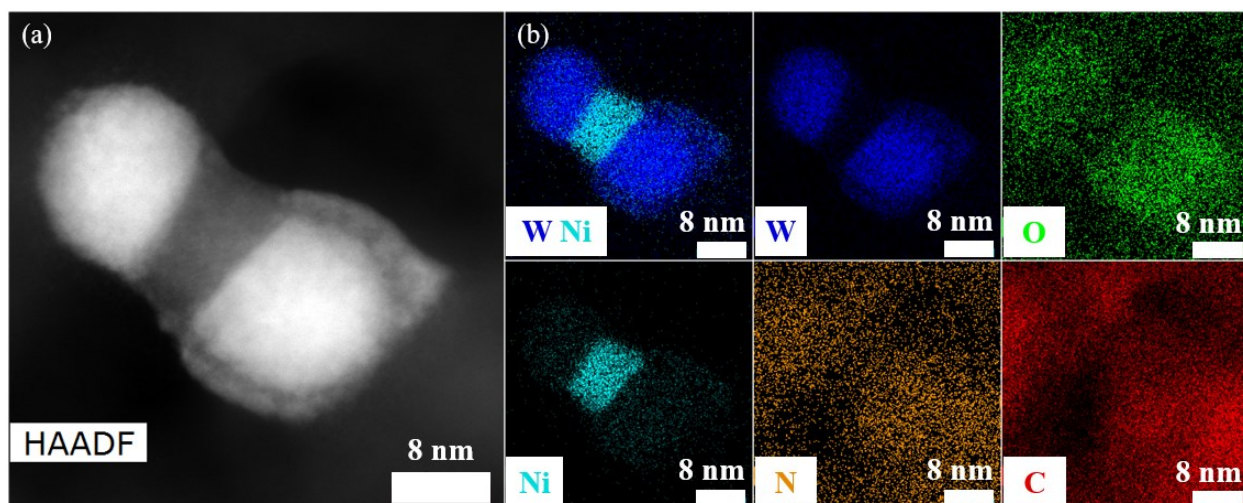


**Figure S7b.** (a) HAADF-STEM; (b) TEM-EDS elemental mapping images of NiW-[M+NC]-H<sub>2</sub>.



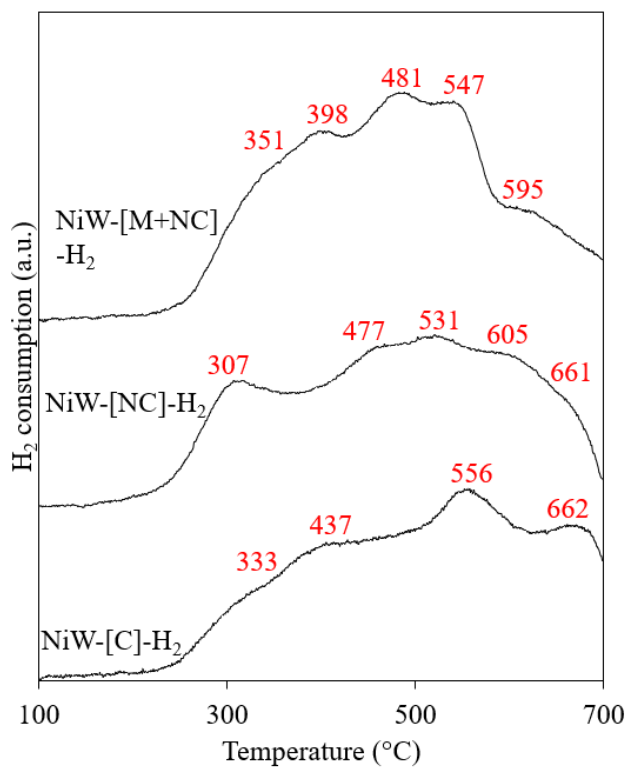


**Figure S8a.** H<sub>2</sub>-TPR profiles obtained for catalysts activated under H<sub>2</sub>.

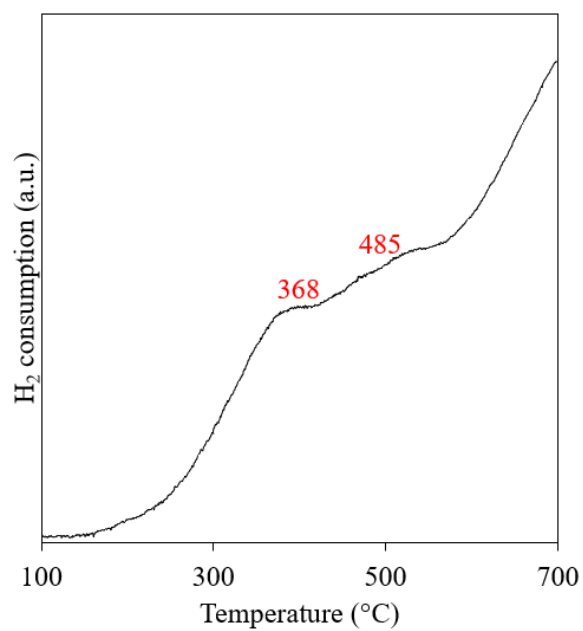


**Figure S8b.** H<sub>2</sub>-TPR pattern of NiW-[NC]-N<sub>2</sub>.

**Table S3.** Polyols' products distribution from cellulose.

Catalyst	Yield of the product (mol%)								Cellulose liquefaction (%) <sup>(i)</sup>
	EG <sup>(a)</sup>	PG <sup>(b)</sup>	BG <sup>(c)</sup>	SOR <sup>(d)</sup>	ERY <sup>(e)</sup>	GLY <sup>(f)</sup>	GA <sup>(g)</sup>	HA <sup>(h)</sup>	
NiW-[NC]-N <sub>2</sub>	20	8	3	-	-	-	4	8	99
NiW-[C]-H <sub>2</sub>	54	6	3	9	3	1	-	-	98
NiW-[NC]-H <sub>2</sub>	51	5	5	8	3	2	-	-	103
NiW-[M+NC]-H <sub>2</sub>	57	6	4	8	4	1	2	-	102

<sup>(a)</sup> EG: ethylene glycol; <sup>(b)</sup> PG: 1,2-propylene glycol; <sup>(c)</sup> BG: 1,2-butanediol; <sup>(d)</sup> SOR: sorbitol; <sup>(e)</sup> ERY: erythritol; <sup>(f)</sup> GLY: glycerol; <sup>(g)</sup> GA: glycolaldehyde; <sup>(h)</sup> HA: hydroxyacetone or acetol, <sup>(i)</sup> the measured uncertainty is less than 5%.

**Table S4.** Textural properties measured over selected catalysts, after one reaction cycle.

Material	S <sub>BET</sub> <sup>(a)</sup> (m <sup>2</sup> .g <sup>-1</sup> )	S <sub>μ</sub> <sup>(b)</sup> (m <sup>2</sup> .g <sup>-1</sup> )	V <sub>p</sub> <sup>(c)</sup> (cm <sup>3</sup> .g <sup>-1</sup> )	V <sub>μ</sub> <sup>(d)</sup> (cm <sup>3</sup> .g <sup>-1</sup> )	D <sub>pore</sub> <sup>(e)</sup> (nm)
NiW-[C]-H <sub>2</sub> -AR	111	47	0.23	0.02	3.8-10.6
NiW-[NC]-H <sub>2</sub> -AR	34	11	0.13	<0.01	3.8-22
NiW-[M+NC]-H <sub>2</sub> -AR	10	5	0.04	<0.01	3.4-16

<sup>(a)</sup> BET surface area; <sup>(b)</sup> micropore surface area; <sup>(c)</sup> total pore volume; <sup>(d)</sup> micropore volume; <sup>(e)</sup> BJH pore diameter calculated on desorption branch.

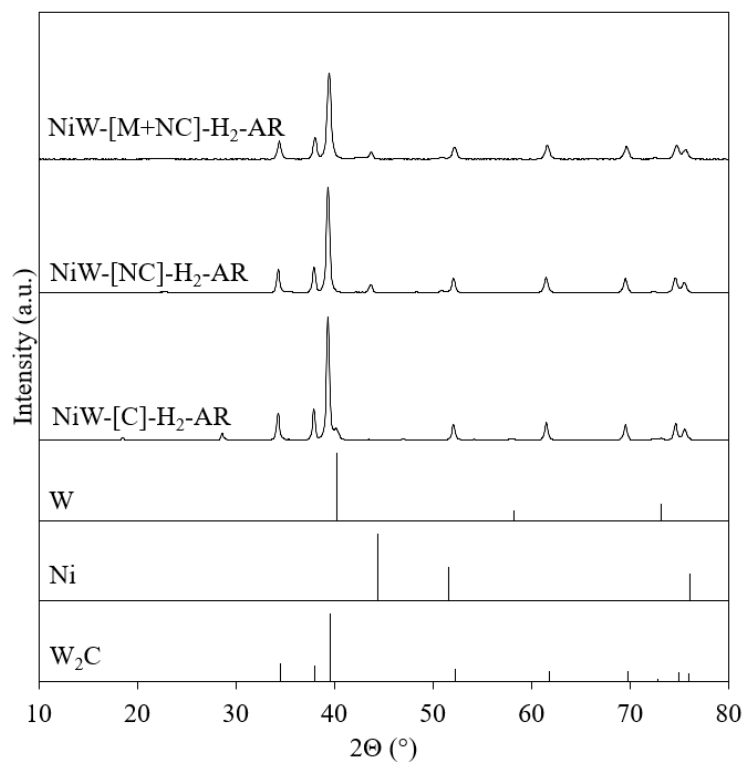


**Figure S9.** XRD diffractograms recorded over selected catalysts, after one reaction.

**Table S5.** crystallite sizes (in nm), calculated from Scherrer equation based on the diffractograms recorded after one reaction cycle.

<b>Material</b>	<b>W<sub>2</sub>C</b>	<b>Ni</b>
NiW-[C]-H <sub>2</sub> -AR	22.0	-
NiW-[NC]-H <sub>2</sub> -AR	22.5	22.0
NiW-[M+NC]-H <sub>2</sub> -AR	19.6	24.6

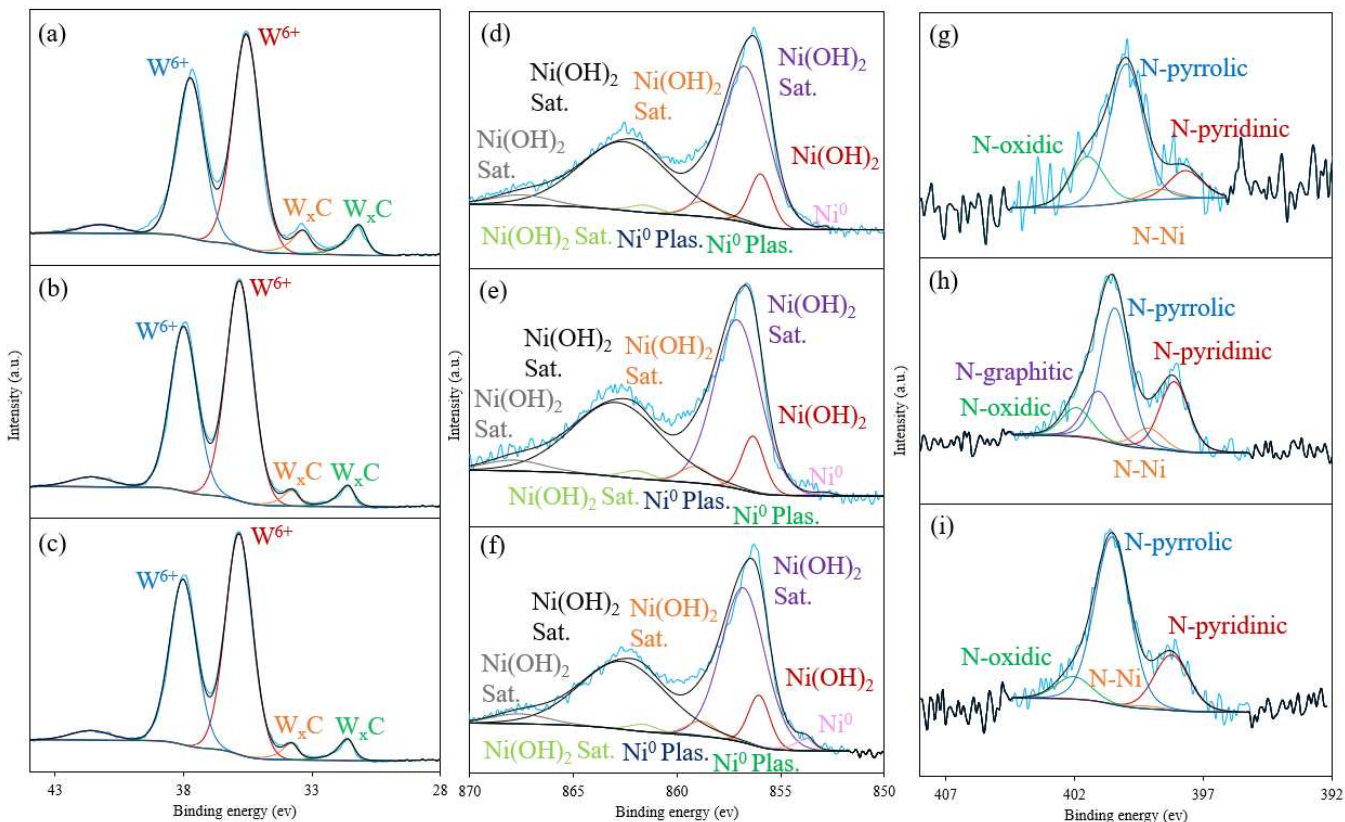


**Figure S10.** XPS results : W 4f in (a) NiW-[C]-H<sub>2</sub>-AR, (b) NiW-[NC]-H<sub>2</sub>-AR, (c) NiW-[M+NC]-H<sub>2</sub>-AR ; Ni 2p in (d) NiW-[C]-H<sub>2</sub>-AR, (e) NiW-[NC]-H<sub>2</sub>-AR, (f) NiW-[M+NC]-H<sub>2</sub>-AR ; N 1s in (g) NiW-[C]-H<sub>2</sub>-AR, (h) NiW-[NC]-H<sub>2</sub>-AR, (i) NiW-[M+NC]-H<sub>2</sub>-AR ;

**Table S6.** XPS surface composition (XPS) registered over selected catalysts, after one reaction cycle.

Material	W XPS (wt%)	Ni XPS (wt%)	mW/mNi
NiW-[C]-H <sub>2</sub> -AR	14.8	3.4	4.35
NiW-[NC]-H <sub>2</sub> -AR	13.5	3.0	4.5
NiW-[M+NC]-H <sub>2</sub> -AR	21.1	4.4	4.8

**Table S7.** Surface proportion of the different Ni, W, N species registered over selected catalysts, after one reaction

Material	Ni		W		N	
	ox. st. (*)	%	ox. st.	%	ox. st.	%
NiW-[C]-H <sub>2</sub> -AR	Ni <sup>2+</sup>	99.8	W <sup>6+</sup>	89	N-pyrid.	12

	Ni <sup>0</sup>	0.2	W <sub>x</sub> C	11	N-Ni	5
					N-pyrro.	61
					N-ox.	22
NiW-[NC]-H <sub>2</sub> -AR	Ni <sup>2+</sup>	99	W <sup>6+</sup>	93	N-pyrid.	23
	Ni <sup>0</sup>	1	W <sub>x</sub> C	7	N-Ni	7
					N-pyrro.	45
					N-graph.	16
				N-ox.	9	
NiW-[M+NC]-H <sub>2</sub> -AR	Ni <sup>2+</sup>	98	W <sup>6+</sup>	88	N-pyrid.	22
	Ni <sup>0</sup>	2	W <sub>x</sub> C	12	N-Ni	1
					N-pyrro.	68
					N-ox.	9

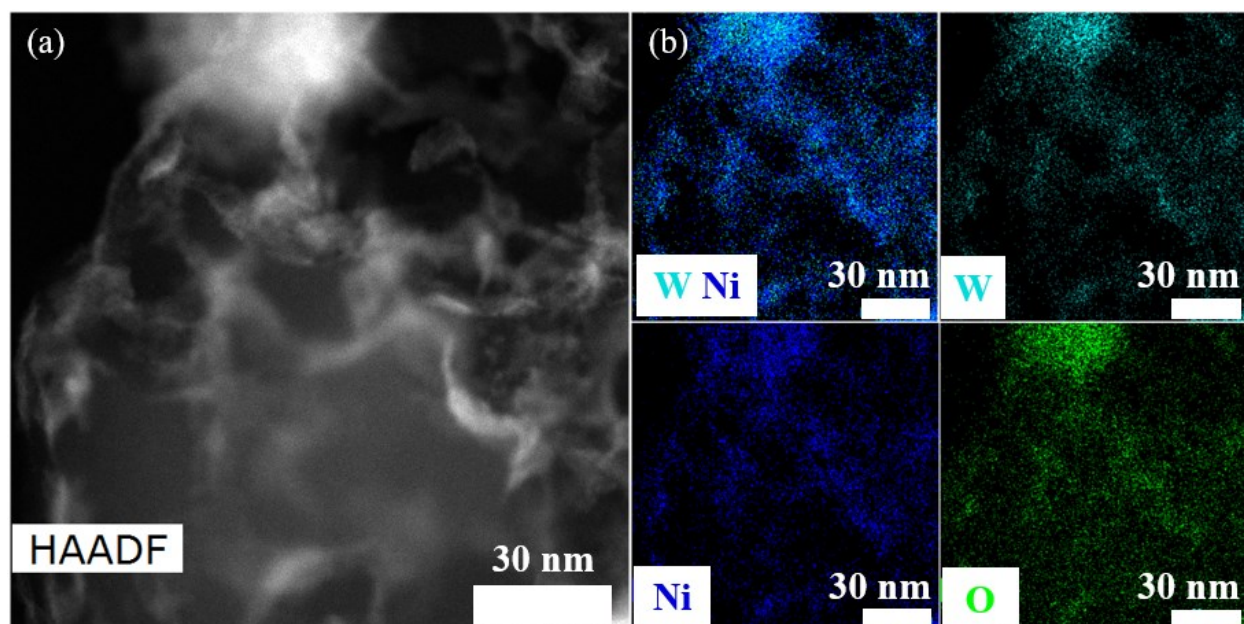


**Figure S11.** (a) HAADF-STEM; (b) TEM-EDS elemental mapping images of NiW-[C]-H<sub>2</sub>-AR.

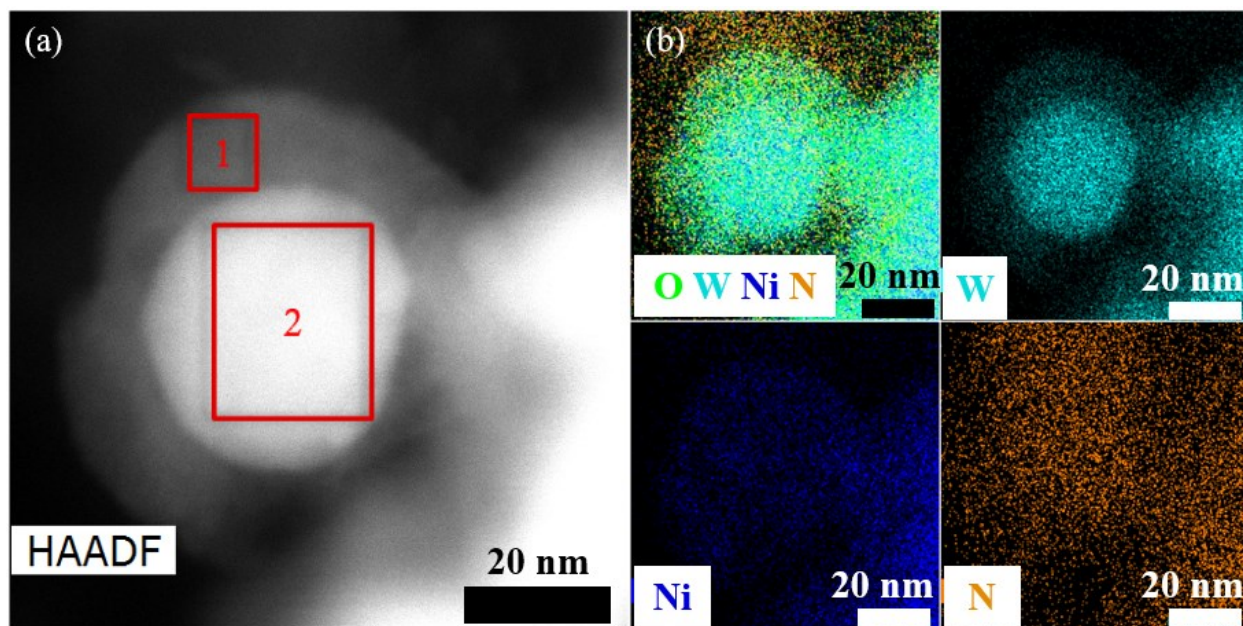


**Figure S12.** (a) HAADF-STEM; (b) TEM-EDS elemental mapping images of NiW-[NC]-H<sub>2</sub>-AR.

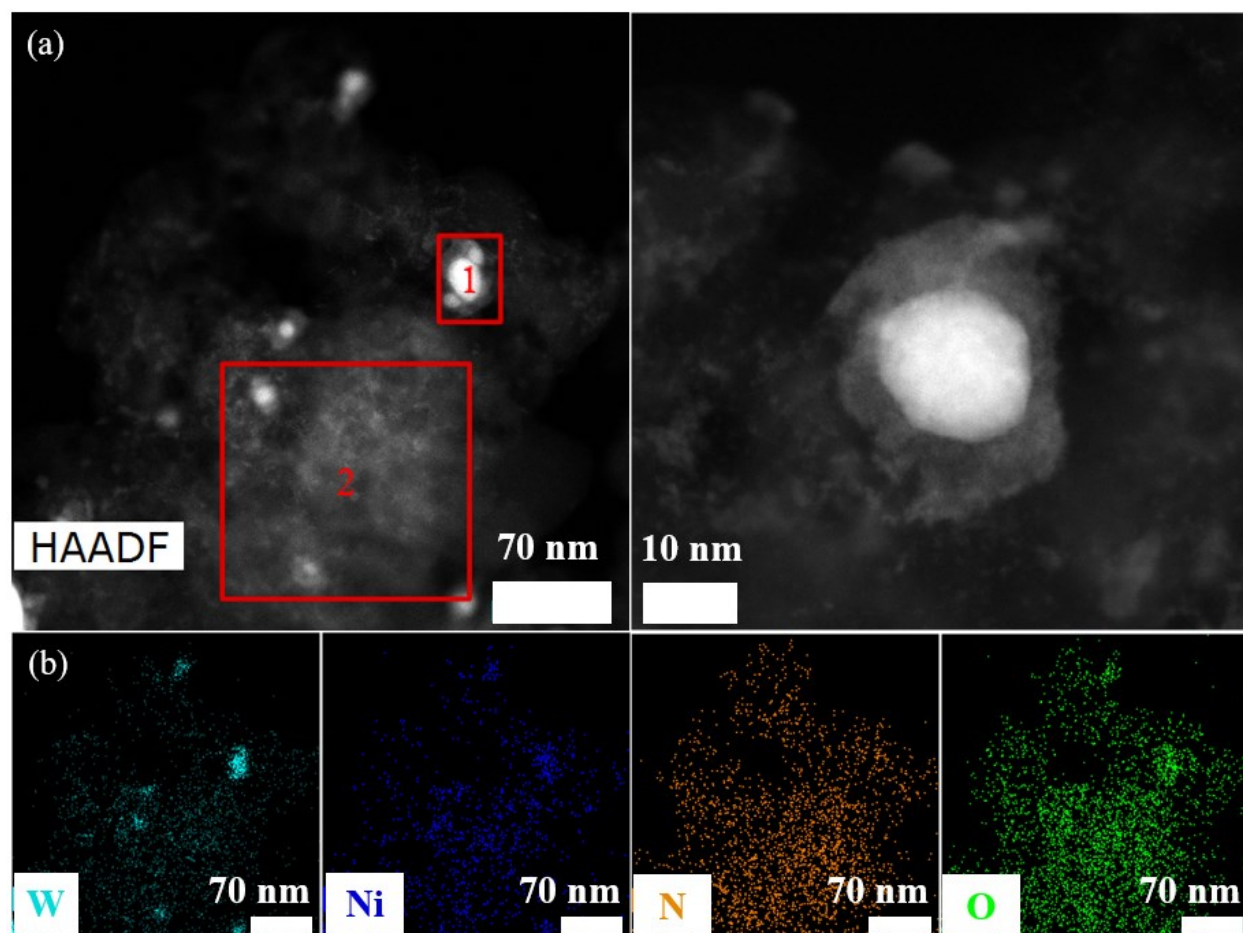


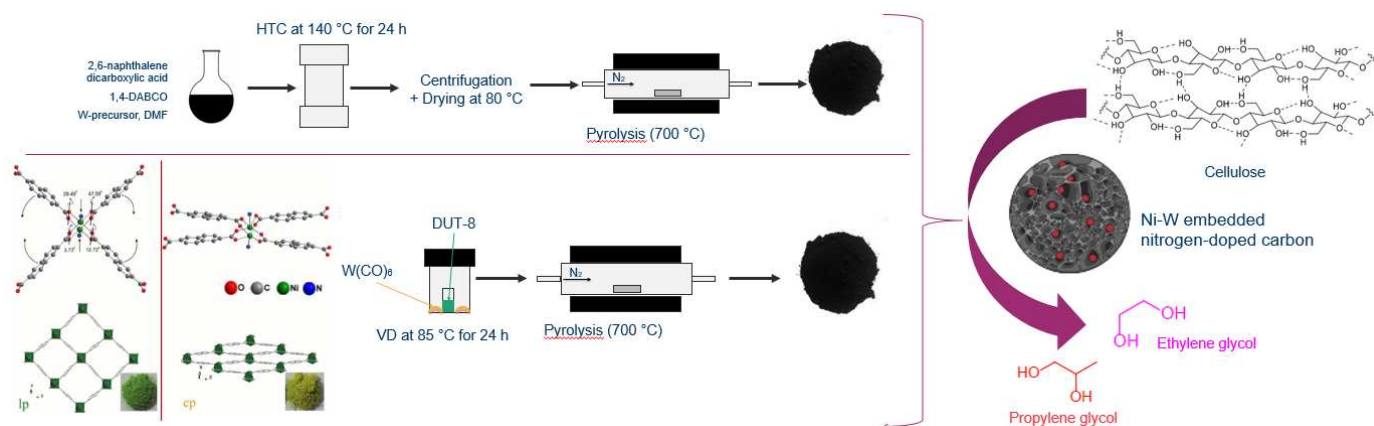


**Figure S13.** (a) HAADF-STEM; (b) TEM-EDS elemental mapping images of NiW-[M+NC]-H<sub>2</sub>-AR.

## References

- (1) Ji, N.; Zhang, T.; Zheng, M.; Wang, A.; Wang, H.; Wang, X.; Chen, J. G. Direct Catalytic Conversion of Cellulose into Ethylene Glycol Using Nickel-Promoted Tungsten Carbide Catalysts. *Angew. Chem. Int. Ed.* **2008**, *47* (44), 8510–8513. <https://doi.org/10.1002/anie.200803233>.
- (2) Zhang, Y.; Wang, A.; Zhang, T. A New 3D Mesoporous Carbon Replicated from Commercial Silica as a Catalyst Support for Direct Conversion of Cellulose into Ethylene Glycol. *Chem Commun* **2010**, *46* (6), 862–864. <https://doi.org/10.1039/B919182H>.
- (3) Yang, Y.; Zhang, W.; Yang, F.; Brown, D. E.; Ren, Y.; Lee, S.; Zeng, D.; Gao, Q.; Zhang, X. Versatile Nickel–Tungsten Bimetallics/Carbon Nanofiber Catalysts for Direct Conversion of Cellulose to Ethylene Glycol. *Green Chem.* **2016**, *18* (14), 3949–3955. <https://doi.org/10.1039/C6GC00703A>.
- (4) Gu, M.; Shen, Z.; Yang, L.; Dong, W.; Kong, L.; Zhang, W.; Peng, B.-Y.; Zhang, Y. Reaction Route Selection for Cellulose Hydrogenolysis into C<sub>2</sub>/C<sub>3</sub> Glycols by ZnO-Modified Ni-W/ $\beta$ -Zeolite Catalysts. *Sci. Rep.* **2019**, *9* (1), 11938. <https://doi.org/10.1038/s41598-019-48103-6>.
- (5) Rodella, C. B.; Barrett, D. H.; Moya, S. F.; Figueroa, S. J. A.; Pimenta, M. T. B.; Curvelo, A. A. S.; Silva, V. T. da. Physical and Chemical Studies of Tungsten Carbide Catalysts: Effects of Ni Promotion and Sulphonated Carbon. *RSC Adv.* **2015**, *5* (30), 23874–23885. <https://doi.org/10.1039/C5RA03252K>.
- (6) Xiao, Z.; Wang, X.; Yang, Q.; Xing, C.; Ge, Q.; Gai, X.; Mao, J.; Ji, J. Fabrication of Immobilized Nickel Nanoclusters Decorated by C N Species for Cellulose Conversion to C<sub>2,3</sub> Oxygenated Compounds: Rational Design via Typical C- and N-Sources. *J. Energy Chem.* **2020**, *50*, 25–36. <https://doi.org/10.1016/j.jechem.2020.02.054>.
- (7) Xiao, Z.; Zhang, Q.; Wang, X.; Ge, Q.; Gai, X.; Mao, J.; Ji, J. Organic Nitrogen Promotes Stability of Metallic Catalysts in Conversion of Bamboo Pulp to Low Carbon Polyols. *J. Fuel Chem. Technol.* **2019**, *47* (6), 675–687. [https://doi.org/10.1016/S1872-5813\(19\)30029-5](https://doi.org/10.1016/S1872-5813(19)30029-5).

# Chapter 4 : MOF-derived Ni-W<sub>x</sub>C catalysts for cellulose hydrogenolysis



This Chapter will be submitted to CHEMCOM in the near future.



#### 4.1. Introduction

The current energy and chemical industries today depend mostly on non-renewable energy sources and significant efforts are currently done to shift to the utilization of renewable biomass<sup>1</sup>. Hitherto, there have been studies on the transformation of cellulose into short carbon polyols (C2,3), including ethylene glycol (EG), propylene glycol (1,2-PG) and glycerol (Gly), which are prevailing intermediates in the manufacture of plastics, pharmaceuticals, food additives, and cosmetics. Cellulose conversion to diols mainly involves 3 types of reactions: cellulose hydrolysis into glucose, retro-aldol cleavage of glucose, and hydrogenation of carbonylated intermediates. For the formation of 1,2-PG, glucose isomerization into fructose is also necessary. Various catalytic systems have been proposed for the hydrogenolysis of cellulose into glycols, most of them containing W species. Among, Zhang *et al.* used an activated carbon (AC)-supported tungsten carbide (W<sub>2</sub>C/AC) catalyst, to obtain an EG yield of 27 %<sup>2</sup>. Besides being a cheap non-noble metal-derived phase, a noteworthy advantage of tungsten carbide over other tungsten species (oxides and metal) is the preferential formation of EG among other polyols due to its Pt-like catalytic behavior. When changing the support by a mesoporous carbon (obtained by replication of a commercial silica) and incorporation nickel nanoparticles, the same group enhanced the EG yield up to 72-76 %<sup>3</sup>. The improvement was attributed to the high dispersion of tungsten carbide, the presence of nickel that enhanced the hydrogenation step, and the better diffusion of reactant and product molecules through the support porosity. Fabičovicová *et al.* compared the hydrogenolysis of cellulose without a catalyst, and over six catalytic systems formed of nickel and/or tungsten on activated carbon in order to distinguish the role of each active component<sup>4</sup>. The two-steps incipient wetness impregnation prepared catalyst, Ni/W/AC, yielded 43.7 % of EG. Drastically lower EG yields were obtained with the Ni/AC+W/AC mixture and the Ni-W/AC catalyst prepared by co-impregnation. By varying the carbon support type, high space-time yields of about 2.5 g polyols (g<sub>catalyst</sub>·h)<sup>-1</sup> were achieved. They also reported that structural changes (formation of NiWO<sub>4</sub>) and leaching of the catalyst are responsible for its deactivation in three runs. Using Beta zeolite-supported Ni-W catalyst (Ni-W/β) doped by ZnO, Gu *et al.* obtained high yields of EG (34.3 %) and PG (35.8 %), PG production being assigned to the promotion of glucose isomerization to fructose by ZnO<sup>5</sup>. Organic functional groups (-SO<sub>3</sub>H, -COOH, -OH, -[C]-N, -NH<sub>2</sub>, etc.) role on cellulose hydrogenolysis has been investigated by a very limited number of studies<sup>6-8</sup>. For instance,

Rodella *et al.* proved that SO<sub>3</sub>H groups not only increase the hydrolysis rate of cellulose but also stabilize the Ni promoter which then led to a smaller, better dispersed W<sub>x</sub>C phase and thus higher selectivity towards EG as compared to the unfunctionalized Ni-W<sub>x</sub>C/C catalyst<sup>6</sup>.

Some of us explored and reported recently<sup>9</sup> the nature of the active species when the support is a commercial carbon with the conclusion that concerning the W<sub>x</sub>C species, no real influence of WC nor W<sub>2</sub>C was evidenced, in contrast to the NiW alloys formation that may induce a significant effect on the transformation. Yang *et al.* prepared Ni-W/C nanofiber catalysts, fabricated *in situ* through the pyrolysis of Ni, W-containing metal-organic framework fibers (Zn-BTC MOF). The metal particles, Ni-rich alloys (NiW, Ni<sub>0.8</sub>W<sub>0.2</sub> and Ni<sub>0.85</sub>W<sub>0.15</sub>), have uniform size distribution centered on 68 nm, evenly dispersed on the hierarchical porous carbon nanofibers. A large productivity varying from 15.3 to 70.8 mol<sub>EG</sub>.h<sup>-1</sup>.g<sub>W</sub><sup>-1</sup> was reported, which is two orders of magnitude higher than with previously reported Ni-W-based catalysts<sup>10</sup>. Based on the above studies, the dispersion and metal accessibility are crucial for both catalytic activity and EG selectivity. An optimized combination of (meso)porosity, Ni and W dispersion, and intimate contact between both elements is desired to stabilize efficient catalysts. However, usual synthetic routes, including co-precipitation, post-impregnation, and carbothermal hydrogen reduction (CHR), are not always able to achieve these characteristics with the difficulty to get uniform metal particles coverage, a satisfying proximity between active elements, and a strong anchorage on a mesoporous support. One method that can overcome this problem is to *in situ* synthesize metals scattered onto a mesoporous carbonaceous network which is formed simultaneously, for instance, through pyrolysis of metal-organic frameworks (MOFs) network. Wang *et al.*<sup>11</sup> highlighted the concepts and strategies of synthesizing MOF-derived porous carbons with different architectures; zero-dimensional (0D) core-shell, nanopolyhedral, and hollow structures, one-dimensional (1D) nanotubes<sup>12</sup> and nanofibers, two-dimensional (2D) graphene nanomeshes and nanoflakes, and three-dimensional (3D) nanoarrays, gradient monoliths and carbon aerogels. The potential applications of those materials in energy, environment, and catalysis fields including for the valorization of lignocellulosic biomass<sup>13</sup>, were reported. Concerning tungsten carbides, Xu *et al.* employed a cage-confinement pyrolysis strategy to synthesize ultrasmall NPs<sup>14</sup>. The authors utilized zeolitic imidazolate frameworks (ZIFs) as a nanoreactor to entrap W(CO)<sub>6</sub>. High temperature pyrolysis gave tungsten carbide nanoparticles with 2 nm sizes, which served as an excellent electrocatalyst for hydrogen evolution reaction. It exhibited very low

overpotential (51 mV) at 10 mA cm<sup>-2</sup>, a Tafel slope of 49 mV per decade, and the highest exchange current density (2.4 mA cm<sup>-2</sup>) among all tungsten/molybdenum catalysts. Other examples exist on the synthesis of tungsten carbide single atom catalysts with high surface areas and phase control based on ZIF-8<sup>15</sup>, UiO-66-NH<sub>2</sub><sup>16</sup>, IRMOF-3<sup>17</sup> architecture. It is noteworthy that, during preparation, the metal center of the MOF (zinc or zirconium) evaporated at high temperatures and the shape of the MOF (prismatic fibers<sup>10</sup>, polyhedral<sup>14,16</sup>, rhombododecahedral<sup>15</sup>) is inherited by the final carbon-based catalysts, while the dimensions shrink and the surface becomes rough. While we previously studied the hydrogenolysis of cellulose using carbon-supported nickel and tungsten carbide catalyst prepared using conventional routes, we are interested here in assessing a route inspired by the above-mentioned strategy for the preparation of carbon-supported Ni-W catalysts. For that we used a Ni-based MOF with encapsulated W species. We report here the results on the characterization of these new catalysts and their behavior for the hydrogenolysis of cellulose.

## 4.2. Experimental

In this chapter, the following characterization techniques were used: XRD, N<sub>2</sub> physisorption, FTIR ATR, XPS, SEM, TEM, TGA, ICP-OES and XPS. For more information regarding the characterization techniques and synthesis routes, please refer to Chapter 2 for all details.

## 4.3. Results and discussion

### 4.3.1. Synthesis and Characterization of materials

The ATR-FTIR spectrum of as-formed DUT-8(Ni) presented in Figure 1 is very similar to that of the rigid DUT-8 geometry obtained from literature data<sup>18</sup>. It contains the characteristic absorption bands at 1630 and 785 cm<sup>-1</sup>, the former corresponding to the asymmetric vibration of the carboxylic group while the latter could be assigned to the  $\nu_s$ N-C3 vibration of the dabco molecule. On the other hand, it is known that dabco is able to form salts with naphthoic acid as hydrogen bonds form between carboxylate anions and the protonated dabco via COO<sup>-</sup>/H-N<sup>+</sup> hydrogen bonds<sup>18</sup>. Indeed, after mixing of H<sub>2</sub>ndc and dabco in DMF, a white crystalline precipitate is formed. ATR-FTIR spectra of the samples issued from the liquid mediated route (DUT-8(Ni)-WNaO-1 and, DUT-8(Ni)-WCO-1) resemble more to the spectrum of closed pores DUT-8(Ni)<sup>18</sup>. Notably the band at 1630 cm<sup>-1</sup> disappeared and a band at 1548 cm<sup>-1</sup> appeared. As for the spectrum of DUT-8(Ni)-WCO-v it matches well that of DUT-8(Ni), which means that the

MOF structure was maintained after W vapor deposition. Two additional bands, appearing at 1950 and 581  $\text{cm}^{-1}$ , are characteristic of the presence of  $\text{W}(\text{CO})_6$ <sup>14</sup>, signaling its successful incorporation.

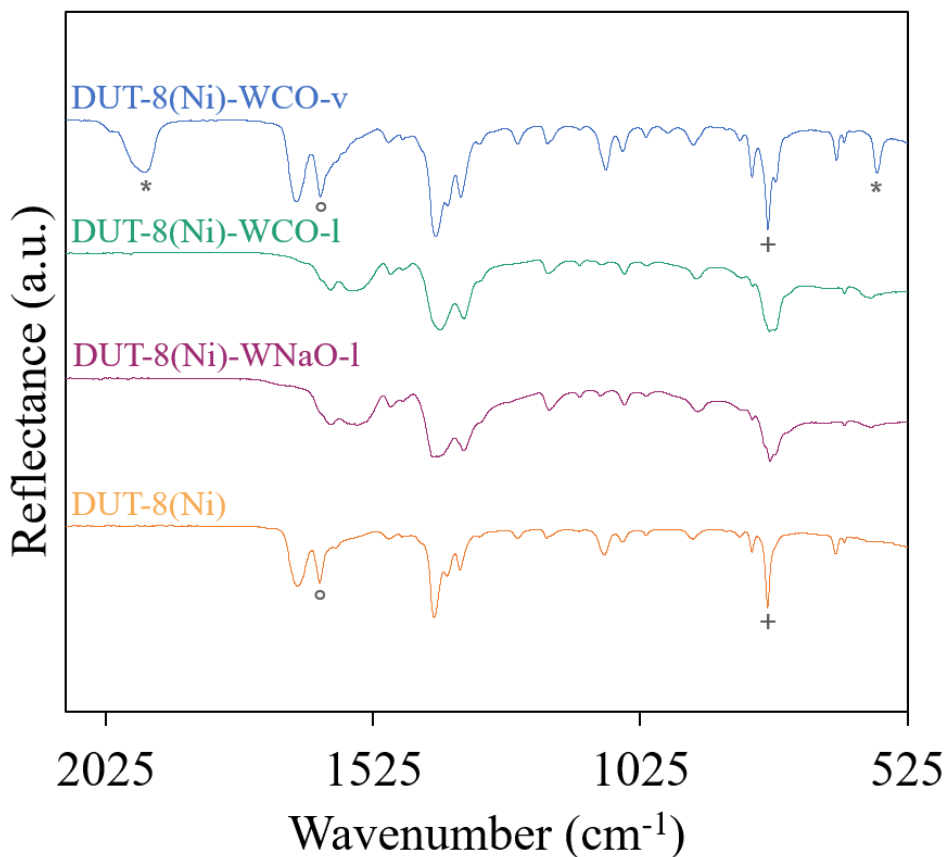


**Figure 1.** ATR-FTIR spectra of DUT-8(Ni) and  $\text{W}(\text{CO})_6$ -incorporated DUT-8(Ni) materials. \*:  $\text{W}(\text{CO})_6$ ; +: ndc-dabco ; °: Ni-ndc-dabco.

Table 1 presents the Ni and W contents of the materials, after final treatment under  $\text{N}_2$  or  $\text{H}_2$ . Concerning the materials prepared using liquid phase incorporation of  $\text{Na}_2\text{WO}_4$  precursor, the experimental W/Ni ratio (0.21-0.22) was lower than the theoretical expected one (0.30). When using  $\text{W}(\text{CO})_6$ , the experimental W/Ni ratio (0.05-0.012) was far below the expected value, due to solubility issues of this precursor in the synthesis solution. Indeed, limited solubility of  $\text{W}(\text{CO})_6$  in DMF did not allow the incorporation of the expected W content in the material, which is why the characteristic bands of  $\text{W}(\text{CO})_6$  were not detected. Concerning the vapor deposition procedure, the experimental W/Ni ratio was close to the expected value of 0.30, which shows that this method involving gas phase  $\text{W}(\text{CO})_6$  deposition is much more efficient than using dissolved  $\text{W}(\text{CO})_6$ . An additional advantage of this method is that it preserves the

MOF structure according to the previously presented ATR results, that is not the case for the liquid-phase incorporation of W precursor.

We notice that the metal contents of the N<sub>2</sub> activated samples is lesser (70-80% of the material) than in the H<sub>2</sub> reduced samples (98-99%). This is due to the reaction of carbon from MOF ligands with H<sub>2</sub>, catalyzed by Ni, during the activation step and leading to the production of CH<sub>4</sub> / NH<sub>3</sub>. Therefore, when activated under H<sub>2</sub>, almost pure mixture of W and Ni are obtained, with only residual carbon at a few percents level of concentration.

**Table 1.** Catalyst metal composition, as determined by ICP-OES analysis<sup>(a)</sup>.

<b>Material</b>	<b>W (wt%)</b>	<b>Ni (wt%)</b>	<b>W/Ni<sup>(a)</sup></b>
NiWNaO-l-N <sub>2</sub>	31.5	46.9	0.21
NiWNaO-l-H <sub>2</sub>	40.4	58.9	0.22
NiWCO-l-N <sub>2</sub>	18.9	52.3	0.12
NiWCO-l-H <sub>2</sub>	13.9	85	0.05
NiWCO-v-N <sub>2</sub>	33.9	38.9	0.28
NiWCO-v-H <sub>2</sub>	44.8	54.1	0.26

<sup>(a)</sup> expected W/Ni was 0.3.

The specificity of the DUT-8 MOF is that it may be synthesized in “rigid” or “flexible” forms, depending on the conditions of synthesis. The rigid version, consisting of nano sized crystallites, shows a typical “Type Ia” nitrogen physisorption isotherm at 77 K and is characterized by its open phase (op) geometry. In contrast, the flexible form is crystalized as macro crystals, undergoes a transformation into a closed phase (cp) upon a desolvation and can be reversibly transformed into the open phase (op) by adsorption of gases or liquids<sup>19,20</sup>. The XRD pattern of DUT-8(Ni) includes peaks from the theoretical calculated patterns<sup>18</sup> of both DUT-8(Ni) open and closed pores geometries, nevertheless the op phase characteristic peaks are more intense (Figure 2). For the XRD patterns of the liquid derived samples (DUT-8(Ni)-WNaO-l and DUT-8(Ni)-WCO-l), we observe a significant alteration of the DUT-8 structure: the peaks become less

intense, the MOF's structure is lost and additional reflections appear. This observation is in line with FTIR-ATR results. As for the diffractogram of DUT-8(Ni)-WCO-v it resembles greatly to that of DUT-8(Ni), with less intense peaks which means that the initial MOF structure was maintained after  $W(CO)_6$  vapor deposition. Hence the XRD results correlate well with the IR-ATR results previously presented.

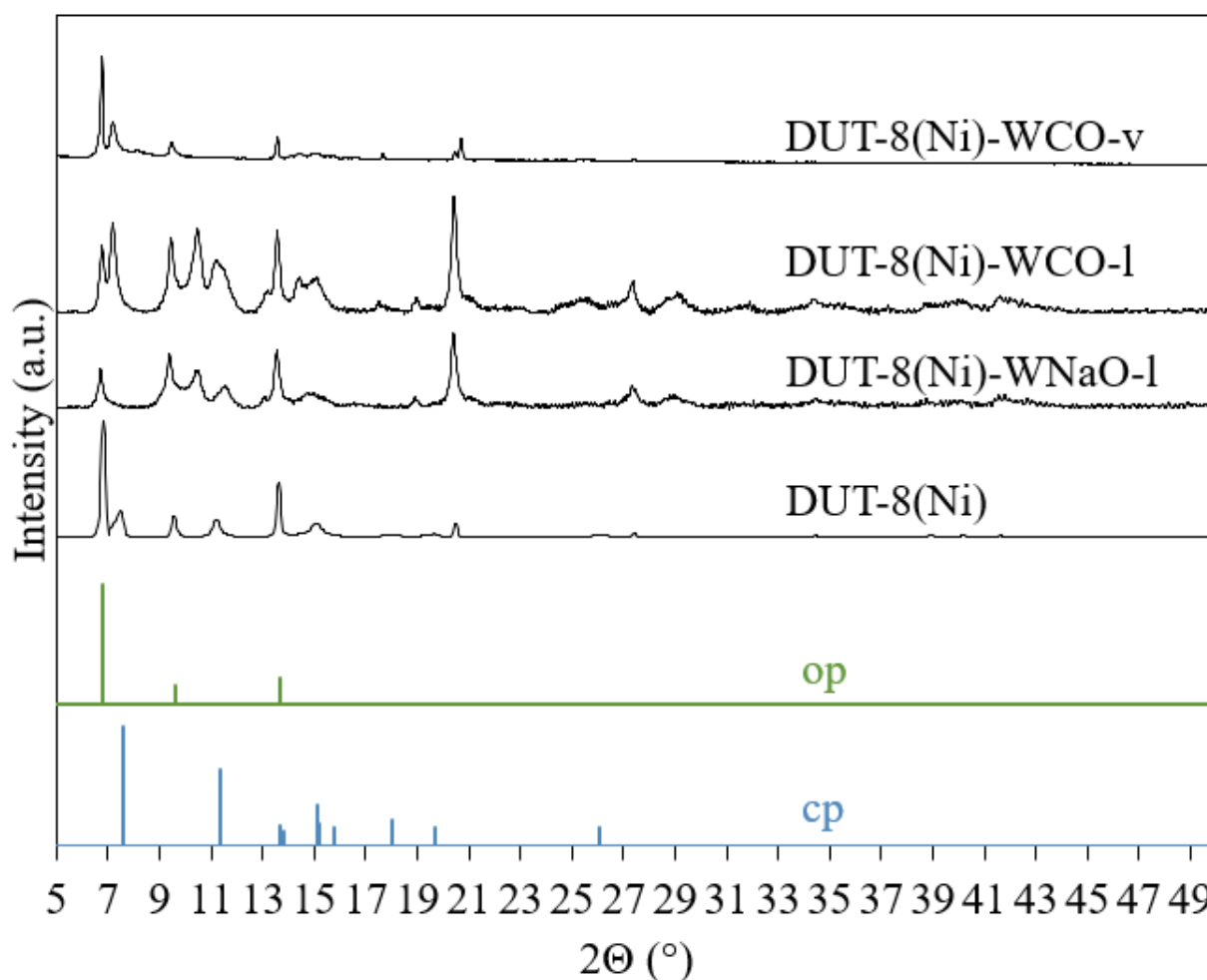


**Figure 2.** XRD diffractograms of W deposited DUT-8 materials.

Figure 3 displays the XRD diffractograms of the pyrolyzed W-deposited DUT-8 materials. The diffractogram of NiWNaO-l-N<sub>2</sub> shows a mixture of WC and W<sub>0.04</sub>Ni<sub>0.96</sub> phases as well as a low intensity signal for the W<sub>2</sub>C phase. The diffractogram of NiWCO-l-N<sub>2</sub> shows a mixture of W<sub>2</sub>C and W<sub>0.06</sub>Ni<sub>0.94</sub> phases. It indicates a successful carburization of W during the treatments under N<sub>2</sub> or H<sub>2</sub>. When the treatment is performed under hydrogen, NiWNaO-l-H<sub>2</sub> presents a W<sub>0.15</sub>Ni<sub>0.85</sub>

alloy phase, that is richer in W than the alloy obtained when treatment is performed under nitrogen (NiWNaO-l-N<sub>2</sub>). In addition, W, Ni<sub>5</sub>W<sub>6</sub>C and Na<sub>2</sub>WO<sub>4</sub> are detected. NiWCO-l-H<sub>2</sub> presents an exclusive W<sub>0.04</sub>Ni<sub>0.96</sub> phase, that is slightly poorer in W as compared to its counterpart pyrolyzed under N<sub>2</sub>. This confirms the absence of carburization due to almost complete loss of carbon during the treatment under H<sub>2</sub>, as preliminarily supposed from element content analysis. For the samples prepared by vapor deposition, NiWCO-v-N<sub>2</sub> pattern displays an alloy (W<sub>0.04</sub>Ni<sub>0.96</sub>) that is the poorest in W. When the reduction was done under hydrogen (NiWCO-v-H<sub>2</sub>) a W<sub>0.17</sub>Ni<sub>0.83</sub> phase that is richer in W as compared to NiWCO-v-N<sub>2</sub>, appeared. Additional W signal is observed. The average nanoparticle diameters were determined using the Scherrer equation and are presented in Table S2. Under H<sub>2</sub> activation, all materials present similar NiW alloys particle sizes around 17-50 nm. Under N<sub>2</sub> activation, tungsten carbide phases are detected : W<sub>2</sub>C nanoparticles (13-21 nm) and larger WC particles (24 nm), and it is noteworthy that the WC phase was only formed for NiWNaO-l-N<sub>2</sub> and W<sub>2</sub>C for NiWNaO-l-N<sub>2</sub> and NiWCO-l-N<sub>2</sub>. It is noteworthy to mention that a Ni<sub>5</sub>W<sub>6</sub>C has been detected with NiWNaO-l-H<sub>2</sub>, which is a fairly close phase to Ni<sub>6</sub>W<sub>6</sub>C, detected on our previous study on commercial carbon support<sup>9</sup>.

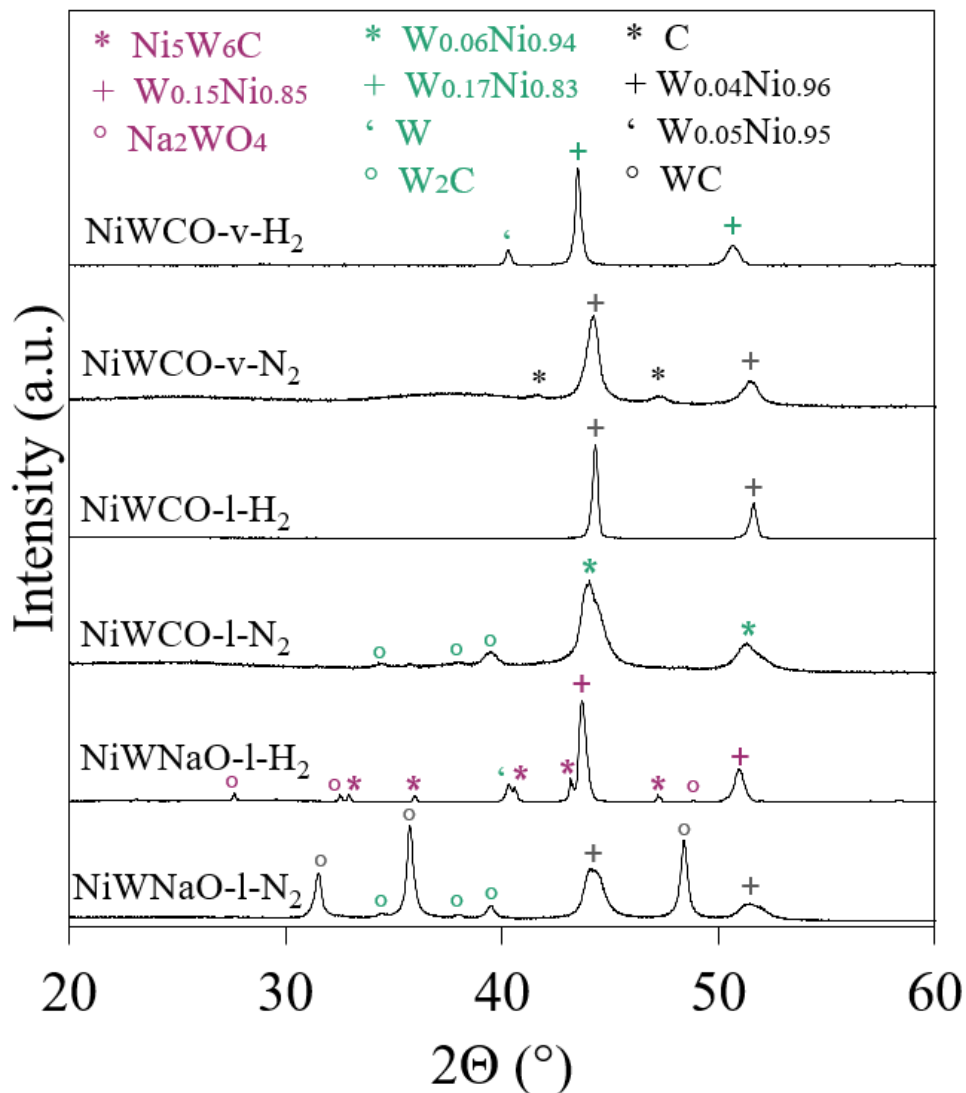


**Figure 3.** XRD diffractograms of activated W-DUT-8 derived samples.

XPS measurements were performed in order to identify electronic environment of metals (W, Ni) as well as their oxidation states. The XPS spectra of the passivated samples, displayed in Figure 4, S1 and S2, exhibit the core level signals for W 4f, Ni 2p, and C 1s. Two tungsten species are detected for all materials:  $W_xC$  ( $4f_{7/2}$ : 31.46 eV and  $4f_{5/2}$ : 33.64 eV), and  $W^{6+}$  ( $4f_{7/2}$ : 35.6 eV,  $4f_{5/2}$ : 37.78 eV).  $WO_3$  has non-stoichiometric properties, since its lattice withdraws a significant number of oxygen vacancies<sup>21</sup>. For all the materials tungsten is oxidized on the surface (> 66 % of  $WO_x$ ). Switching the synthesis route from in-situ liquid mediated route to vapor deposition, it increases the residual  $W_xC$  content ( $W_2C$  cannot be differentiated from WC by XPS), to a maximum of 34 % for NiWCO-v- $H_2$  (Table S3). Two oxidation states of Ni are also observed for



all samples: metallic nickel  $\text{Ni}^0$  ( $2p_{3/2}$ : 852.6 eV and 2 plasmon loss peaks : 856.3 eV and 858.7 eV) and the oxidized nickel species,  $\text{Ni}^{2+}$  ( $2p_{3/2}$ : 854.9 eV and 5 satellites : 855.7 eV, 857.7 eV, 860.5 eV, 861.5 eV, and 866.5 eV)<sup>22</sup>. The small shifts of binding energy observed between different catalysts might stem from the formation of a Ni-N-C structure<sup>23</sup>. NiWNaO-1- $\text{N}_2$  retains more  $\text{Ni}^0$  (98 %) at the surface, compared to the hydrogen-reduced samples (40 %), (Table S3). This trend is observed for all samples, suggesting that the presence of residual carbon fraction, in  $\text{N}_2$ -treated samples, can protect nickel phase toward reoxidation during passivation step. Moreover, asymmetrical C 1s peak of the XPS spectra at 284.5 eV (C-N) proves the considerable modification of the  $\text{sp}^2$  carbon atoms on the support surface (Figure 4.c). It is mainly due to the carbonization of organic nitrogen during the nitrogen pyrolysis at 700 °C. It would also be expected to obtain a signal around 283.5 eV, which is the C 1s carbide signature<sup>24</sup>, but the signal is probably merged with the intense C-C bonds photopeak. The rest of the C 1s peaks are usually assigned to oxygen-containing carbonaceous bands (C=O and O-C=O)<sup>25</sup>.

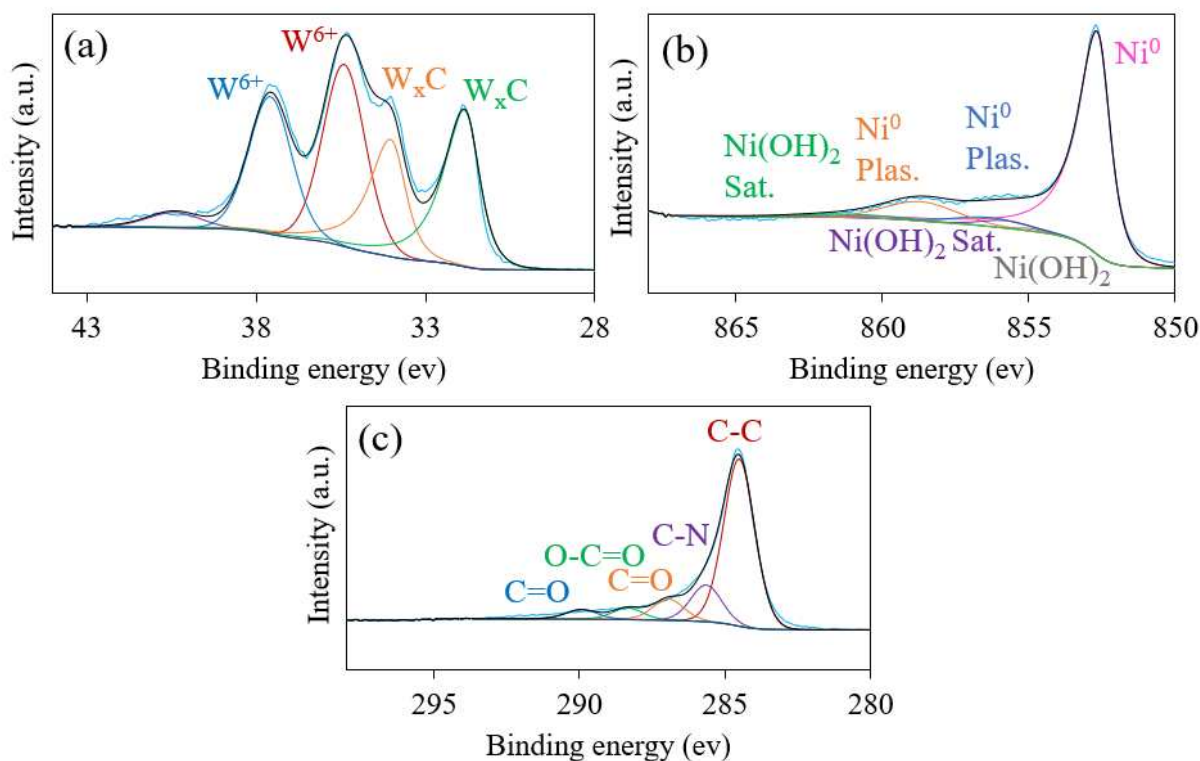


**Figure 4.** XPS results for (a) W 4f, (b) Ni 2p, (c) C 1s in NiWCO-v- $\text{N}_2$ .

N<sub>2</sub> isotherms of the pre-pyrolysis materials are presented in Figure 5, and the related textural properties listed in Table 2. All isotherms are of type I, characteristic of microporous solids. A small N<sub>2</sub> uptake at p/p<sub>0</sub> above 0.9 is observed, that could be ascribed to an intra-particle porosity. The hysteresis does not close under p/p<sub>0</sub> = 0.3, which signals that irreversible chemical adsorption might be occurring on DUT-8(Ni)<sup>26</sup> surface, this phenomenon is less expressed for the W@DUT-8 materials. DUT-8(Ni) material presents a high surface area of 2067 m<sup>2</sup>.g<sup>-1</sup> and micropores of about 2 nm. The surface area is smaller than the one found in literature (2635 m<sup>2</sup>.g<sup>-1</sup>)<sup>18</sup>. Furthermore, all W@DUT-8 materials exhibited relatively large surface areas in the range of 1439-1743 m<sup>2</sup>.g<sup>-1</sup>, that are less than that of DUT-8(Ni) due to the porosity filled with W precursors.

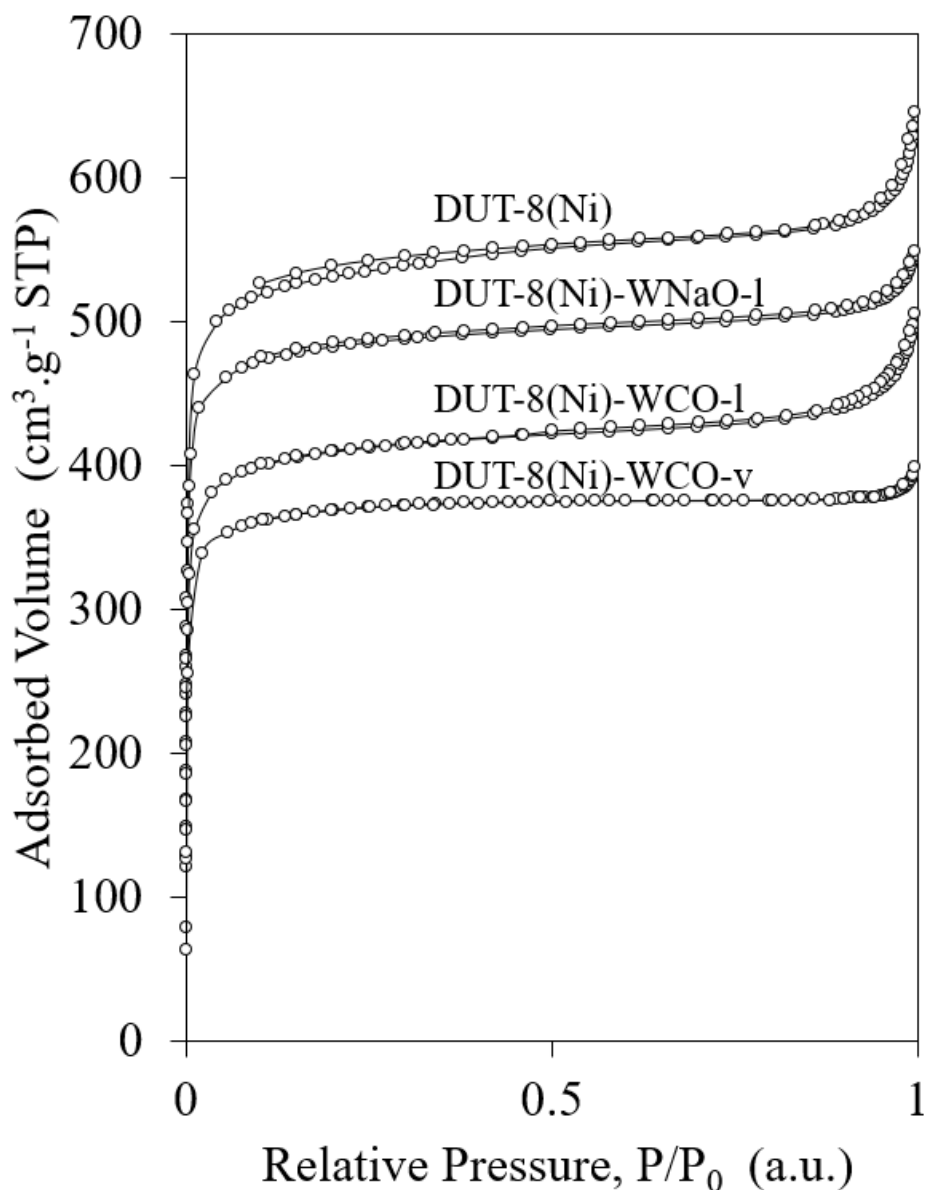


**Figure 5.** N<sub>2</sub> sorption isotherms of W@DUT-8 materials (DUT-8(Ni)-WNaO-1 isotherm was shifted upwards by 30 cm<sup>3</sup>.g<sup>-1</sup>).

After pyrolysis, the textural properties of the carbon materials were determined from N<sub>2</sub> adsorption-desorption isotherms, presented in Figure 6 and Table 2. All H<sub>2</sub> reduced materials displayed <5 m<sup>2</sup>.g<sup>-1</sup> surface areas. All materials pyrolyzed under N<sub>2</sub> exhibited a decrease of surface area and an increase in pore diameter, when compared with pristine material. This demonstrated that the thermal treatment induced a collapse of the parent microporosity, occurring during the DUT-8 structure loss and reflected by a shift from type I to type II isotherm. An impressive decrease of the surface area was noticed for NiWNaO-1-N<sub>2</sub> (from 1743 to 95

$\text{m}^2 \cdot \text{g}^{-1}$ ), and comparable trends are observed for the other two samples (from 1598 to  $112 \text{ m}^2 \cdot \text{g}^{-1}$  for NiWCO-I-N<sub>2</sub> and from 1439 to  $104 \text{ m}^2 \cdot \text{g}^{-1}$  for NiWCO-v-N<sub>2</sub>). The strong modifications in textural properties is obviously associated to the high metallic content of the materials after N<sub>2</sub> pyrolysis and the collapse of the MOF porosity upon thermal treatment.

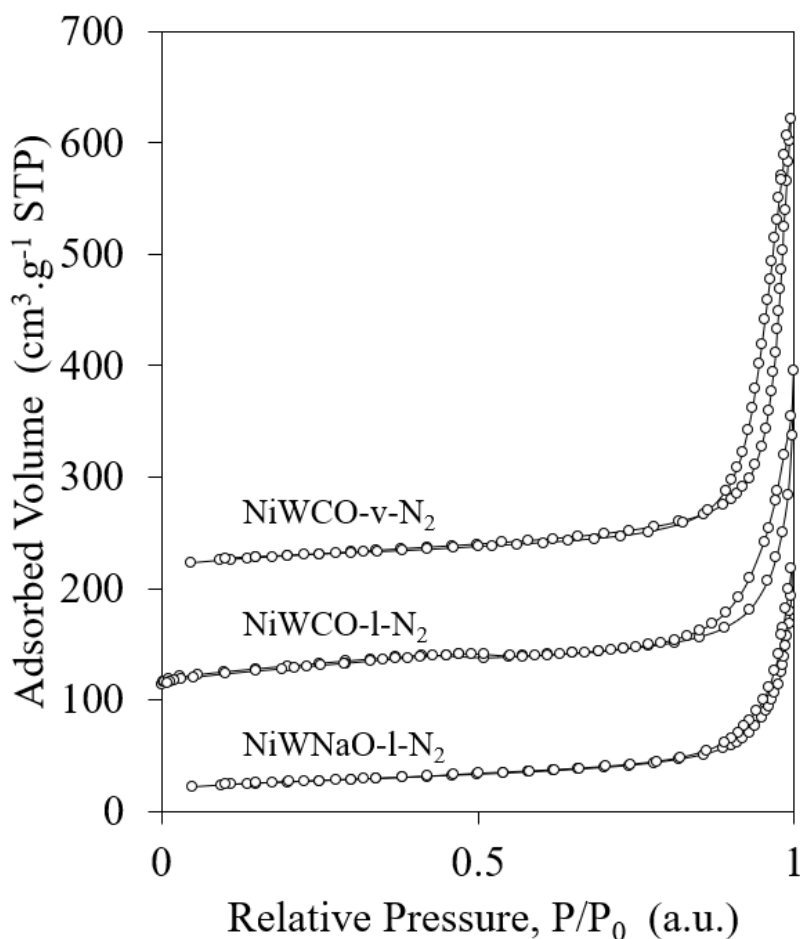


**Figure 6.** N<sub>2</sub> sorption isotherms of NiW catalysts having different tungsten loadings (NiWCO-I-N<sub>2</sub> and NiWCO-v-N<sub>2</sub> isotherms were shifted upwards by  $100 \text{ cm}^3 \cdot \text{g}^{-1}$  and  $200 \text{ cm}^3 \cdot \text{g}^{-1}$  respectively).

**Table 2.** Textural properties of W@DUT-8 materials and NiW functionalized carbons.

Sample	$S_{\text{BET}}^{(a)}$ ( $\text{m}^2 \cdot \text{g}^{-1}$ )	$S_{\mu}^{(b)}$ ( $\text{m}^2 \cdot \text{g}^{-1}$ )	$V_p^{(c)}$ ( $\text{cm}^3 \cdot \text{g}^{-1}$ )	$V_{\mu}^{(d)}$ ( $\text{cm}^3 \cdot \text{g}^{-1}$ )	$D_{\text{pore}}^{(e)}$ (nm)
DUT-8(Ni)	2067	2029	0.94	0.83	1-2

DUT-8(Ni)-WNaO-l	1743	1737	0.78	0.70	1-2
DUT-8(Ni)-WCO-l	1598	1561	0.74	0.63	1-2
DUT-8(Ni)-WCO-v	1439	1438	0.60	0.58	1-2
NiWNaO-l-N <sub>2</sub>	95	50	0.22	0.02	4-24
NiWCO-l-N <sub>2</sub>	112	37	0.28	0.01	2-20
NiWCO-v-N <sub>2</sub>	104	36	0.53	0.02	3-21

[a] BET surface area; [b] micropore surface area; [c] total pore volume; [d] micropore volume; [e] BJH pore diameter calculated on desorption branch.

SEM images of DUT-8(Ni) materials show a particle size average particle size of 200-500 nm (Figure S3), which is consistent with a rigid geometry obtained in previous study for the DUT-8 phase<sup>18</sup>. Analysis of the W-containing materials, prepared by liquid incorporation, shows clear aggregation of the W element outside of the MOF cages (Figures S4, S5). It demonstrated the poor efficiency of the liquid-mediated incorporation to achieve a good dispersion of the W inside the MOF porosity, and that whatever the precursor used. On the contrary, such external aggregation of the W phase was not observed when vapor phase deposition is applied, DUT-8(Ni)-WCO-v (Figure S6). A homogeneous distribution of C, N, Ni and W in DUT-8(Ni)-WCO-v was identified by energy-dispersive X-ray spectroscopy elemental mapping (Figure S6.c). The morphologies and the nanostructures of the pyrolyzed materials were further examined by SEM and TEM. The N<sub>2</sub> activated samples (Figures 7, S7, S9) preserve the morphology of DUT-8, with a clearly observed aggregate-like morphology of 200-800 nm elementary particles. After thermal treatment under N<sub>2</sub>, the W heterogeneous dispersion is retained in the material, with clear brighter – large particles observed outside of the Ni-C porous network (Figures S7, S9). On the contrary, very small W-containing NPs homogeneously dispersed on the aggregate surface can be observed in Figure 7 for the material resulting from vapor deposition route (NiWCO-v-N<sub>2</sub>). Particle size, on the basis of the SEM images, is estimated in the 5-35 nm interval, with an average size of 25 nm. When the samples are activated under H<sub>2</sub>, a completely different morphology is obtained (Figures S8, S10, S11). Due to the low residual carbon content (always visible for NiWNaO-l-H<sub>2</sub>, Figure S8, and NiWCO-l-H<sub>2</sub>, Figure S10), porous metallic skeletons are observed and the large heterogeneities in W phase dispersion are no more observed. Notably,

the NiWCO-v-H<sub>2</sub> do not show any residual amorphous carbonaceous phase below the metallic skeleton (Figure S11).

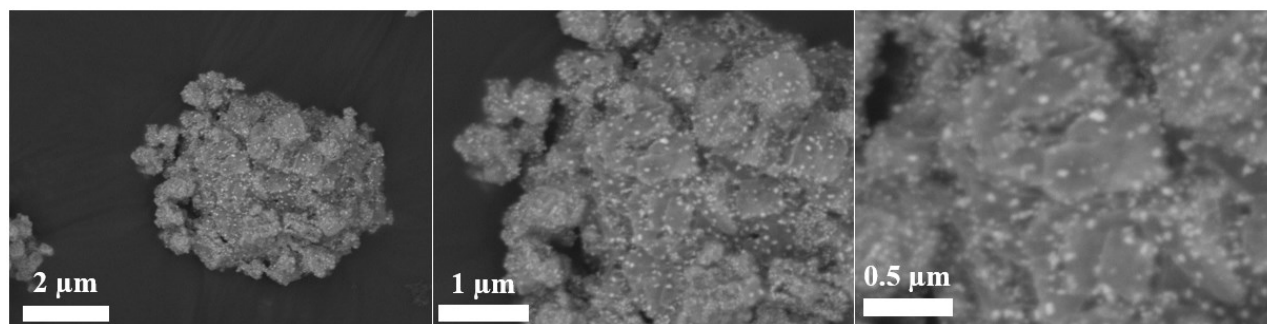


**Figure 7.** SEM images of NiWCO-v-N<sub>2</sub>.

Selected catalysts were characterized by aberration-corrected scanning transmission electron microscopy (STEM). Among the samples pyrolyzed under N<sub>2</sub> NiWCO-v-N<sub>2</sub> presented the smallest particles size (average size of 2.7 nm) with a homogeneous dispersion of W and Ni particles throughout the analyzed samples (Figure 8, S16). W and Ni particles cover the same areas, a clear separation was not detected, which is favourable for the possible synergy between the 2 metals. Lower dispersion of the Ni and W elements are obtained on the samples prepared by liquid-mediated incorporation. Indeed, NiWNaO-l-N<sub>2</sub> presents an average particle size of 13.8 nm, with a satisfying proximity between Ni element and W element, as identified by EDS elemental mapping (Figure S12b). The largest average metal particles are obtained for NiWCO-l-N<sub>2</sub>, for which an average particle size of ~15 nm is measured (Figure S13). On the contrary of what was observed for NiWNaO-l-N<sub>2</sub>, NiWCO-l-N<sub>2</sub> presents significant segregation between Ni and W, almost pure and individual particles are observed (Figure S13). As previously mentioned, the limited solubility of the W(CO)<sub>6</sub> precursor is at the origin of a limited diffusion inside the MOF pores, resulting as observed by TEM in a poor dispersion in the final material with a limited interaction with Ni phase.

The images issued from the observation of the samples pyrolyzed under H<sub>2</sub> are presented in Figures S14, S15 and S17. First of all, far larger metal particles are observed, in line with the metallic skeletons observed by SEM. The metal sintering can be associated to the deteriorative effect of hydrogen on carbon content in the material, leading to almost pure metal catalysts. Therefore, the absence of carbon at the interface results in a facilitated sintering. The particle

size observed are, for the three samples, higher than 30 nm, forming aggregates of metal particles larger of which size can exceed several hundreds of nanometers. Due to the absence of carbon in the hydrogen activated solids, W and Ni elements are in close proximity, which agrees with the XRD analysis previously presented and pointing out the formation of Ni-W alloys (Figure 3).

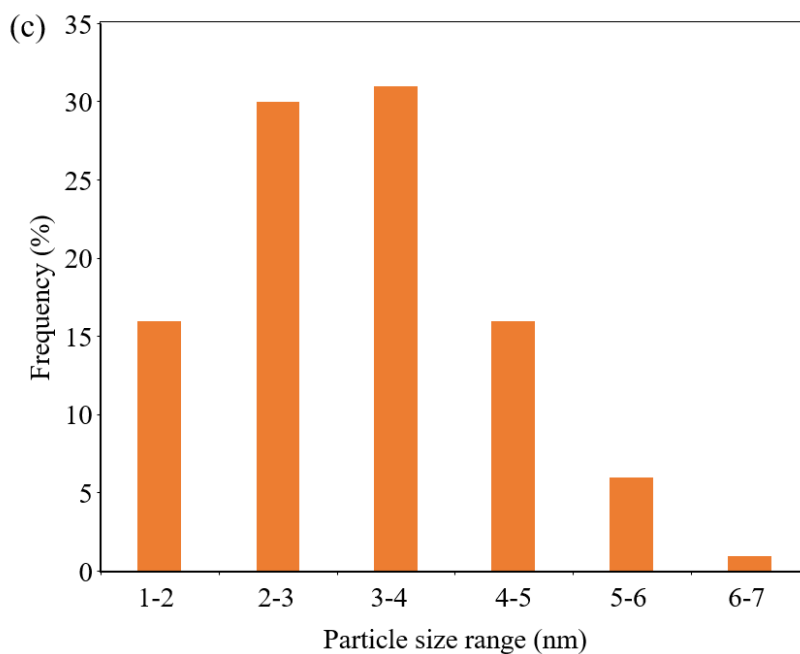
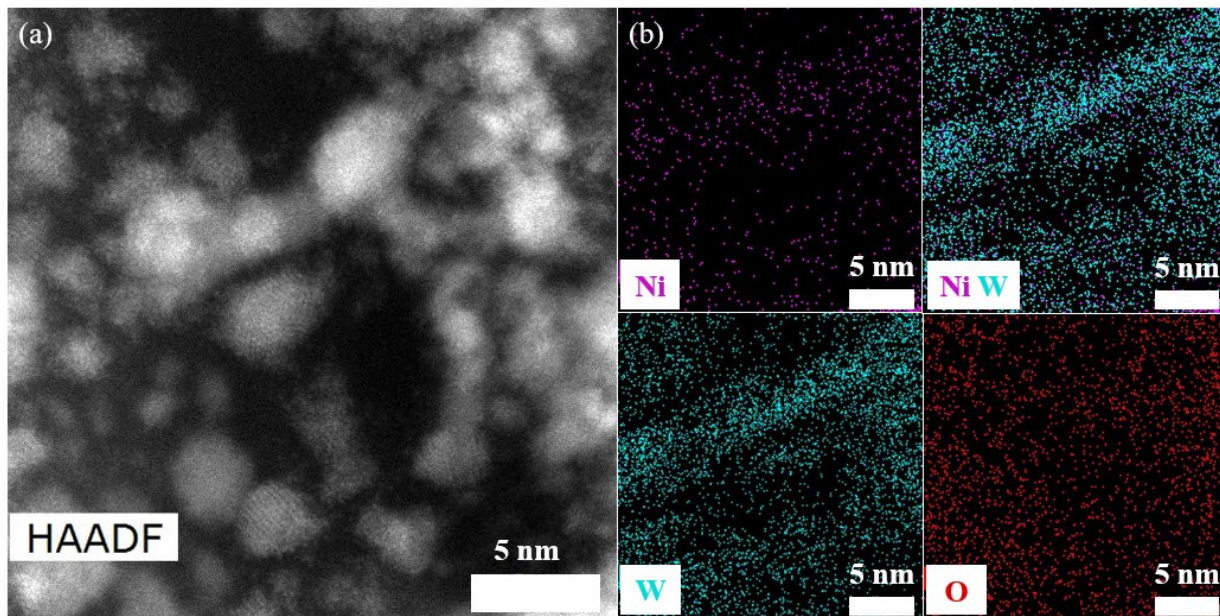


**Figure 8.** (a) HAADF-STEM; (b) TEM-EDS elemental mapping images of NiWCO-v-N<sub>2</sub>. (c) Particle size distribution histogram of NiWCO-v-N<sub>2</sub> calculated from image a and images like a.

To conclude, the W precursor nature, the mode of incorporation over DUT-8(Ni) MOF, and the activation atmosphere are determining aspects for the final properties of the materials. Therefore, the use of liquid mediated incorporation leads to poor dispersion of Ni and W phases inside the microporous DUT-8 phase, especially when the tungsten carbonyl precursor is used due to its limited solubility in water. Better W dispersion is reached by vapor phase deposition of tungsten carbonyl precursor. Thermal activation under nitrogen atmosphere leads to the formation of Ni-W metallic particles, supported over porous carbon. The dispersion of the Ni and W element prior to the thermal treatment conditions the final dispersion stage and element dispersion. Therefore, better dispersion and proximity between metal is obtained for NiWCO-v-N<sub>2</sub> prepared by vapor phase deposition. When thermal treatment under H<sub>2</sub> is conducted, it induces a complete consumption of the carbon matter, leading to purely metallic material. Then, in the absence of residual carbon, significant sintering of alloyed Ni-W metal phase occurs, resulting in poor textural properties and large crystal grain size.

#### ***4.3.2. Catalytic conversion of cellulose***

Hydrogenolysis of cellulose into polyols (EG, PG) occurs over Ni-W based catalysts. W and Ni species contribute respectively to the retro-aldol cleavage and hydrogenation of unsaturated intermediates<sup>4</sup>. Phase formed during synthesis is particularly important, especially the formation of NiW alloys that may present a positive effect catalyst efficiency<sup>9</sup>. Figure 9 and Table S4 display the catalytic results in the cellulose hydrogenolysis of the Ni/W catalysts derived from the different synthesis pathways. The conditions were that of our previous study with Ni-W<sub>x</sub>C/AC<sup>9</sup>, T = 245 °C, under 60 bar of H<sub>2</sub>.

The catalysts prepared with Na<sub>2</sub>WO<sub>4</sub> precursor, and all of those activated under H<sub>2</sub> gave the lowest reaction yields, with cumulated EG+PG yields below 28%. It clearly demonstrated that the hydrogen activation is not preferable for these catalysts, on the contrary of what was reported in the literature for conventional carbon supported Ni-W catalysts. However, this can be correlated to the fact that, when W-loaded MOF precursors are activated under H<sub>2</sub>, no more carbon remains in the catalysts and significant sintering of the metal phase occurs. Then, the catalytic activity reported for these catalysts are far from the results obtained over NiW optimized catalysts, for which cumulated EG+PG yields reaching 78% are reported<sup>2,3</sup>. Besides, two catalysts gave better results, with EG+PG yields in the 52-56% range: NiWCO-l-N<sub>2</sub> and



NiWCO-v-N<sub>2</sub>. These two materials have been prepared with W(CO)<sub>6</sub> as W precursor and a pyrolysis step performed under N<sub>2</sub> (to retain sufficient carbon in the final material to limit metal sintering). NiWCO-I-N<sub>2</sub> presents W<sub>2</sub>C and Ni<sub>0.94</sub>W<sub>0.06</sub> phases, while NiWCO-v-N<sub>2</sub> presents only the Ni<sub>0.94</sub>W<sub>0.06</sub> phase (Table S2). Therefore, the alloyed phase is involved in the reaction, as concluded for a previous work on 5%Ni-30W<sub>x</sub>C/AC<sup>9</sup>. However, the improved dispersion, higher W content, and better metal repartition observed for NiWCO-v-N<sub>2</sub> can also contribute to the slightly higher activity obtained with this material. The results obtained here with these last two catalysts compete with the best results reported in the literature with reported cumulated EG+PG yield of 68%, and total products' yield (including other molecules such as glycerol) of 84%<sup>9</sup>.

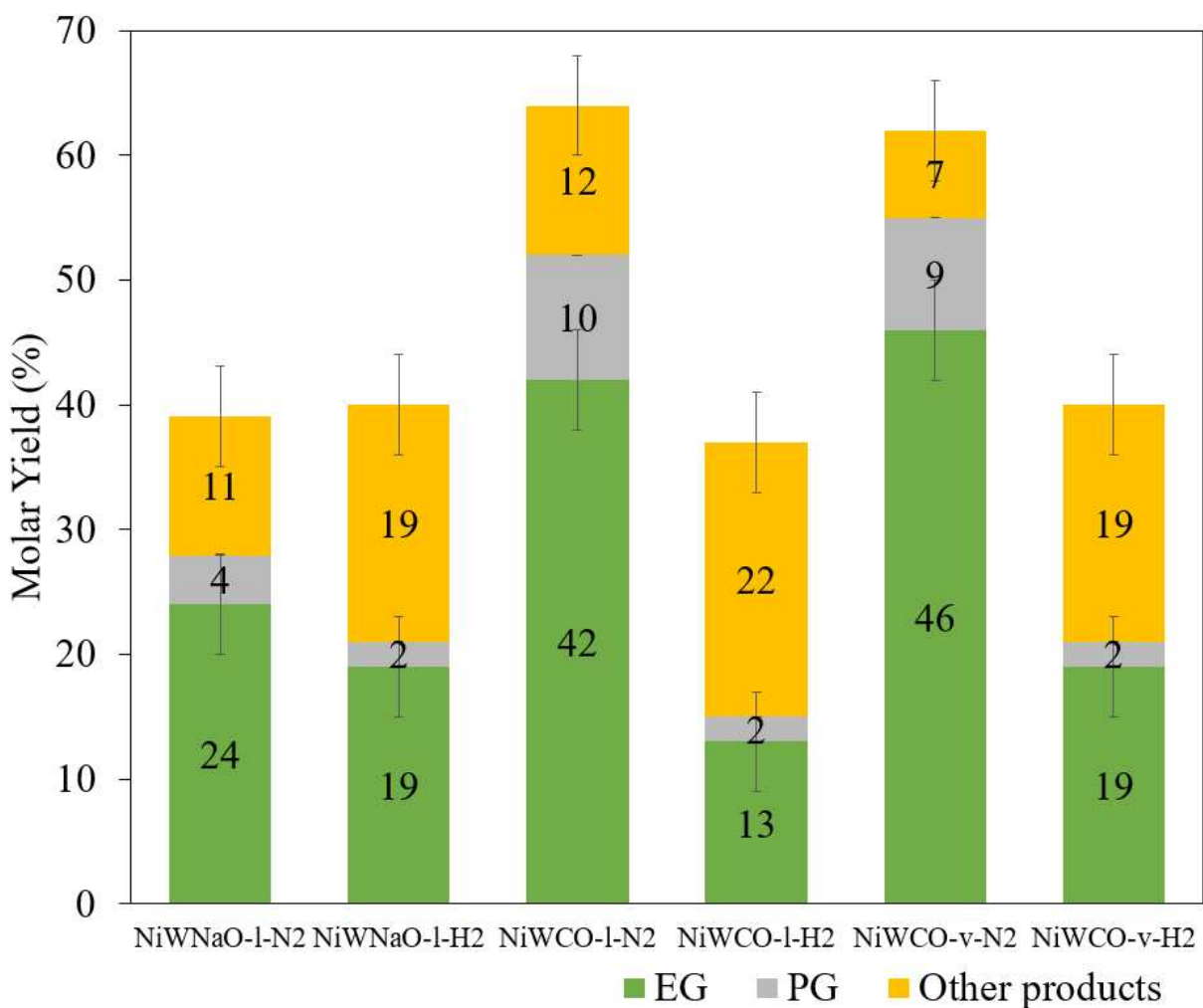


**Figure 9.** Products molar yields over NiW catalysts derived from different synthesis pathways. Reaction conditions: 0.50 g cellulose, 0.15 g catalyst, 50 mL water, 60 bar H<sub>2</sub>, 1000 rpm, 245°C, and 1 hour.

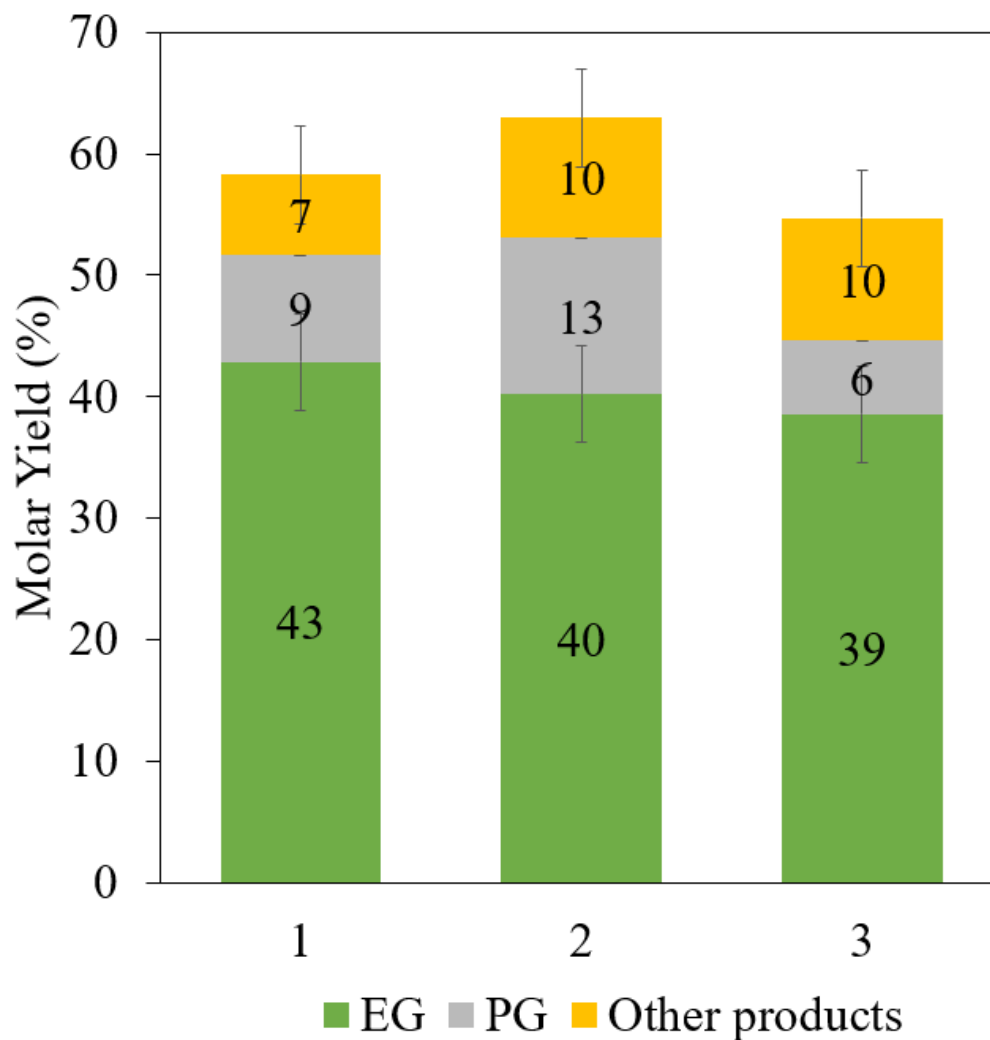


**Figure 10.** Recycling experiments on the conversion of cellulose into polyols over NiWCO-v-N<sub>2</sub>. Reaction conditions: 0.50 g cellulose, 0.15 g catalyst, 50 mL water, 60 bar H<sub>2</sub>, 1000 rpm, 245°C, and 1 hour.

The materials presented above were active for the hydrogenolysis of cellulose into glycols. Considering the promising activity obtained in terms of cumulated glycols yield, we assessed the stability of NiWCO-v-N<sub>2</sub> catalyst under recycling experiments (Figure 10). The same reaction conditions were applied between each run, without any reactivation treatment in-between. The cumulated yield of glycols could remain relatively stable for 2 runs, before a slight loss of

efficiency measured at the third run even if the efficiency remains in the error interval of the first cycle. The reaction solutions after the first run were recovered and metal species quantified by ICP-OES (Table 4). After the first run, a leaching of 7.4% of total W and 1.3% of total Ni was measured. W loss was in the same range as that for the benchmark catalyst Ni-W<sub>2</sub>C/AC, however, Ni species were more stable (1.3% after cycle n°1 vs. 9.2% in our previous work<sup>9</sup>). The metal leaching of Ni is stable over the recycling experiments at ~1%. On the contrary, W leaching significantly decreases over the three cycles to become close to ~1 % meaning that after removal of a fraction of soluble fraction of W phase, the residual W is stable upon leaching. Considering that the change in activity is relatively modest between the first and third cycle, it could be assumed that the 7-8% of the W dissolved are not significantly contributing to the catalyst activity. NiWCO-v-N<sub>2</sub> was characterized after reaction. The XRD pattern of NiWCO-v-N<sub>2</sub> is preserved after reaction (Figure S18) with the presence of W<sub>0.04</sub>Ni<sub>0.96</sub> alloy confirmed after reaction. In addition, applying the Scherrer equation on the diffractogram reflection leads to comparable metal crystal size (13 nm after reaction, vs 12 nm before reaction) showing a limited sintering. The TEM images, presented in Figure S20, showed the presence of two populations of particles. Most of the particles are retaining limited size (and then do not suffered of significant sintering – see Figure S20c). however, surface large particles, with size in the 10-40 nm, are observed. In all cases, particles (low sizes and large sizes) are presenting Ni-W mixed composition. The textural properties, after reaction; remained close to the values measured for the pristine catalyst (Table S5; S<sub>BET</sub>: 107 m<sup>2</sup>.g<sup>-1</sup> after reaction, vs. 104 m<sup>2</sup>.g<sup>-1</sup> for the fresh catalyst) and the isotherm curve type remains unchanged (Figure S19). The non-variation of those physico-chemical properties stand behind its resilience over various catalytic runs. Then, post-reaction characterization shows a satisfying stability of both catalyst structure and catalyst texture, in line with the limited changes in catalyst activity.

**Table 4.** Concentration of Ni and W with the corresponding leaching proportion.

Material	Concentration <sup>(a)</sup> (mg.L <sup>-1</sup> )		Leaching (%)	
	Ni	W	Ni	W
NiWCO-v-N <sub>2</sub> (run 1)	14.6	75.7	1.3	7.4
NiWCO-v-N <sub>2</sub> (run 2)	13.4	19.4	1.1	1.9

---

<sup>(a)</sup> obtained by ICP-EOS of in the liquid reaction medium.

#### 4.4. Conclusion

We studied the preparation of transition metals (nickel-tungsten) based catalysts supported on porous carbons, through pyrolysis of W deposited DUT-8(Ni) porous MOF materials. The synthesis process includes in a first step the hydrothermal synthesis of hybrid W@DUT-8(Ni), through a liquid-mediated or a vapor deposition route, followed by pyrolysis under an inert atmosphere (H<sub>2</sub> or N<sub>2</sub>). Amorphous carbon-supported nickel and tungsten materials with attractive surface areas (>100 m<sup>2</sup>.g<sup>-1</sup>) are obtained after thermal treatment under N<sub>2</sub>, despite the high metal loadings reached (total of 70-80 wt.%). On the contrary, thermal treatment under H<sub>2</sub> leads to almost pure metal catalysts (residual carbon <0.5 wt.%) on which porosity fully collapsed. Regarding the application as catalysts for the hydrogenolysis of cellulose, molar yields of up to 24% in ethylene glycol (EG) and 4% in propylene glycol (PG) were obtained at 245 °C and 1 hour reaction time using Na<sub>2</sub>WO<sub>4</sub> derived catalyst. When W(CO)<sub>6</sub> was used as the W precursor, the glycol yields significantly increase, with EG yields at 46% and PG yield at 9%. The activity enhancement is associated to the formation of W<sub>0.04</sub>Ni<sub>0.96</sub> alloyed phase, instead of a mixture of Tungsten carbide and Ni(0) phases. Notably, the MOF derived catalyst demonstrated a great catalytic stability upon three recycling tests, which is confirmed by limited solubility of Ni and W, and retained structural and textural characteristics. This study then demonstrated the feasibility of using utilized Ni-containing MOF as a precursor for the production of NiW/C catalysts active and stable for cellulose conversion under severe hydrothermal reaction conditions.

#### 4.5. References

- (1) Kumar, A. K.; Sharma, S. Recent Updates on Different Methods of Pretreatment of Lignocellulosic Feedstocks: A Review. *Bioresour. Bioprocess.* **2017**, *4* (1), 7. <https://doi.org/10.1186/s40643-017-0137-9>.
- (2) Ji, N.; Zhang, T.; Zheng, M.; Wang, A.; Wang, H.; Wang, X.; Chen, J. G. Direct Catalytic Conversion of Cellulose into Ethylene Glycol Using Nickel-Promoted Tungsten Carbide Catalysts. *Angew. Chem. Int. Ed.* **2008**, *47* (44), 8510–8513. <https://doi.org/10.1002/anie.200803233>.
- (3) Zhang, Y.; Wang, A.; Zhang, T. A New 3D Mesoporous Carbon Replicated from Commercial Silica as a Catalyst Support for Direct Conversion of Cellulose into Ethylene Glycol. *Chem Commun* **2010**, *46* (6), 862–864. <https://doi.org/10.1039/B919182H>.
- (4) Fabičovicová, K.; Malter, O.; Lucas, M.; Claus, P. Hydrogenolysis of Cellulose to Valuable Chemicals over Activated Carbon Supported Mono- and Bimetallic Nickel/Tungsten Catalysts. *Green Chem* **2014**, *16* (7), 3580–3588. <https://doi.org/10.1039/C4GC00664J>.
- (5) Gu, M.; Shen, Z.; Yang, L.; Dong, W.; Kong, L.; Zhang, W.; Peng, B.-Y.; Zhang, Y. Reaction Route Selection for Cellulose Hydrogenolysis into C2/C3 Glycols by ZnO-Modified Ni-W/ $\beta$ -Zeolite Catalysts. *Sci. Rep.* **2019**, *9* (1), 11938. <https://doi.org/10.1038/s41598-019-48103-6>.
- (6) Rodella, C. B.; Barrett, D. H.; Moya, S. F.; Figueroa, S. J. A.; Pimenta, M. T. B.; Curvelo, A. A. S.; Silva, V. T. da. Physical and Chemical Studies of Tungsten Carbide Catalysts: Effects of Ni Promotion and Sulphonated Carbon. *RSC Adv.* **2015**, *5* (30), 23874–23885. <https://doi.org/10.1039/C5RA03252K>.
- (7) Xiao, Z.; Wang, X.; Yang, Q.; Xing, C.; Ge, Q.; Gai, X.; Mao, J.; Ji, J. Fabrication of Immobilized Nickel Nanoclusters Decorated by C N Species for Cellulose Conversion to C2,3 Oxygenated Compounds: Rational Design via Typical C- and N-Sources. *J. Energy Chem.* **2020**, *50*, 25–36. <https://doi.org/10.1016/j.jechem.2020.02.054>.
- (8) Xiao, Z.; Zhang, Q.; Wang, X.; Ge, Q.; Gai, X.; Mao, J.; Ji, J. Organic Nitrogen Promotes Stability of Metallic Catalysts in Conversion of Bamboo Pulp to Low Carbon Polyols. *J. Fuel Chem. Technol.* **2019**, *47* (6), 675–687. [https://doi.org/10.1016/S1872-5813\(19\)30029-5](https://doi.org/10.1016/S1872-5813(19)30029-5).
- (9) Goc, F.; Epicier, T.; Perret, N.; Rataboul, F. Preparation of Carbon-Supported Tungsten Carbides: Comparative Determination of Surface Composition and Influence on Cellulose Transformation into Glycols. *ChemCatChem* **2023**, e202201496. <https://doi.org/10.1002/cctc.202201496>.
- (10) Yang, Y.; Zhang, W.; Yang, F.; Brown, D. E.; Ren, Y.; Lee, S.; Zeng, D.; Gao, Q.; Zhang, X. Versatile Nickel–Tungsten Bimetallics/Carbon Nanofiber Catalysts for Direct Conversion of Cellulose to Ethylene Glycol. *Green Chem.* **2016**, *18* (14), 3949–3955. <https://doi.org/10.1039/C6GC00703A>.
- (11) Wang, C.; Yao, Y.; Li, J.; Yamauchi, Y. Metal–Organic Frameworks: A Robust Platform for Creating Nanoarchitected Carbon Materials. *Acc. Mater. Res.* **2022**, accountsmr.1c00258. <https://doi.org/10.1021/accountsmr.1c00258>.
- (12) Wang, X.; Dong, A.; Hu, Y.; Qian, J.; Huang, S. A Review of Recent Work on Using Metal–Organic Frameworks to Grow Carbon Nanotubes. *Chem. Commun.* **2020**, *56* (74), 10809–10823. <https://doi.org/10.1039/D0CC04015K>.

- (13) Liao, Y.-T.; Matsagar, B. M.; Wu, K. C.-W. Metal–Organic Framework (MOF)-Derived Effective Solid Catalysts for Valorization of Lignocellulosic Biomass. *ACS Sustain. Chem. Eng.* **2018**, *6* (11), 13628–13643. <https://doi.org/10.1021/acssuschemeng.8b03683>.
- (14) Xu, Y.-T.; Xiao, X.; Ye, Z.-M.; Zhao, S.; Shen, R.; He, C.-T.; Zhang, J.-P.; Li, Y.; Chen, X.-M. Cage-Confinement Pyrolysis Route to Ultrasmall Tungsten Carbide Nanoparticles for Efficient Electrocatalytic Hydrogen Evolution. *J. Am. Chem. Soc.* **2017**, *139* (15), 5285–5288. <https://doi.org/10.1021/jacs.7b00165>.
- (15) Jiang, B.; Sun, H.; Yuan, T.; He, W.; Zheng, C.; Zhang, H.-J.; Yang, J.; Zheng, S. Framework-Derived Tungsten Single-Atom Catalyst for Oxygen Reduction Reaction. *Energy Fuels* **2021**, *35* (9), 8173–8180. <https://doi.org/10.1021/acs.energyfuels.1c00758>.
- (16) Chen, W.; Pei, J.; He, C.-T.; Wan, J.; Ren, H.; Wang, Y.; Dong, J.; Wu, K.; Cheong, W.-C.; Mao, J.; Zheng, X.; Yan, W.; Zhuang, Z.; Chen, C.; Peng, Q.; Wang, D.; Li, Y. Single Tungsten Atoms Supported on MOF-Derived N-Doped Carbon for Robust Electrochemical Hydrogen Evolution. *Adv. Mater.* **2018**, *30* (30), 1800396. <https://doi.org/10.1002/adma.201800396>.
- (17) Kim, J.; Neumann, G. T.; McNamara, N. D.; Hicks, J. C. Exceptional Control of Carbon-Supported Transition Metal Nanoparticles Using Metal–Organic Frameworks. *J. Mater. Chem. A* **2014**, *2* (34), 14014. <https://doi.org/10.1039/C4TA03050H>.
- (18) Kavoosi, N.; Bon, V.; Senkovska, I.; Krause, S.; Atzori, C.; Bonino, F.; Pallmann, J.; Paasch, S.; Brunner, E.; Kaskel, S. Tailoring Adsorption Induced Phase Transitions in the Pillared-Layer Type Metal–Organic Framework DUT-8(Ni). *Dalton Trans.* **2017**, *46* (14), 4685–4695. <https://doi.org/10.1039/C7DT00015D>.
- (19) Melix, P.; Paesani, F.; Heine, T. A Ligand Field Molecular Mechanics Study of CO<sub>2</sub> - Induced Breathing in the Metal–Organic Framework DUT-8(Ni). *Adv. Theory Simul.* **2019**, *2* (11), 1900098. <https://doi.org/10.1002/adts.201900098>.
- (20) Krylov, A.; Vtyurin, A.; Petkov, P.; Senkovska, I.; Maliuta, M.; Bon, V.; Heine, T.; Kaskel, S.; Slyusareva, E. Raman Spectroscopy Studies of the Terahertz Vibrational Modes of a DUT-8 (Ni) Metal–Organic Framework. *Phys. Chem. Chem. Phys.* **2017**, *19* (47), 32099–32104. <https://doi.org/10.1039/C7CP06225G>.
- (21) Di Valentin, C.; Pacchioni, G. Spectroscopic Properties of Doped and Defective Semiconducting Oxides from Hybrid Density Functional Calculations. *Acc. Chem. Res.* **2014**, *47* (11), 3233–3241. <https://doi.org/10.1021/ar4002944>.
- (22) Biesinger, M. C.; Payne, B. P.; Lau, L. W. M.; Gerson, A.; Smart, R. St. C. X-Ray Photoelectron Spectroscopic Chemical State Quantification of Mixed Nickel Metal, Oxide and Hydroxide Systems. *Surf. Interface Anal.* **2009**, *41* (4), 324–332. <https://doi.org/10.1002/sia.3026>.
- (23) Besson, M.; Gallezot, P.; Pinel, C. Conversion of Biomass into Chemicals over Metal Catalysts. *Chem. Rev.* **2014**, *114* (3), 1827–1870. <https://doi.org/10.1021/cr4002269>.
- (24) Krasovskii, P. V.; Malinovskaya, O. S.; Samokhin, A. V.; Blagoveshchenskiy, Y. V.; Kazakov, V. A.; Ashmarin, A. A. XPS Study of Surface Chemistry of Tungsten Carbides Nanopowders Produced through DC Thermal Plasma/Hydrogen Annealing Process. *Appl. Surf. Sci.* **2015**, *339*, 46–54. <https://doi.org/10.1016/j.apsusc.2015.02.152>.
- (25) Zhang, S.; Zhang, H.; Zhang, W.; Yuan, X.; Chen, S.; Ma, Z.-F. Induced Growth of Fe-N x Active Sites Using Carbon Templates. *Chin. J. Catal.* **2018**, *39* (8), 1427–1435. [https://doi.org/10.1016/S1872-2067\(18\)63107-9](https://doi.org/10.1016/S1872-2067(18)63107-9).

- (26) Xing, Z.; Ju, Z.; Zhao, Y.; Wan, J.; Zhu, Y.; Qiang, Y.; Qian, Y. One-Pot Hydrothermal Synthesis of Nitrogen-Doped Graphene as High-Performance Anode Materials for Lithium Ion Batteries. *Sci. Rep.* **2016**, *6* (1), 26146. <https://doi.org/10.1038/srep26146>.

#### 4.6. Supplementary information

**Table S1.** Main elements of the preparation of the materials.

Sample name <i>(W@DUT-8 materials)</i>	Sample name <i>(pyrolyzed materials)</i>	Tungsten precursor	Pyrolysis atmosphere
DUT-8(Ni)	-	-	-
DUT-8(Ni)-WNaO-I	NiWNaO-I-N <sub>2</sub>	Na <sub>2</sub> WO <sub>4</sub> ·2H <sub>2</sub> O	N <sub>2</sub>
	NiWNaO-I-H <sub>2</sub>	Na <sub>2</sub> WO <sub>4</sub> ·2H <sub>2</sub> O	H <sub>2</sub>
DUT-8(Ni)-WCO-I	NiWCO-I-N <sub>2</sub>	W(CO) <sub>6</sub>	N <sub>2</sub>
	NiWCO-I-H <sub>2</sub>	W(CO) <sub>6</sub>	H <sub>2</sub>
DUT-8(Ni)-WCO-v	NiWCO-v-N <sub>2</sub>	W(CO) <sub>6</sub>	N <sub>2</sub>
	NiWCO-v-H <sub>2</sub>	W(CO) <sub>6</sub>	H <sub>2</sub>

**Table S2.** NiW functionalized carbons crystallite sizes (nm) calculated from Scherrer's equation.

NiWNaO-I- N <sub>2</sub>	NiWNaO-I- H <sub>2</sub>	NiWCO-I- N <sub>2</sub>	NiWCO-I- H <sub>2</sub>	NiWCO-v-N <sub>2</sub>	NiWCO-v- H <sub>2</sub>
W <sub>2</sub> C	Ni <sub>5</sub> W <sub>6</sub> C	W <sub>2</sub> C			W
21	50	13			28
WC					
4					
Ni <sub>0.96</sub> W <sub>0.04</sub>	Ni <sub>0.85</sub> W <sub>0.15</sub>	Ni <sub>0.94</sub> W <sub>0.06</sub>	Ni <sub>0.96</sub> W <sub>0.04</sub>	Ni <sub>0.96</sub> W <sub>0.04</sub>	Ni <sub>0.83</sub> W <sub>0.17</sub>
8	17	8	28	12	19



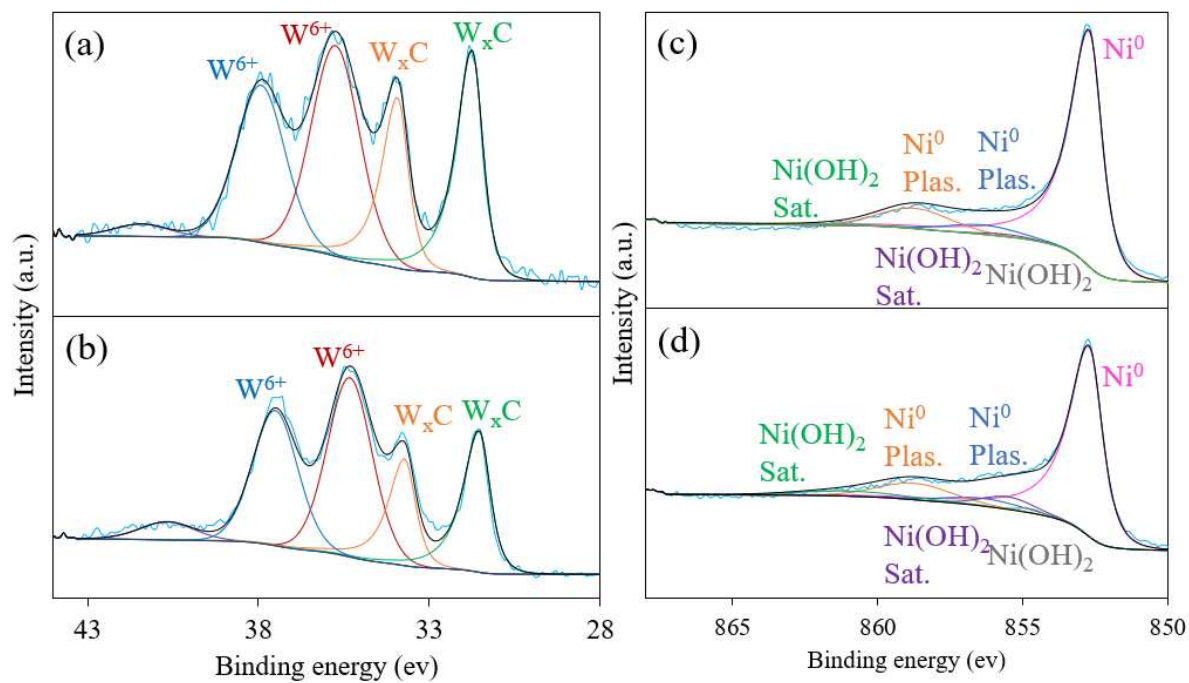


**Figure S1.** W 4f XPS results for (a) NiWNaO-I-N<sub>2</sub>, (b) NiWCO-I-N<sub>2</sub>; Ni 2p in (c) NiWNaO-I-N<sub>2</sub>, (d) NiWCO-I-N<sub>2</sub>.

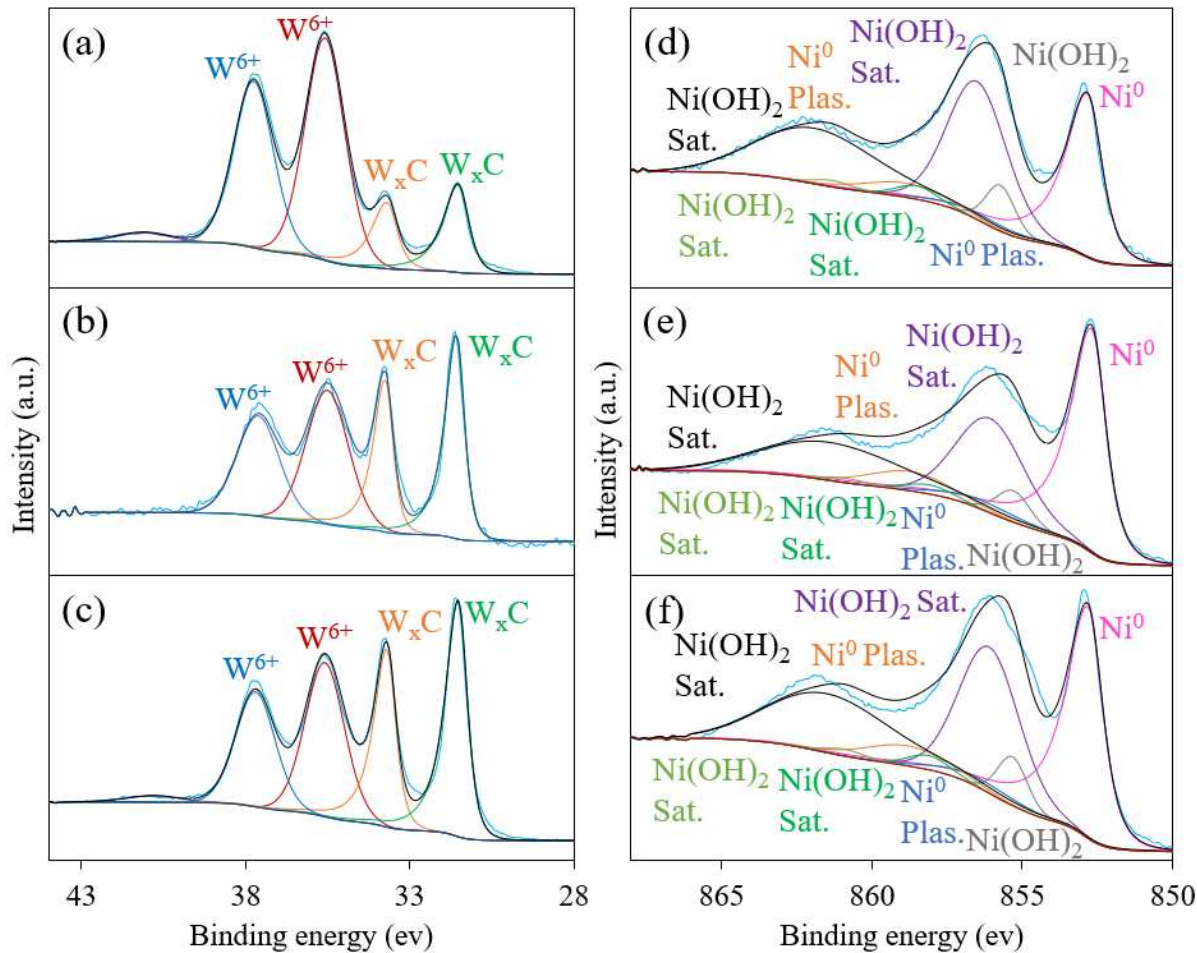


**Figure S2.** W 4f XPS results for (a) NiWNaO-l-H<sub>2</sub>, (b) NiWCO-l-H<sub>2</sub>, (c) NiWCO-v-H<sub>2</sub>; Ni 2p in (d) NiWNaO-l-H<sub>2</sub>, (e) NiWCO-l-H<sub>2</sub>, (f) NiWCO-v-H<sub>2</sub>.

**Table S3.** Relative surface abundances of the different species, in the pre-reaction carbon samples hydrothermally synthesized and functionalized with W and Ni.

Material	Ni		W	
	oxidation state	%	oxidation state	%
NiWNaO-l-N <sub>2</sub>	Ni <sup>2+</sup>	2	W <sup>6+</sup>	74
	Ni <sup>0</sup>	98	W <sub>x</sub> C	26
NiWNaO-l-H <sub>2</sub>	Ni <sup>2+</sup>	65	W <sup>6+</sup>	87
	Ni <sup>0</sup>	35	W <sub>x</sub> C	13
NiWCO-l-N <sub>2</sub>	Ni <sup>2+</sup>	12	W <sup>6+</sup>	78
	Ni <sup>0</sup>	88	W <sub>x</sub> C	22
NiWCO-l-H <sub>2</sub>	Ni <sup>2+</sup>	52	W <sup>6+</sup>	71

	Ni <sup>0</sup>	48	W <sub>x</sub> C	29
NiWCO-v-N <sub>2</sub>	Ni <sup>2+</sup>	7	W <sup>6+</sup>	70
	Ni <sup>0</sup>	93	W <sub>x</sub> C	30
NiWCO-v-H <sub>2</sub>	Ni <sup>2+</sup>	59	W <sup>6+</sup>	66
	Ni <sup>0</sup>	41	W <sub>x</sub> C	34

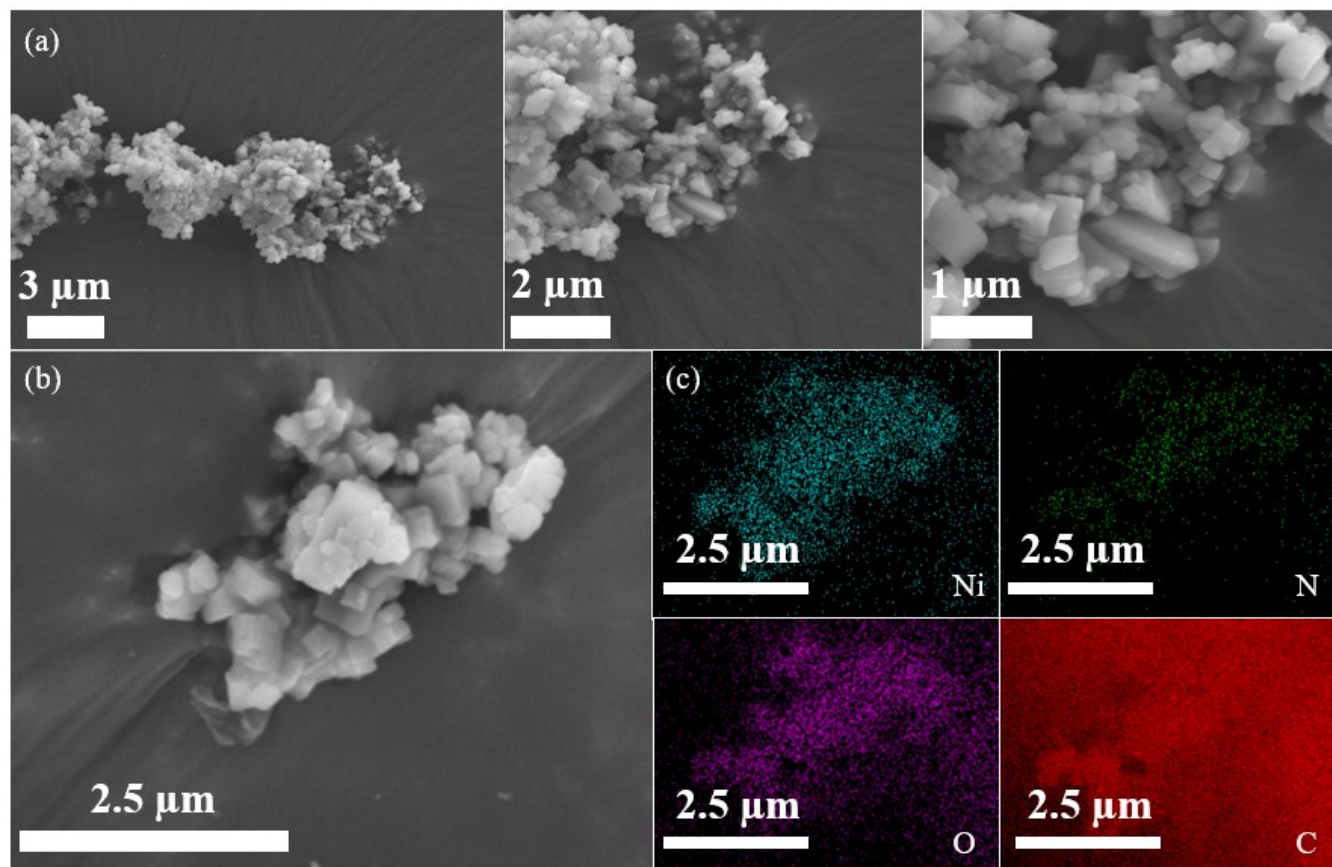


**Figure S3.** (a-b) SEM and (c) SEM-EDS elemental mapping images of DUT-8(Ni).

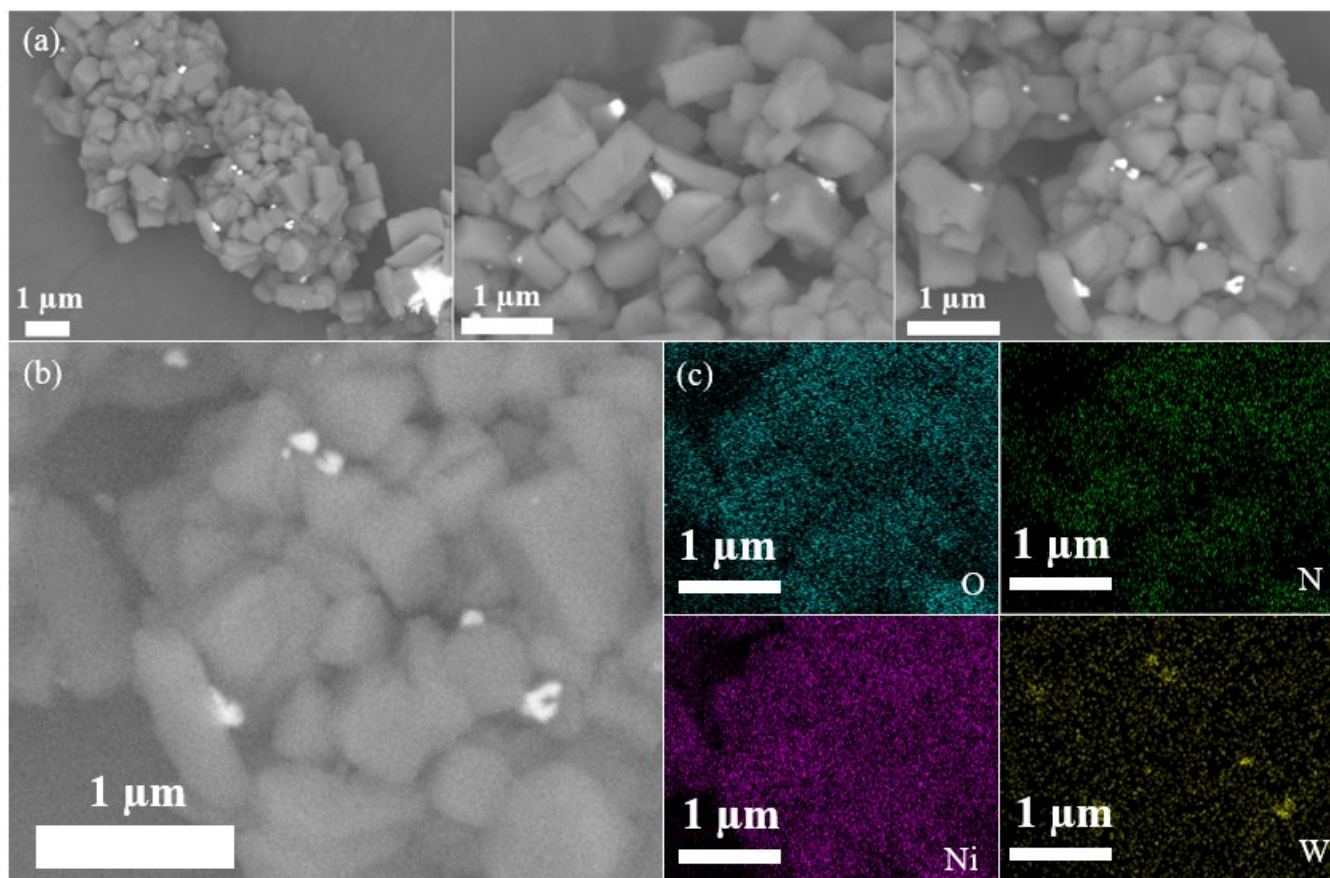


**Figure S4.** (a-b) SEM and (c) SEM-EDS elemental mapping images of DUT-8(Ni)-WNaO-l.



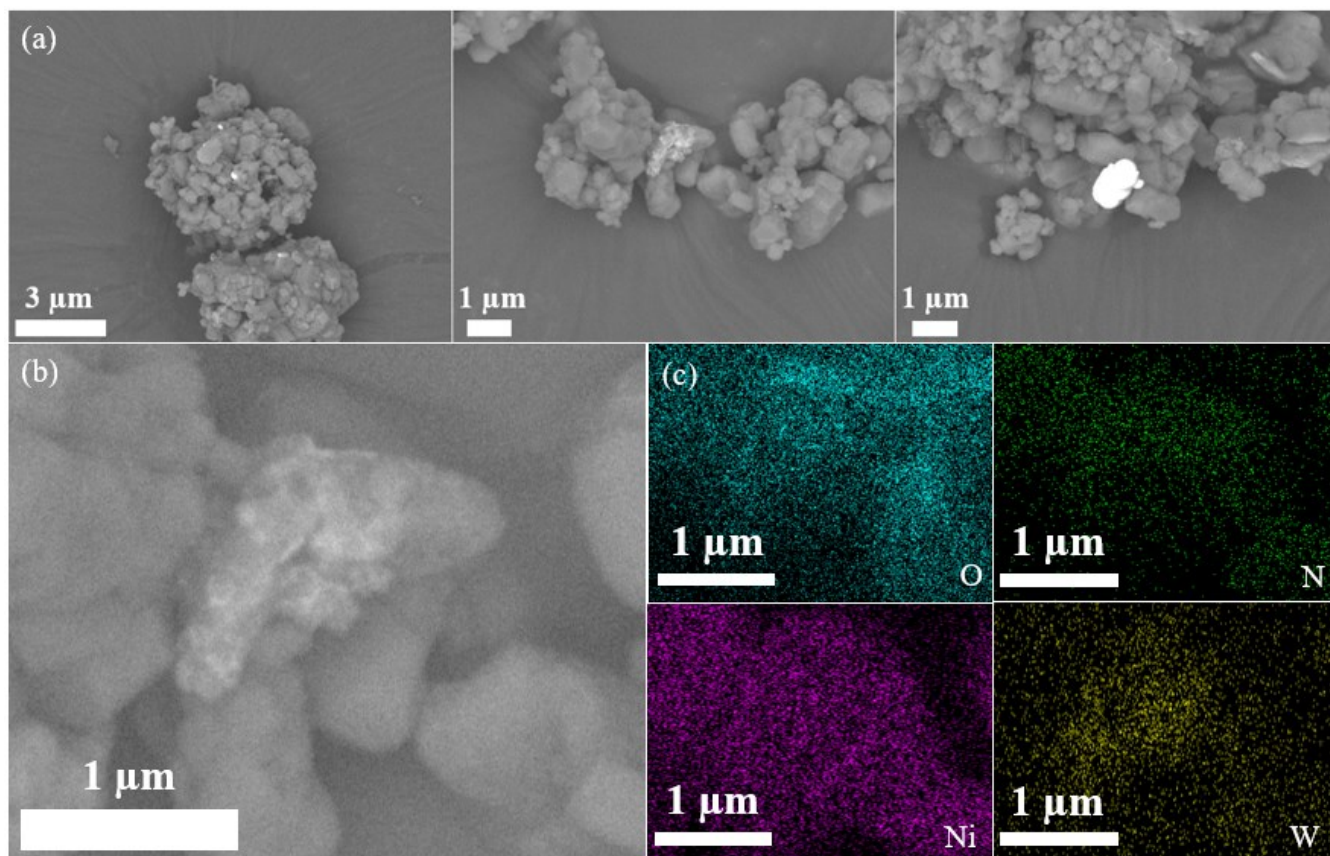


**Figure S5.** (a-b) SEM and (c) SEM-EDS elemental mapping images of DUT-8(Ni)-WCO-I.

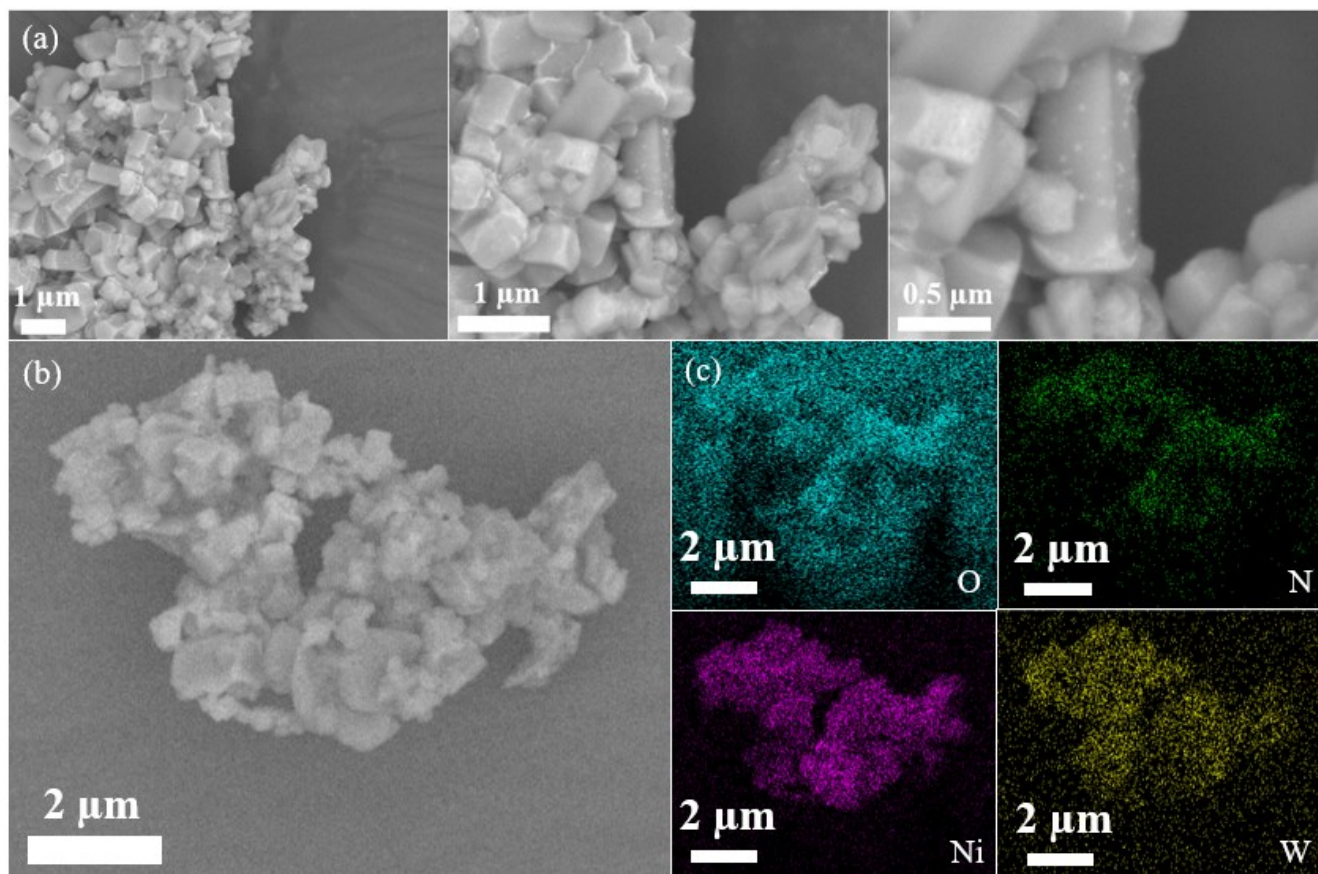


**Figure S6.** (a-b) SEM and (c) SEM-EDS elemental mapping images of DUT-8(Ni)-WCO-v.

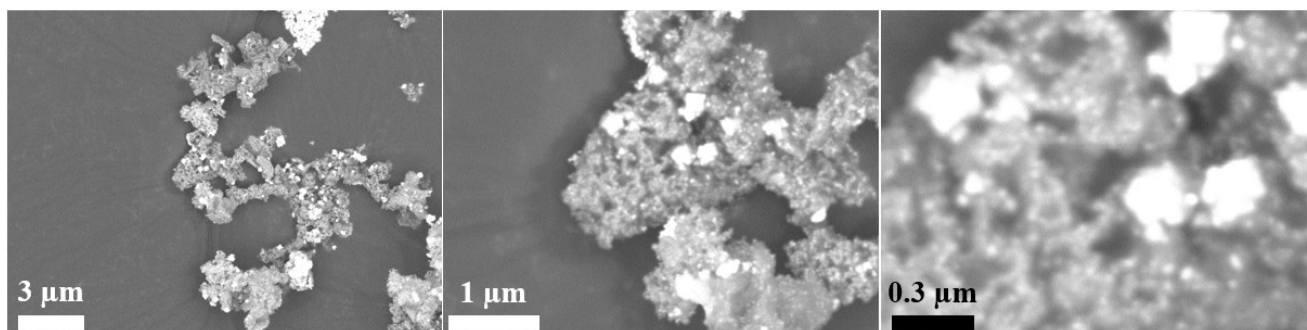


**Figure S7.** SEM images of NiWNaO-I-N<sub>2</sub>.

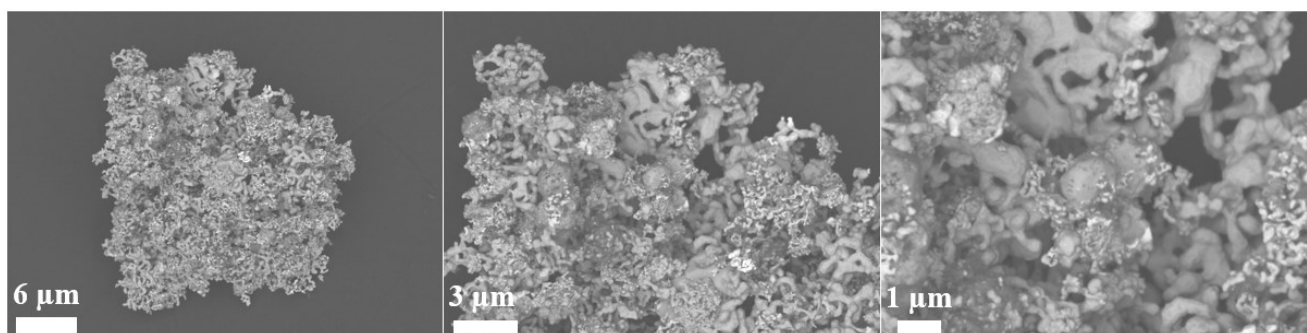


**Figure S8.** SEM images of NiWNaO-l-H<sub>2</sub>.

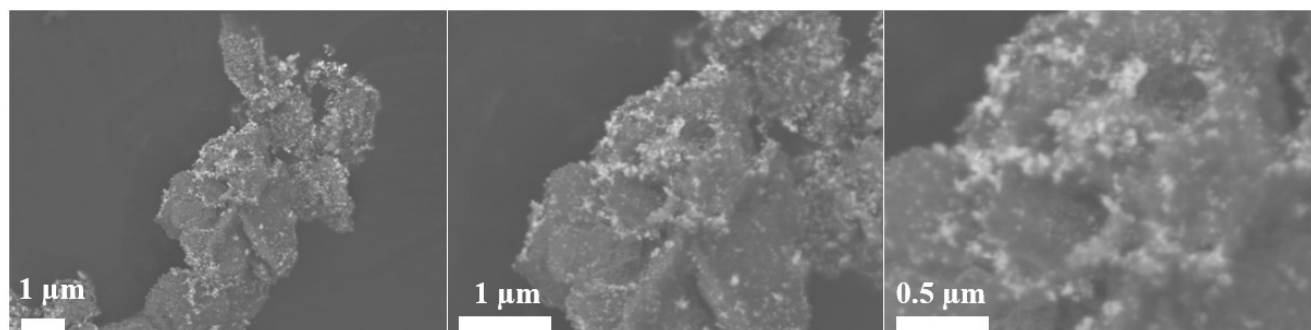


**Figure S9.** SEM images of NiWCO-l-N<sub>2</sub>.

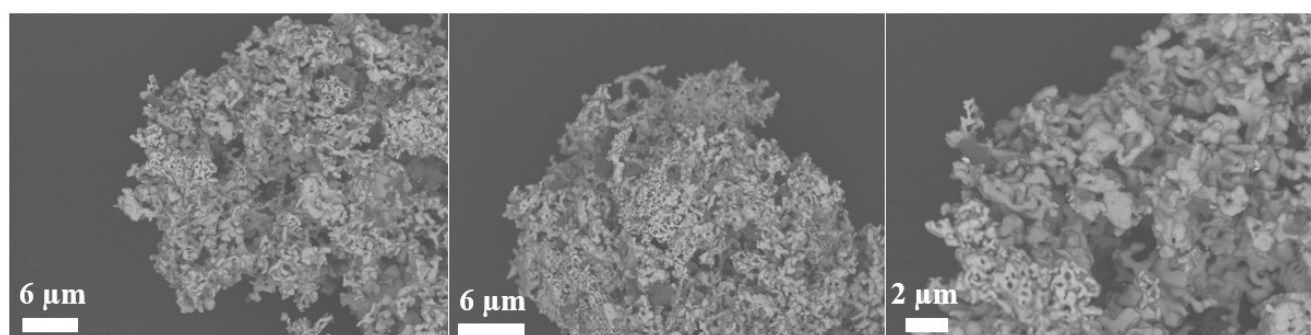


**Figure S10.** SEM images of NiWCO-l-H<sub>2</sub>.

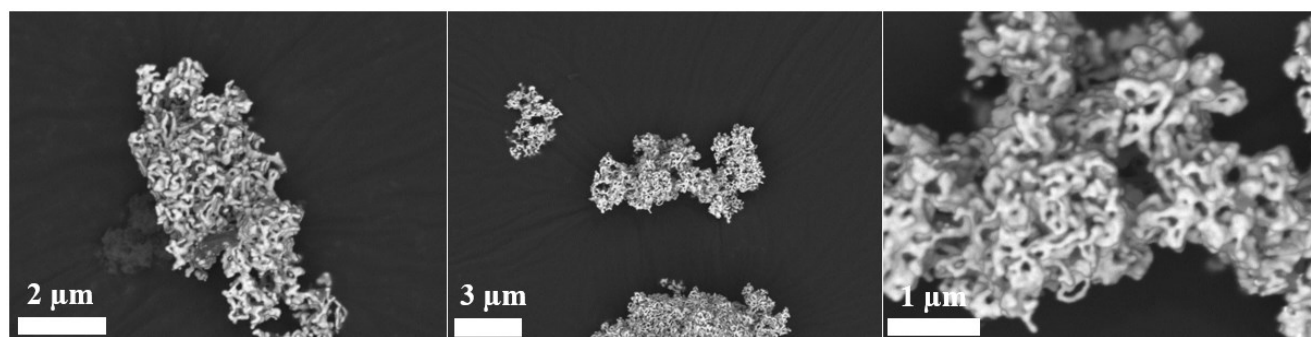


**Figure S11.** SEM images of NiWCO-v-H<sub>2</sub>.



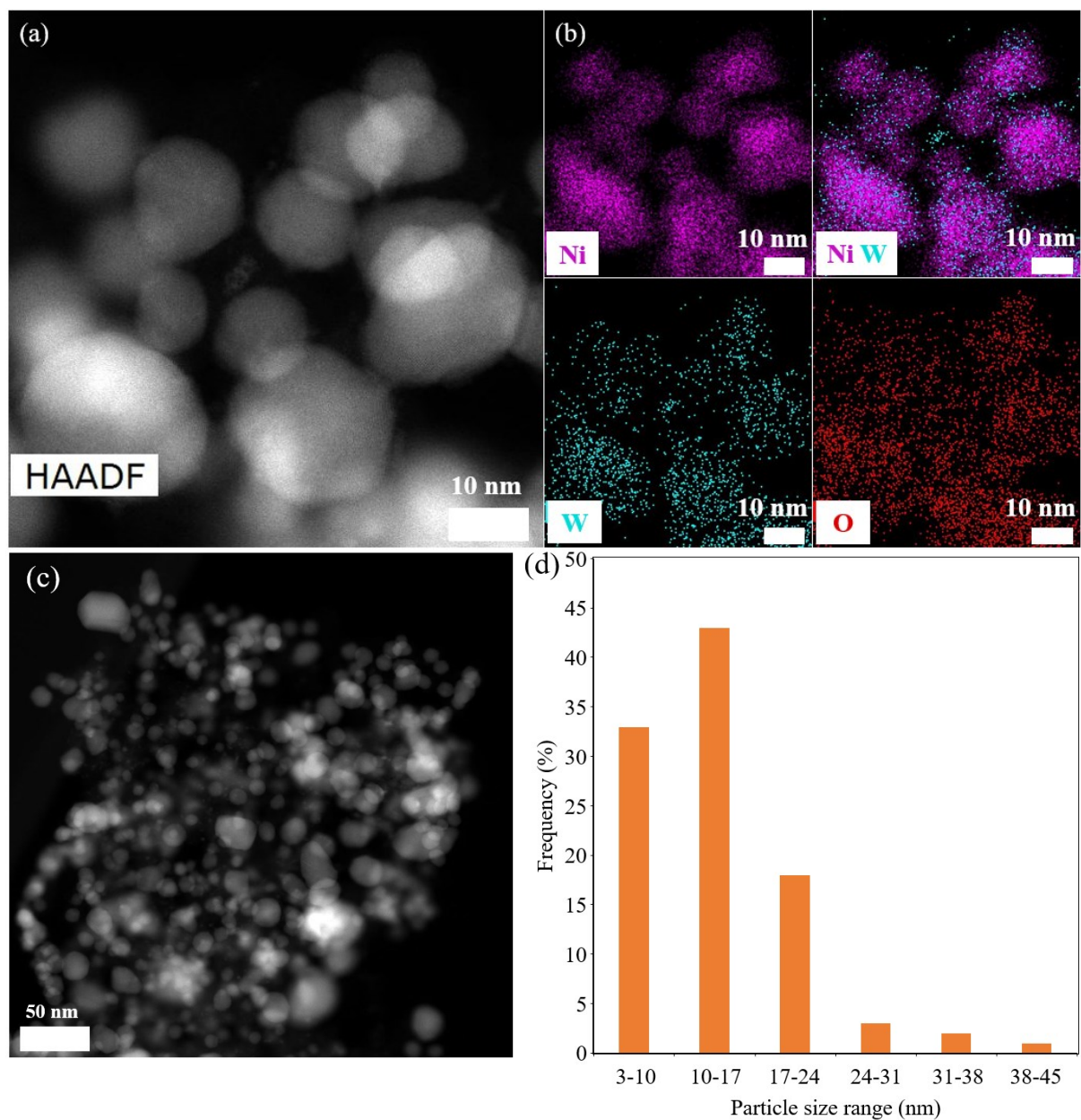


**Figure S12.** (a) HAADF-STEM; (b) TEM-EDS elemental mapping images of NiWNaO-I-N<sub>2</sub>; (c) HAADF-STEM at 50 nm magnification of NiWNaO-I-N<sub>2</sub>; (d) Particle size distribution histogram of NiWNaO-I-N<sub>2</sub> calculated from a and c images and images like a and c.



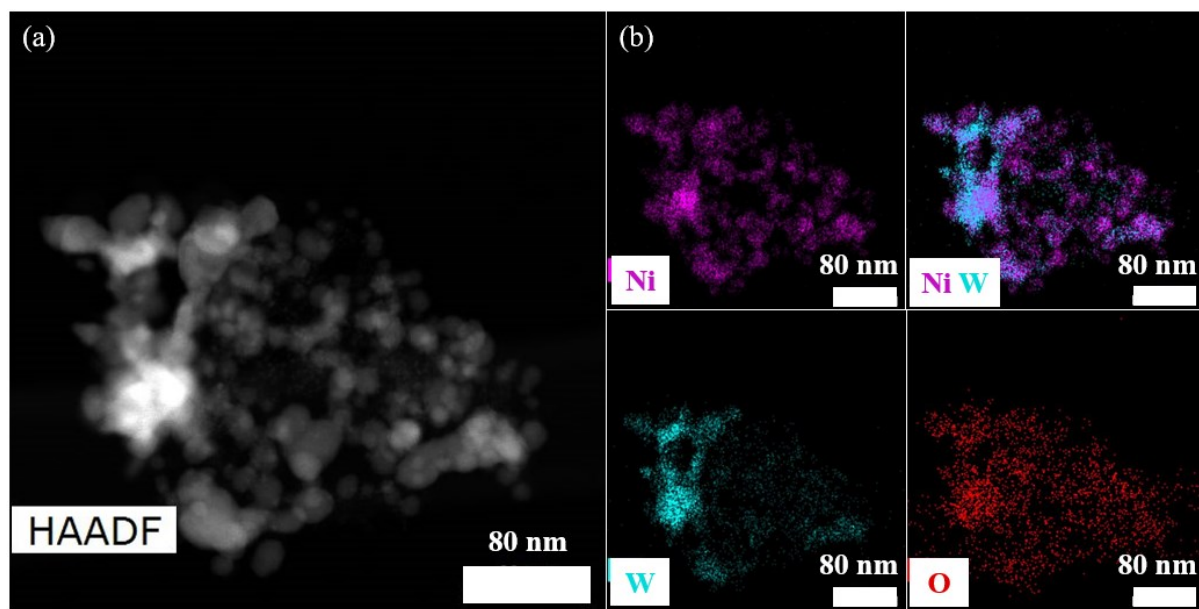


**Figure S13a.** (a) HAADF-STEM; (b) TEM-EDS elemental mapping images of NiWCO-1-N<sub>2</sub>.

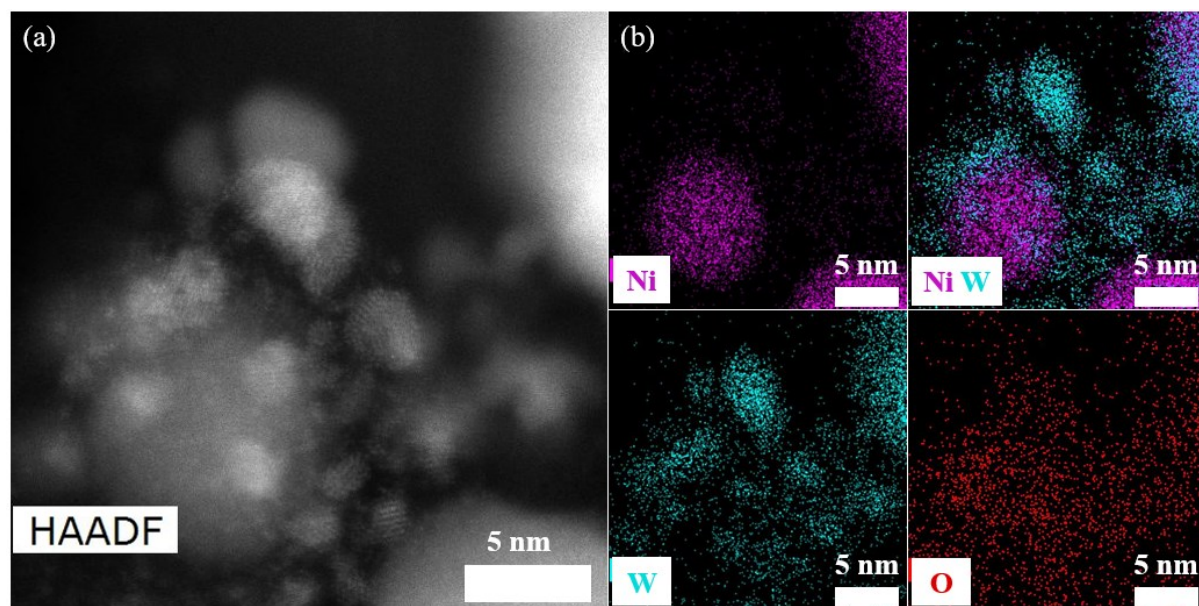


**Figure S13b.** (a) HAADF-STEM; (b) TEM-EDS elemental mapping images of NiWCO-1-N<sub>2</sub>.

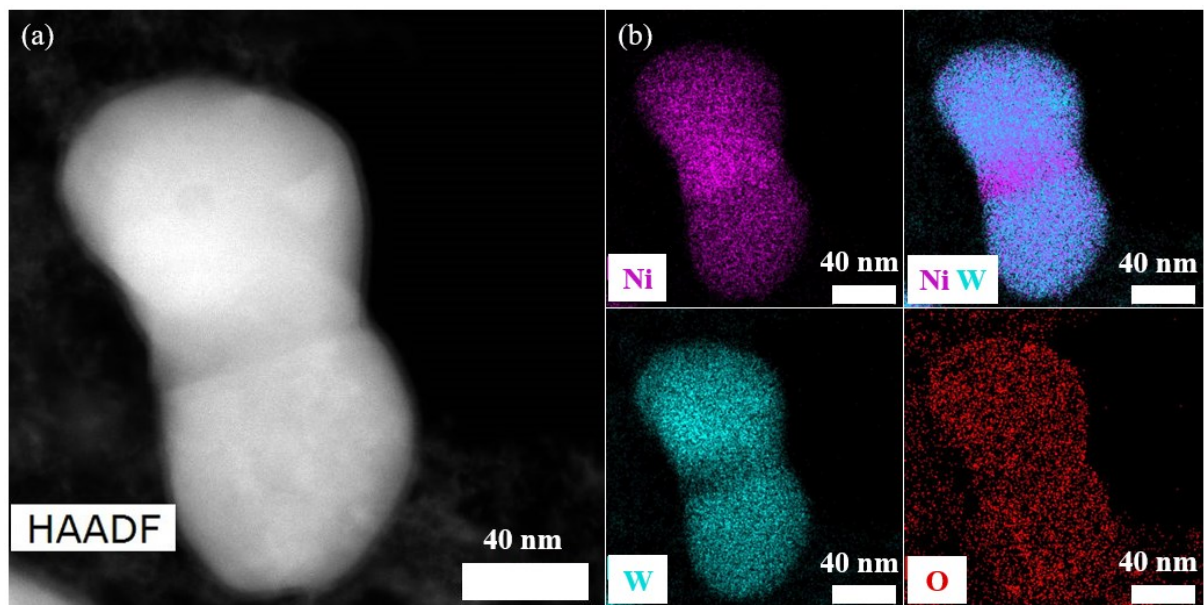


**Figure S14.** (a) HAADF-STEM; (b) TEM-EDS elemental mapping images of NiWNaO-l-H<sub>2</sub>.

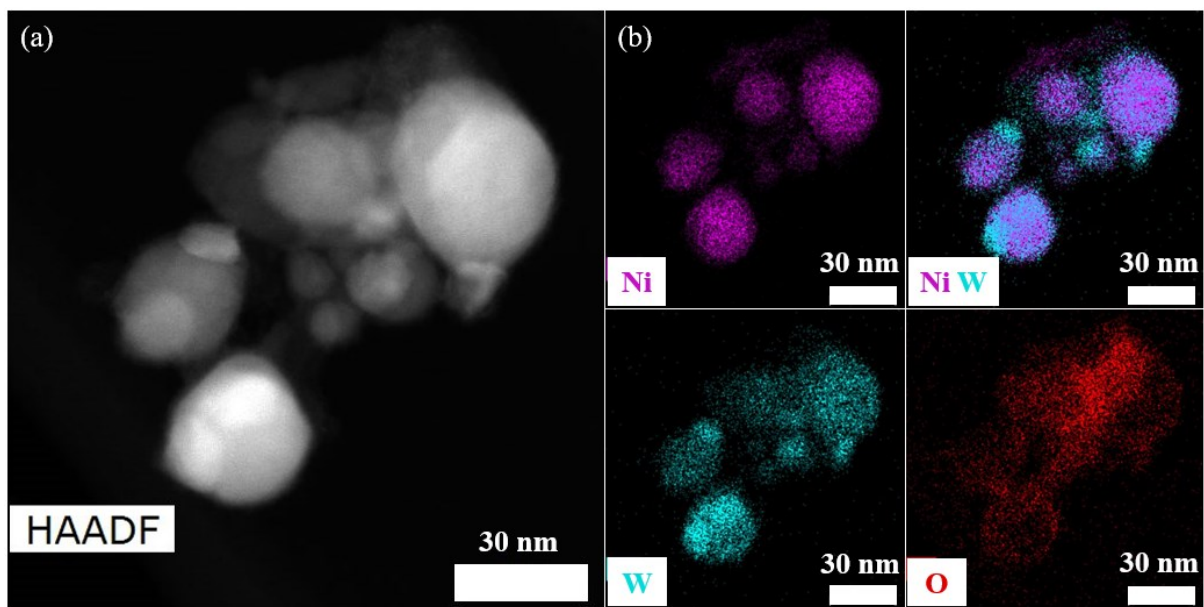


**Figure S15.** (a) HAADF-STEM; (b) TEM-EDS elemental mapping images of NiWCO-l-H<sub>2</sub>.

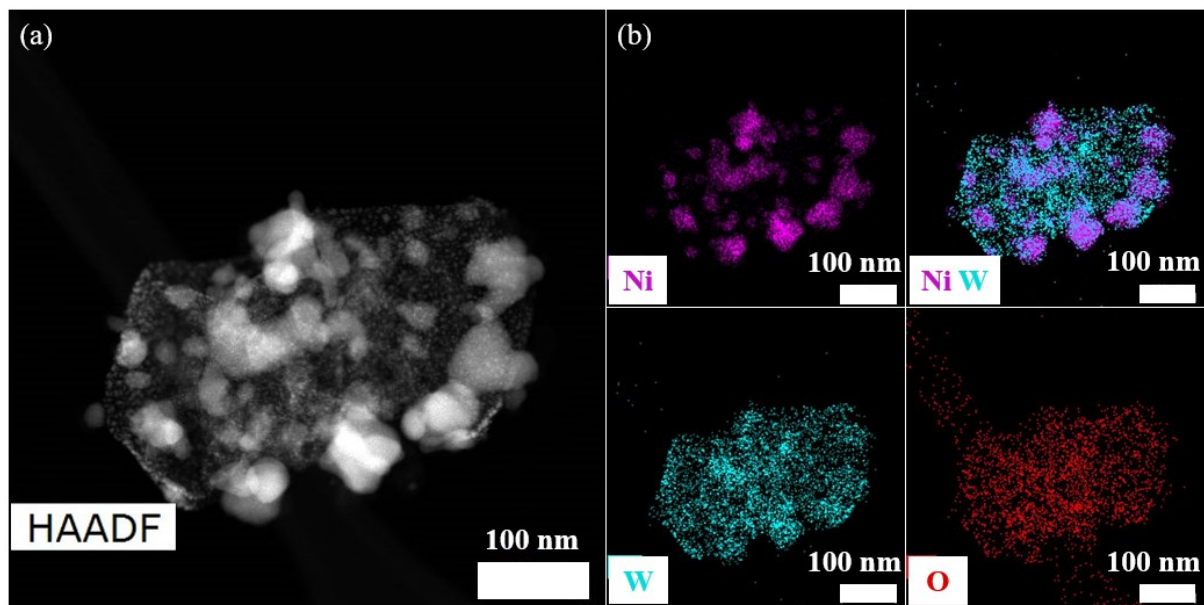


**Figure S16.** (a) HAADF-STEM; (b) TEM-EDS elemental mapping images of the catalyst; NiWCO-v-N<sub>2</sub>.

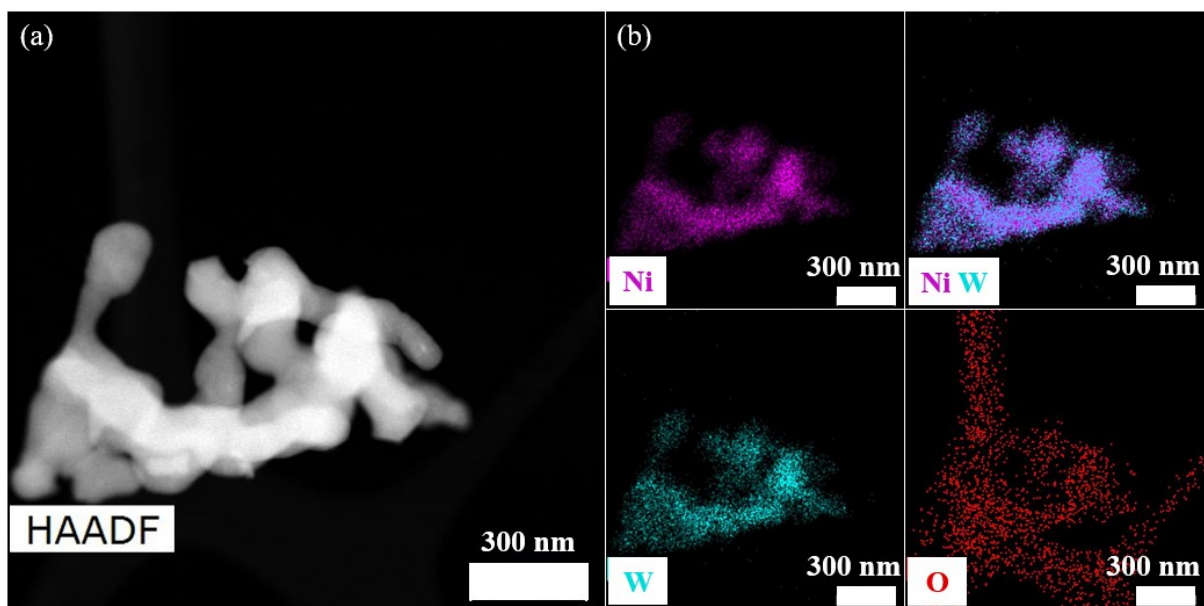


**Figure S17a.** (a) HAADF-STEM; (b) TEM-EDS elemental mapping images of NiWCO-v-H<sub>2</sub>.

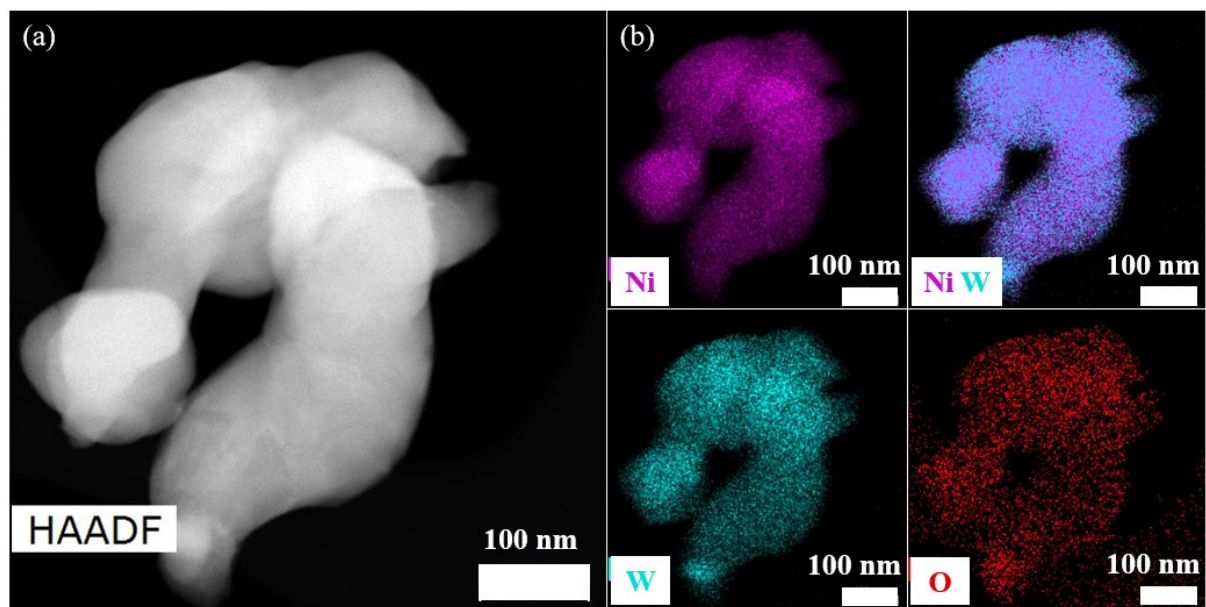


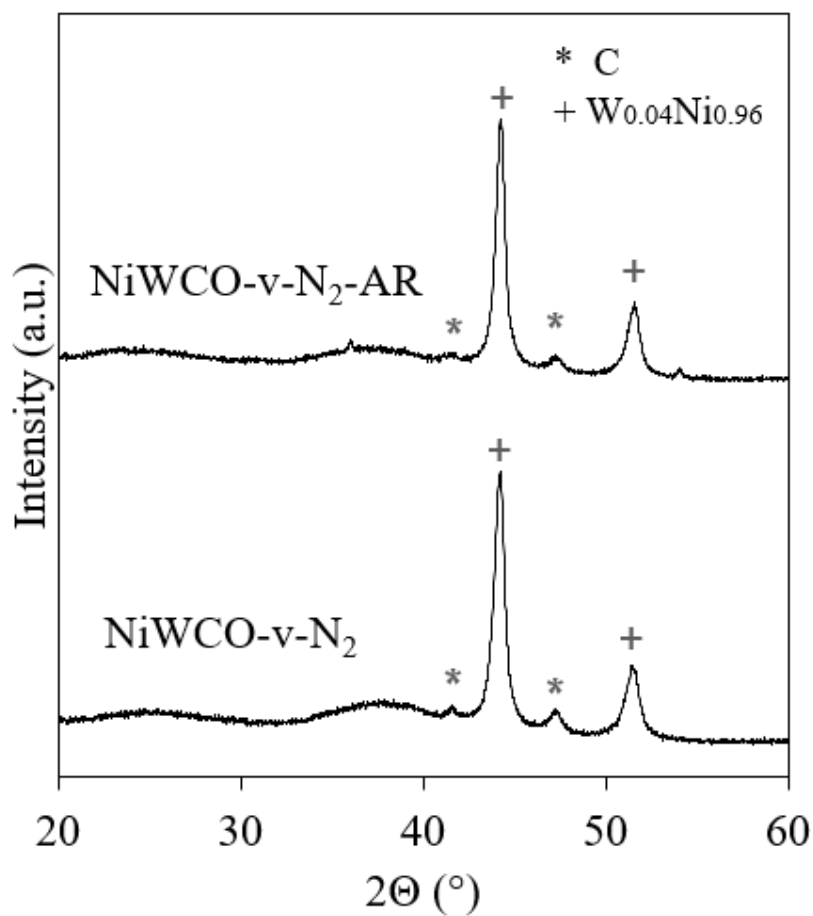
**Figure S17b.** (a) HAADF-STEM; (b) TEM-EDS elemental mapping images of NiWCO-v-H<sub>2</sub>.



**Table S4.** Polyols' products distribution from cellulose hydrogenolysis.

Catalyst	Yield of the product (mol%)								Carbon balance (%)
	EG <sup>(a)</sup>	PG <sup>(b)</sup>	BG <sup>(c)</sup>	SOR <sup>(d)</sup>	ERY <sup>(e)</sup>	GLY <sup>(f)</sup>	GA <sup>(g)</sup>	HA <sup>(h)</sup>	
NiWNaO-I-N <sub>2</sub>	24	4	3	6	1	2	-	-	77
NiWNaO-I-H <sub>2</sub>	19	2	3	2	1	1	7	4	84
NiWCO-I-N <sub>2</sub>	42	10	5	3	1	1	1	2	71
NiWCO-I-H <sub>2</sub>	13	2	6	-	-	1	7	8	83
NiWCO-v-N <sub>2</sub>	46	9	5	1	-	-	1	-	77
NiWCO-v-H <sub>2</sub>	19	2	3	2	1	1	7	4	69

<sup>(a)</sup> EG: ethylene glycol; <sup>(b)</sup> PG: 1,2-propylene glycol; <sup>(c)</sup> BG: 1,2-butanediol; <sup>(d)</sup> SOR: sorbitol; <sup>(e)</sup> ERY: erythritol; <sup>(f)</sup> GLY: glycerol; <sup>(g)</sup> GA: glycolaldehyde; <sup>(h)</sup> HA: hydroxyacetone or acetol.

**Figure S18.** XRD diffractograms of NiWCO-v-N<sub>2</sub> prior and after reaction.

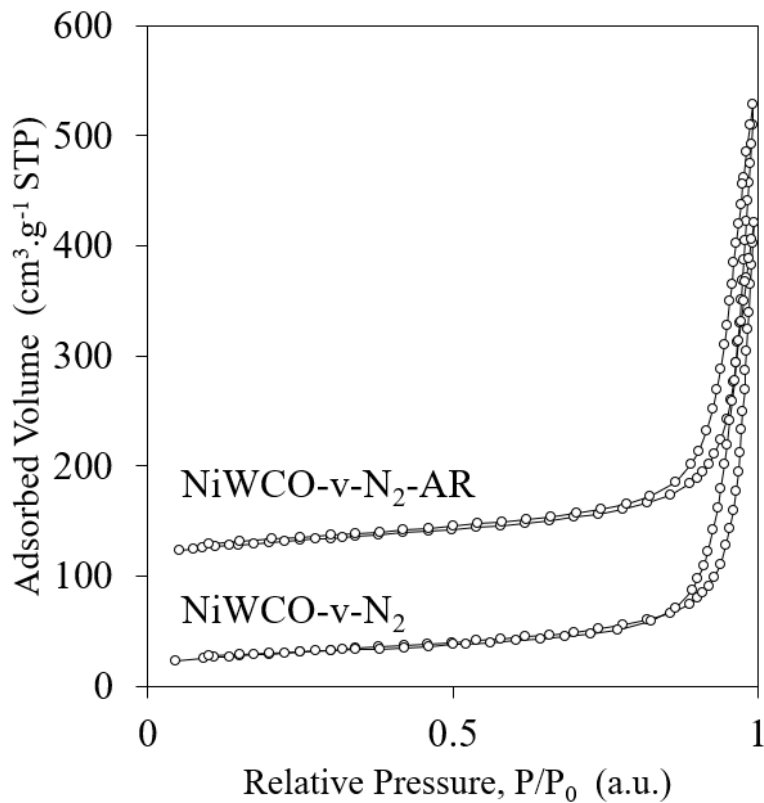


**Figure S19.** N<sub>2</sub> sorption isotherms of NiWCO-v-N<sub>2</sub> prior and after reaction (NiWCO-v-N<sub>2</sub>-AR isotherm was shifted upwards by 100 cm<sup>3</sup>.g<sup>-1</sup>).

**Table S5.** Textural properties of W@DUT-8 materials and NiW functionalized carbons.

Sample	S <sub>BET</sub> <sup>(a)</sup> (m <sup>2</sup> .g <sup>-1</sup> )	S <sub>μ</sub> <sup>(b)</sup> (m <sup>2</sup> .g <sup>-1</sup> )	V <sub>p</sub> <sup>(c)</sup> (cm <sup>3</sup> .g <sup>-1</sup> )	V <sub>μ</sub> <sup>(d)</sup> (cm <sup>3</sup> .g <sup>-1</sup> )	D <sub>pore</sub> <sup>(e)</sup> (nm)
NiWCO-v-N <sub>2</sub>	104	36	0.53	0.02	3-21
NiWCO-v-N <sub>2</sub> -AR	107	28	0.56	0.01	4-34

[a] BET surface area; [b] micropore surface area; [c] total pore volume; [d] micropore volume; [e] BJH pore diameter calculated on desorption branch.

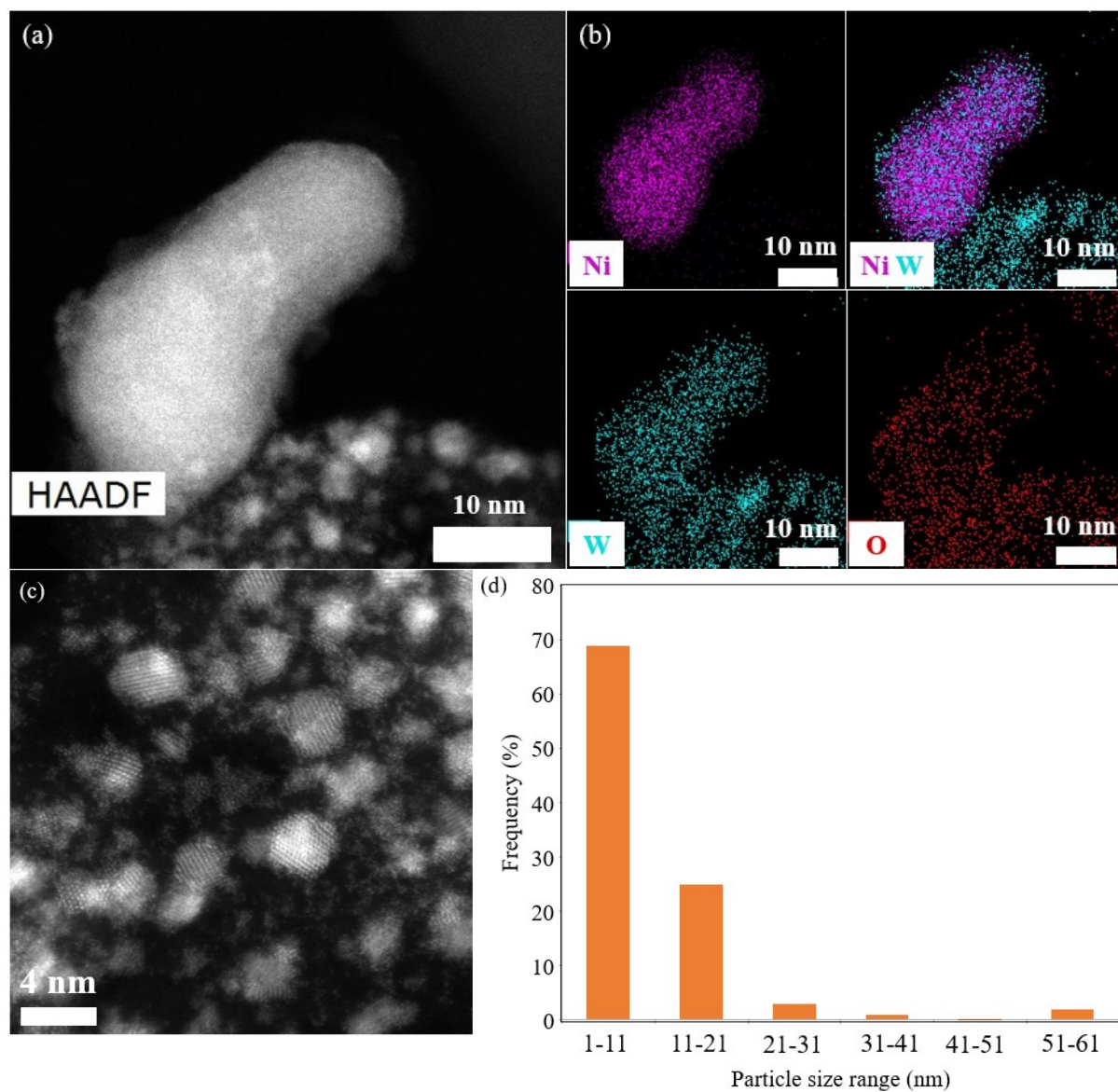
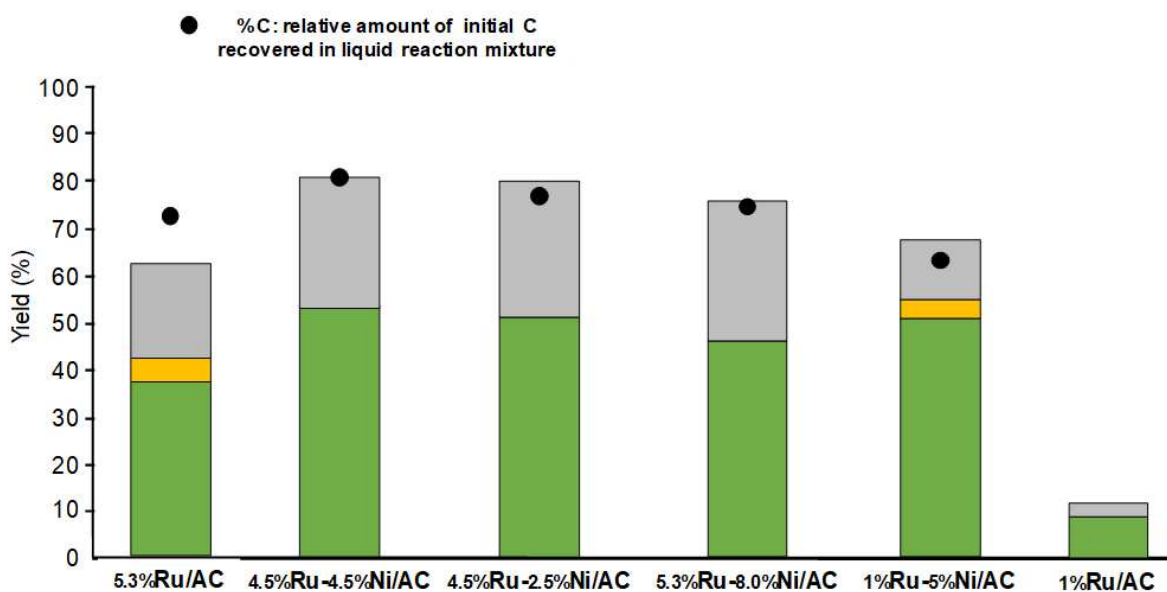
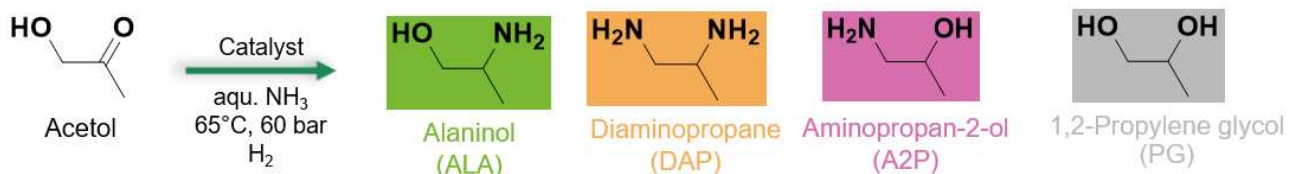


**Figure S20.** (a) HAADF-STEM; (b) TEM-EDS elemental mapping images of NiWCO-v-N<sub>2</sub>-AR. (c) HAADF-STEM at 2 nm magnification of NiWCO-v-N<sub>2</sub>-AR; (d) Particle size distribution histogram of NiWCO-v-N<sub>2</sub>-AR calculated from a and c images and images like a and c.

# Chapter 5 : Catalytic reductive amination of acetol over Ruthenium based catalysts



This Chapter has been submitted to Greenchemistry in 2023.



## 5.1. Introduction

In the general context of sustainable chemistry, biosourced amines are of fundamental interest as end-products or as intermediates especially for the polymer industry. Direct renewable resources of amines are very scarce and only concern amino acids and polymeric chitin.<sup>1-2</sup> Therefore, to date the formation of biosourced amines mainly relies on the amination of molecules easily obtained from renewable resources especially those presenting hydroxyl or carbonyl functions.

In the frame of our recent study<sup>3</sup> on the catalytic transformation of polysaccharides into biosourced ethylene and propylene glycol, HO-CH<sub>2</sub>-CH<sub>2</sub>-OH and CH<sub>3</sub>-CH(OH)-CH<sub>2</sub>-OH, respectively, we were interested in forming amino-derivatives of these glycols. This was inspired by the recent study of Sels and coll. who reported the aminolysis of glucose and xylose by alkylamines into the corresponding secondary or tertiary alkylamino-derivatives of ethylene and propylene glycol.<sup>4-5</sup> Depending on the conditions and substrates, yields between 30-80% were obtained for derivatives like TMEDA in the presence of a Ru/C catalyst. These alkyl amines are considered as important products, however we believe that the primary amine equivalents are also of prime interest, as monomers for the synthesis of partly biosourced polyamides.<sup>6-7</sup> Therefore, we investigated the formation of primary amines derived from propylene glycol namely 2-aminopropanol (alaninol) CH<sub>3</sub>-CH(NH<sub>2</sub>)-CH<sub>2</sub>-OH, 1-aminopropane-2-ol CH<sub>3</sub>-CH(OH)-CH<sub>2</sub>-NH<sub>2</sub> and 1,2-diaminopropane CH<sub>3</sub>-CH(NH<sub>2</sub>)-CH<sub>2</sub>-NH<sub>2</sub>.

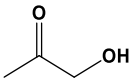
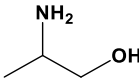
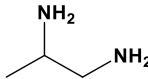
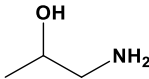
The direct amination of ethylene and propylene glycols or related molecules is not straightforward and, since the early report from Baiker *et al.* who reacted ethylene glycol with dimethylamine in the presence of Cu/Al<sub>2</sub>O<sub>3</sub> catalyst,<sup>8</sup> only few studies have been reported (see Table S1 in Supplementary Information). Overall, most of them involve NH<sub>3</sub> as aminating reagent to form primary amines, and the maximum reported yield of alaninol is around 60% with a Co/La<sub>3</sub>O<sub>4</sub> catalyst.<sup>9</sup>

Since the direct amination of alcohols is still a challenging catalytic reaction<sup>10-11</sup> especially with biosourced substrates,<sup>12-16</sup> an alternative route is the catalytic reductive amination of a carbonyl function in the presence of hydrogen. This methodology has been well developed as shown by recent reviews.<sup>17-25</sup> Concerning heterogeneous catalysts, after the early studies on Ni-Raney®, systems based on precious metals were employed, particularly Ru. In general, the reductive amination is described for reactants having one oxygenated function, *e.g.* carbonyl. Biosourced reactants may possess other reactive functions like hydroxyl, rendering a selective transformation

more difficult. Among them, furan derivatives have been by far the most studied because of the high reactivity of the carbonyl function leading to interesting products with preserved aromatic ring (5-hydroxymethyl-2-furfuryl amine, 2,5-bis(aminomethyl)furan).<sup>17, 20, 23</sup>

Based on this we envisaged the formation of amines from glycols by the reductive amination of the biosourced intermediates of these glycols, *e.g.* glycoaldehyde  $\text{O}=\text{CH}-\text{CH}_2-\text{OH}$  and acetol  $\text{CH}_3-\text{C}(=\text{O})-\text{CH}_2-\text{OH}$ , respectively. To the best of our knowledge, there are only a couple of examples describing the reductive amination of glycoaldehyde with catalysts based on supported Ru.<sup>26-28</sup> More reports exist concerning acetol, but this remains limited (Table 1). They only concern the formation of primary amine derivatives using heterogeneous catalysis. This transformation is very challenging due to the need to combine conditions that are harsh enough to activate ammonia but mild enough to control the reaction.<sup>29</sup> Liang *et al.* reported the reductive amination with 5%Ru/ZrO<sub>2</sub> of a variety of aldehydes and ketones, with the example of acetol producing alaninol in 26% yield. The catalyst was formed of partly reduced Ru giving RuO<sub>2</sub> particles able to promote acid activation of the carbonyl group into imine intermediate, and Ru<sup>0</sup> particles for hydrogenation into amine. Trégner *et al.* proposed the use of 69%NiO/Al<sub>2</sub>O<sub>3</sub> for a gas phase transformation giving at full conversion 45% yield of alaninol.<sup>30</sup> More recently, Sheng *et al.* reported among a wide range of carbonyl compounds the formation of alaninol (70%) from acetol and aqueous NH<sub>3</sub> or ammonia acetate catalyzed by Co<sub>2</sub>P nanorods under low H<sub>2</sub> pressure.<sup>31</sup> In a different kind of study, Shin *et al.* reported the formation of optically active (L)-alaninol by asymmetric reductive amination using (S)- $\alpha$ -methylbenzylamine in the presence of a 10%Pd/SBA-15, a 30%Pd/NaY catalyst giving higher conversion but lower enantiomeric excess.<sup>32</sup>

**Table 1.** Literature data on the reductive amination of acetol with NH<sub>3</sub>

Conditions	Reactant conversion (%)	Main aminated products yield (%)		Ref.	
					

5%Ru/ZrO <sub>2</sub>					
25% aqu.NH <sub>3</sub>	not given	26	10	not given	27
30 bar H <sub>2</sub>					
65 °C, 6 h					
69%NiO/Al <sub>2</sub> O <sub>3</sub>					
1 bar NH <sub>3</sub>	100	45	traces	3	30
1 bar H <sub>2</sub>					
130 °C, gas phase					
Co <sub>2</sub> P nanorods					
25% aqu.NH <sub>3</sub>	96	70	not given	not given	31
5 bar H <sub>2</sub>					
100 °C, 10 h					
10%Pd/SBA-15					
(S)- $\alpha$ -methylbenzylamine	80	not given 80% <i>ee</i> <sup>(a)</sup>	not given	not given	32
3.5 bar H <sub>2</sub>					

<sup>(a)</sup> *ee*: enantiomeric excess

Globally alaninol is always the main amino product due to the higher reactivity of the carbonyl function, and products like 1,2-diaminopropane CH<sub>3</sub>-CH(NH<sub>2</sub>)-CH<sub>2</sub>-NH<sub>2</sub> and 1-aminopropane-2-ol CH<sub>3</sub>-CH(OH)-CH<sub>2</sub>-NH<sub>2</sub> were rarely observed or even mentioned. However, in all cases a significant amount of propylene glycol is formed. Figure 1 summarises the different pathways that could lead to these products. Acetol can be mono-aminated into alaninol (route 1a) or 1-diaminopropane-2-ol (route 1b), or directly di-aminated into 1,2-aminopropane (route 1c). The scarce literature (Table 1) indicates that route 1a is privileged whatever the conditions. 1,2-Diaminopropane can also be formed from routes 2a and 2b. Here the literature presents only studies concerning route 2b, with a paper describing the use of Ni-Raney® in the presence of K<sub>2</sub>CO<sub>3</sub> under drastic conditions (170 °C, 15 h) giving 90% selectivity for 55% conversion.<sup>33</sup> Also, a patent from BASF claims the use of metal supported catalysts at 120 bar and 165 °C giving 93% selectivity for 85% conversion.<sup>34</sup> Besides, the reductive amination competes with the simple reduction into propylene glycol (route 1d), but at this stage the transformation of the latter into aminated derivatives is far less likely under such conditions (see Table S1).

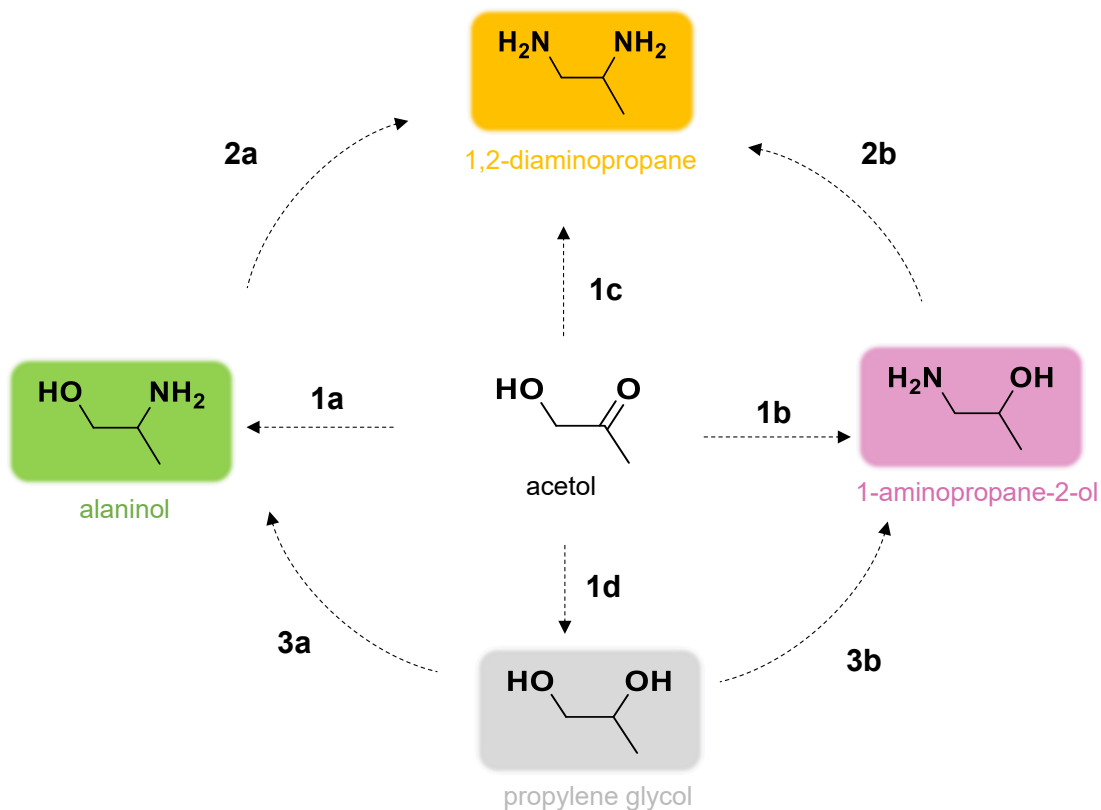


**Figure 1.** Possible reaction pathways involved in the reductive amination of acetol by H<sub>2</sub>/NH<sub>3</sub>.

We present here a study on the formation of primary amino-derivatives of propylene glycol, by the reductive amination of acetol by NH<sub>3</sub> in solution. For that, we investigated the properties of catalysts based on Ru active element. Effect of various reaction conditions and catalyst composition will be presented, as well as the much more challenging sequential formation of aminated products from sugars and cellulose.

## 5.2. Experimental

In this chapter, the following characterization techniques were used: XRD, N<sub>2</sub> physisorption, XPS, TEM, TGA, ICP-OES, <sup>13</sup>C NMR and XPS. For more information regarding the characterization techniques and synthesis routes, please refer to Chapter 2 for all details.

## 5.3. Results and discussion

### 5.3.1. Initial studies with 5.3%Ru/AC catalyst

In the Introduction we saw that several catalysts based on metals like Ru, Ni, Pd, Co, supported on oxides or carbons, have been assessed for the production of amino-derivatives of ethylene and

propylene glycol, starting from either the glycols themselves (Table S1), their carbonylated derivatives (Table 1), and even sugars.<sup>5</sup>

We focused the first part of this study on a Ru/AC catalyst for the synthesis of alaninol from acetol, such system having been never used for this reaction. For that we initially prepared a catalyst with a 5.3%Ru/AC composition (see Section 3.2 for characterization details). As a first set of experiments, the effect of reaction conditions were evaluated, time, temperature, and H<sub>2</sub> pressure. Figure 2 presents the results obtained with aqueous NH<sub>3</sub>, employing reaction conditions inspired from the literature.<sup>27, 31</sup>

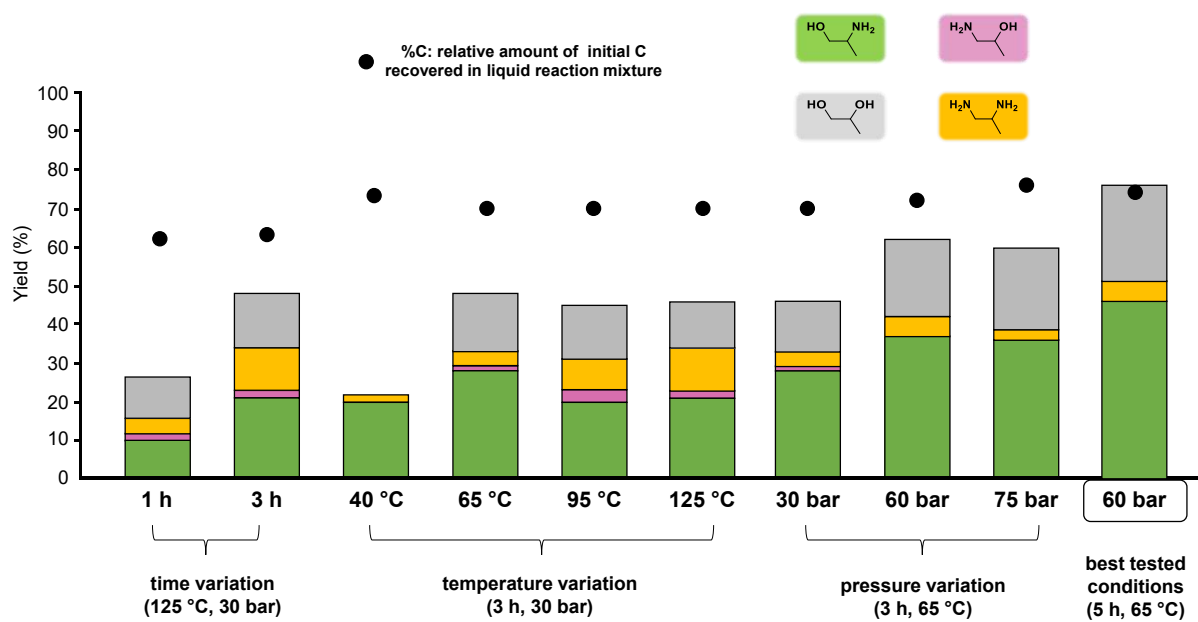


**Figure 2.** Condition variations for the reductive amination of acetol in the presence of 5.3%Ru/AC. Conditions set: 100 mL of 25% aqueous NH<sub>3</sub>, 10 g of acetol, 1 g of catalyst.

We first evaluated the reaction time at 125 °C under 30 bar of H<sub>2</sub>. After 3 h the overall amine yield reached 35%, much more than after 1 h of reaction (15%). The selectivity corresponds to literature data, e.g. the clearly predominant formation of alaninol (22% yield) (Figure 1, route 1a) and a lower amount of the two other amines (routes 1b and 1c). The side reaction forming propylene glycol (route 1d) is significant (12%) confirming the difficulty to get a very selective transformation. However, by decreasing the temperature down to 65 °C, the yield into the amino-derivatives, and especially alaninol was slightly higher (29% yield). Going further down to 40 °C,

the reaction became restricted to the routes 1a and 2a (and/or 1c) with the main formation of alaninol, but in a lower amount (20%). The H<sub>2</sub> pressure was then evaluated from 30 to 75 bar, and a pressure of 60 bar, despite forming more undesired propylene glycol, gave the best result in terms of amine formation (43%). With these conditions of temperature (65 °C) and pressure (60 bar) we reinvestigated the reaction time and a significant increase in amines was observed after 5 hours with yields up to 50% including 45% of alaninol.

In summary, among those evaluated, a temperature of 65 °C, a pressure of 60 bar and a time of 5 hours gave the highest amino-derivatives yield. If we compare to the rare reports in the literature, these conditions are close to those of Liang *et al.* for acetol amination with the Ru/ZrO<sub>2</sub> catalyst (30 bar, 65 °C, 6 h). Our results support their findings, for example the lesser influence of pressure on the selectivity over temperature, while a high temperature is not particularly suitable for the formation of the target amines.<sup>27</sup>

In the experiments presented in Figure 2, acetol was never detected in the post-reaction solution so the conversion of the reactant was complete. However, the amount of products quantified by NMR did not always match with the carbon present in the liquid phase (%C in Figure 2). A <sup>13</sup>C NMR spectrum of a reaction mixture obtained after 3 h at 65 °C under 75 bar, is displayed in Figure S3. It clearly indicates the presence of signals other than those associated with the products. These signals are due to non-identified side-products explaining the gap between the %C in solution and the total yield of quantified products. For comparison, a spectrum displayed in Figure S4 corresponding to a reaction mixture obtained after 5 h at 65 °C under 60 bar for which the %C in solution matches with the total amount of quantified products (see Figure 2) does not present such signals. Note that these signals are not due to ethylene glycol and/or related aminated derivatives, and not to dimethylpiperazines that may form as side-product.<sup>35</sup> Also, we obtained a 60-70% mass balance, *e.g.* about 30-40% of initial amount of C are not recovered in the liquid phase. We attempted to collect the gas phase to see if any gaseous products have been formed that may explain the lack of global mass balance (see Experimental section for details). Analysis indicates the presence of only H<sub>2</sub> and H<sub>2</sub>O in the gaseous sample. Therefore, no transformation into gaseous products happened, which is not surprising according to the low reaction temperature. The gap of mass balance may be due organic molecules remaining adsorbed on the surface of the catalyst.

As a first conclusion, one can say that a 5.3%Ru/AC catalyst was able to transform acetol into propylene glycol-derived amines in a 50% yield under relatively mild conditions, and the selectivity can be adjusted by choosing the appropriate reaction conditions.

### **5.3.2. Variation of catalyst composition**

#### **5.3.2.1. Characterization of catalysts**

After these first experiments with a 5.3%Ru/AC catalyst, we explored the potential of catalysts presenting different compositions, with in particular Ru associated to Ni which has also shown a potential in amination reactions,<sup>36-38</sup> to report here the first study of bimetallic Ru-Ni/AC catalysts for amination reactions. Different compositions of 1%Ru-5%Ni, 4.5%Ru-4.5%Ni, 4.5%Ru-2.5%Ni, and 5.3%Ru-8%Ni, were prepared by co-impregnation (see Experimental section for details) and characterized. For all compositions, XRD diffractograms (Figure 3) indicate the absence of signals due to metallic Ru (JCPDS 006-0663, main peak at 43.4°), which implies the presence of small metal nanoparticles (< 4 nm). The three main peaks associated with metallic Ni ( $2\theta = 44.3^\circ, 51.6^\circ, 76.2^\circ$ ) are detected for 5.3%Ru-8%Ni/AC due to its high Ni loading. A main crystallite size of 23 nm can be estimated based on Scherrer equation. The peaks are consistent with a fcc Fm-3m structure with a lattice parameter  $a = 3.53 \text{ \AA}$ , which can be attributed to either pure Ni ( $a = 3.45\text{-}3.54 \text{ \AA}$ ) or RuNi alloy ( $a = 3.54\text{-}3.62 \text{ \AA}$ ). There is no formation of RuNi alloy with a hcp structure (P 63/mmc) like previously reported.<sup>39</sup> The main peak attributed to Ni or RuNi can also be perceived in 1%Ru-5%Ni/AC, but it overlaps with a peak from the carbon support, which prevents an accurate estimation of crystallite size.

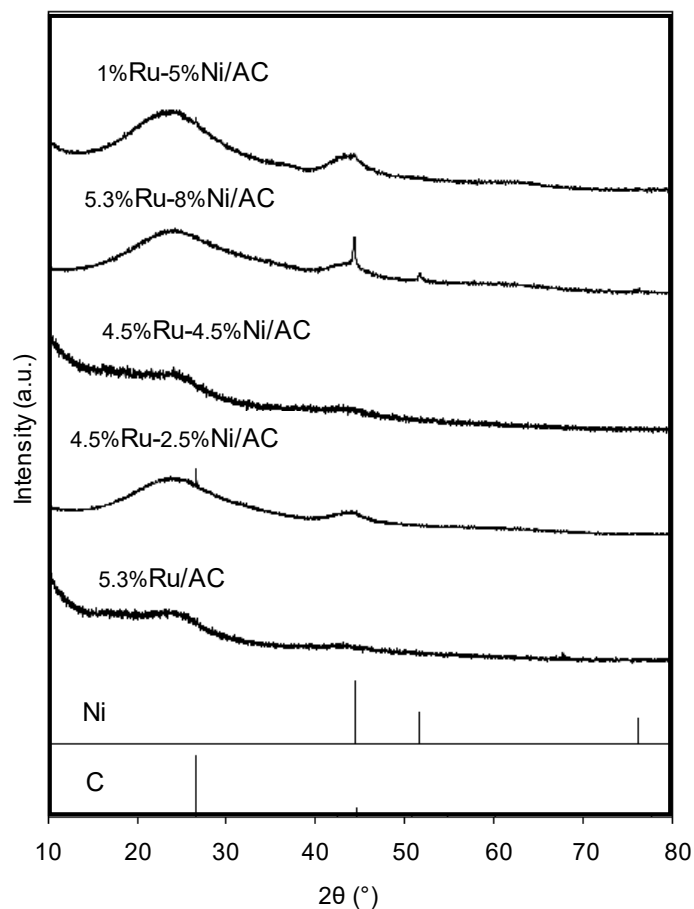


**Figure 3.** XRD diffractograms of carbon-supported Ru catalysts. Peak assignments based on ICDD files C (PDF 00-025-0284) and Ni (PDF 04-002-7521).

Textural properties of these materials are presented in Table 3. Naked activated carbon presents a surface area of  $905 \text{ m}^2 \cdot \text{g}^{-1}$ , retained for all Ru and Ni-Ru containing catalysts. Samples present type IV isotherms with H3-hysteresis loops at  $p/p_0$  range 0.30-0.99, suggesting the presence of both micropores and mesopores with a wedge-shaped pores arrangement (Figure S5).

**Table 3.** Textural properties of carbon-supported Ru and Ru-Ni catalysts

Catalyst	$S_{\text{BET}}^{(a)}$ ( $\text{m}^2 \cdot \text{g}^{-1}$ )	$S_{\mu}^{(b)}$ ( $\text{m}^2 \cdot \text{g}^{-1}$ )	$V_p^{(c)}$ ( $\text{cm}^3 \cdot \text{g}^{-1}$ )	$V_{\mu}^{(d)}$ ( $\text{cm}^3 \cdot \text{g}^{-1}$ )	$d_{\text{pore}}^{(e)}$ (nm)
5.3%Ru/AC	925	565	0.40	0.25	4-5
4.5%Ru-4.5%Ni/AC	940	540	0.40	0.25	4-5



<sup>(a)</sup> BET surface area; <sup>(b)</sup> micropore surface area; <sup>(c)</sup> total pore volume; <sup>(d)</sup> micropore volume; <sup>(e)</sup> BJH pore diameter calculated on desorption branch

XPS measurements were performed on selected catalysts to identify the chemical states of the different elements. The Ru 3d, Ru 3p, Ni 2p, and C 1s core level XPS spectra of passivated 5.3%Ru/AC, 4.5%Ru-4.5%Ni/AC, and 1%Ru-5%Ni/AC are displayed in Figure 4. Table 4 reports the surface content of Ru and Ni and the oxidation state repartition of the different elements.

For all the samples, the C 1s spectra overlap with Ru 3d spectra (Figure 4a-c). Four main peaks are identified, located at 290.2 eV, 287.5 eV, 286.2 eV and 284.5 eV corresponding to C-C, C=O, C-O and C-C bonds, respectively.<sup>40</sup> For 5.3%Ru/AC, one oxidation state of Ru can be observed on Ru 3d spectrum, Ru(OH)<sub>2</sub>, from the passivation layer (3d<sub>5/2</sub>: 281 eV and 1 satellite: 283.7 eV; 3d<sub>3/2</sub>: 285.3 eV and 1 satellite: 287.9 eV) which was previously reported.<sup>41-42</sup> In order to further verify the oxidation state of Ru, we analyzed the Ru 3p<sub>3/2</sub> spectrum (Figure 4d). The peaks at 462.5 eV and 465.5 eV (satellite peak) are also correlated to Ru(OH)<sub>2</sub>.<sup>42-43</sup> 5.3%Ru/AC presents 14 at% of Ru concentration on the surface (Table 4) which is higher than the bulk composition determined by ICP-EOS (0.7 at% of Ru in 5.3%Ru/AC, see Experimental section).

For 4.5%Ru-4.5%Ni/AC (Figure 5a) and 1%Ru-5%Ni/AC (Figure 5b), only Ru<sup>2+</sup> associated with the passivation layer is observed, as previously. However, the main peaks were shifted by 0.4 eV due to Ru-Ni interactions,<sup>39</sup> (3d<sub>5/2</sub>: 280.6 eV and 1 satellite: 282 eV; 3d<sub>3/2</sub>: 284.8 eV and 1 satellite: 286.2 eV).<sup>41</sup> Two oxidation states of Ni are also observed for all samples (Figure 5), (1) nickel Ni<sup>0</sup> (2p<sub>3/2</sub>: 852.6 eV and 2 plasmon loss peaks: 856.3 eV and 858.7 eV), (2) oxidized nickel species, Ni(OH)<sub>2</sub>, due to the passivation step (2p<sub>3/2</sub>: 854.9 eV and 5 satellites: 855.7 eV, 857.7 eV, 860.5 eV, 861.5 eV, and 866.5 eV).<sup>44</sup> 4.5%Ru-4.5%Ni/AC and 1%Ru-5%Ni/AC exhibit 6 and 5% of Ni<sup>0</sup> at the surface, which could be attributed to the hydrogen spillover capability of Ru to Ni.<sup>45</sup> 4.5%Ru-4.5%Ni/AC presents 14 at% of Ru and 7 at% of Ni concentrations on the surface (Table 4), which is higher than the bulk composition determined by ICP-EOS (0.6 at% of Ru and 1 at% of Ni, Table 1). 1%Ru-5%Ni/AC presents 9 at% of Ru and 10 at% of Ni concentrations on the surface (Table 4), which is higher than the bulk composition determined by ICP-EOS (0.2 at% of Ru and 1.1 at% of Ni, see Experimental section).

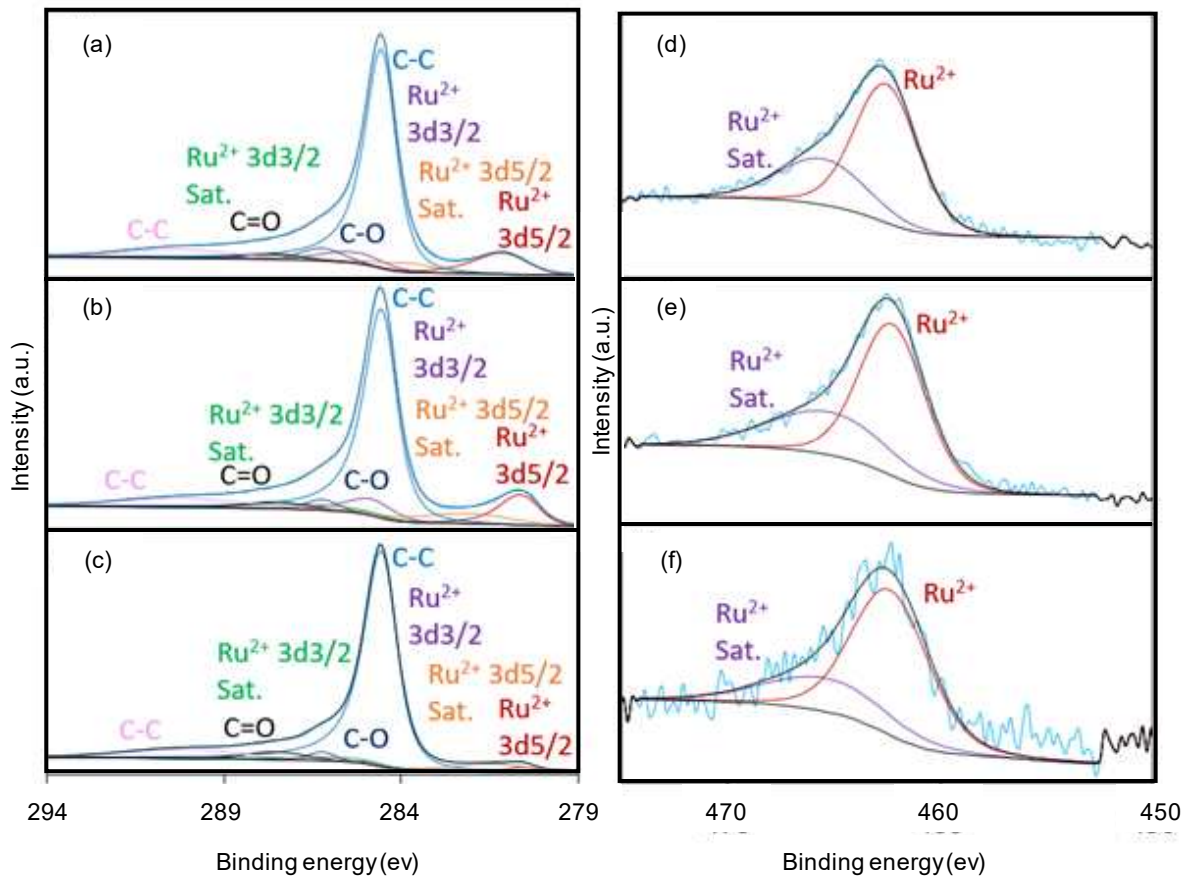


**Figure 4.** C 1s and Ru3d XPS spectra of (a) 5.3%Ru/AC, (b) 4.5%Ru-4.5%Ni/AC, (c) 1%Ru-5%Ni/AC; Ru 3p spectra of (d) 5.3%Ru/AC, (e) 4.5%Ru-4.5%Ni/AC, (f) 1%Ru-5%Ni/AC.

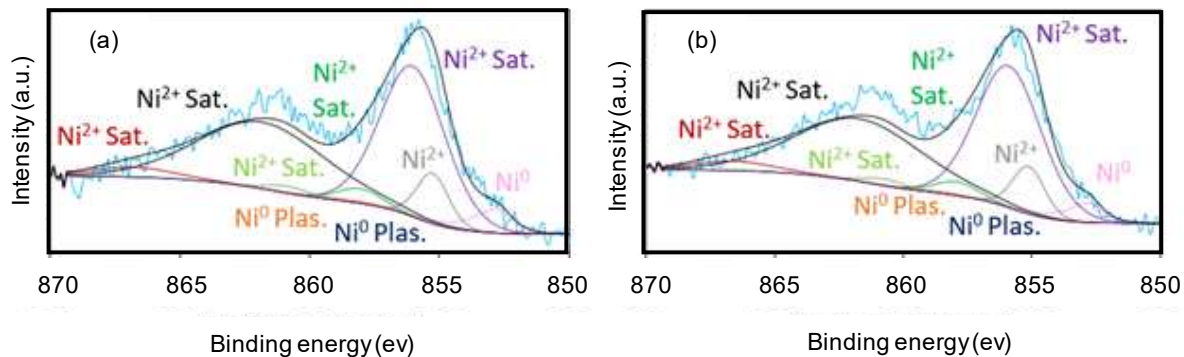


**Figure 5.** Ni 2p XPS spectra of (a) 4.5%Ru-4.5%Ni/AC, (b) 1%Ru-5%Ni/AC.

**Table 4.** Atomic concentration and abundance of Ru and Ni species in carbon-supported catalysts, based on XPS data

Catalyst	Ru (at%)	Ru oxidation state (%)	Ni (at%)	Ni oxidation state (%)
5.3%Ru/AC	14	Ru <sup>2+</sup> 100	-	-
4.5%Ru-4.5%Ni/AC	14	Ru <sup>2+</sup> 100	7	Ni <sup>2+</sup> 94; Ni <sup>0</sup> 6
1%Ru-5%Ni/AC	9	Ru <sup>2+</sup> 100	10	Ni <sup>2+</sup> 95; Ni <sup>0</sup> 5

These catalysts were also characterized by aberration-corrected scanning transmission electron microscopy (STEM). Results are presented in Figure 6. 5.3%Ru/AC possesses the smallest particles size (1.4 nm) with a good dispersion of Ru particles (Figure 6a-c). Slightly bigger particles are observed in 4.5%Ru-4.5%Ni/AC (2.5 nm, Figure 6d-f) and 1%Ru-5%Ni/AC (2.1 nm, Figure 6g-i), which might be related to the presence of NiRu alloy particles. In any case, such small particle sizes correlate well with the CO chemisorption results (< 4 nm) (Table S2).

The slight increase of the particle size between 5.3%Ru/AC, 1%Ru-5%Ni/AC and 4.5%Ru-4.5%Ni/AC respectively could be related to the bimetallic character, or rather due to the increase in the Ni loading.<sup>46</sup>

TEM-EDS elemental mapping confirms the homogeneous elemental dispersion of Ni and Ru (Figures 7 and Figures S6-S8). Figure 7a shows a representative high angle annular dark-field (HAADF) image of the 1%Ru-5%Ni/AC catalyst. Metal particles smaller than 5 nm were found evenly dispersed on the carbon support. The composition of these particles was elucidated using energy-dispersive X-ray spectroscopy (X-EDS) presented in Figure 7b. Ru and Ni cover the same areas and a clear separation was not detected. Therefore, the intimate contact and the homogeneous scattering between Ru and Ni indicate that the nanoparticles are Ru-Ni alloys.

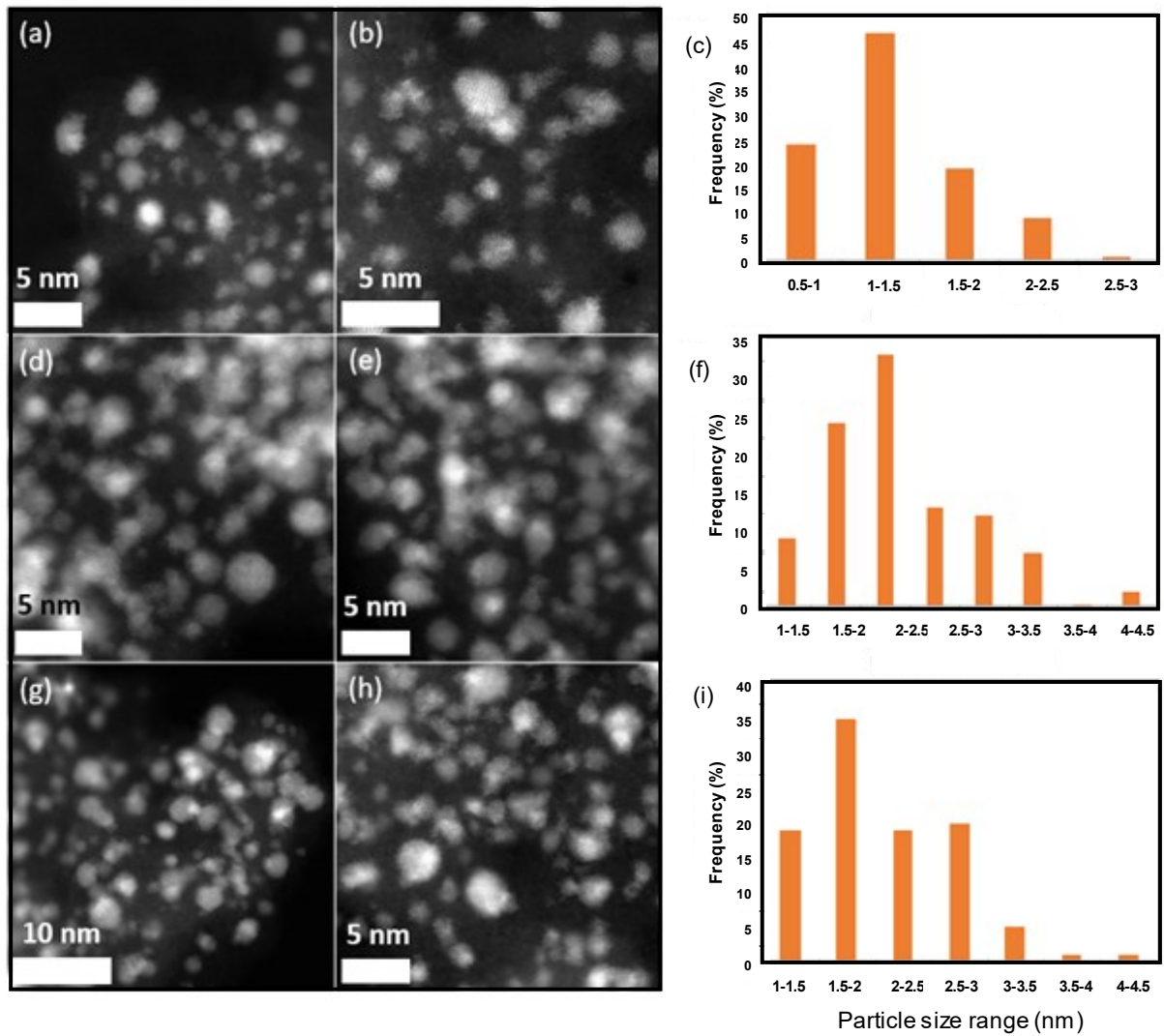


**Figure 6.** HAADF-STEM images and associated particles (100) size distribution histogram of (a, b, c) 5.3%Ru/AC, (d, e, f) 4.5%Ru-4.5%Ni/AC, (g, h, i) 1%Ru-5%Ni/AC.

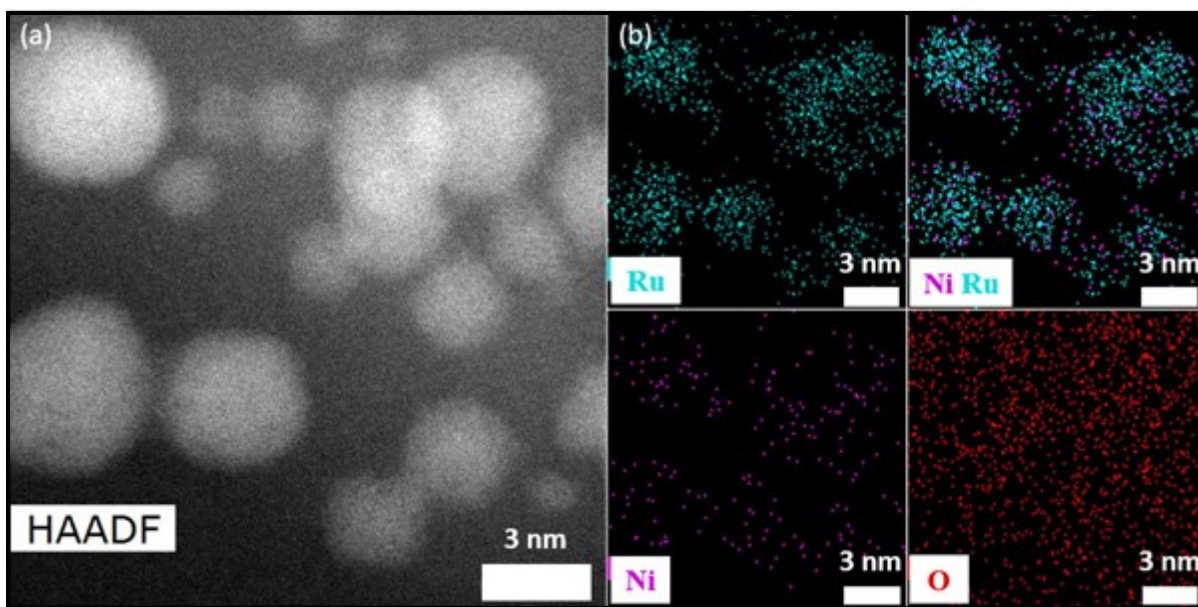


**Figure 7.** (a) HAADF-STEM; (b) TEM-EDS elemental mapping images of 1%Ru-5%Ni/AC.

#### 5.3.2.2. Catalytic application

The bimetallic Ru-Ni/AC catalysts were then involved in the amination of acetol under the optimized reaction conditions (65 °C, 60 bar of H<sub>2</sub>). The results obtained after 3 h are presented in Figure 8. We noticed that the incorporation of Ni had a significant influence on the catalytic results. For example, the 4.5%Ru-4.5%Ni/AC system gave a yield of alaninol up to 53%. Moreover, it was very selective into this amine (64%) since the only by-product was propylene glycol. Variations of the Ru and Ni proportions did not lead to significant changes on the selectivity. However, the Ni content seems to impact the carbon balance, *e.g.* the presence of products strongly adsorbed on the surface, where the best results were obtained with 4.5%Ru-4.5%Ni/AC (80%). One may note that while the 1%Ru/AC gave poor results (10% of amines), when associated to 5%Ni, the resulting 1%Ru-5%Ni/AC gave a cumulated yield of more than 55% of amines with an additional yield in propylene glycol of 10%. Here Ru can play a role on the direct hydrogenation of acetol to propylene glycol.<sup>47</sup>

It is worth noting that the carbon balance in liquid phase was always consistent with the product quantified by NMR analyses.

In summary, bimetallic Ru and Ni systems are very efficient to transform acetol into alaninol despite the competitive hydrogenation into propylene glycol. In the composition range we

investigated, it appears difficult at this stage to get more information on the actual role of each metal species. However, there is an evident synergy of the two metals due to the formation of an alloy, and due to the positive influence of the Ni introduction on amines yield (from 42% for 5.3%Ru/AC to 52% for 4.5%Ru-4.5%Ni/AC) and the reduction of Ru content that boosted amines selectivity (from 67% for 4.5%Ru-4.5%Ni/AC to 85% for 1%Ru-5%Ni/AC). Those values are much higher than the literature values.<sup>27</sup>

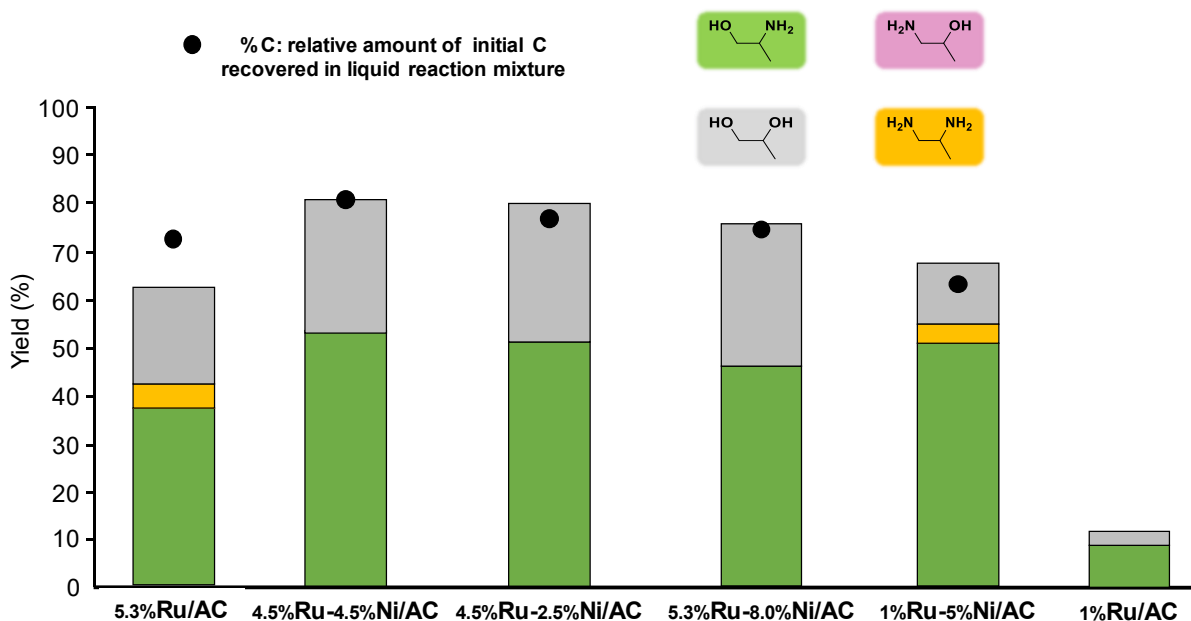


**Figure 8.** Acetol amination with Ru-Ni/AC catalysts. Conditions: 100 mL of 25% aqueous  $\text{NH}_3$ , 10 g of acetol, 1 g of catalyst, 65 °C, 60 bar  $\text{H}_2$ , 3 h.

Note that we investigated the stability of the different products under the reaction conditions (with a different catalytic system). This is presented in Supplementary information (Figures S9 and S10). Globally, alaninol and propylene glycol showed to be stable at 95 and 30%, respectively, indicated that side-reactions occurred on these products, however not towards aminated products.

### 5.3.3. Recycling studies with 4.5%Ru-4.5%Ni/AC catalyst

Results presented in Figure 2 seem indicate that different reaction times imply a variation of selectivities despite a complete conversion. Such variations are expected in the case of deactivation of the catalyst. Recycling studies have been performed with the 4.5%Ru-4.5%Ni catalyst (see Experimental section for details) (Figure 9). First, the catalyst is sufficiently stable to be reused, with similar acetol conversion for 3 cycles but with a slight variation in products selectivities

towards the production of more propylene glycol (Figure 9a). Moreover, some Ru and Ni species are lixiviated as measured by ICP-OES. Especially, the relative loss of Ni in solution was found to increase over the 3 runs but remaining limited to a total of 8% compared to the amount on the catalyst (Figure 9b). Besides Ru loss was in the range of 15%, which is still limited. A hot filtration experiment was conducted with the 5.3%Ru-8%Ni catalyst in order to assess the activity of leached ions from the catalyst (Figure 9c). For that the catalyst was removed from the reaction mixture at the reaction temperature after a first run (Run 1'), and a reaction was performed in the absence of catalyst after addition of fresh acetol (Run 2'). As a result, the concentration of products after Run 2' was comparable to that quantified after Run 1', therefore the Ru and Ni leached species (8 and 3% from catalyst content, respectively) did not contribute to the formation of the target products.

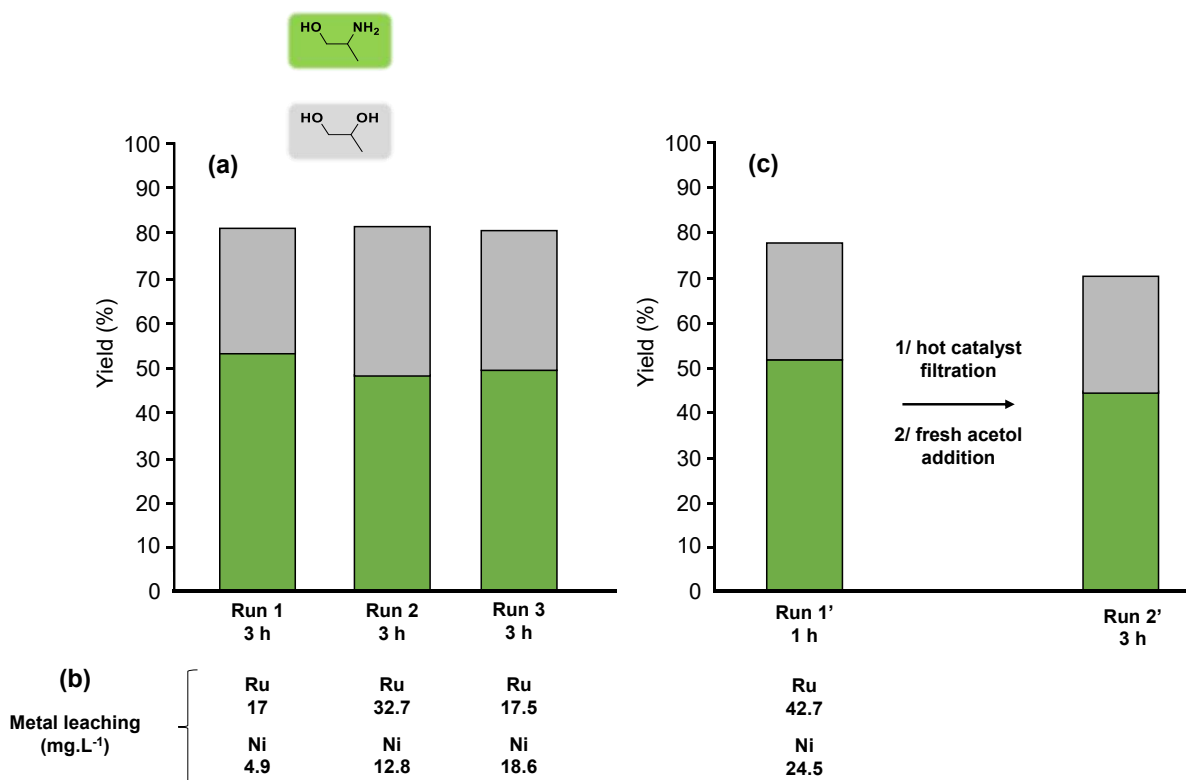


**Figure 9.** Stability experiments with 4.5%Ru-4.5%Ni/AC. (a) Reusability; (b) Leaching extent of metals into the liquid phase after each run with initial metals content of 450 mg.L<sup>-1</sup> for both Ru and Ni. (c) Efficiency of leached species with 5.3%Ru-8%Ni/AC with initial metals content of 530 mg.L<sup>-1</sup> for Ru and 800 mg.L<sup>-1</sup> for Ni. Conditions for Run 1: 100 mL of 25% aqueous NH<sub>3</sub>, 10 g of acetol, 1 g of catalyst, 65 °C, 60 bar H<sub>2</sub>. For Runs 2 and 3 the amount of acetol was adapted to the amount of catalyst.

Some characterisations of the used catalyst are presented in Supplementary information (Figure S11-S14, Tables S3 and S4). First, XRD analysis does not indicate any structural changes during the catalytic reaction. Besides, we noticed a significant decrease of BET surface area down to  $430 \text{ m}^2 \cdot \text{g}^{-1}$ , the microporosity being the most affected. Therefore, textural features appear to be not essential for the catalytic efficiency. Also, XPS data show that the relative concentration of Ru atoms at the surface was divided by a factor 2 at the benefit of Ni, which is coherent with the predominant lixiviation of Ru compared to Ni observed by ICP-EOS. The catalytic behaviour was clearly not affected by these changes, at least for 3 cycles, which is quite promising for a longer-term application.

#### ***5.3.4. Reactivity of acetol biosourced precursors***

Finally, we attempted to get the aminated products directly from the biosourced precursors of acetol. Here, in addition to reductive amination, the transformation involves a C-C bond cleavage (retro-aldol) in the precursor backbone. As presented in the Introduction, the group of Sels reported the formation of alkyl di-amines by reacting glucose or xylose with alkyl amines under  $\text{H}_2$  in the presence of a Ru/C catalyst.<sup>5</sup> However, no example was reported with  $\text{NH}_3$ . On the other hand, the efficiency of a 5%Ni-30% $\text{W}_2\text{C}/\text{AC}$  catalyst for the retro-aldol cleavage of (poly)saccharides leading to glycols under  $\text{H}_2$ , thanks to the presence of W carbide, has been reported.<sup>3, 48</sup> Therefore, we first assessed the latter to perform amination of acetol with  $\text{NH}_3$ . A poor yield of less than 10% of aminated products was obtained; apparently, Ni does not perform amination and this was confirmed using a 5.3%Ni/AC catalyst leading to the same results (data not presented). It seems that the presence of Ru is necessary, as in the case of the bimetallic systems we introduced in the previous sections.

As a consequence, Ru- $\text{W}_x\text{C}/\text{AC}$  catalyst would be of interest. However, while catalysts like Ru/ $\text{WC}^{49}$  or Ru- $\text{W}/\text{C}^{50-51}$  are known, the system Ru- $\text{W}_x\text{C}$  has never been described. Here we successfully prepared this material by co-impregnation of Ru and W precursors followed by a carburization under  $\text{H}_2$  flow at  $700 \text{ }^\circ\text{C}$  (see Experimental section for details). We obtained a 7.5%Ru-36% $\text{W}_x\text{C}/\text{AC}$  material despite targeting a loading of 5 wt% of Ru and 30 wt% of W (to be coherent with the 5%Ni-30% $\text{W}_2\text{C}/\text{AC}$  catalyst). The slight difference is due to the difficulty of accurately control the carburization process that may lead to loss of carbon support. Nevertheless, the metal loading is very close and pertinent enough to apply this system in the catalytic transformation. Characterization data are presented in Supplementary information (Figures S15-S18, Tables S5



and S6). XRD diffractogram indicates that the W species consist of a mixture of  $W_2C$  (main peaks at  $2\theta = 34.5^\circ$ ,  $39.3^\circ$  and  $37.9^\circ$ , ICSD 00-035-0776) and WC (main peaks at  $2\theta = 31.4^\circ$ ,  $35.6^\circ$  and  $48.3^\circ$ , ICSD 00-051-0939) hexagonal carbides. The wide peak at  $2\theta = 43.4^\circ$  corresponds to small nanoparticles of hexagonal metallic ruthenium. 7.5%Ru-36% $W_xC/AC$  exhibits particles with an average size of 30 nm with a good dispersion of Ru particles on the W aggregates, based on TEM analysis. The presence of large particles is consistent with the high metal loading that was impregnated on the surface. Note that differences exist compared to the Ni- $W_xC/AC$  system for which only the  $W_2C$  phase was observed along with NiW and NiWC alloys.<sup>3</sup> Also, a noticeable decrease in the surface area is observed for 7.5%Ru-36% $W_xC/AC$  ( $593\text{ m}^2\cdot\text{g}^{-1}$ , compared to the carbon support), that was less significant with Ni- $W_xC/AC$ . This could be associated to the higher metal loading. Such high loading should induce: (1) a significant carbon porosity restructuring during thermal treatment steps and sintering of the tungsten and Ru phases; (2) the significant increase in weight density of the material with the decrease of the carbon proportion; (3) reduction and formation of  $CH_4$  from carbon in the presence of Ru. Concerning XPS analysis for 7.5%Ru-36% $W_xC/AC$ , 3 main peaks of C 1s spectrum are identified, located at 290.2 eV, 286.2 eV and 284.5 eV and corresponding to C-C, C-O and C-C bonds, respectively (unlike 5.3%Ru/AC, the peak assigned to C=O does not appear).<sup>40</sup> Two oxidation states of Ru can be observed on Ru 3d spectrum: metallic ruthenium  $Ru^0$  ( $3d_{5/2}$ : 279.9 eV and  $3d_{3/2}$ : 284.2 eV), and  $Ru(OH)_2$ , from the passivation layer ( $3d_{5/2}$ : 281 eV and 1 satellite : 283.7 eV;  $3d_{3/2}$ : 285.3 eV and 1 satellite : 287.9 eV ; the same as for 5.3%Ru/AC).<sup>41</sup> The Ru  $3p_{3/2}$  spectrum displays peaks at 458 eV and 467.8 eV (satellite peak) that are assigned to metallic Ru, while those at 462.5 eV and 465.5 eV (satellite peak) are correlated to  $Ru(OH)_2$ . Two tungsten species are detected: (1)  $W_xC$  ( $4f_{7/2}$ : 31.46 eV and  $4f_{5/2}$ : 33.64 eV); (2)  $W^{6+}$  ( $4f_{7/2}$ : 35.6 eV,  $4f_{5/2}$ : 37.78 eV). Tungsten is highly oxidized on the surface (81% of  $WO_x$ ). The presence of oxycarbides at the surface of tungsten carbide catalysts are well known. These phases exhibit non-stoichiometric properties, since the lattices exhibit a significant number of oxygen vacancies.<sup>52</sup> These oxygen vacancies enhance the surface conductivity of catalysts,<sup>53-54</sup> and thus the transfer of electrons and charged particles. These properties, in addition to the high reduction/carburization temperature ( $700^\circ\text{C}$ ) must explain the partial reduction of  $Ru^{2+}$  to  $Ru^0$  (7%), which was not observed for the RuNi/AC catalysts (reduced at  $450^\circ\text{C}$ ). 7.5%Ru-36% $W_xC/AC$  presents 10 at% of Ru (lesser than in 5.3%Ru/AC) and 45 at% of W concentrations on the surface.

Concerning the catalytic application, 7.5%Ru-36%W<sub>x</sub>C/AC was quite efficient for the reductive amination of acetol, although at a lesser extent than the Ru-Ni/AC systems presented above: a global amine yields around 30% was obtained with in details, 25% of alaninol, 3% of 1,2-diaminopropane, 1% of 1-aminopropane-2-ol, and 25% of propylene glycol.

Encouraged by this result, we replaced acetol with its direct precursor, glucose. We expect the W<sub>x</sub>C sites to perform the retro-aldol cleavage of glucose into acetol, and the Ru sites the reductive amination into target products. However, despite varying the reaction conditions, we did not observe aminated products. Changing the substrate to fructose, a certain reactivity was observed, with a total yield of aminated products of 9% (Figure 10) including alaninol (1%) and 1,2-diaminopropane (1%). Interestingly amines derived from ethylene glycol, especially ethanol amine (5%), were also observed.

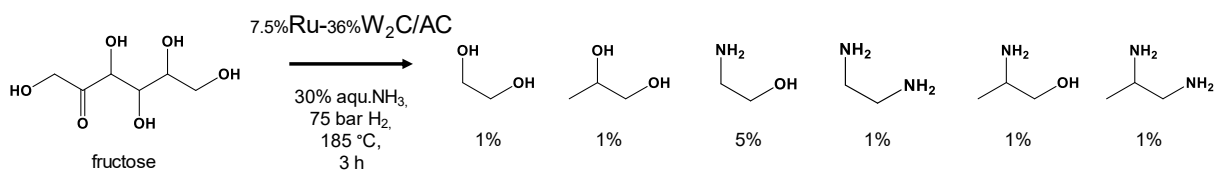


**Figure 10.** Fructose transformation into amino-derivatives of ethylene and propylene glycol. Conditions: 10 g fructose, 1 g 7.5%Ru-36%W<sub>x</sub>C/AC, 300 mL of 25% aqueous NH<sub>3</sub>, 180 °C, 75 bar H<sub>2</sub>, 3 h.

<sup>13</sup>C NMR spectra of reaction mixtures obtained after glucose and fructose transformation are presented in Figure S19. In the case of glucose, the presence of many signals in the aromatic area may be due to furan derivatives, which are not present with fructose. It is well known that fructose is more reactive than glucose, for example for dehydration reactions. Apparently, it is also more prone to undergo fast amine attack despite a less electrophile carbonyl site leading to linear aminated products rather than aromatic compounds.

7.5%Ru-36%W<sub>x</sub>C/AC was not able to aminate neither ethylene nor propylene glycol in these conditions (data not presented). Therefore, the formation of the amines from these sugars clearly comes from the reductive amination of the carbonylated intermediates, glycoaldehyde and acetol. While the reactivity of sugars remains limited, with the one-pot production of primary amines

leading to low yields due to the use of ammonia, this study represents the first example of primary amines obtained from the heterogeneously catalytic aminolysis of sugars.

To advance towards a better comprehension of this process, the two consecutive steps were conducted separately, with the challenge to start from cellulose. In the previous work of Zhang *et al.*, soluble  $H_2WO_4$  was used to form glycolaldehyde, that was then aminated into ethanol amine.<sup>27</sup> For our study, the heterogeneous system  $W_2C/AC$  was chosen for the first step (the synthesis and characterization of this catalyst have been presented elsewhere<sup>3, 55</sup>). We obtained 12% yield of acetol from cellulose (Figure 11), which is notably lesser (35-60%) than in recent studies using bi-metallic system  $Ni-SnO_x/Al_2O_3$ ,<sup>56</sup>  $Sn-Si/C$ ,<sup>57</sup>  $Sn-Ni/SiO_2$ ,<sup>58</sup> or  $SnFe/C$  under similar conditions.<sup>59</sup> After this first stage, the 30% $W_2C/AC$  catalyst was removed by filtration, then 50 mL of  $NH_3$  aqueous solution and 0.70 g of 7.5% $Ru-36\%W_xC/AC$  catalyst were added in the reaction mixture containing acetol among all other components (sugars, liquefied cellulosic oligomers...). Here a certain reactivity was observed and it was possible to obtain alaninol and propylene glycol in 18 and 27% yields respectively, relative to acetol, and corresponding to 2% yield of alaninol relative to cellulose. This is the first time that such aminated products were obtained from cellulose by a 2-steps procedure only involving heterogeneous catalysts.

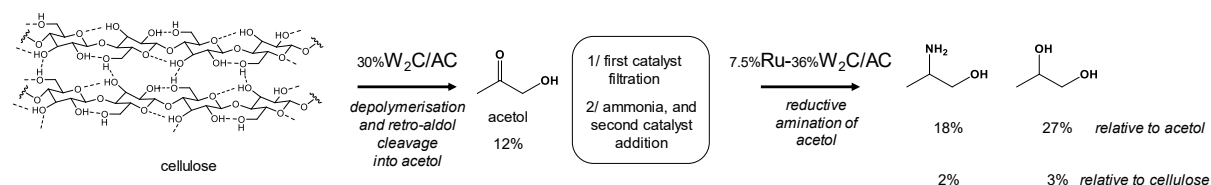


**Figure 11.** Sequential transformation of cellulose into alaninol via *acetol* formation. Conditions: Step 1: 2 g cellulose, 0.75 g 30% $W_2C/AC$ , 100 mL  $H_2O$ , 40 bar  $H_2$ , 235 °C, 0.5 h; Step 2: 100 mL  $H_2O$  + 50 mL of 30% aqueous  $NH_3$ , 0.70 g 7.5% $Ru-36\%W_xC/AC$ , 75 bar  $H_2$ , 65 °C, 3 h.

#### 5.4. Conclusion

We report in this paper the synthesis and full characterization of a family of  $Ru-Ni/AC$  catalysts prepared by a co-impregnation route. Such catalysts have been used for the first time for reductive amination of acetol and the 4.5% $Ru-4.5\%Ni/AC$  system appeared to be highly efficient in the presence of aqueous  $NH_3$  (65 °C, 60 bar  $H_2$ , 3-5 h) to form primary amines derived from propylene glycol. Here, up to 55% amine yield was obtained including 50% of alaninol. A certain synergy between  $Ni$  and  $Ru$  has been demonstrated. The potential of catalyst reuse was assessed during 3 successive cycles demonstrating a good stability of the material. We also explored the direct

aminolysis of sugars. For that an original catalyst 7.5%Ru-36%W<sub>x</sub>C/AC was prepared by one-pot co-impregnation and carburization and characterized. Starting from fructose, this catalyst gave up to 9 wt% of primary amines were obtained (aqueous NH<sub>3</sub>, 180 °C, 75 bar H<sub>2</sub>, 3 h), which is the first example of the formation of primary amines directly from carbohydrates. To go further we used a combination of 30%W<sub>2</sub>C/AC and .5%Ru-36%W<sub>x</sub>C/AC for a sequential transformation of robust cellulose into aminated derivatives through the intermediate formation of acetol (40 bar H<sub>2</sub>, 235 °C, 0.5 h), and 2% of alaninol were obtained aqueous NH<sub>3</sub>, 75 bar H<sub>2</sub>, 65 °C, 3 h) which is the first example of the formation of this amine by such route and in the presence of only heterogeneous catalysis. This overall study on the reductive amination of bio-sourced substrates by NH<sub>3</sub>, from simple reactant to a polycarbohydrate with heterogeneous efficient and robust heterogeneous catalysts is of prime importance towards the formation of bio-sourced primary amines by green synthetic methods.

## 5.5. References

1. Froidevaux, V.; Negrell, C.; Caillol, S.; Pascault, J.-P.; Boutevin, B., Biobased Amines: From Synthesis to Polymers; Present and Future. *Chem. Rev.* **2016**, *116* (22), 14181-14224.
2. Wu, H.; Li, H.; Fang, Z., Hydrothermal amination of biomass to nitrogenous chemicals. *Green Chem.* **2021**, *23* (18), 6675-6697.
3. Goc, F.; Epicier, T.; Perret, N.; Rataboul, F., Preparation of Carbon-Supported Tungsten Carbides: Comparative Determination of Surface Composition and Influence on Cellulose Transformation into Glycols. *ChemCatChem* **2023**, *15* (8), e202201496.
4. Pelckmans, M.; Mihaylov, T.; Faveere, W.; Poissonnier, J.; Van Waes, F.; Moonen, K.; Marin, G. B.; Thybaut, J. W.; Pierloot, K.; Sels, B. F., Catalytic Reductive Aminolysis of Reducing Sugars: Elucidation of Reaction Mechanism. *ACS Catal.* **2018**, *8* (5), 4201-4212.
5. Pelckmans, M.; Vermandel, W.; Van Waes, F.; Moonen, K.; Sels, B. F., Low-Temperature Reductive Aminolysis of Carbohydrates to Diamines and Aminoalcohols by Heterogeneous Catalysis. *Angewandte Chemie International Edition* **2017**, *56* (46), 14540-14544.
6. Ullrich, M.; Weinelt, F.; Winnacker, M., Biobased Polyamides: Academic and Industrial Aspects for Their Development and Applications. Springer Berlin Heidelberg: Berlin, Heidelberg, pp 1-69.
7. Winnacker, M.; Rieger, B., Biobased Polyamides: Recent Advances in Basic and Applied Research. *Macromolecular Rapid Communications* **2016**, *37* (17), 1391-1413.
8. Runeberg, J.; Baiker, A.; Kijenski, J., Copper catalyzed amination of ethylene glycol. *Applied Catalysis* **1985**, *17* (2), 309-319.
9. Yue, C.-J.; Di, K.; Gu, L.-P.; Zhang, Z.-W.; Ding, L.-L., Selective amination of 1,2-propanediol over Co/La<sub>3</sub>O<sub>4</sub> catalyst prepared by liquid-phase reduction. *Mol. Catal.* **2019**, *477*.
10. Podyacheva, E.; Afanasyev, O. I.; Vasilyev, D. V.; Chusov, D., Borrowing Hydrogen Amination Reactions: A Complex Analysis of Trends and Correlations of the Various Reaction Parameters. *ACS Catal.* **2022**, *12* (12), 7142-7198.
11. Bähn, S.; Imm, S.; Neubert, L.; Zhang, M.; Neumann, H.; Beller, M., The Catalytic Amination of Alcohols. *ChemCatChem* **2011**, *3* (12), 1853-1864.
12. Gupta, N. K.; Reif, P.; Palenicek, P.; Rose, M., Toward Renewable Amines: Recent Advances in the Catalytic Amination of Biomass-Derived Oxygenates. *ACS Catal.* **2022**, *12* (16), 10400-10440.
13. Hameury, S.; Bensalem, H.; De Oliveira Vigier, K., Sustainable Amination of Bio-Based Alcohols by Hydrogen Borrowing Catalysis. *Catalysts* **2022**, *12* (11), 1306.
14. Rong, Y.; Ji, N.; Yu, Z.; Diao, X.; Li, H.; Lei, Y.; Lu, X.; Fukuoka, A., Lignin amination valorization: heterogeneous catalytic synthesis of aniline and benzylamine from lignin-derived chemicals. *Green Chem.* **2021**, *23* (18), 6761-6788.
15. Pelckmans, M.; Renders, T.; Van de Vyver, S.; Sels, B. F., Bio-based amines through sustainable heterogeneous catalysis. *Green Chem.* **2017**, *19* (22), 5303-5331.
16. Pera-Titus, M.; Shi, F., Catalytic Amination of Biomass-Based Alcohols. *ChemSusChem* **2014**, *7* (3), 720-722.
17. Truong, C. C.; Mishra, D. K.; Suh, Y.-W., Recent Catalytic Advances on the Sustainable Production of Primary Furanic Amines from the One-Pot Reductive Amination of 5-Hydroxymethylfurfural. *ChemSusChem* **2023**, *16* (1), e202201846.
18. Liu, J.; Song, Y.; Ma, L., Earth-abundant Metal-catalyzed Reductive Amination: Recent Advances and Prospect for Future Catalysis. *Chemistry – An Asian Journal* **2021**, *16* (17), 2371-2391.

19. Nandhu, C. T.; Aneesa, T.; Anilkumar, G., Advances and perspectives in the rhodium catalyzed reductive amination reactions. *Journal of Organometallic Chemistry* **2022**, 965-966, 122332.
20. Saini, M. K.; Kumar, S.; Li, H.; Babu, S. A.; Saravanamurugan, S., Advances in the Catalytic Reductive Amination of Furfural to Furfural Amine: The Momentous Role of Active Metal Sites. *ChemSusChem* **2022**, 15 (7), e202200107.
21. Reshi, N. U. D.; Saptal, V. B.; Beller, M.; Bera, J. K., Recent Progress in Transition-Metal-Catalyzed Asymmetric Reductive Amination. *ACS Catal.* **2021**, 11 (22), 13809-13837.
22. Irrgang, T.; Kempe, R., Transition-Metal-Catalyzed Reductive Amination Employing Hydrogen. *Chem. Rev.* **2020**, 120 (17), 9583-9674.
23. He, J.; Chen, L.; Liu, S.; Song, K.; Yang, S.; Riisager, A., Sustainable access to renewable N-containing chemicals from reductive amination of biomass-derived platform compounds. *Green Chem.* **2020**, 22 (20), 6714-6747.
24. Murugesan, K.; Senthamarai, T.; Chandrashekar, V. G.; Natte, K.; Kamer, P. C. J.; Beller, M.; Jagadeesh, R. V., Catalytic reductive aminations using molecular hydrogen for synthesis of different kinds of amines. *Chem. Soc. Rev.* **2020**, 49 (17), 6273-6328.
25. Wei, Y.; Wu, X.; Wang, C.; Xiao, J., Transfer hydrogenation in aqueous media. *Catalysis Today* **2015**, 247, 104-116.
26. Faveere, W.; Mihaylov, T.; Pelckmans, M.; Moonen, K.; Gillis-D'Hamers, F.; Bosschaerts, R.; Pierloot, K.; Sels, B. F., Glycolaldehyde as a Bio-Based C2 Platform Chemical: Catalytic Reductive Amination of Vicinal Hydroxyl Aldehydes. *ACS Catal.* **2020**, 10 (1), 391-404.
27. Liang, G.; Wang, A.; Li, L.; Xu, G.; Yan, N.; Zhang, T., Production of Primary Amines by Reductive Amination of Biomass-Derived Aldehydes/Ketones. *Angewandte Chemie International Edition* **2017**, 56 (11), 3050-3054.
28. Kusema, B.; Yan, Z.; Streiff, S. Improved process for preparing N-substituted alkanolamines and/or N-substituted diamines from glycolaldehyde under milder reaction conditions under relatively mild reaction conditions using a metal supported noble metal catalyst in an alkanol solvent. WO2021114166, 2021.
29. Verma, R.; Jing, Y.; Liu, H.; Aggarwal, V.; Kumar Goswami, H.; Bala, E.; Ke, Z.; Kumar Verma, P., Employing Ammonia for Diverse Amination Reactions: Recent Developments of Abundantly Available and Challenging Nitrogen Sources. *Eur. J. Org. Chem.* **2022**, 2022 (25), e202200298.
30. Trégner, T.; Trejbal, J.; Rushswurmova, N.; Zapletal, M., Reductive Amination of 1-Hydroxy-2-propanone Over Nickel and Copper Catalysts. *Chem. Biochem. Eng. Q.* **2017**, 31 (4), 455-470.
31. Sheng, M.; Fujita, S.; Yamaguchi, S.; Yamasaki, J.; Nakajima, K.; Yamazoe, S.; Mizugaki, T.; Mitsudome, T., Single-Crystal Cobalt Phosphide Nanorods as a High-Performance Catalyst for Reductive Amination of Carbonyl Compounds. *JACS Au* **2021**, 1 (4), 501-507.
32. Shin, C.-K.; Kim, S.-H.; Chang, K.-H.; Lee, H.-C.; Kim, G.-J., New Synthesis of Optically Active (L)-Alaninol over Palladium Supported Catalysts. In *Studies in Surface Science and Catalysis*, Rhee, H.-K.; Nam, I.-S.; Park, J. M., Eds. Elsevier: 2006; Vol. 159, pp 313-316.
33. Yu, Q.-W.; Li, Y.-N.; Zhang, Q.; Wang, W.-Q.; Mei, S.-N.; Hui, F.; Shi, J.; Zhao, F.-W.; Yang, J.-M.; Lu, J., Synthesis of 1,2-propanediamine via reductive amination of isopropanolamine over Raney Ni under the promotion of K<sub>2</sub>CO<sub>3</sub>. *Chem. Pap.* **2019**, 73 (8), 2019-2026.
34. Eidamshaus, C.; Melder, J.-P.; Pastre, J.; Pallasch, H.-J. Method for continuous production of 1,2-propylenediamine and dimethyldiethylenetriamine. WO2019105782, 2019.

35. Takanashi, T.; Nakagawa, Y.; Tomishige, K., Amination of alcohols with ammonia in water over Rh-In catalyst. *Chem. Lett.* **2014**, *43* (6), 822-824.
36. Cheng, D.; Wang, Z.; Xia, Y.; Wang, Y.; Zhang, W.; Zhu, W., Catalytic amination of diethylene glycol with tert-butylamine over Ni-Al<sub>2</sub>O<sub>3</sub> catalysts with different Ni/Al ratios. *RSC Adv.* **2016**, *6* (Copyright (C) 2019 American Chemical Society (ACS). All Rights Reserved.), 102373-102380.
37. Jehng, J.-M.; Chen, C.-M., Amination of polyethylene glycol to polyetheramine over the supported nickel catalysts. *Catal. Lett.* **2001**, *77* (Copyright (C) 2019 American Chemical Society (ACS). All Rights Reserved.), 147-154.
38. Wei, Y.; Ni, W.; Zhang, C.; You, K.; Zhao, F.; Chen, Z.; Ai, Q.; Luo, H. a., Highly Dispersed and Stable Hydrotalcite-Derived NiCu/MgAlO Alloy Catalyst for Efficient Amination of Cyclohexanol to Cyclohexylamine in the Vapor Phase. *ACS Sustainable Chemistry & Engineering* **2022**, *10* (40), 13367-13379.
39. Cardona-Farreny, M.; Lecante, P.; Esvan, J.; Dinoi, C.; del Rosal, I.; Poteau, R.; Philippot, K.; Axet, M. R., Bimetallic RuNi nanoparticles as catalysts for upgrading biomass: metal dilution and solvent effects on selectivity shifts. *Green Chem.* **2021**, *23* (21), 8480-8500.
40. Martin, D. J.; Qiu, K.; Shevlin, S. A.; Handoko, A. D.; Chen, X.; Guo, Z.; Tang, J., Highly Efficient Photocatalytic H<sub>2</sub> Evolution from Water using Visible Light and Structure-Controlled Graphitic Carbon Nitride. *Angewandte Chemie International Edition* **2014**, *53* (35), 9240-9245.
41. Ma, Z.; Zhao, S.; Pei, X.; Xiong, X.; Hu, B., New insights into the support morphology-dependent ammonia synthesis activity of Ru/CeO<sub>2</sub> catalysts. *Catalysis Science & Technology* **2017**, *7* (1), 191-199.
42. Morgan, D. J., Resolving ruthenium: XPS studies of common ruthenium materials. *Surface and Interface Analysis* **2015**, *47* (11), 1072-1079.
43. Feng, B.; Chen, C.; Yang, H.; Zhao, X.; Hua, L.; Yu, Y.; Cao, T.; Shi, Y.; Hou, Z., Ionic Liquid-Promoted Oxidant-Free Dehydrogenation of Alcohols with Water-Soluble Ruthenium Nanoparticles in Aqueous Phase. *Advanced Synthesis & Catalysis* **2012**, *354* (8), 1559-1565.
44. Biesinger, M. C.; Payne, B. P.; Lau, L. W. M.; Gerson, A.; Smart, R. S. C., X-ray photoelectron spectroscopic chemical state quantification of mixed nickel metal, oxide and hydroxide systems. *Surface and Interface Analysis* **2009**, *41* (4), 324-332.
45. Li, D.; Atake, I.; Shishido, T.; Oumi, Y.; Sano, T.; Takehira, K., Self-regenerative activity of Ni/Mg(Al)O catalysts with trace Ru during daily start-up and shut-down operation of CH<sub>4</sub> steam reforming. *Journal of Catalysis* **2007**, *250* (2), 299-312.
46. Soszka, E.; Jędrzejczyk, M.; Kocemba, I.; Keller, N.; Ruppert, A. M., Ni-Pd/ $\gamma$ -Al<sub>2</sub>O<sub>3</sub> Catalysts in the Hydrogenation of Levulinic Acid and Hydroxymethylfurfural towards Value Added Chemicals. *Catalysts* **2020**, *10* (9), 1026.
47. Wang, Y.; Furukawa, S.; Song, S.; He, Q.; Asakura, H.; Yan, N., Catalytic Production of Alanine from Waste Glycerol. *Angewandte Chemie International Edition* **2020**, *59* (6), 2289-2293.
48. Ji, N.; Zhang, T.; Zheng, M.; Wang, A.; Wang, H.; Wang, X.; Chen, J. G., Direct catalytic conversion of cellulose into ethylene glycol using nickel- promoted tungsten carbide catalysts. *Angew. Chem., Int. Ed.* **2008**, *47* (44), 8510-8513.
49. Griboval-Constant, A.; Giraudon, J. M.; Twagishema, I.; Leclercq, G.; Rivas, M. E.; Alvarez, J.; Pérez-Zurita, M. J.; Goldwasser, M. R., Characterization of new Co and Ru on  $\alpha$ -WC catalysts for Fischer-Tropsch reaction: Influence of the carbide surface state. *Journal of Molecular Catalysis A: Chemical* **2006**, *259* (1), 187-196.

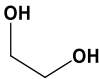
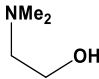
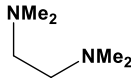
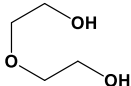
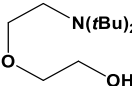
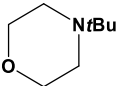
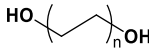
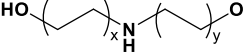
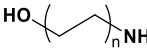
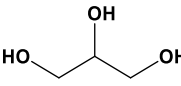
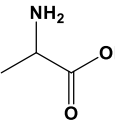
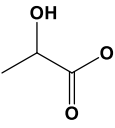
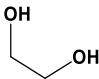
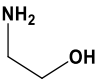
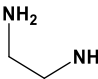
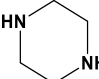
50. Zheng, M.-Y.; Wang, A.-Q.; Ji, N.; Pang, J.-F.; Wang, X.-D.; Zhang, T., Transition Metal–Tungsten Bimetallic Catalysts for the Conversion of Cellulose into Ethylene Glycol. *ChemSusChem* **2010**, *3* (1), 63-66.
51. Ribeiro, L. S.; Órfão, J. J. M.; Pereira, M. F. R., Insights into the effect of the catalytic functions on selective production of ethylene glycol from lignocellulosic biomass over carbon supported ruthenium and tungsten catalysts. *Bioresour. Technol.* **2018**, *263*, 402-409.
52. Di Valentin, C.; Pacchioni, G., Spectroscopic Properties of Doped and Defective Semiconducting Oxides from Hybrid Density Functional Calculations. *Accounts of Chemical Research* **2014**, *47* (11), 3233-3241.
53. Huang, Z.-F.; Song, J.; Pan, L.; Zhang, X.; Wang, L.; Zou, J.-J., Tungsten Oxides for Photocatalysis, Electrochemistry, and Phototherapy. *Advanced Materials* **2015**, *27* (36), 5309-5327.
54. Hong, S. H.; Ahn, S. H.; Choi, J.; Kim, J. Y.; Kim, H. Y.; Kim, H.-J.; Jang, J. H.; Kim, H.; Kim, S.-K., High-activity electrodeposited NiW catalysts for hydrogen evolution in alkaline water electrolysis. *Applied Surface Science* **2015**, *349*, 629-635.
55. Goc, F., Transformation de biomasse lignocellulosique en glycols et dérivés aminés par des catalyseurs à base de carbures de tungstène supportés. *PhD Thesis, Université Claude-Bernard Lyon 1* **2022**.
56. Deng, T.; Liu, H., Direct conversion of cellulose into acetol on bimetallic Ni-SnOx/Al<sub>2</sub>O<sub>3</sub> catalysts. *Journal of Molecular Catalysis A: Chemical* **2014**, *388-389*, 66-73.
57. Wang, H.; Zhu, C.; Liu, Q.; Tan, J.; Wang, C.; Liang, Z.; Ma, L., Selective Conversion of Cellulose to Hydroxyacetone and 1-Hydroxy-2-Butanone with Sn–Ni Bimetallic Catalysts. *ChemSusChem* **2019**, *12* (10), 2154-2160.
58. Liu, X.; Liu, X.; Xu, G.; Zhang, Y.; Wang, C.; Lu, Q.; Ma, L., Highly efficient catalytic conversion of cellulose into acetol over Ni–Sn supported on nanosilica and the mechanism study. *Green Chem.* **2019**, *21* (20), 5647-5656.
59. Li, S.-c.; Deng, Y.-l.; Wang, H.-y.; Wang, C.-g.; Ma, L.-l.; Liu, Q.-y., Production of acetol and lactic acid from cellulose hydrogenolysis over Sn-Fe@C catalysts. *Journal of Fuel Chemistry and Technology* **2022**, *50* (3), 314-325.



## 5.6. Supplementary Information

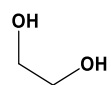
### 5.6.1. Literature

**Table S1.** Literature data on the reductive amination of ethylene and propylene glycol and related reactants

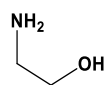
Conditions	Reactant	Main products		Ref.	
	conversion (%)	yield (%)			
9%Cu/Al <sub>2</sub> O <sub>3</sub>				1	
Me <sub>2</sub> NH	91	62	19		
1 bar H <sub>2</sub>					
25 wt%H <sub>2</sub> O					
230 °C					
NiAl <sub>2</sub> O <sub>4</sub> -NiO				2	
<i>t</i> Bu <sub>2</sub> NH	72	50	9		
5 bar H <sub>2</sub>					
200 °C					
15%Ni/Al <sub>2</sub> O <sub>3</sub>				3	
30% aqu.NH <sub>3</sub>	96	not given	not given		
9 bar H <sub>2</sub>					
100 °C					
2%Ru <sub>1</sub> 8.6%Ni <sub>7</sub> /MgO				4	
30% aqu.NH <sub>3</sub>	100	43	18		
2 equiv. NaOH					
10 bar H <sub>2</sub>					
220 °C, 4 h					
9%Ni3%Cu/MgO					5
gaseous NH <sub>3</sub>	24	4	7	10	
10 bar H <sub>2</sub>					
190 °C, 4 h					

5%Co/Al<sub>2</sub>O<sub>3</sub>

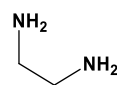
THF  
6 bar NH<sub>3</sub>  
30 bar H<sub>2</sub>  
180 °C



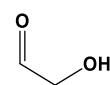
20



14



traces

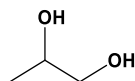


2

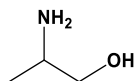
6

10%Co/La<sub>3</sub>O<sub>4</sub>

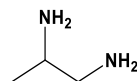
aqu. NH<sub>3</sub>  
no H<sub>2</sub>  
160 °C, 6 h



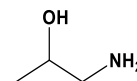
68



60



traces

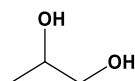


6

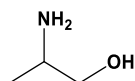
7

5%Rh-5%In/AC

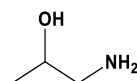
aqu. NH<sub>3</sub>  
50 bar H<sub>2</sub>  
180 °C, 160 h



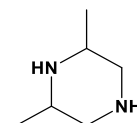
38



5



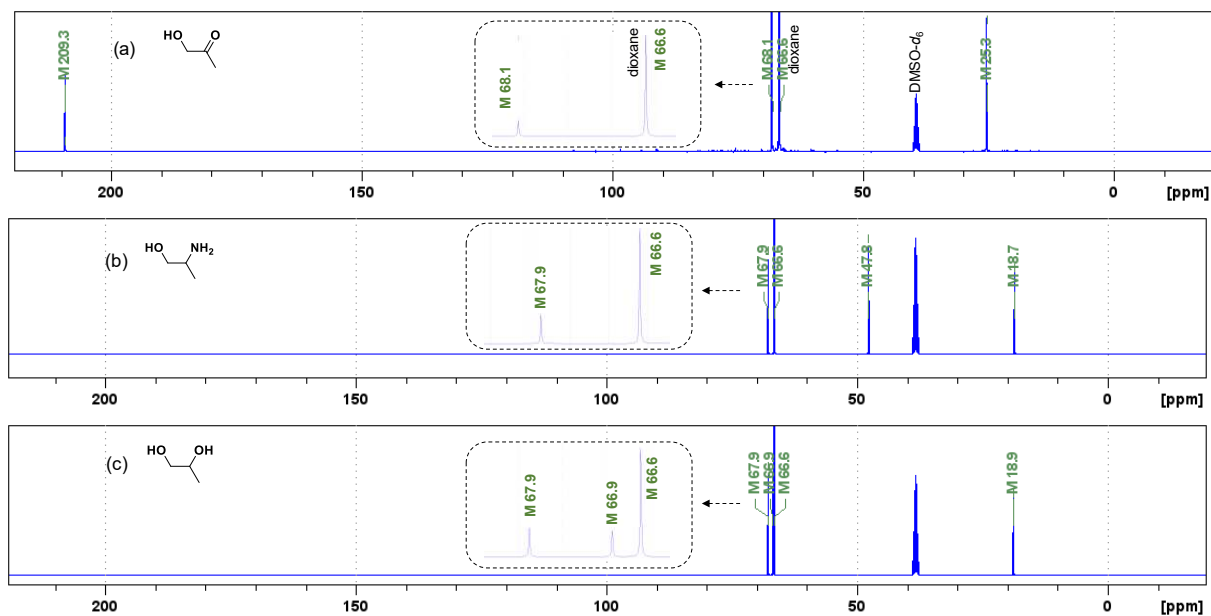
6



4

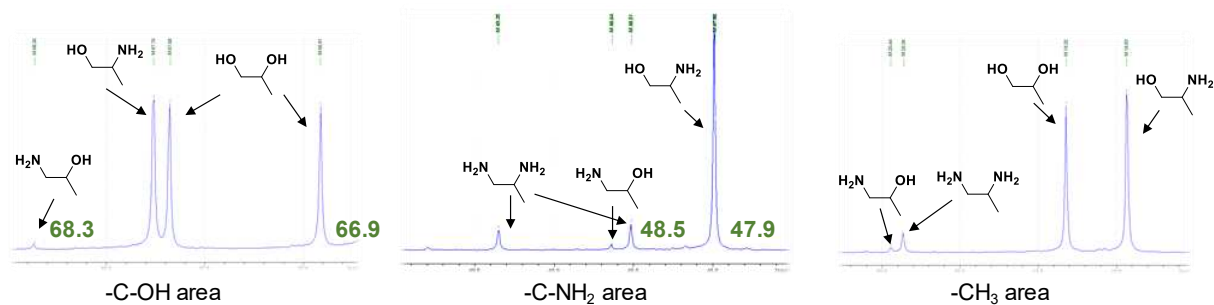
8

### 5.6.2. Experimental section

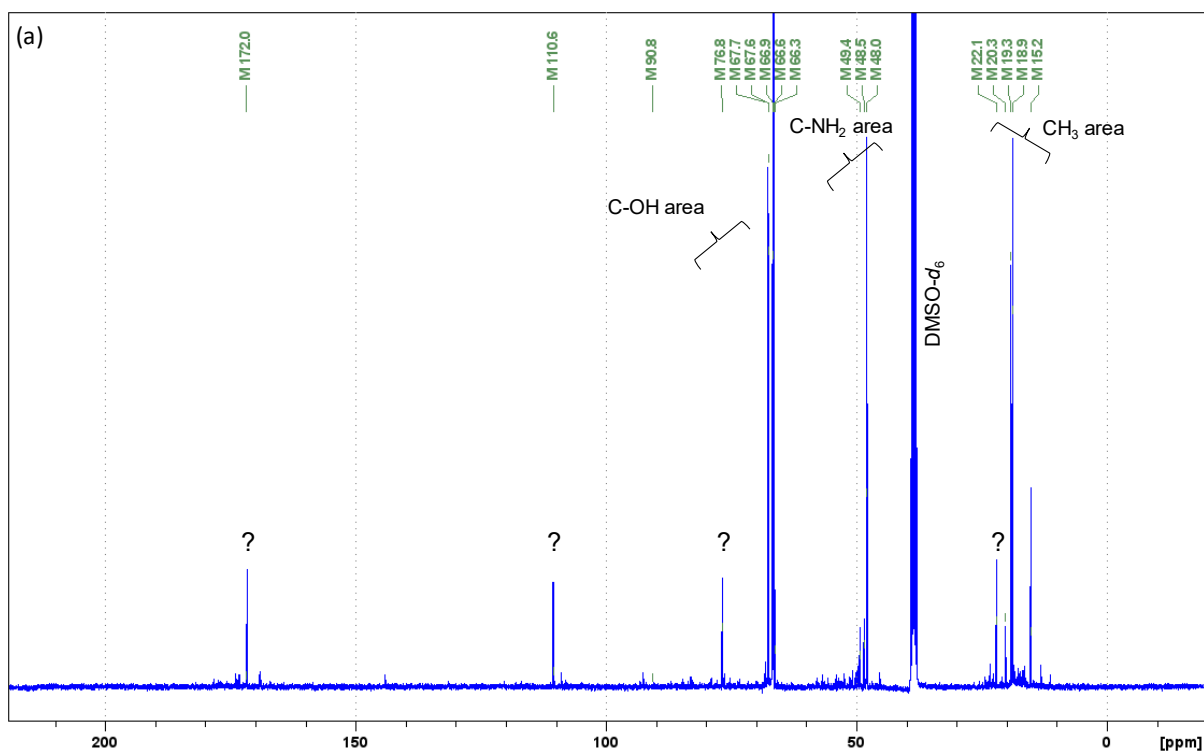


**Figure S1.**  $^{13}\text{C}$  NMR spectra in  $\text{DMSO-}d_6$  of the reactant and the two main products (a) acetol, (b) alaninol and (c) propylene glycol, in the presence of dioxane as internal standard.

**5.6.3. Reaction mixture analysis after reductive amination of acetol**



**Figure S2.** Areas of  $^{13}\text{C}$  NMR spectrum of a typical reaction mixture after catalytic acetol reactivity highlighting the chemical shifts of signals used for quantification of products.



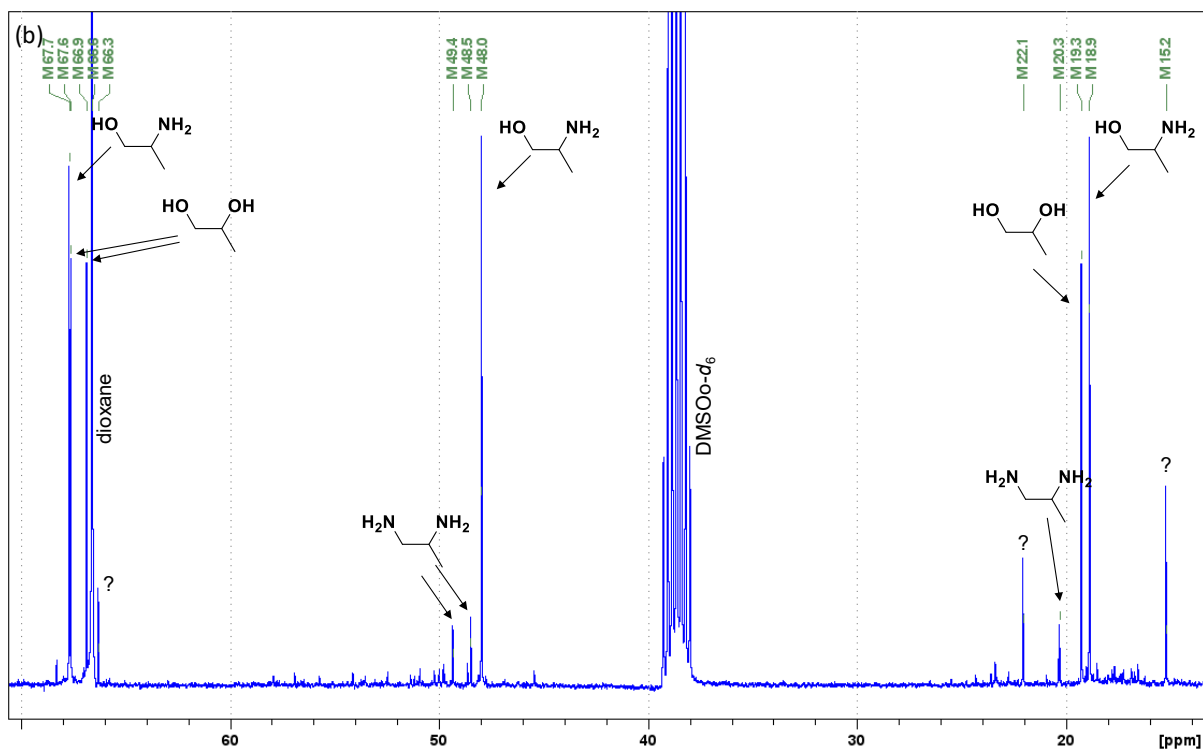


**Figure S3.**  $^{13}\text{C}$  NMR spectrum in  $\text{DMSO-}d_6$  of a reaction mixture after acetol reactivity in the presence of 5.3%Ru/AC. (a) Full spectrum. (b) Focus on product areas. “?”: unknown products. Conditions: 100 mL of 25% aqueous  $\text{NH}_3$ , 10 g of acetol, 1 g of catalyst, 65 °C, 75 bar  $\text{H}_2$ , 3 h.

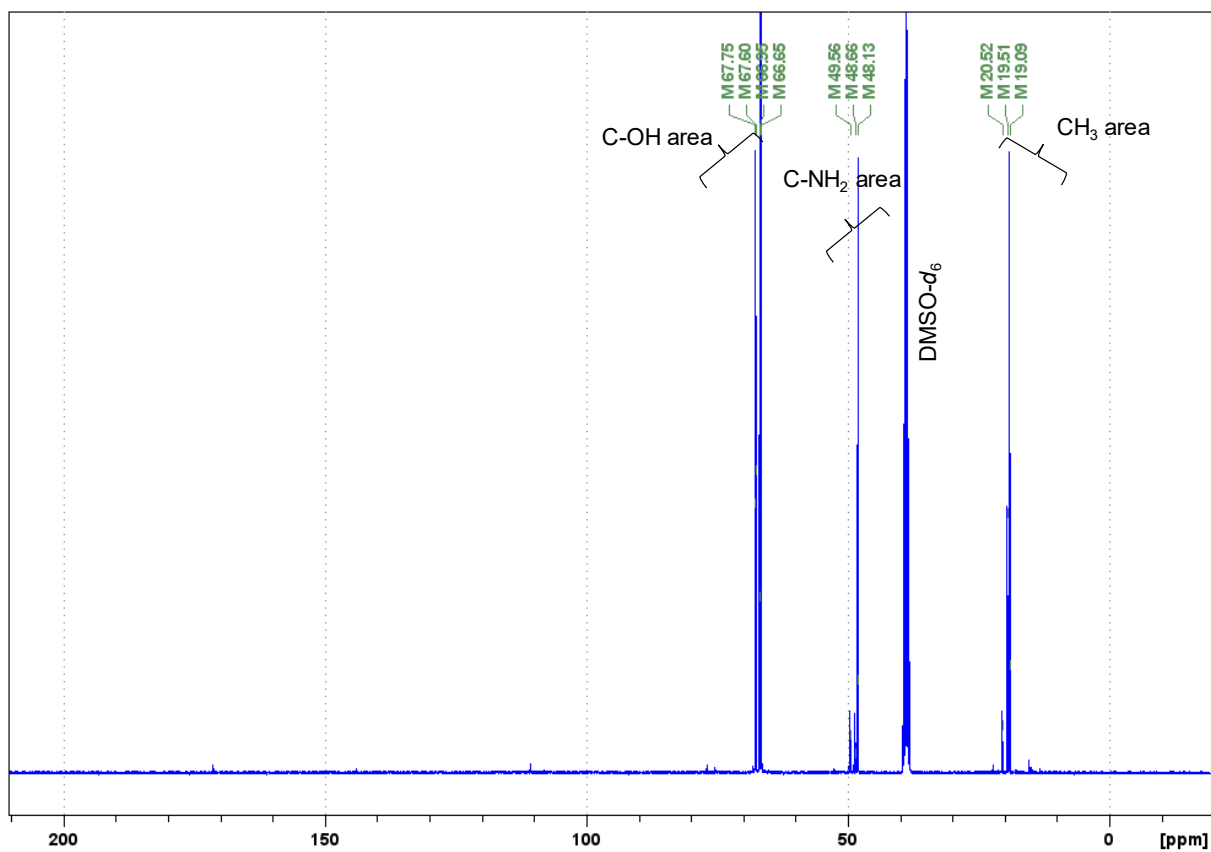


**Figure S4.**  $^{13}\text{C}$  NMR spectrum in  $\text{DMSO-}d_6$  of a reaction mixture after acetol reactivity in the presence of 5.3%Ru/AC. Conditions: 100 mL of 25% aq.  $\text{NH}_3$ , 10 g of acetol, 1 g of catalyst, 65  $^\circ\text{C}$ , 60 bar  $\text{H}_2$ , 5 h.

#### 5.6.4. Characterisation of carbon-supported Ru and Ru-Ni catalysts

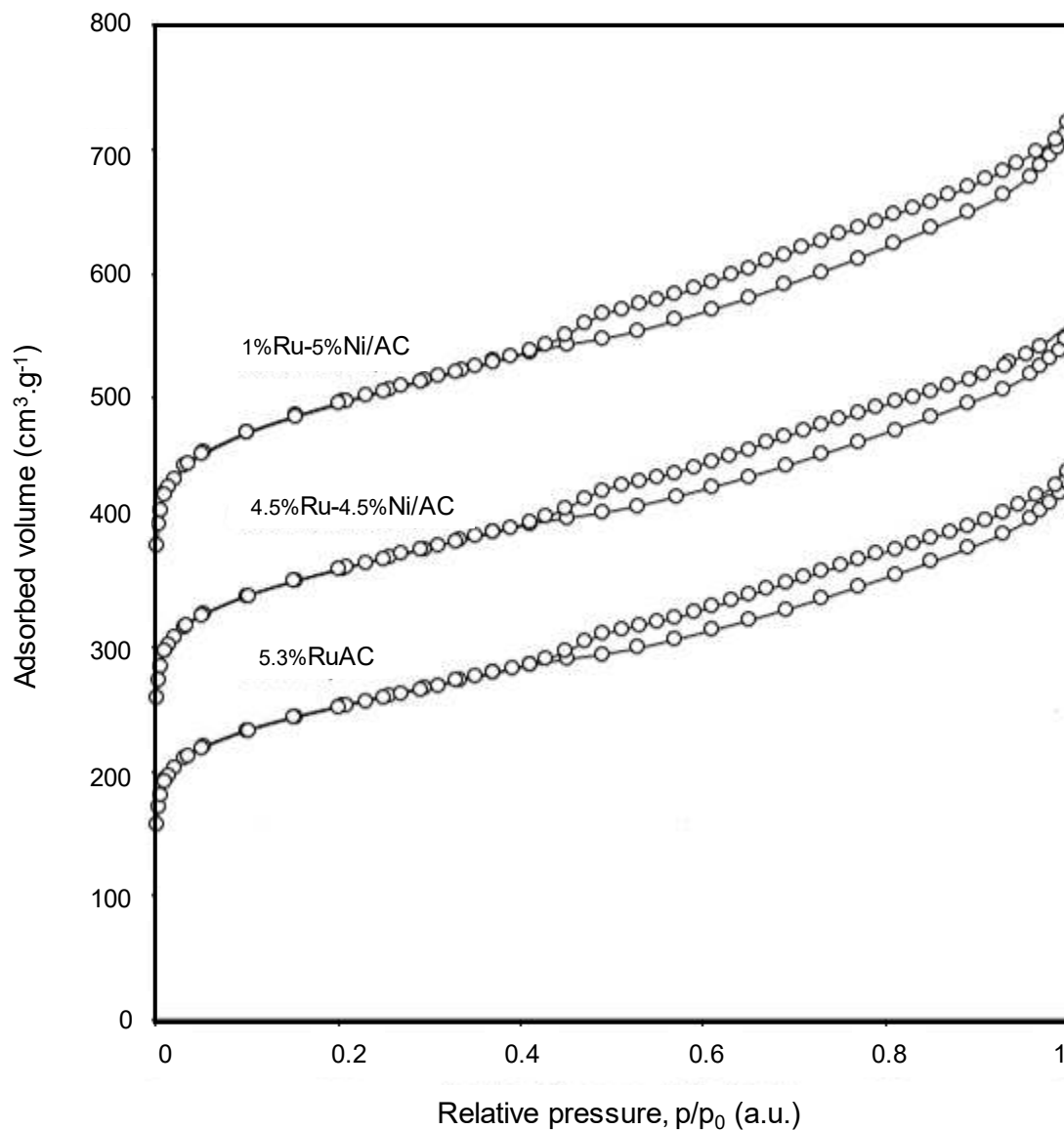


**Figure S5.** N<sub>2</sub> sorption isotherms of some microporous carbon-supported Ru and Ru-Ni catalysts (4.5%Ru-4.5%Ni/AC and 1%Ru-5%Ni/AC isotherms were shifted upwards by 100 cm<sup>3</sup>.g<sup>-1</sup> and 200 cm<sup>3</sup>.g<sup>-1</sup> respectively).

**Table S2.** CO chemisorption measurements: CO chemisorbed per mass of catalyst (CO uptake) and metal particle size ( $d_{CO}$ ) for carbon-supported Ru catalysts

Catalyst	CO uptake (mmol.g <sup>-1</sup> )	$d_{CO}$ (nm)
5.3%Ru/AC	0.34	1.3

4.5%Ru-4.5%Ni/AC	0.50	2.1
1%Ru-5%Ni/AC	0.22	3.9

Particle sizes were estimated using a stoichiometry CO/Ru and CO/Ni of 1. However, for supported Ru catalysts, CO chemisorption is known to depend on particle size and the ratio CO/Ru increases for small sizes (below 2 nm).<sup>9</sup> The results show that the size are below 4 nm for all the catalysts.

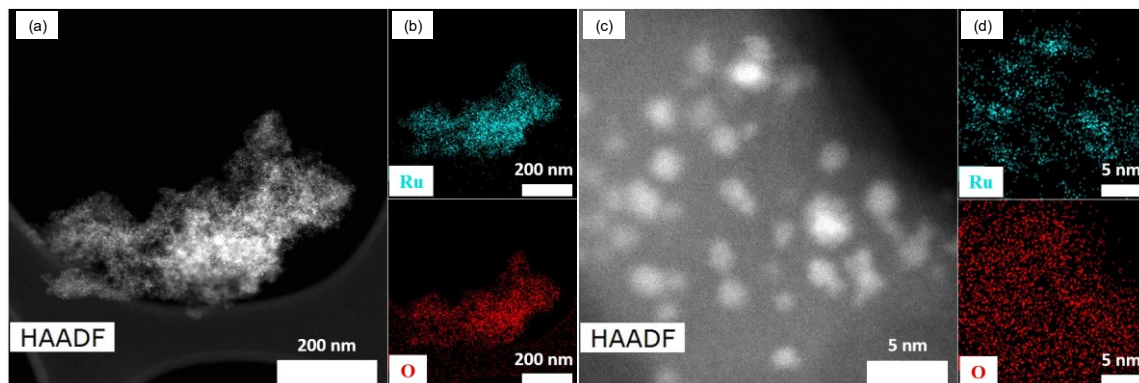


**Figure S6.** (a, c) HAADF-STEM; (b, d) TEM-EDS elemental mapping images of 5.3%Ru/AC.

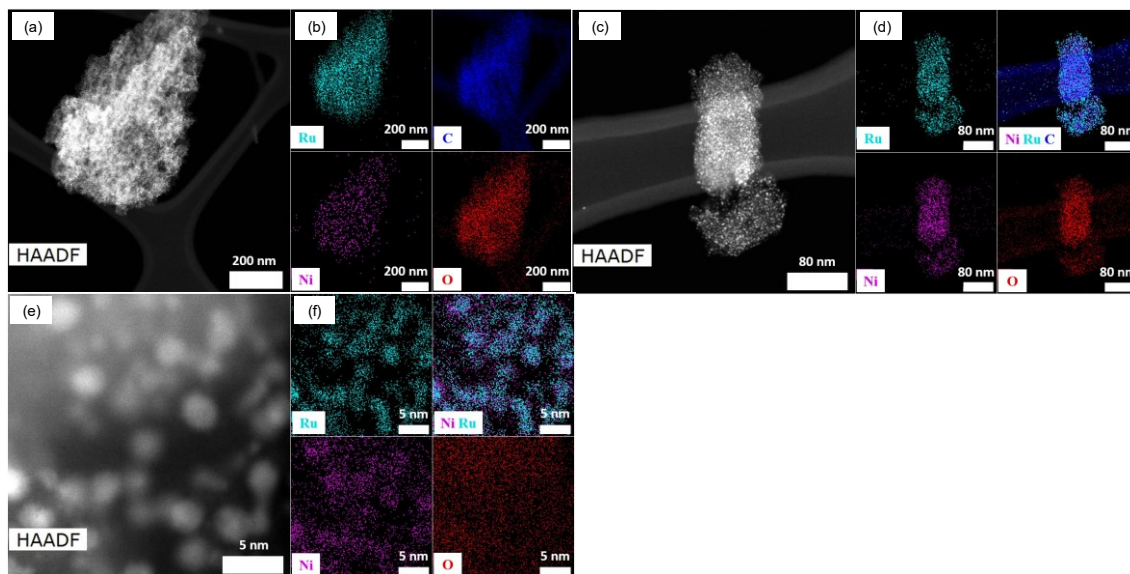


**Figure S7.** (a, c, e) HAADF-STEM; (b, d, f) TEM-EDS elemental mapping images of 4.5%Ru-4.5%Ni/AC.

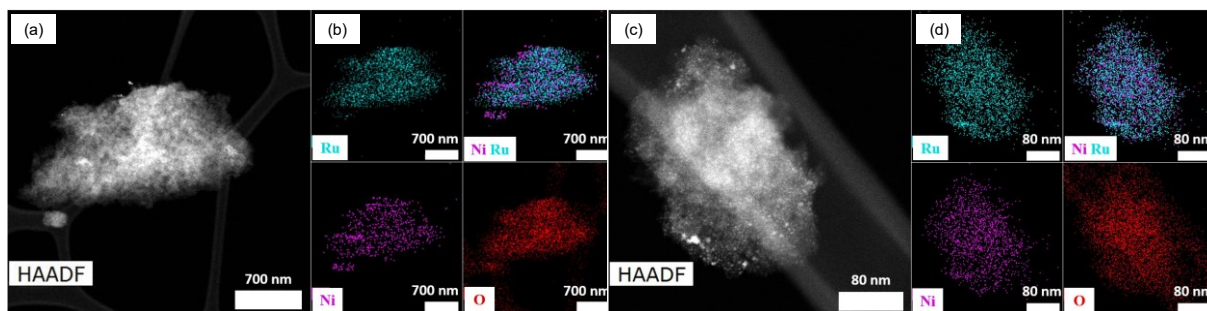


**Figure S8.** (a, c) HAADF-STEM; (b, d) TEM-EDS elemental mapping images of 1%Ru-5%Ni/AC.



### 5.6.5. Reactivity study of products

As the scarce literature presented in Table 1 in main text gives little information about the formation mechanisms of the different products, we further studied the possible pathways presented in Figure 1 in main text. The reactivity of propylene glycol, alaninol and 1-aminopropane-2-ol were assessed with 7%Ru-36%W<sub>x</sub>C/AC, since the 4 possible products were obtained from acetol using this catalyst.

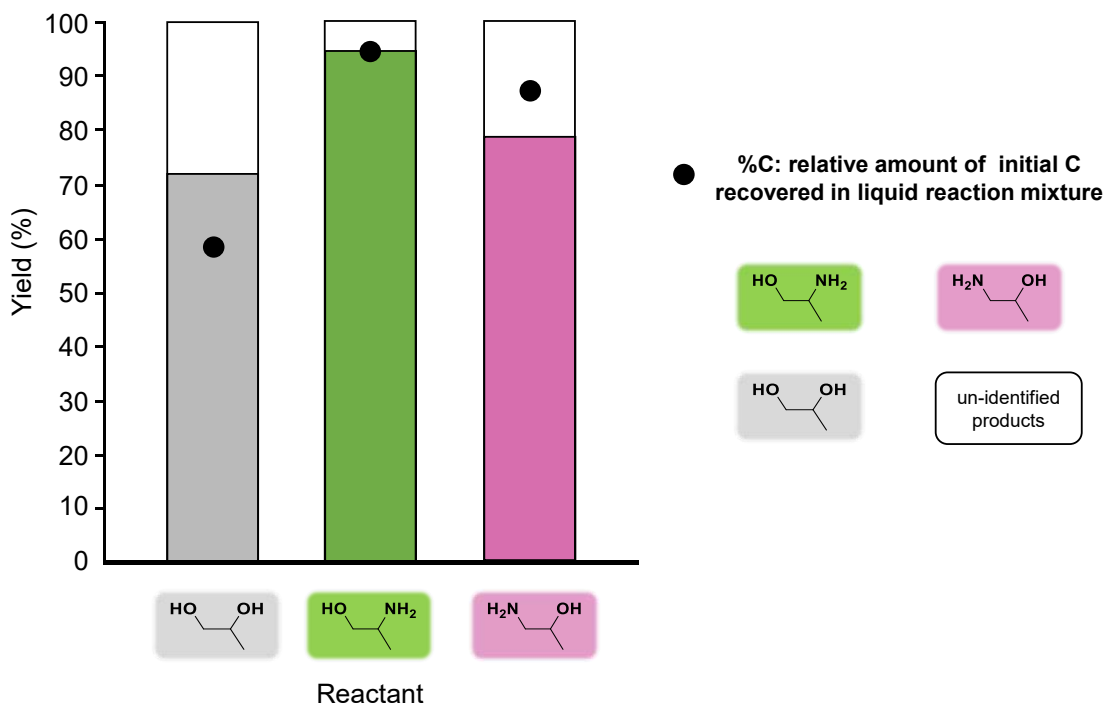


**Figure S9.** Reactivity of compounds identified during the reductive amination of acetol. Conditions: 0.12 mol of reactant, 100 mL of 25% aqueous NH<sub>3</sub>, 1 g of 7.5%Ru-36%W<sub>x</sub>C/AC, 65 °C, 60 bar H<sub>2</sub>, 3 h.

It was confirmed that these 3 compounds are quite stable in the reaction conditions corresponding to that of their formation. Note that we could not identify all the products in the liquid phase.

Despite some conversion (30%) no amine was formed from propylene glycol. Moreover, alaninol is the most stable reactant. Finally, 1-aminopropane-2-ol did not form 1,2-diaminopropane which might explain the lack of literature on this transformation.

Since 1,2-diaminopropane did not form from alaninol nor 1-aminopropane-2-ol, it is possible that the formation of this product occurred during other steps, for example from very reactive intermediates appearing during the global transformation like imines through possible

cyclization/decyclization steps. It is also possible that it occurs through successive reaction without desorption from the surface of an alkoxy intermediate derived from alaninol. Nevertheless, these reactions are not privileged since the diamine was always obtained in low amounts. Most importantly, it was confirmed that propylene glycol was obtained by direct reduction of acetol *via* a side-reaction, without implication of any amino-alcohols derivatives. To summarize, we revisited the possible pathways indicated in Figure 1 in main text. The reaction scheme is quite clear, with 2 main routes 1a and 1d, and 2 very minor routes 1b and 1c.

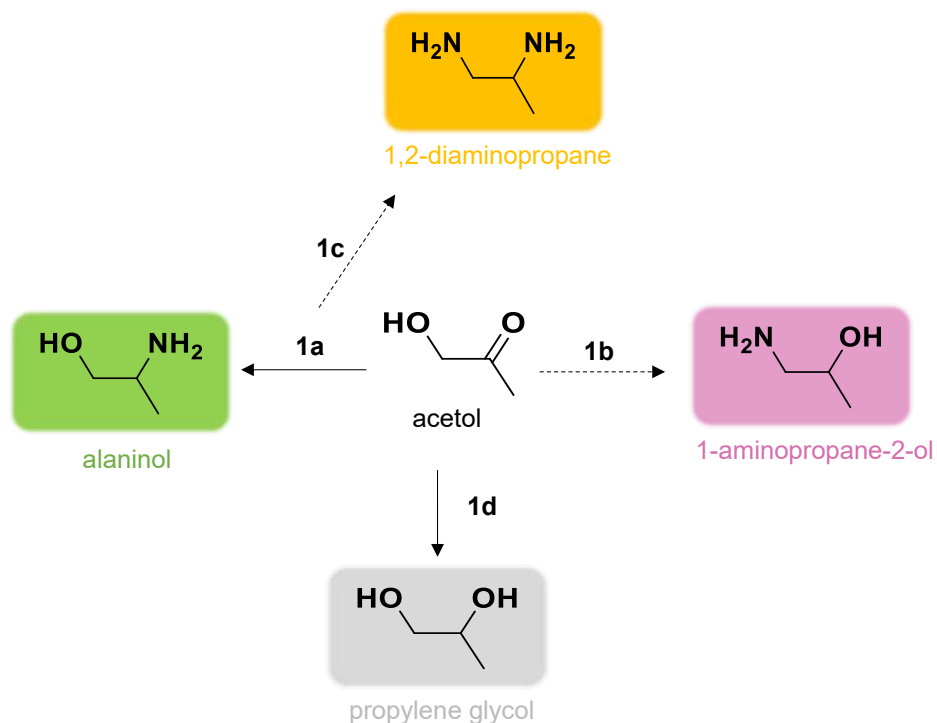


**Figure S10.** New proposed reaction scheme for the reductive amination of acetol by  $\text{H}_2/\text{NH}_3$ .

5.6.6. Characterisation of 4.5%Ru-4.5%Ni/AC recovered after a catalytic reaction

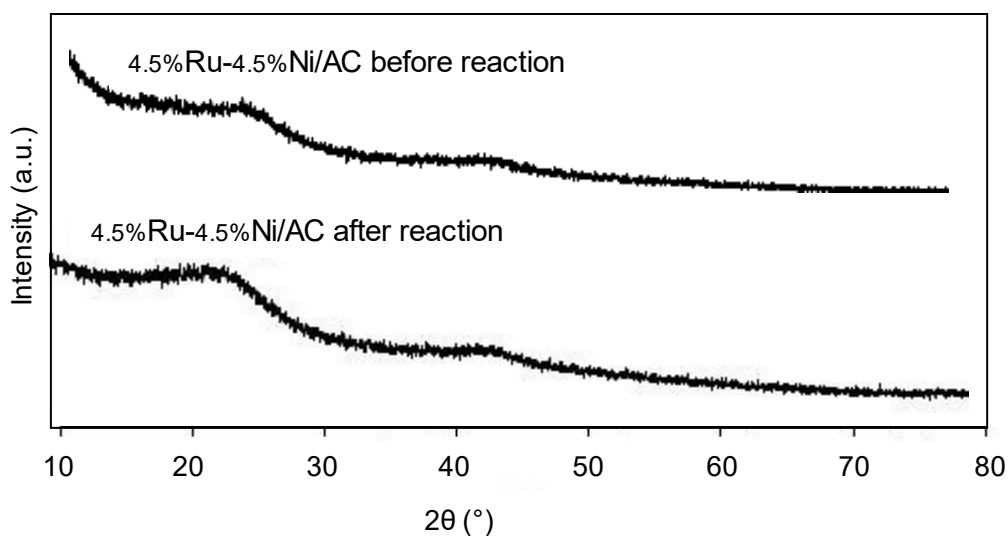


Figure S11. XRD pattern of 4.5%Ru-4.5%Ni/AC recovered after reaction.

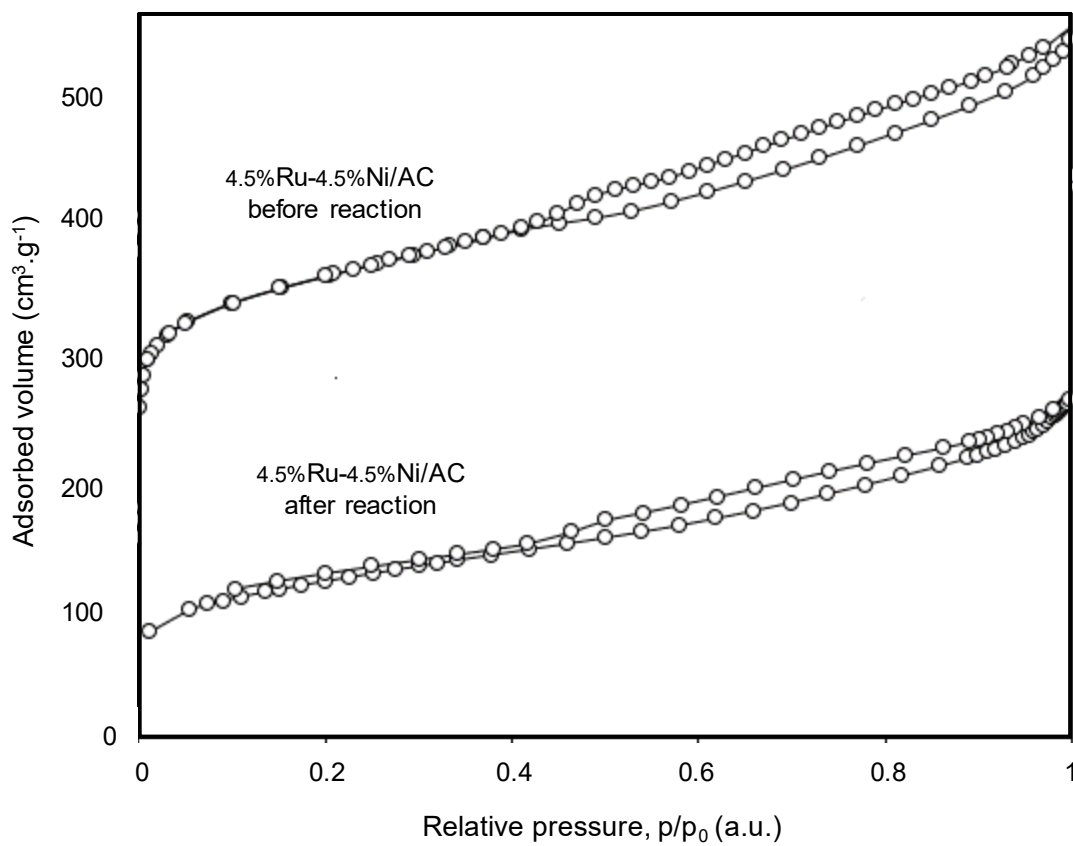
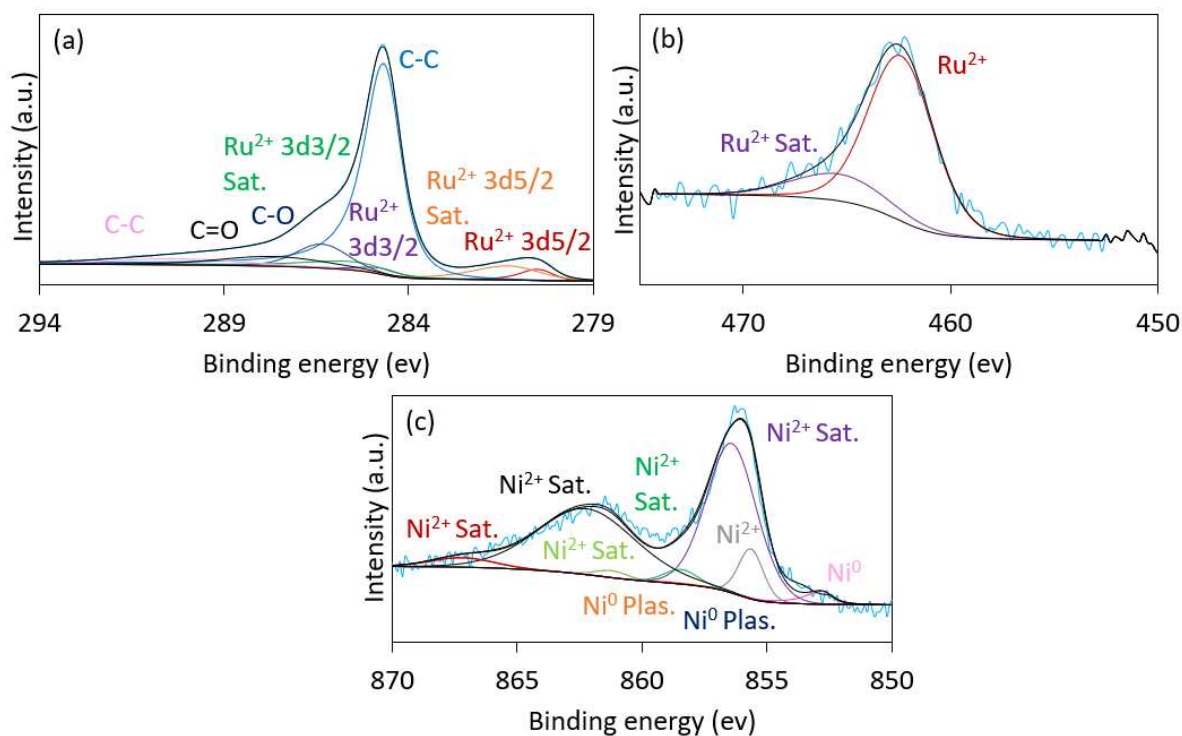


Figure S12. XRD pattern of 4.5%Ru-4.5%Ni/AC recovered after reaction.

**Table S3.** Textural properties of 4.5%Ru-4.5%Ni/AC recovered after reaction

Catalyst	$S_{\text{BET}}^{(a)}$ ( $\text{m}^2\cdot\text{g}^{-1}$ )	$S_{\mu}^{(b)}$ ( $\text{m}^2\cdot\text{g}^{-1}$ )	$V_{\text{p}}^{(c)}$ ( $\text{cm}^3\cdot\text{g}^{-1}$ )	$V_{\mu}^{(d)}$ ( $\text{cm}^3\cdot\text{g}^{-1}$ )	$d_{\text{pore}}^{(e)}$ (nm)
4.5%Ru-4.5%Ni/AC before reaction	940	540	0.40	0.25	4-5
4.5%Ru-4.5%Ni/AC after reaction	435	240	0.39	0.12	4-5

(a) BET surface area; (b) micropore surface area; (c) total pore volume; (d) micropore volume; (e) BJH pore diameter calculated on desorption branch

**Figure S13.** XPS results of : (a) C 1s; (b) Ru 3p ; (c) Ni 1s in 4.5%Ru-4.5%Ni/AC recovered after reaction.

**Table S4.** Atomic concentration and abundance of Ru and Ni species of 4.5%Ru-4.5%Ni/AC recovered after reaction., based on XPS data

Catalyst	Ru (at%)	Ru oxidation state (%)	Ni (at%)	Ni oxidation state (%)
4.5%Ru-4.5%Ni/AC before reaction	14	Ru <sup>2+</sup> 100	7	Ni <sup>2+</sup> 94; Ni <sup>0</sup> 6
4.5%Ru-4.5%Ni/AC after reaction	7	Ru <sup>2+</sup> 100	10	Ni <sup>2+</sup> 97; Ni <sup>0</sup> 3

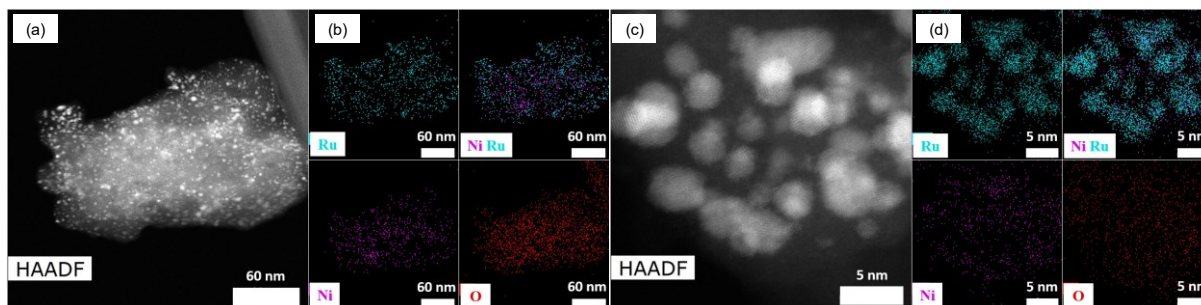


**Figure S14.** (a, c) HAADF-STEM; (b, d) TEM-EDS elemental mapping images of 4.5%Ru-4.5%Ni/AC recovered after reaction.

5.6.7. Characterisation of 7.5%Ru-36%W<sub>x</sub>C/AC

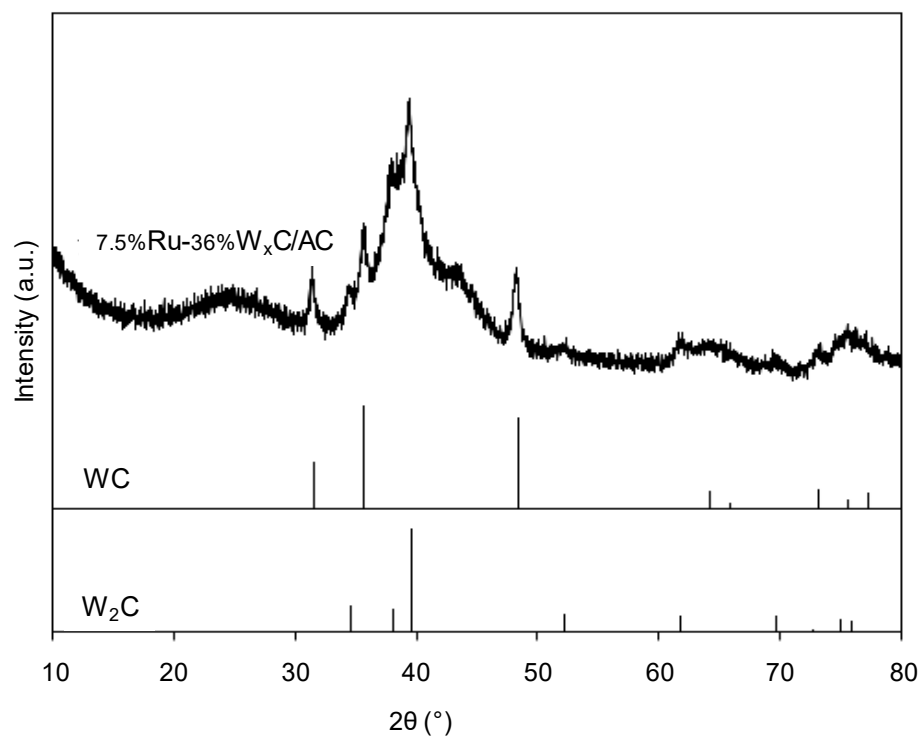
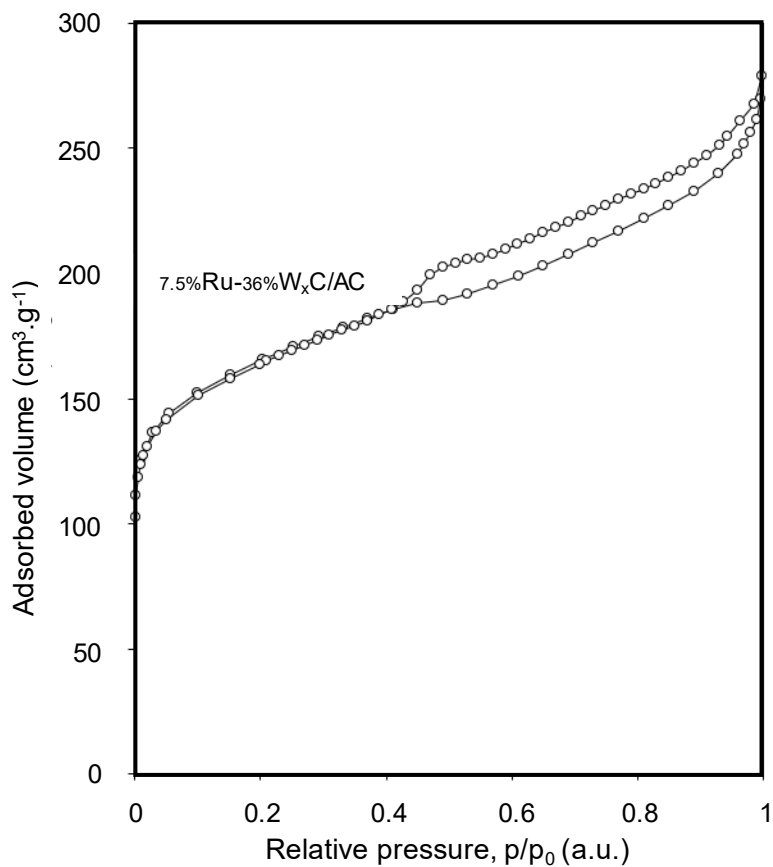


Figure S15. XRD pattern of 7.5%Ru-36%W<sub>x</sub>C/AC.



**Figure S16.** N<sub>2</sub> sorption isotherm of 7.5%Ru-36%W<sub>x</sub>C/AC.

**Table S5.** Textural properties of 7.5%Ru-36%W<sub>x</sub>C/AC

Catalyst	S <sub>BET</sub> <sup>(a)</sup> (m <sup>2</sup> .g <sup>-1</sup> )	S <sub>μ</sub> <sup>(b)</sup> (m <sup>2</sup> .g <sup>-1</sup> )	V <sub>p</sub> <sup>(c)</sup> (cm <sup>3</sup> .g <sup>-1</sup> )	V <sub>μ</sub> <sup>(d)</sup> (cm <sup>3</sup> .g <sup>-1</sup> )	d <sub>pore</sub> <sup>(e)</sup> (nm)
7.5%Ru-36%W <sub>x</sub> C/AC	595	375	0.20	0.15	4-5

<sup>(a)</sup> BET surface area; <sup>(b)</sup> micropore surface area; <sup>(c)</sup> total pore volume; <sup>(d)</sup> micropore volume; <sup>(e)</sup> BJH pore diameter calculated on desorption branch

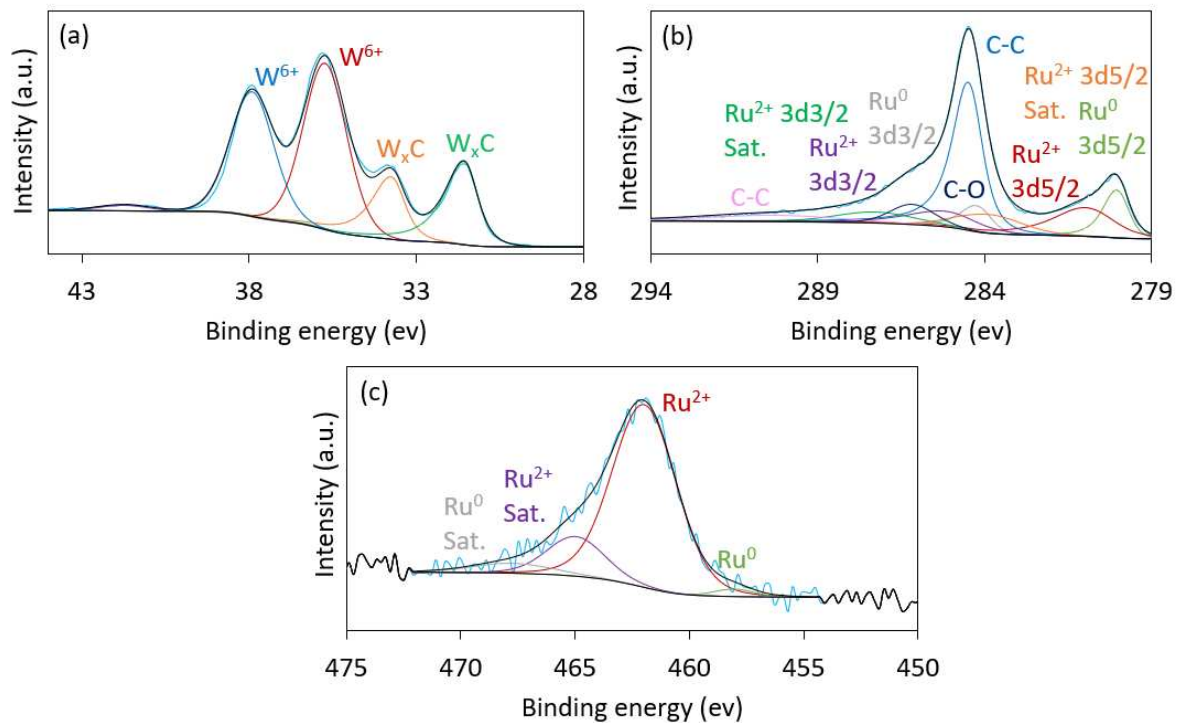


**Figure S17.** XPS results of: (a) W 4f; (b) C 1s; (c) Ru 3p in 7.5%Ru-36% $W_xC/AC$ .

**Table S6.** Atomic concentration and abundance of 7.5%Ru-36% $W_xC/AC$ , based on XPS data

Catalyst	Ru (at%)	Ru oxidation state (%)	W (at%)	W oxidation state (%)
7.5%Ru-36% $W_xC/AC$	10	$Ru^{2+}$ 93; $Ru^0$ 7	45	$W^{6+}$ 81; $W_xC$ 19



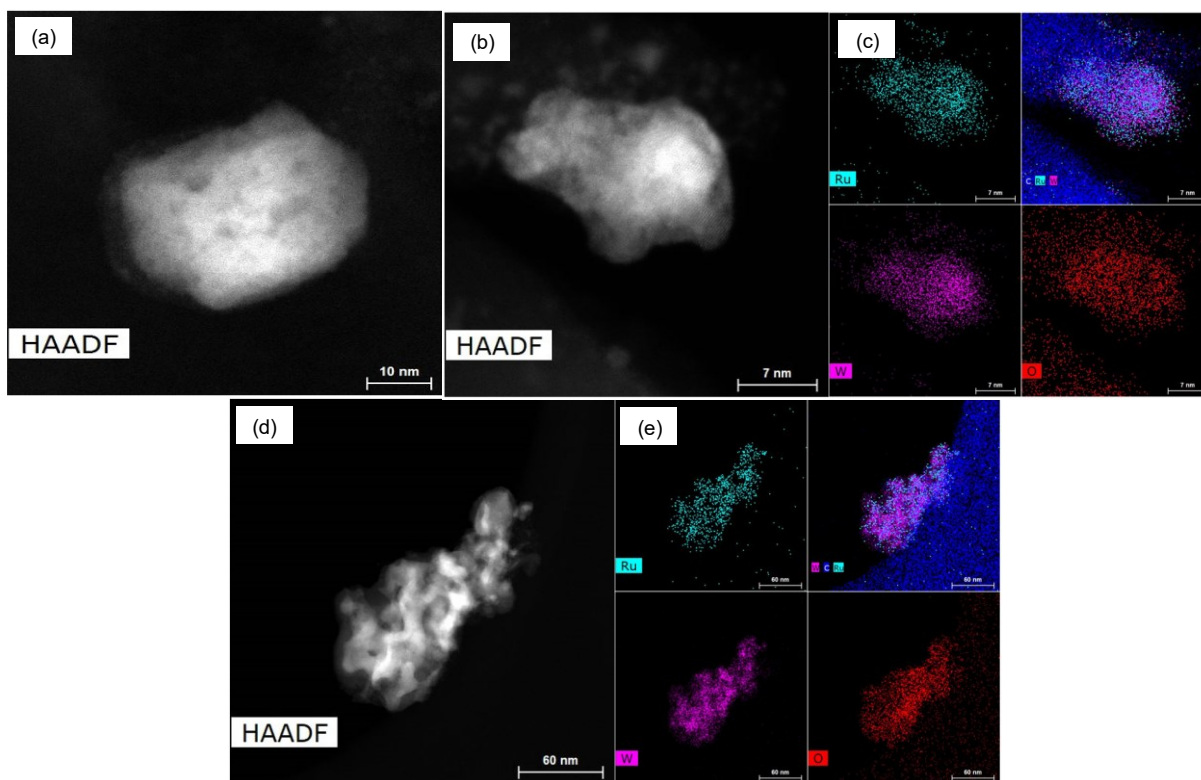


**Figure S18.** (a, b, d) HAADF-STEM; (c, e) TEM-EDS elemental mapping images of 7.5%Ru-36%W<sub>x</sub>C/AC.

### 5.6.8. Reactivity study of acetol biosourced precursors

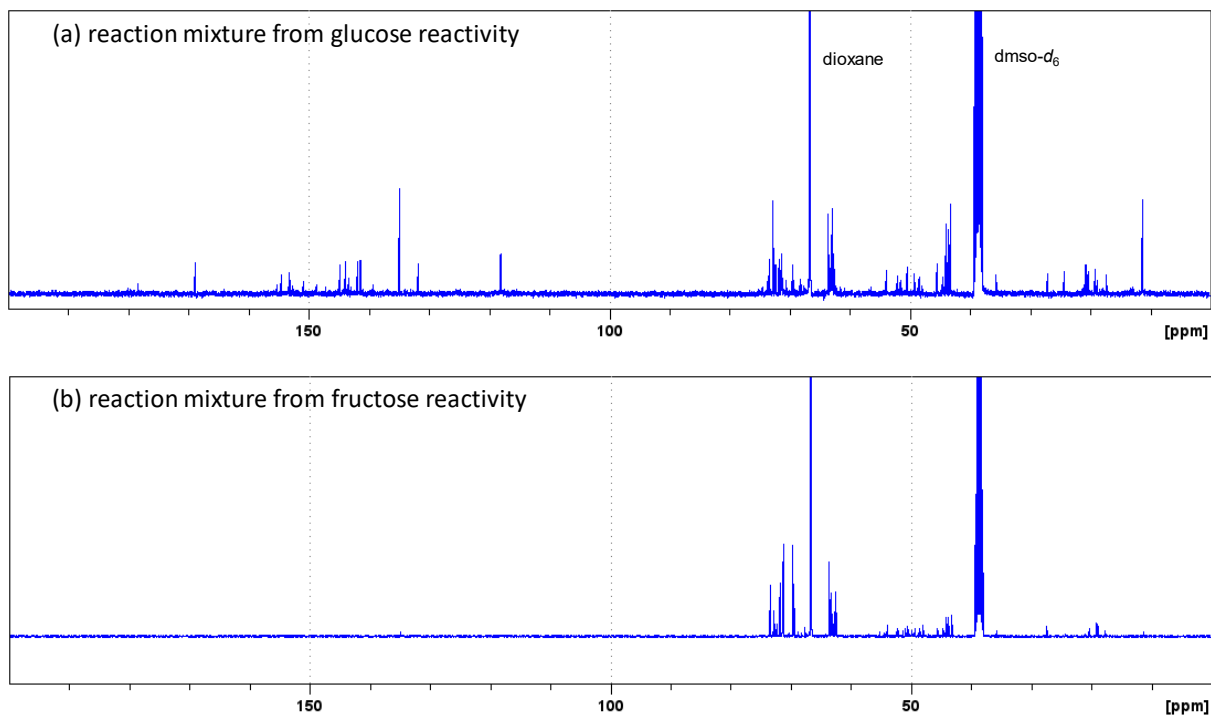


**Figure S19.**  $^{13}\text{C}$  NMR spectra in  $\text{DMSO-}d_6$  of the mixture after the reaction of (a) glucose and (b) fructose. Conditions: 10 g fructose, 1 g 7.5%Ru-36% $\text{W}_x\text{C}/\text{AC}$ , 300 mL of 25% aqueous  $\text{NH}_3$ , 75 bar  $\text{H}_2$ , 180  $^\circ\text{C}$ , 3 h.

### 5.6.9. References

- <sup>1</sup> J. Runeberg, A. Baiker and J. Kijenski, Copper catalyzed amination of ethylene glycol, *Appl. Catal.*, 1985, **17**, 309.
- <sup>2</sup> D. Cheng, Z. Wang, Y. Xia, Y. Wang, W. Zhang and W. Zhu, Catalytic amination of diethylene glycol with tert-butylamine over Ni-Al<sub>2</sub>O<sub>3</sub> catalysts with different Ni/Al ratios, *RSC Adv.*, 2016, **6**, 102373.
- <sup>3</sup> J.-M. Jehng, and C.-M. Chen, Amination of polyethylene glycol to polyetheramine over the supported nickel catalysts, *Catal. Lett.*, 2001, **77**, 147.
- <sup>4</sup> Y. Wang, S. Furukawa, S. Song, Q. He, H. Asakura and N. Yan, Catalytic production of alanine from waste glycerol, *Angew. Chem. Int. Ed.*, 2020, **59**, 2289.
- <sup>5</sup> Y. Wei, W. Ni, C. Zhang, K. You, F. Zhao, Z. Chen, Q. Ai and H.a. Luo, Highly Dispersed and stable hydrotalcite-derived NiCu/MgAlO alloy catalyst for efficient amination of cyclohexanol to cyclohexylamine in the vapor phase, *ACS Sustain. Chem. Eng.*, 2022, **10**, 13367.
- <sup>6</sup> X. Lei, G. Gu, Y. Hu, H. Wang, Z. Zhang and S. Wang, Structural requirements for chemoselective ammonolysis of ethylene glycol to ethanolamine over supported cobalt catalysts, *Catalysts*, 2021, **11**, 736.
- <sup>7</sup> C.-J. Yue, K. Di, L.-P. Gu, Z.-W. Zhang and L.-L. Ding, Selective amination of 1,2-propanediol over Co/La<sub>3</sub>O<sub>4</sub> catalyst prepared by liquid-phase reduction, *Mol. Catal.*, 2019, 477.
- <sup>8</sup> T. Takanashi, Y. Nakagawa and K. Tomishige, Amination of alcohols with ammonia in water over Rh-In catalyst, *Chem. Lett.*, 2014, **43**, 822.
- <sup>9</sup> C.-H. Yang, and J.G. Goodwin, *React. Kinet. Catal. Lett.* 1982, **20**, 13.

# Conclusion and perspectives

During this thesis work we made a contribution to the synthesis of glycols and their amino derivatives in a more sustainable production approach, from lignocellulosic biomass, using supported catalysts based on tungsten carbide nickel and ruthenium.

A very detailed study on the preparation of Ni-W<sub>x</sub>C/NC (x = 1 or 2) bimetallic catalysts was carried out. The hydrothermal catalytic conversion of cellulose induces severe deactivation of metallic catalysts, notably by acid leaching and sintering. In chapter 3, we studied a series of transition metals (nickel-tungsten) based catalysts supported on porous carbon (C) or N-doped porous carbons (NC). Porous (N-doped) carbon supports were prepared by hydrothermal conversion of natural polymers, followed by pyrolysis under inert atmosphere. Metals deposition was performed by wet impregnation. Hence, an amorphous nitrogen-doped carbon with a hierarchical porosity and surface area up to 286 m<sup>2</sup>.g<sup>-1</sup> was obtained from the hydrothermal-pyrolysis treatment of chitosan. The variation of the reducing atmosphere of the catalyst gave different phases of tungsten carbides; tungsten semi-carbide (W<sub>2</sub>C) and tungsten mono-carbide (WC). Regarding the application to cellulose conversion, molar yields up to 20% in ethylene glycol (EG) and 8% in propylene glycol (PG) were obtained by reaction at 245 °C for 1 hour using nitrogen-activated catalyst. When the catalyst was activated under hydrogen, the EG yield was increased to 51% while the PG yield remained low (5%). Very interestingly, the N-doping of carbon supports proved an interest by inducing a positive influence on the catalytic stability in recycling tests. Since high glycols yield was obtained, it's noteworthy that the basicity of the support didn't affect the acidity of the oxycarbide phase that operates the RAC reaction. The EG yield remained stable during 3 reaction cycles for the N-doped catalyst, as compared to the carbon catalyst, which presented an important deactivation after 3 cycles. For the latter the metal leaching in solution was the double of the one measured with the nitrogen doped material, but a high quantity of metals remained in the material. What explains this activity deterioration is the loss of surface active species that were much easier to loose, than in the case of the N-doped sample, since there were no nitrogenous groups to anchor them.

In chapter 4, we studied the possibility to obtain active and stable NiW-carbon catalysts for the hydrogenolysis of cellulose into glycols, starting from a MOF precursor, DUT-8(Ni) (DUT =

Dresden University of Technology). The preparation includes the hydrothermal synthesis of hybrid W@DUT-8(Ni), through a liquid-mediated or a vapor deposition route of a W precursor, Na<sub>2</sub>WO<sub>4</sub> or W(CO)<sub>6</sub>. The synthesis is followed by pyrolysis under an reductive or inert atmosphere (H<sub>2</sub> or N<sub>2</sub>) to obtain the Ni,W-carbon catalyst. For instance, an amorphous nickel-tungsten carbide nitrogen-doped carbon with a hierarchical porosity and high surface area of up to 112 m<sup>2</sup>.g<sup>-1</sup> was obtained. In addition, the variation of the reduction atmosphere of the catalyst yielded different NiW alloys. The mass ratio of W/Ni was between 0.3 and 1 for all materials, much lower than the one obtained in chapter 3, that was 6. Regarding the application, molar yields of up to 24% in ethylene glycol (EG) and 4% in propylene glycol (PG) were obtained at 245 °C and 1 hour reaction time using a Na<sub>2</sub>WO<sub>4</sub> derived catalyst. When W(CO)<sub>6</sub> was used, the EG yield was increased up to 46% and the PG yield to 9%. The glycols yield was lower than the one obtained in chapter 3, nevertheless it was higher than the yield obtained by using a MOF-derived system for the first time in the literature. The Ni<sub>0.96</sub>W<sub>0.04</sub> alloy seems to be the active phase since the best yields were obtained over the material containing this phase only. Notably, the MOF derived catalyst demonstrated a great catalytic stability in recycling tests where the EG yield remained almost constant during 3 reaction cycles.

Nitrogen-containing molecules are widely used for the synthesis of pharmaceuticals, polymers, surfactants, agrochemicals, and dyes. Among them, short-chain primary amines of interest include alaninol, 1-aminopropan-2-ol, and diaminopropane. Therefore, there is a great interest to form such amines from biosourced reactants. However, effective heterogeneous catalytic systems that allow amination under mild conditions in aqueous phase are still lacking. The amination of sugars and polysaccharides was very complex, therefore it was decided to focus on a cellulose intermediate amination, the acetol. This intermediate was selected thanks to its cheaper price than glycolaldehyde (that doesn't even exist in its monomer form, but in dimer form). Hence acetol amination allows the obtaining of more useful products from an industrial point of view. In chapter 5, we report the use of a highly efficient and robust catalyst system Ru-Ni/AC (AC: activated carbon), for the reductive amination of acetol. It's noteworthy that the materials of chapter 3 and 4 were not active to this reaction. Up to 55% amine yield was obtained including 50% of alaninol. The catalyst has been reused during 3 cycles demonstrating a good stability. It's of no surprise that the alaninol was obtained with the highest yield, since the carbonyl group of acetol is much more reactive than its hydroxyl group, resulting in a high selectivity towards the secondary amine. As a

prospective study, extension to the reactivity of (poly)carbohydrates (glucose, fructose, cellulose) has been attempted, with a lesser efficiency. Nevertheless, some alaninol formation has been obtained for the first time from cellulose following sequential reactions.

In order to improve and deepen this work, several study perspectives are possible. For instance, these new results should be correlated with the reactivity of cellulose, by *operando* characterizations to determine the exact nature of the active sites under reaction conditions. Secondly, a complete study on the wood resource should be done to evaluate the effect of morphology and composition, in particular the impact of the presence of lignin on the formation of the various products and on the effectiveness of the catalyst.

Regarding the final objective of the project, the formation of amine derivatives. It is important to reevaluate the composition of the catalysts and the reaction conditions in order to determine a possible route for the reductive amination of the more complex molecules that are sugars and polysaccharides.

Finally, from this fundamental work are issued the following valorization:

- Scientific publications

3 publications are being submitted at the moment :

**ACS Applied Nano Materials**

*“Cellulose conversion to glycols over carbon supported Ni-WxC nanocatalyst: N-Doping effect on catalyst stability”*

**ChemCatChem**

*“MOF-derived Ni-WxC/carbon catalysts: Application to cellulose conversion into glycols”*

**ChemSusChem**

*“Ru-Ni/C catalysts for the reductive amination of hydroxyacetone into propylene glycol-derived primary amines”*

- Presentation in international and national congresses :

**ISGC2022: Oral Presentation entitled**

*“Nickel Tungsten species supported on natural polymers-derived carbons for cellulose hydrogenolysis”*

**GECAT2023 : Poster Presentation entitled**

*“ Cellulose conversion to glycols over DUT-8(Ni) derived nickel-tungsten/carbons”*

**SCF2023: Oral Presentation entitled:**

*“New insights on the catalytic reductive amination of acetol over RuM/AC catalyst”*